



HAL
open science

Thermomechanical treatment of the $\text{Al}_{0.3}\text{CoCrFeMnNi}$ complex concentrated alloy

Dorian Hachet

► **To cite this version:**

Dorian Hachet. Thermomechanical treatment of the $\text{Al}_{0.3}\text{CoCrFeMnNi}$ complex concentrated alloy. Inorganic chemistry. Université de Bordeaux; Université libre de Bruxelles (1970-..), 2021. English. NNT : 2021BORD0265 . tel-03523320

HAL Id: tel-03523320

<https://theses.hal.science/tel-03523320>

Submitted on 12 Jan 2022

HAL is a multi-disciplinary open access archive for the deposit and dissemination of scientific research documents, whether they are published or not. The documents may come from teaching and research institutions in France or abroad, or from public or private research centers.

L'archive ouverte pluridisciplinaire **HAL**, est destinée au dépôt et à la diffusion de documents scientifiques de niveau recherche, publiés ou non, émanant des établissements d'enseignement et de recherche français ou étrangers, des laboratoires publics ou privés.

THÈSE EN COTUTELLE PRÉSENTÉE
POUR OBTENIR LE GRADE DE

DOCTEUR DE

L'UNIVERSITÉ DE BORDEAUX

ET DE L'UNIVERSITÉ LIBRE DE BRUXELLES

ÉCOLE DOCTORALE SCIENCES CHIMIQUES (UB)

FACULTE POLYTECHNIQUE (ULB) SPÉCIALITÉ MATERIAUX

Par Dorian HACHET

**TRAITEMENT THERMOMECHANIQUE DE L'ALLIAGE
CONCENTRE COMPLEXE $Al_{0.3}CoCrFeMnNi$**

Interactions entre déformation, recristallisation et précipitation

Sous la direction de Stéphane GORSSE (UB)
et de Stéphane GODET (ULB)

Soutenue le 22 novembre 2021

Membres du jury :

Mme DELPLANCKE Marie-Paule
M. MASSART Thierry
Mme FRACZKIEWICZ Anna
M. ALLAIN Sébastien
M. JACQUES Pascal
M. MITHIEUX Jean-Denis

Prof.	ULB	Président
Prof.	ULB	Secrétaire
Prof.	Mines de Saint Etienne	Rapporteur
Prof.	Université de Lorraine	Rapporteur
Prof.	UCL	Examineur
Dr.	APERAM	Examineur

Titre : Traitement thermomécanique de l'alliage concentré complexe $\text{Al}_{0.3}\text{CoCrFeMnNi}$

Résumé : Les alliages à haute entropie sont une nouvelle famille d'alliages métalliques. Plutôt que de se baser sur un élément principal, comme le fer dans les aciers, ces alliages sont constitués de plusieurs éléments principaux mélangés en des proportions similaires. De cette nouvelle famille, l'alliage de Cantor, de composition équimolaire CoCrFeMnNi , a émergé du fait de sa microstructure monophasée cubique face centrée et de l'activation du maillage pendant sa déformation. Ainsi, il est devenu une base pour de nouvelles optimisations chimiques et/ou microstructurales. Ce manuscrit s'intéresse à cet alliage auquel 6 at.% d'aluminium ont été ajoutés, permettant la formation d'une phase cubique centrée ordonnée appelée B2, plus dure que la matrice. Cet alliage est appelé C+Al. L'objectif est de comprendre comment cet alliage se comporte lorsque soumis à différentes étapes thermomécaniques utilisées conventionnellement en industrie, et comprendre l'influence de la phase B2. Plus précisément, les interactions entre déformation, recristallisation et précipitation seront étudiées lors d'essais de compression à chaud, de laminage à froid et de recuits. Un acier inoxydable austénitique de grade 304L et l'alliage de Cantor, sont utilisés comme points de comparaison pour identifier les spécificités des alliages à haute entropie et de C+Al. De façon générale, les alliages à haute entropie monophasés se sont révélés proche de l'acier 304L, avec toutefois un renforcement par solution solide plus élevé à même teneur en éléments interstitiel et des cinétiques de croissance de grains plus lentes. Les traitements thermomécaniques classiques et notamment le développement d'une nouvelle route procédé se sont révélés efficaces pour optimiser la distribution de la phase B2. Une large gamme de microstructures a ainsi été atteinte se traduisant en une large gamme de propriétés en traction repoussant le classique compromis résistance-ductilité.

Mots clés : Alliage à haute entropie, Traitement thermomécanique, Recristallisation, Précipitation, CALPHAD

Title : Thermomechanical treatment of $\text{Al}_{0.3}\text{CoCrFeMnNi}$ complex concentrated alloy

Abstract : High-entropy alloys have emerged recently as a new family of metallic alloys. Rather than being based on one principal elements, as iron in steels, these alloys are constituted of multiple principal elements mixed in similar ratios. From this new family, Cantor's alloy, of equimolar composition CoCrFeMnNi , stood out due to its single-phase face centred cubic microstructures and to the activation of twinning during its deformation. Hence, it became a base alloy for further microstructural and/or chemical optimisations. This manuscript focuses on this alloy with the addition of 6 at.% of aluminium to enable the formation of an ordered body centred cubic phase called B2, harder than the matrix. This alloy is called C+Al. The aim is to understand how this alloy behaves when submitted to conventional thermomechanical treatments used in industry, and the influence of the B2 phase. More precisely, the interactions between deformation recrystallisation and precipitation are studied during hot compression tests, cold rolling and subsequent annealing treatments. Closely related alloys, such as an austenitic stainless steel of grade 304L and Cantor's alloy, are used as references to identify the specificities of high-entropy alloys and of C+Al. Overall, single-phase high-entropy alloys revealed close to the 304L steel, with an increased solid solution strengthening at similar contents in interstitial elements and slower grain growth kinetics. Conventional thermomechanical treatments and more especially the development of a new processing route revealed successful to optimise the distribution of the B2 phase. A large range of microstructures was obtained translating to a wide range of tensile properties pushing forward the well-known strength-ductility trade-off.

Keywords : High-entropy alloys, Thermomechanical treatment, Recrystallisation, Precipitation, CALPHAD

Unité de recherche

Laboratoire 4MAT de l'université libre de Bruxelles situé à Avenue F.D. Roosevelt, 50
1050 Bruxelles, Belgique

Institut de chimie de la matière condensée de Bordeaux de l'université de Bordeaux
situé au 87 avenue du Docteur Schweitzer 33608 PESSAC cedex, France

All the figures of this manuscript are accessible in larger size by clicking on the mention [Full-size](#) at the end of their legend.

ACKNOWLEDGEMENTS

I first acknowledge Professors S. Allain (univ. Lorraine), M-P. Delplancke (ULB), A. Fraczkiwicz (Mines de Saint-Etienne), P. Jacques (UCL), T. Massart (ULB) and Doctor J-D. Mithieux (Aperam) to have accepted to be part of my PhD jury. I thank you in advance for your constructive comments and discussions.

I thank my two PhD supervisors, Professors S. Godet and S. Gorsse. They accompanied me all the way through the long walk of the thesis. Thank you for all the discussions and feedback, for all the reading and revisions, and for the trust that you granted me. Thank you also for passing on your love of metals – and everything that goes with it: recrystallisation, precipitation, dislocations... – and your love of clarity and conciseness. Special thanks to S. Godet who introduced me to J-L. Doumont's vision of scientific communication.

I acknowledge partner universities and labs that agreed to take from their time to perform experiments on my alloy. I first deeply thank Eng. M. Sinnaeve and his colleagues at the workshop of the IMAP lab in UCL for their patience and their flexibility. I could not have gone very far without the several ingots you managed to cast. I acknowledge Dr A. Schmitz and the team of CRM Liège for letting me use their dilatometer, but also for the debriefings. I thank Prof. J. Sietsma and Eng. N. Geerlofs from TU Delft and Prof. N. Bozzolo and Eng. G. Fiorucci from Mines ParisTech at Sophia Antipolis for the hot compression experiments. I thank them for the experiments they performed despite the difficult sanitary situation at this moment. I also acknowledge Prof. R. Banerjee from UNT and his team for accepting to perform APT experiments. Last but not least, I thank F. Peyrouzet for its rapidity on finding TEM slots in the facilities of CEA Grenoble when I needed it the most, but also for all our enriching interactions.

My PhD would not have been the same without the pleasant atmosphere of the 4MAT lab. Coffee breaks, lunch times, card games and all the events organised throughout the years contributed to making of these four years an enjoyable experience. I would like to truly thank all the members of the lab for their cheeriness, but also for their help and support. Moreover, I acknowledge Colin – and more especially for his *contre à l'aveugle* and the subsequent *danse de la victoire* –, Gilles, Omar, Didier, Suzanne, Patrizio for their help in the lab. Special thanks to Tiriana who always agreed to take from her time to help me, even outside of the context of my PhD.

This pleasant working atmosphere also contributed to hold many scientific discussions that made me push further my interpretations and expectations. In addition to my above-named supervisors, I would like to thank Loïc – that might have taken some interest in my alloy despite the absence of martensitic transformation –, Benjamin, Odeline, Gaëlle and Eve-Line. I also liked these discussions as I discovered other facets of metallurgy that I do not explore in this work.

An aspect that I particularly liked during these four years is supervising and working with interns and students. More than just a one-way teaching, they always brought their own visions and questioned my interpretations. Thanks to Alexandre, Sara and especially Murilo. I hope their experiences were as enriching as it was for me.

TABLE OF CONTENT

ACKNOWLEDGEMENTS	6
TABLE OF CONTENT	7
LIST OF ACRONYMS	10
0. INTRODUCTION AND MOTIVATION	12
0.1. A DEFINITION OF MULTICOMPONENT ALLOYS	12
0.2. A FOCUS ON CANTOR'S ALLOY AND ITS DERIVATIVES	15
0.3. ORGANISATION OF THIS MANUSCRIPT	17
CHAPTER 1. STATE OF THE ART	19
INTRODUCTION	19
1.1. EFFECT OF DEFORMATION ON MICROSTRUCTURES	20
1.1.1. <i>Stage A: Formation of 2D arrays of stacking faults</i>	21
1.1.2. <i>Stage B: The onset of twinning</i>	24
1.1.3. <i>Stage C: limitation of the twinning rate</i>	25
1.1.4. <i>Stage D: deformation at large strains</i>	25
1.1.5. <i>The influence of chemical inhomogeneity: from pure metals to MCAs</i>	26
1.2. THE THEORY OF RECRYSTALLISATION	27
1.2.1. <i>Movement of boundaries</i>	27
1.2.2. <i>Static recrystallisation</i>	29
1.2.3. <i>Dynamic recrystallisation</i>	30
1.3. PRECIPITATION	33
1.3.1. <i>Phase transformation (stability and kinetics)</i>	33
1.3.2. <i>Interactions with recrystallisation</i>	35
1.3.3. <i>Strengthening due to second phases</i>	36
CONCLUSIONS	39
CHAPTER 2. EFFECT OF PRECIPITATION ON THE HOT COMPRESSION OF C6Al	40
INTRODUCTION	40
2.1. MATERIALS AND METHODS	41
2.1.1. <i>Materials</i>	41
2.1.2. <i>Processing</i>	42
2.1.3. <i>Nomenclature</i>	43
2.1. RESULTS	43
2.1.1. <i>Before compression</i>	44
2.1.2. <i>Compression tests</i>	46
2.1.3. <i>Microstructures after compression of $\epsilon VM = 0.6$</i>	48
2.2. DISCUSSION	51
2.2.1. <i>Hot compression of 304L</i>	51
2.2.2. <i>Hot compression of C6Al</i>	53
2.2.3. <i>Comparison between 304L and C6Al</i>	55
CONCLUSIONS	57

CHAPTER 3. COLD ROLLING AND THE INTERACTIONS BETWEEN RECRYSTALLISATION AND PRECIPITATION DURING SUBSEQUENT ANNEALING	58
INTRODUCTION	58
3.1. MATERIALS AND METHODS.....	59
3.1.1. <i>Materials</i>	59
3.1.2. <i>Processing</i>	59
3.1.3. <i>Nomenclature</i>	60
3.2. RESULTS	60
3.2.1. <i>Development of the microstructure during rolling</i>	61
3.2.2. <i>Annealing treatments after H-CR58</i>	64
3.2.3. <i>Effect of CR intensity</i>	68
3.3. DISCUSSION.....	70
3.3.1. <i>Deformed state</i>	70
3.3.2. <i>Microstructure evolution during annealing</i>	72
3.3.3. <i>Influence of rolling intensity</i>	76
CONCLUSIONS.....	77
CHAPTER 4. A WIDE RANGE OF TENSILE PROPERTIES FROM THE SINGLE ALLOY C6AL	78
INTRODUCTION	78
4.1. MATERIALS AND METHODS.....	79
4.1.1. <i>Material composition</i>	79
4.1.2. <i>Processing</i>	79
4.1.3. <i>Nomenclature</i>	80
4.2. RESULTS	80
4.2.1. <i>Microstructures</i>	80
4.2.2. <i>Tensile properties</i>	82
4.3. DISCUSSION.....	84
4.3.1. <i>Strengthening contributions</i>	84
4.3.2. <i>Work-hardening</i>	87
CONCLUSIONS.....	90
CHAPTER 5. DEVELOPMENT OF MICROSTRUCTURES WITH INCREASED WORK-HARDENING THROUGH INTRAGRANULAR PRECIPITATION	91
INTRODUCTION	91
5.1. MATERIALS AND METHODS.....	92
5.1.1. <i>Materials</i>	92
5.1.2. <i>Processing</i>	93
5.1.3. <i>Nomenclature</i>	94
5.2. RESULTS	94
5.2.1. <i>Microstructures after RX and RX+CR</i>	94
5.2.2. <i>Comparison between RX+800°C and RX+CR+800°C</i>	94
5.2.3. <i>Tensile properties</i>	97
5.3. DISCUSSION.....	99
5.3.1. <i>Precipitation</i>	99
5.3.2. <i>Work-hardening behaviour</i>	101
CONCLUSIONS.....	109

CHAPTER 6. WHAT MAKES CANTOR AND C6AL SO SPECIAL (OR NOT)	110
INTRODUCTION	110
6.1. MATERIALS AND METHODS.....	111
6.1.1. <i>Materials</i>	111
6.1.2. <i>Processing</i>	112
6.1.3. <i>Nomenclature</i>	112
6.2. RESULTS	112
6.2.1. <i>Cold rolling step</i>	112
6.2.2. <i>Annealing treatments</i>	114
6.2.3. <i>Tensile tests</i>	115
6.3. DISCUSSION.....	117
6.3.1. <i>Deformed state</i>	117
6.3.2. <i>Recrystallisation kinetics</i>	118
6.3.3. <i>Tensile properties</i>	120
CONCLUSIONS.....	122
7. GLOBAL SUMMARY, CONCLUSIONS AND PERSPECTIVES	123
7.1. SUMMARY AND CONCLUSIONS.....	123
7.2. PERSPECTIVES	126
A. MATERIALS AND METHODS	128
A.1. FROM RAW MATERIALS TO SAMPLES	128
A.1.1. <i>Casting</i>	128
A.1.2. <i>Processing</i>	129
A.1.3. <i>Sample preparation</i>	130
A.2. CHARACTERISATION	130
A.2.1. <i>Analysis by X-ray diffraction</i>	130
A.2.2. <i>Microstructural characterization</i>	132
A.2.3. <i>Mechanical characterization</i>	136
A.3. PHASES OF INTEREST IN C+AL	137
A.3.1. <i>The FCC phase</i>	137
A.3.2. <i>The second phases</i>	138
B. RÉSUMÉ SUBSTANTIEL [FR]	140
REFERENCES	145

LIST OF ACRONYMS

Acronyms are listed below in alphabetic order.

Acronym	Full name
BCC	Body centred cubic
BSE	Backscattered electrons
C+Al	Al _x CoCrFeMnNi with x=5-6%
CALPHAD	Calculation of phase diagrams
CCA	Complex concentrated alloy
CR	Cold rolling
CTM	Compression-testing machine
dRV	Dynamic recovery
dRX	Dynamic recrystallisation
DSC	Differential scanning calorimetry
EBS	Electron backscattered diffraction
EDS	Energy dispersive spectroscopy
FCC	Face centred cubic
GND	Geometrically necessary dislocation
GOS	Grain orientation spread
HAGB	High-angle grain boundary
HEA	High-entropy alloy
ICP-OES	Inductively coupled plasma linked to optical emission spectroscopy
IPF	Inverse pole figure
K-S OR	Kurdjumov-Sachs orientation relationship
LAGB	Low-angle grain boundary
M	Taylor factor
MCA	Multicomponent alloy
nRXZ	Non-recrystallised zones
ODF	Orientation density figure
ODFN	Onset driving forces for nucleation
PCP	Precipitate
PF	Pole figure
PSN	Particle stimulated nucleation
RMS	Root mean square
RX	Recrystallisation stage
RXZ	Recrystallised zones
SE	Secondary electrons
SEM	Scanning electron microscope
SFE	Stacking fault energy
sRX	Static recrystallisation
SSD	Statistically stored dislocation
TC	Texture component
TEM	Transmission electron microscope
T _H	Homologous temperature
TMT	Thermomechanical treatment
TRIP	Transformation-induced plasticity
TTT	Transformation-temperature-time diagram
TWIP	Twinning-induced plasticity

UTS	Ultimate tensile strength
WHC	Work-hardening capacity (difference between UTS and YS)
WHR	Work-hardening rate
XRD	X-ray diffraction
YS	Yield strength
Z	Zener-Hollomon parameter

0. INTRODUCTION AND MOTIVATION

0.1. A definition of multicomponent alloys

From our forks to the most high-tech applications, metallic materials are found everywhere in today's society. Few of these materials are composed of a single chemical element. The wide majority are blends, called alloys, composed of combinations of many chemical elements. More than half of the periodic table is used nowadays to produce metallic alloys ¹. One single alloy typically combines eight of these elements mixed in various proportions. Until recently, alloys were all designed according to the same alloying strategy. An alloy is built around a principal chemical element that consists in 60 to 90% of the material. For example, iron is the principal element in steels. Small quantities of other elements, e.g. carbon, chromium, nickel, etc., are then added to tune the alloy properties according to its specific application. Such alloys are called conventional alloys. If represented on a ternary phase diagram, as in **Fig. 0.1**, this alloying strategy explores the edges of the triangle, in black. The example of the structural steel of grade A36 is given in the same figure. It is composed of iron with traces of carbon, silicon, copper, sulphur and phosphorus.

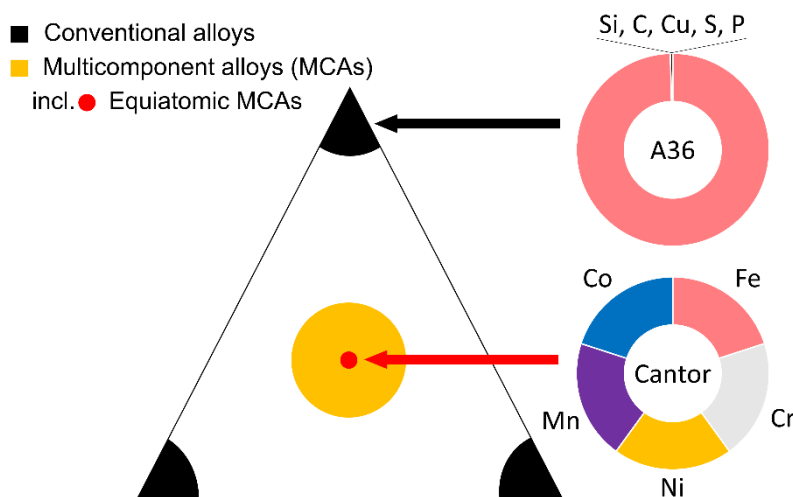


Fig. 0.1 Ternary phase diagram where conventional and multicomponent alloys are located. Chemical compositions of A36 and Cantor's alloy are given as examples [based on Li *et al.* ²]. [Full-size](#).

By freeing from this conventional alloying strategy, a new type of alloying paradigm arose. These alloys – designated as multicomponent ³ or multi-principal-element alloys ⁴ – are based on the combination of several principal elements in similar proportions. They correspond to the centre of phase diagrams (orange circle in **Fig. 0.1**). The example of Cantor's alloy, an equiatomic mixture of cobalt, chromium, iron, manganese and nickel is given in the same figure. These alloys were not considered so far because of the brittleness implied by their concentrated chemical compositions. Indeed, the commonly accepted Gibb's phase rule states that the number of stable phases increases with the number of constituents. A large number of stable phases is synonym of brittleness due to the increased boundary area between phases that often present different strengths. Hence, these compositions did not draw much interest. What made multicomponent alloys (MCAs) so interesting is that some compositions form a limited number of phases ⁵ or even proved single phase ³. The formation of these simple microstructures was explained by their large configurational entropy, also called high-entropy effect,

detailed next. Moreover, their large configurational entropy was supposed to induce lattice distortion, sluggish diffusion and cocktail effects, granting MCAs exceptional properties⁴. These three last effects are then discussed.

High-entropy effect – Configurational entropy relates to the number of possible atomic arrangements in the lattice. In supersaturated solid solutions, as observed in MCAs, the number of such arrangements is large, suggesting a large configurational entropy. The configurational entropy ΔS_{conf} is calculated with the following formula:

$$\Delta S_{conf} = -R \sum x_i \ln x_i \quad (\text{Eq. 0.1})$$

with R the gas constant and x_i the concentration of the component i in the mixture⁶. As an example, the configurational entropy is 0.07R in single-phase A36 and 1.6R in single-phase Cantor's alloy. It was proposed that this increase in entropy decreases the overall Gibb's free energy of supersaturated solid solutions, making them more stable. The designation *high-entropy alloy* comes from this principle. It led to the preference of equiatomic alloys (red dot in **Fig. 0.1**), called high-entropy alloys (HEA), maximizing configurational entropy^{3,5}. The high-entropy effect was recently reconsidered. Configurational entropy alone was shown not to be sufficient to predict the stabilization of supersaturated solid solutions over intermetallic compounds^{7,8}. Rather than being universal in MCAs, the stability of supersaturated solid solutions should be considered on a case-by-case basis. The reconsideration of this principle led to a significant widening of the multicomponent alloy window with increasing interest given to non-equiatomic compositions (orange circle in **Fig. 0.1**).

Lattice distortion, sluggish diffusion and cocktail effects – The three other effects were not formulated as answers to experimental findings. They were created as theoretical consequences of the concentrated chemical compositions of MCAs. They result from the juxtaposition of different chemical elements in the lattice of MCAs. Because these elements present different intrinsic properties, e.g. atomic size, lattice distortions arise (**Fig. 0.2**) inducing increased solid solution strengthening but also reduced electrical and thermal conductivities^{4,9}. In addition, this disordered structure is supposed to induce sluggish diffusion. Recent simulation and experimental data permitted to reconsider these two effects⁸. Overall, these new results highlight that a high number of constituents, i.e. a high configurational entropy, is not sufficient to result in superior properties. For example, Varvenne *et al.* highlighted that solid solution strengthening depends on the nature of the constituents much more than on their number^{10,11}. Moreover, recent diffusion studies contradict the sluggish diffusion effect, positioning MCAs within the range of diffusion velocities presented by conventional alloys. Finally, the cocktail effect encompasses the large alloying possibilities permitted by the new high entropy alloying strategy. Their concentrated compositions are supposed to offer combinations of properties that could not be achieved with conventional alloys.

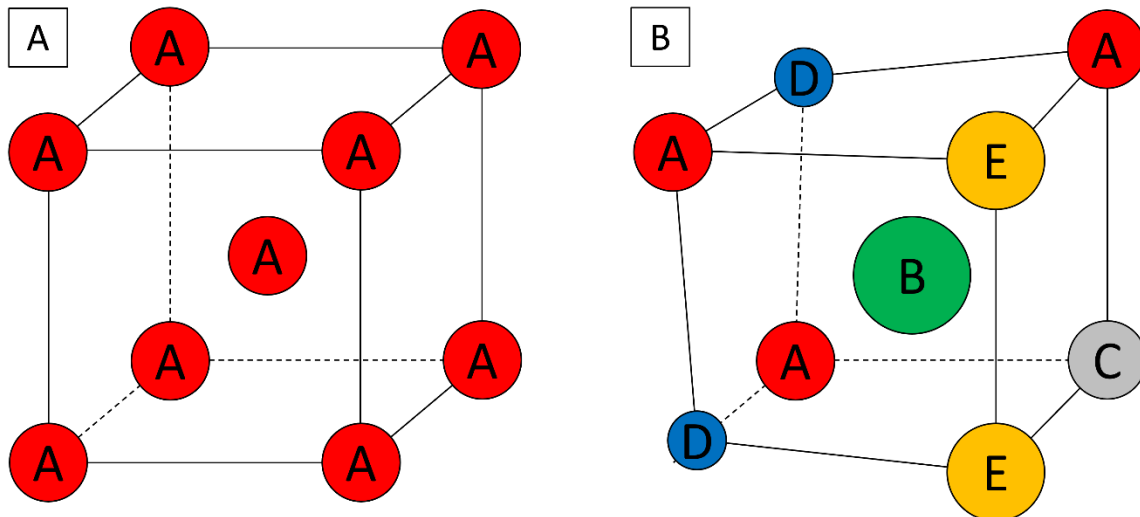


Fig. 0.2 (A) Body centred cubic (BCC) unit cell composed of a single chemical element A. (B) BCC unit cell composed of several chemical elements A-E presenting different atomic radii. Lattice distortions arise (Adapted from ¹²). [Full-size](#).

Even without concrete proofs, these effects became headlines of this new field bringing much attention to it. Their reassessment permitted to reconsider what makes a multicomponent composition interesting. While, at first, research was limited by narrow definitions – proportions of components below 35 at.%, more than five components, high configurational entropy – studies tend to expand their definitions of MCAs to encompass wider chemical and alloying complexities ¹³. Furthermore, research does not limit to HEAs anymore, with their single-phase microstructures, but also takes rising interest in complex concentrated alloys (CCAs), presenting multiphase microstructures. The denomination MCA includes both HEAs and CCAs.

The development of MCAs, and especially CCAs, opens a large compositional domain to explore. So far, 39 chemical elements out of the 82 found in nature were used to develop MCAs. From these 39 elements, there exists almost 4 million equiatomic compositions composed of 3 to 6 constituents, and much more if non-equiatomic compositions are also considered. New strategies are required to explore such large number of alloying possibilities. At first, this compositional screening was performed experimentally with the massive use of arc furnaces. The resulting as-cast materials were then characterized without further homogenization in more than two thirds of the cases ¹⁴. The unknown thermal history and the chemical inhomogeneity of as-cast materials biased the early research on MCAs resulting in early generalisations, such as the high-entropy effect. This strategy has been replaced in recent years by the use of thermodynamic simulations, such as CALPHAD and high-throughput methods ^{15,16}. The coupling of these two last methods permits to identify concentrated compositions optimising specific properties. Phase diagrams but also thermodynamic variables with their evolutions versus composition and temperature can be calculated. The reliability of such methods was assessed recently ¹⁷.

In attempts to reduce the complexity of this wide compositional domain, MCAs were separated in seven families ^{14,18,19}. Five out of these seven, along with their constitutive elements, are represented in **Fig. 0.3** adapted from Gorsse *et al.* ¹⁸. In the figure, each node represents one of the 110 equiatomic compositions considered. The precious metal MCAs, developed to concurrent the costly pure precious metals, and the MCAs containing interstitial elements, such as carbon or boron, complete the list of MCA families. These families are often extensions of conventional alloying families. For example, the family of 3d transition metal MCAs, centred around Cantor's alloy, is an extension of austenitic

stainless steels and nickel-based superalloys. The same consideration applies for MCA bronze and brasses, light metal MCAs (extension of light metal alloys such as aluminium or magnesium alloys), precious metal MCAs and refractory metal MCAs. In each case, the new multicomponent compositions were developed to answer specific needs that were unsuccessfully fulfilled by conventional alloys. Promising results were already obtained on MCAs related to resistance to high temperature oxidation for aeronautic purposes^{20,21}, resistance to irradiation to be incorporated in the cores of nuclear plants^{22–24} or exceptional toughness at cryogenic temperatures^{25–27}. More emphasis is now given to this last promising result, obtained on Cantor's alloy.

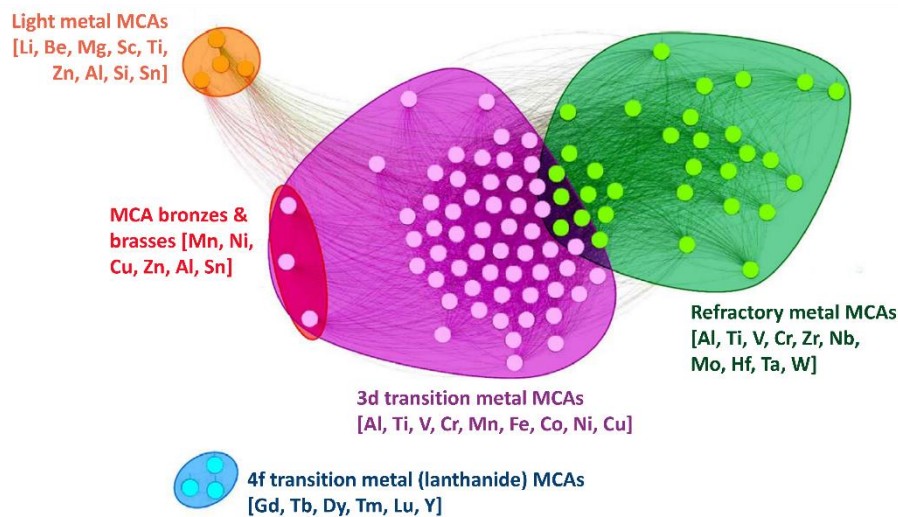


Fig. 0.3 Alloy network analysis (ANA) of 110 equiatomic CCAs. Each node corresponds to a unique composition. The compositions sharing one or more elements are linked by a line. The closer the compositions of CCAs, the closer they are represented forming five alloy families¹⁸. [Full-size](#).

0.2. A focus on Cantor's alloy and its derivatives

Cantor's alloy is an equiatomic mixture of cobalt, chromium, iron, manganese and nickel. Surprisingly, it presents a single-phase face centred cubic (FCC) microstructure, first observed by Brian Cantor in 2004³. In addition to its single-phase microstructure, it exhibits interesting tensile properties, especially at cryogenic temperatures.

Usually, lowering the deformation temperature typically results in an increase in strength coupled to a reduction in ductility. In the best cases, cryogenic steels have constant ductility from ambient to cryogenic temperatures^{28–30}. Cantor's alloy proved experimentally to depart from this conventional behaviour. From 20°C to -196°C, both its strength and its ductility increase²⁵. These remarkable properties at cryogenic temperatures are attributed to the softness of its single-phase FCC microstructure³ and to the intensification of mechanical twinning when temperature decreases^{25,31}.

Due to these remarkable mechanical properties, but also to its early development in the history of MCAs, Cantor's alloy has drawn much interest from the scientific community. It remains the most widely studied MCA so far. On top of that, it became a base for further chemical optimisations.

Numerous optimization strategies have been applied on Cantor's alloy up to now, taking strong inspirations from those used on conventional alloys nowadays. Examples are the addition of interstitial elements, such as carbon or boron^{32–36}, or the addition of small quantities of new elements^{37–47}. The result of this diversification is illustrated in **Fig. 0.4A** compiling the tensile properties from 62 publications^{25,26,32,34–58,58–90}. On this graph, and similarly in **Fig. 0.4B**, the engineering tensile strength and maximum engineering strain levels, called total elongations in the figures, are reported.

This choice was adopted to fit with the tensile properties of the conventional alloying families given in background. It was adopted despite the non-standard sizes of some tensile specimens used in the references that could alter the stress/strain measurements after necking. These figures are rather to give a general idea of the shapes of the envelopes rather than a precise point to point comparison.

While tensile properties of Cantor's alloy are restricted to a narrow envelope (in black), the properties of its derivatives expand (in blue), covering much of the conventional alloy property range. Several of these new compositions manage to push back the strength-ductility trade-off, extending this second envelope towards higher strength and ductility, i.e. towards the top right of the diagram.

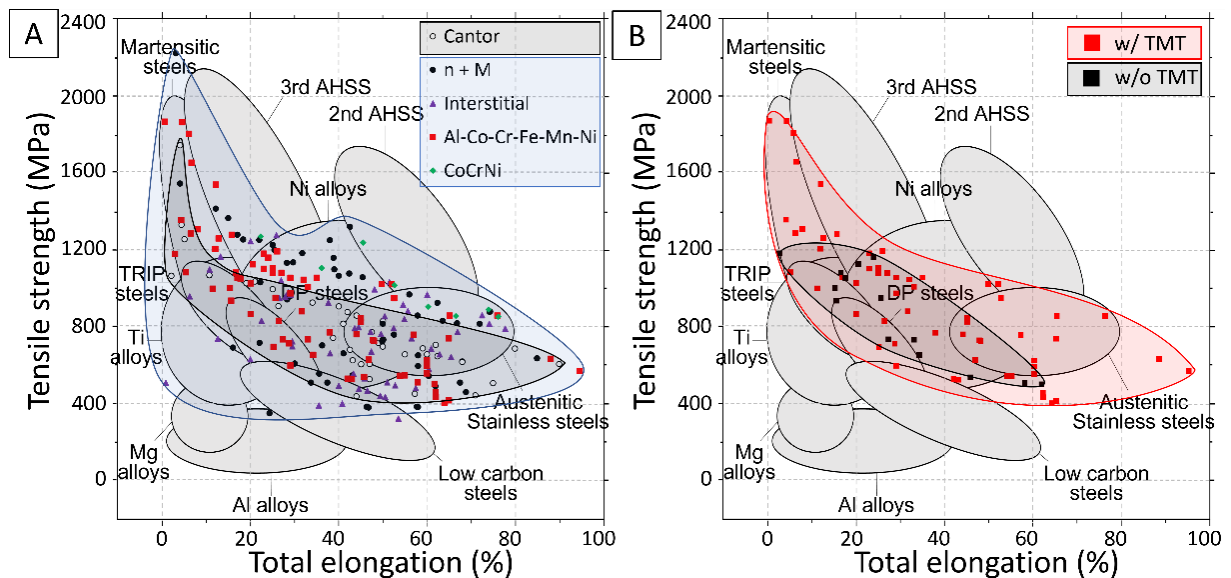


Fig. 0.4 (A) Room temperature engineering tensile strength vs total elongation for Cantor's alloy and its derivatives (n stands for non-equiatomic compositions and M for compositions with chemical substitutions). (B) Same graph limited to the Al-Co-Cr-Fe-Mn-Ni system presenting the tensile properties with (w/) or without (w/o) thermomechanical treatment (TMT). For comparison purposes, the tensile properties of the conventional alloying families are given in background. 2nd and 3rd AHSS stand for the two generations of advanced high-strength steels, DP steels for dual-phase steels and TRIP steels for transformation-induced plasticity steels. [Full-size.](#)

The different alloying strategies considered in **Fig. 0.4A** aim at pushing back the strength-ductility trade-off through different mechanisms. First, research has focused on the strengthening of the supersaturated FCC solid solution of Cantor's alloy through the exploration of non-equiatomic compositions and the addition of interstitial elements. This strategy aims at increasing lattice distortion and solid solution strengthening. By remaining single phase FCC, the obtained alloys benefit from a large toughness and the activation of twinning during deformation, as observed in Cantor's alloy.

Other alloying strategies aim at increasing strength through the stabilisation of new phases within the FCC matrix. This is mainly achieved via the substitution of elements in Cantor's alloy or through the addition of small quantities of new elements. The addition of aluminium in Cantor's alloy, i.e. the Al-Co-Cr-Fe-Mn-Ni system, or in its sub-systems has received the largest interest, with a particular focus on $\text{Al}_{0.3}\text{CoCrFeNi}$, containing 7 at.% of aluminium. Four different second phases, in addition to the FCC matrix, were observed in this system^{61–66,91}: Cr-rich body centred cubic (BCC), (Ni, Al)-rich B2 (ordered BCC), (Ni, Al)-rich L1_2 (ordered FCC) and the σ phase (Cr-rich tetragonal). Thermodynamic calculations enabled to understand in which temperature ranges these phases are stable, and under which

conditions they could form ^{65,92}. Thermomechanical treatments (TMT) are used on these multiphase systems in order to control the formation of the desired phases, their size, morphology and fraction.

TMT, besides shaping the material into the desired dimensions, has been extensively applied to MCAs in the last 10 years to optimise microstructures. **Fig. 0.4B** shows the effect of TMT on the tensile properties of 22 MCAs belonging to the Al-Co-Cr-Fe-Mn-Ni system ^{38,39,41,43–47,56–69}. While the data points corresponding to as-cast materials (i.e. without TMT corresponding to the black envelope) are restricted to the centre of the figure, TMT permitted a widening of the property range, especially to higher strength or to larger ductility (red envelope).

TMT consists in a sequence of deformation and annealing steps. Deformation stages primarily form the material into the desired shape. It also stores energy in the material in the form of defects. This energy determines the activation and kinetics of microstructural transformations, such as precipitation and softening mechanisms. These can activate during deformation or during subsequent annealing treatments. The choice of the annealing temperature and time determines the nature of the precipitates formed, if any, but also their fraction, morphology and size. Controlled TMT allows complex microstructures such as lamellar ^{44,45,61,69}, heterogeneous ^{58,59,67} or equiaxed ^{63–65} to be obtained. By varying TMT, variations in yield strength from 160 to 1800 MPa were observed in Al_{0.3}CoCrFeNi ⁶⁶, resulting from the presence of different populations of precipitates in more or less deformed FCC matrices.

The properties obtained after TMT, including those of the Al-Co-Cr-Fe-Mn-Ni system, are promising. Nonetheless, the MCAs designed and characterized so far are still far from equalling those of some conventional alloying families, such as second and third generations of advanced high-strength steels (**Fig. 0.4**). To pursue the quest for materials pushing back the strength-ductility trade-off, but also to better understand the metallurgy of MCAs, this manuscript proposes to focus on the multicomponent composition Al_{0.3}CoCrFeMnNi, including 6 at.% of aluminium. It will be referred to as C+Al hereafter. The addition of aluminium in the Cantor alloy enables the formation of the B2 phase in the FCC matrix, as already reported in this system ⁹³. The choice of the 6 at.% of aluminium is based on two opposing criteria. First, at aluminium contents lower than 7 at.%, the alloy maintains a single-phase FCC domain at high temperature. The presence of this single-phase FCC domain is essential to be able to easily form the material through rolling or other processes. Secondly, the volume fraction of second phases, and hence their strengthening propensity, increases with increasing aluminium content. The choice of the 6 at.% of aluminium is hence a compromise between these two criteria with an aluminium content as high as possible while maintaining a wide single-phase FCC domain at high temperature. Moreover, C+Al is kept as close as possible to Cantor's alloy to benefit from the wide literature on this alloy as a base reference ^{25,31,94–98,51,55,99,100,48,101}.

0.3. Organisation of this manuscript

This manuscript focuses on the behaviour of C+Al when submitted to thermomechanical processing. We will follow the microstructural transformations of C+Al throughout a conventional processing route used in industry. We chose to focus on the process of rolling accounting for half of today's steel production ¹⁰². The investigated processing route includes hot and cold rolling, and subsequent annealing treatments. Six chapters compose this manuscript. They are briefly presented below.

Chapter 1

The current knowledge on the evolutions of microstructures during TMT is detailed in this chapter. It focuses on the specific case of FCC materials with low stacking fault energy (SFE). This chapter is divided in three parts: evolution of microstructures during deformation, recrystallisation and precipitation.

Chapter 2

This chapter focuses on the behaviour of C+Al when submitted to compression tests between 900 and 1100°C. The results obtained on C+Al are compared to those obtained on an austenitic stainless steel of grade 304L to better understand the specificities of the complex concentrated alloy.

Chapter 3

This chapter focuses on the evolution of microstructures during cold rolling and subsequent annealing treatments. A special focus is given to the understanding of the interactions between recrystallisation and precipitation that arise during annealing treatments at around 900°C.

Chapter 4

Based on chapter 3, three microstructures are selected to represent the wide range of microstructures observed. Their tensile properties are the interest of this chapter. The strengthening and deformation mechanisms are identified and correlated with the corresponding microstructures.

Chapter 5

An innovative processing route is developed with the aim of coupling large yield strength and large work-hardening capacity. The work-hardening response is modelled analytically to identify the different contributions of the various strengthening and work-hardening mechanisms.

Chapter 6

The final chapter focuses on the comparison of C+Al with three other FCC alloys presenting low SFE and similar chemical compositions. Deformation by cold rolling, recrystallisation and grain growth kinetics, and tensile properties are discussed.

This manuscript ends with a summary and the main conclusions that can be made on the behaviour of C+Al during TMT. The advantages and disadvantages of the studied composition C+Al are given, especially when compared to conventional alloys or other widely studied MCAs. Recommendations are given for the future design of MCAs. Perspectives are drawn for further work aiming at pushing forward the study on C+Al or other closely related compositions. Finally, in annexe A at the end of the manuscript, the materials and methods used are presented.

Chapter 1.

STATE OF THE ART

Introduction

Metallic materials consist in the juxtaposition of assemblies of crystals, called grains. In each grain, atoms are bound to each other through metallic bonds and organised as specific crystalline structures. Three of these are of interest in the context of this work: face centred cubic (FCC), body centred cubic (BCC) and tetragonal. Each grain might differ from its neighbours: first by its crystalline structure; but also by its orientation, defined as the rotation from a macroscale reference to the grain axis systems.

Metallic materials rarely contain a single chemical element. They almost always are blends, also called alloys. The crystalline structures defined above are hence composed of blends of atoms of different elements. The local chemical composition is used to measure the repartition of the elements in the lattice. In this work, it is expressed with atomic fractions (number of atoms of one chemical element measured in a limited volume divided by the total number of atoms in this volume), if not indicated otherwise. The coupling between a crystalline structure and a chemical composition defines a *phase*. These might be called directly by the name of their crystalline structure, as it will be the case here for the FCC phase, but they might also have a specific name, as it will be the case for the σ phase.

Properties of metallic materials are defined by their chemical composition but also by their microstructural features. These features include the volume fractions of the different phases present, their size and morphology. The presence of defects, such as dislocations, also play a role. In order to control these features, thermomechanical processing is often used. It consists in a series of deformation and/or annealing stages at the end of which the treated material reaches the desired structure and properties. During these steps, the microstructure experiences various transformations. Understanding and modelling these structural transformations have been of great interest in the past century. This chapter details the current understanding of three of these transformations: deformation, recrystallisation and precipitation, that are addressed in the three subsequent sections.

1.1. Effect of deformation on microstructures

When submitted to an external stress, a material accommodates by a change in its shape. This change in shape is first reversible – it is called elasticity. If the load is released, the material comes back to its initial shape without any damage. For some types of materials, this stage results in large and observable strains, e.g. up to 1000% for elastomers. For others, such as metals, elasticity is imperceptible. Steels yield at strains much lower than 1%. But all materials present this elastic regime.

When elasticity becomes insufficient to accommodate the external loading, plasticity begins. From this point on – called the yield strength –, the change in shape becomes irreversible. In metallic materials, this irreversibility comes from the displacement of dislocations. These dislocations are linear defects in the arrangement of the metallic lattice structure. They are characterized by their Burgers vector \vec{b} , defining the slip direction, and their unit line \vec{l} . Perpendicular \vec{b} and \vec{l} define an *edge* dislocation. Parallel \vec{b} and \vec{l} define a *screw* dislocation. In practice, dislocations often present mixed character. The plane defined by \vec{b} and \vec{l} is the slip plane in which dislocations move. Pure screw dislocations do not present a defined slip plane as their \vec{b} and \vec{l} are parallel. The movement of dislocations involves the breaking and formation of atomic bonds, explaining its irreversibility. It results in the step-by-step displacement of the slip planes on each-other. The sum of these slip steps results in a macroscopic deformation that accommodates the applied stress.

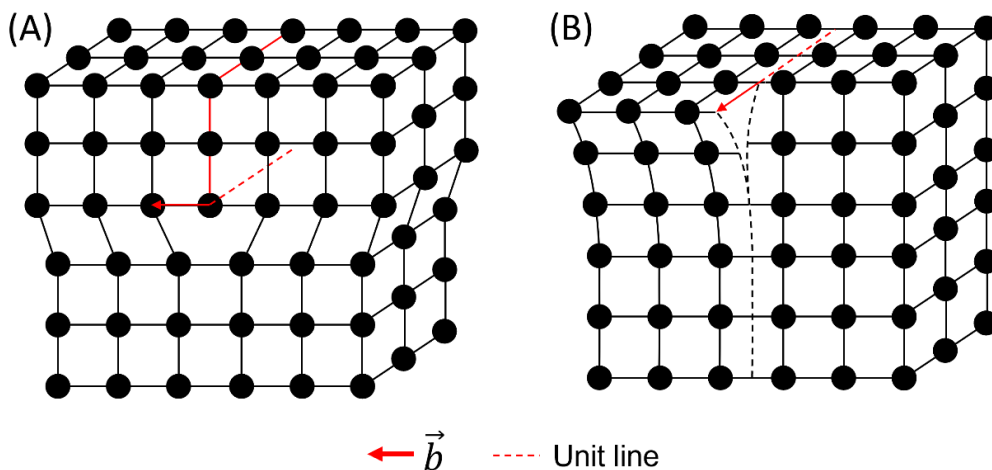


Fig. 1.1 (A) Edge dislocation. (B) Screw dislocation. The dotted red line indicates the unit line. The slip plane is determined by Burgers vector and unit line. [Full-size](#).

Other deformation mechanisms, such as the formation of stacking faults or of mechanical twins, might be activated at different stages of straining. Their activation depends on the deformation conditions, i.e. temperature, strain and strain rate, but also on material parameters, such as the stacking fault energy (SFE). All of these deformation mechanisms contribute to the macroscopic deformation of the material and to its work-hardening. This last parameter is often used to describe how a material behaves when deformed. It is defined by the amount of stress required to deform the material for a small deformation step. It increases with strain but its rate of increase evolves throughout deformation. It is common to plot its strain derivative ($d\sigma/d\varepsilon$) versus true strain or true stress. **Fig. 1.2** presents typical tensile curves of low (in red) and high (in black) SFE materials and their corresponding work-hardening rates (WHR). In the case of materials with low SFE, it is typically divided in four stages, A to D. This section details how the deformed structure develops by describing these four stages in four sub-sections. The particular case of a FCC material presenting a low SFE and deformed at room temperature is studied here.

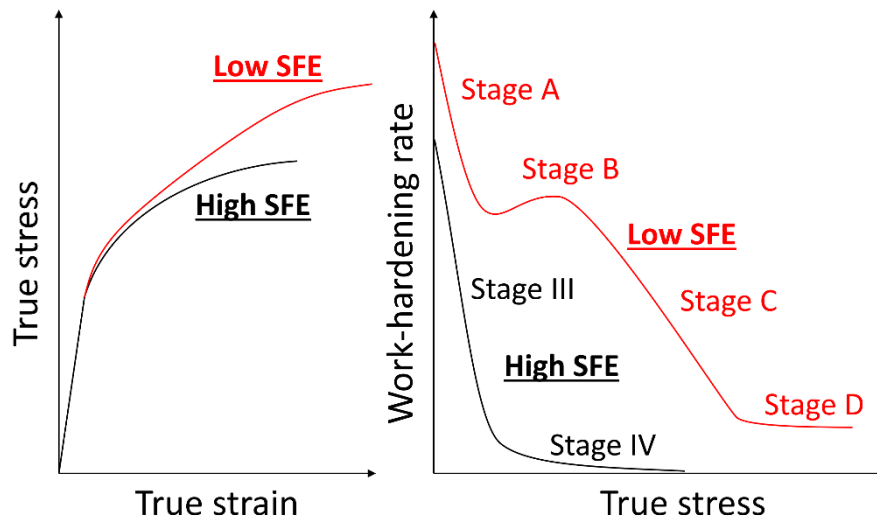


Fig. 1.2 Schematic representation of work-hardening regimes in polycrystalline FCC metals (Adapted from ¹⁰³). [Full-size.](#)

1.1.1. Stage A: Formation of 2D arrays of stacking faults

During the first stage of plastic deformation, more and more dislocations form from different sources, i.e. grain boundaries, interfaces with precipitates or inclusions, and Frank-Read sources within grains.

Newly formed dislocations are called *perfect* dislocations. They glide on most densely packed planes and directions, where their movement is facilitated by the proximity of atoms. In the case of FCC crystals, slip systems are $\{111\}$ planes with Burgers vectors of $\frac{a}{2} \langle 110 \rangle$, a being the lattice parameter. Dislocations are able to glide on a specific slip system if the applied shear stress exceeds the *critical resolved shear stress*, τ_c , of this slip system. The activation of a specific slip system depends on the intensity and direction of the applied stress.

The glide of dislocations on their slip systems first results in a displacement. $\{111\}$ planes glide on each other by steps corresponding to the norm of the Burgers vector of the involved dislocations. At the same time, the collegial movement of dislocations on multiple neighbouring glide planes results in a local rotation of the lattice. Starting from the undeformed state (**Fig. 1.3A**), a displacement alone would result in a situation similar to case **Fig. 1.3B** where an additional displacement sideways, in the direction of slip, adds to the accommodation of the vertical applied strain. Such behaviour is not observed on single crystals. This is the coupling of displacement and rotation that results in the accommodation of the external strains (**Fig. 1.3C**). The consequences of dislocation slip on the surface of a single crystal are shown in (**Fig. 1.3D**).

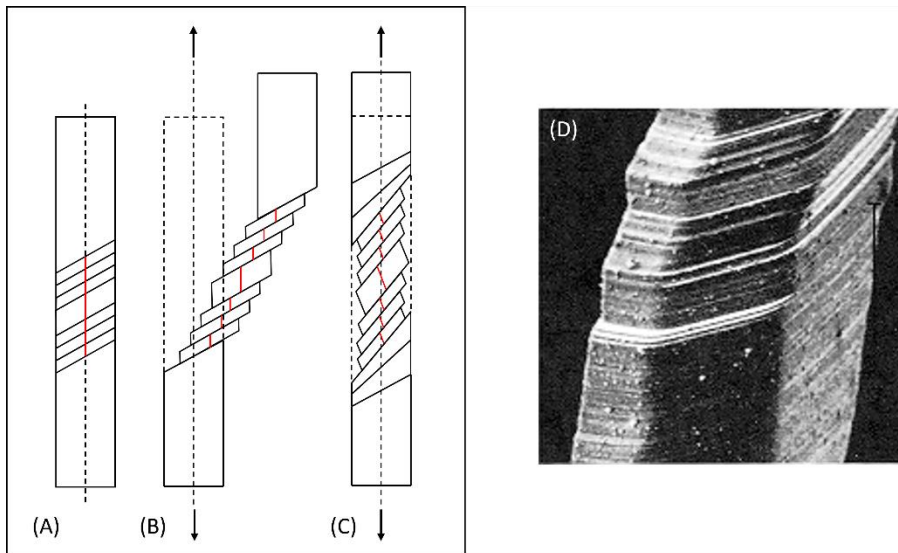


Fig. 1.3 (A-C) Sketches illustrating dislocation slip. (A) Undeformed state, (B) Displacement without rotation and (C) Displacement and rotation. The red line highlights the influence of rotation. (D) Typical slip marks on the surface of a single crystal deformed in tension¹⁰⁴. [Full-size](#).

In addition to slip, occurring on a specific slip system, dislocations are able to cross-slip or to climb in order to jump to another slip system. Screw dislocations, that do not present a defined slip plane, can cross-slip from their $\{111\}$ slip plane to another $\{111\}$ plane. Edge dislocations can climb perpendicularly to their Burgers vectors to attain another slip plane. This last mechanism requires the diffusion of vacancies and hence occurs only at high temperature.

To accommodate a randomly oriented external strain, multiple slip systems must operate simultaneously. The orientation, number and intensity of the activated slip systems are determined by the orientation of the crystal and of the applied strain. The shape change is then accommodated by the sum of the individual displacements and rotations¹⁰⁵.

The multiplication of dislocations on multiple slip systems results in their interactions. First, dislocation stress fields induce their attraction and repulsion depending on their orientation. It results either in the annihilation of dislocations, if two opposite dislocations meet on the same slip system, or in the formation of dislocation arrangements, such as dislocation dipoles or tilt boundaries. These phenomena are called dynamic recovery (dRV). Secondly, dislocations of different slip systems might intersect. The result of such intersection, also called jog, presents a slip system with a larger critical resolved shear stress. They are hence often immobile.

Dislocation arrangements and jogs are obstacles for further slip. Their multiplication on a slip system results in the increase in its critical resolved shear stress. A larger shear stress on this slip system is hence required for dislocations to keep moving on this slip system. This phenomenon is called *work-hardening*. The dislocations forming obstacles and those piled-up on them are stored within the lattice. They constitute the *stored energy*, i.e. the energy stored in the form of defects (dislocations, jogs, etc...) in the material during deformation¹⁰⁶.

The crystallographic orientation of a grain, and hence of its slip systems, determines its stored energy¹⁰⁷. The Taylor factor (M) depicts this link¹⁰⁸. A grain presenting a large Taylor factor requires a large amount of slip, stores efficiently defects and hence presents a large stored energy after deformation. It depends on the deformation mode.

In practice, the *perfect* dislocations might dissociate in two *partial* dislocations. These partials glide on the same planes as their parent and present Burgers vectors of $\frac{a}{6} \langle 112 \rangle$. For example, the perfect dislocation with slip system $[011]_{(1\bar{1}1)}$ might dissociate as follows:

$$\frac{a}{2}[011]_{(1\bar{1}1)} \rightarrow \frac{a}{6}[121]_{(1\bar{1}1)} + \frac{a}{6}[\bar{1}21]_{(1\bar{1}1)} \quad (\text{Eq. 1. 1})$$

This dissociation is controlled by the material SFE, being favoured at low values of SFE. This parameter is first function of chemical composition. Some elements, such as manganese, decrease the SFE, while others, like aluminium, present an opposite effect. Moreover, the SFE is also function of temperature, increasing with increasing temperature. Dissociations are hence less likely at high temperatures, e.g. during hot rolling, than at low temperatures, e.g. during tensile testing at cryogenic temperatures. The value of the SFE determines the activation of additional deformation mechanisms such as mechanical twinning or deformation-driven phase transformation. This parameter can be assessed experimentally, for example by measuring the distance between dislocation partials in the TEM. However, and especially in MCAs, this distance can significantly vary throughout the material resulting in large uncertainties in the measured SFE^{109,110}. SFEs are more readily assessed using *ab initio*^{111,112} or thermodynamic calculations¹¹³, using for example the formula from Olson et Cohen¹¹⁴.

At the difference of a perfect dislocation, the Burgers vector of a partial dislocation does not correspond to a vector of the FCC lattice; i.e. a vector linking two equivalent atomic positions. Hence, the dissociation into partials results in the formation of a local fault in the stacking of crystallographic planes, called stacking fault. The leading partial creates this fault while the trailing partial corrects it, leaving behind a non-faulted structure.

Stacking faults might interact with dislocations or other stacking faults. These processes result in the formation of immobile defects, such as Lomer-Cottrell locks, that hinder further slip on their slip planes in the same way as dislocation jogs do. In materials presenting large SFE, perfect dislocations bypass obstacles by cross slipping to other slip planes. In the case of materials with low SFE, partials must first recombine in a perfect dislocation before being able to cross slip. Cross slipping hence requires larger stress and is less likely. Consequently, dislocations mainly remain in their 2D slip planes and do not interact with dislocations in others, forming 2D arrays of stacking faults¹⁰⁶. The same phenomenon limits dRV in FCC alloys with low SFE.

As the deformation temperature increases, the mobility of perfect dislocations increases¹¹⁵. They are also less likely to dissociate into partials. It results in easier cross slipping between slip planes. Dislocation climb also activates when vacancy diffusion becomes large enough. Hence, materials with low SFE can experience a transition from the formation of 2D arrays of stacking faults with limited dRV at low temperature, to a more homogeneous deformation with extended dRV at larger temperatures.

The evolution of stress between deformation is a balance between work-hardening and dRV. The multiplication of dislocations causes work-hardening but also raises the driving force for dynamic recovery. In stage A, dRV increases with strain inducing the observed decrease in WHR¹¹⁶. It is similar to the stage III observed in materials with large SFE where dRV is also activated¹¹⁷. Because the stress for cross slip is larger in materials with low SFE, the strain hardening rates are larger in stage A than in stage III¹¹⁸.

1.1.2. Stage B: The onset of twinning

The onset of stage B marks the distancing between the behaviours of materials with low and high SFE. In materials with low SFE, additional deformation mechanisms are activated resulting in an increase in work-hardening. This section focuses on the activation of twinning during deformation – also called mechanical twinning –, as it is the case in the materials of interest in this work. Martensitic transformation can also result in such an increase but it will not be treated here.

Mechanical twinning is present in many FCC materials, such as steels¹¹⁹, Cu-Al alloys¹²⁰, but also in FCC HEAs^{25,63,121}. The SFE is a necessary condition for the activation of mechanical twinning. In steels, the critical value of the SFE was reported at 40 mJ/m^2 ¹²². Above this value, steels deform solely by dislocation slip. Below 40 mJ/m^2 , mechanical twinning is activated and adds to dislocation slip. As the SFE decreases with decreasing temperature, mechanical twinning is more intense at low deformation temperatures as was recently observed in Cantor's HEA²⁵. At the opposite, mechanical twinning is rarely observed during deformation at elevated temperatures where the SFE is larger.

A low SFE is a necessary but not sufficient condition for the activation of mechanical twinning during deformation. Indeed, Allain *et al.* showed that between two alloys presenting the same SFE only the one containing carbon exhibited mechanical twinning^{123,124}. The presence of interstitial carbon atoms in the lattice decreases the critical resolved shear stress for twinning resulting in an easier activation of twinning¹²⁵. Similar results have been obtained on MCAs recently³². Moreover, interstitial nitrogen seems to present similar effect than carbon on mechanical twinning¹²⁶.

Twinning differs from dislocation slip because it does not imply any breaking of atomic bonds. Rather than planes slipping on each other, a part of the $\{111\}$ plane rotates 180° around the twinning boundary oriented in the $\langle 112 \rangle$ direction. It results in a strain increment in the direction of shear as shown in **Fig. 1.4B**. In practice, mechanical twins are shaped as convex lenses, being elongated in their twinning direction and narrow in the perpendicular direction (**Fig. 1.4C**).

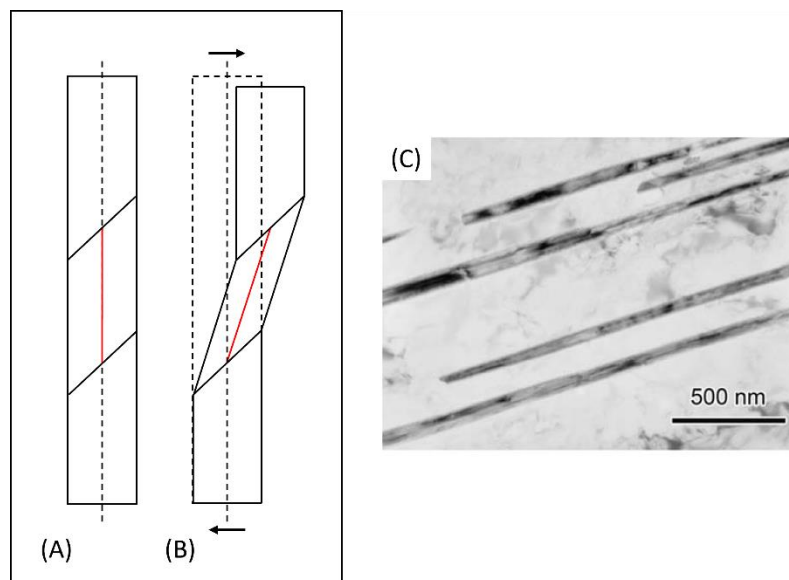


Fig. 1.4 Deformation twinning. (A-B) sketches of (A) undeformed state and (B) twinned crystal. The red line highlights the rotation of the twin compared to the matrix. (C) Deformation twins in an austenitic stainless steel of grade 316L¹²⁷. [Full-size](#).

From the onset of stage B, mechanical twinning adds to dislocation slip as another way to accommodate the applied strain. Perfect dislocation, gliding on $\langle 110 \rangle$ directions, can hence meet twin boundaries, formed along $\langle 112 \rangle$ directions – both on $\{111\}$ planes. Mechanical twins act as new

obstacles for dislocation slip inducing the observed increase in WHR¹²⁸. As mechanical twins multiply with increasing strain, dislocation slip is increasingly impeded. This effect is known as dynamic Hall-Petch effect, meaning a continuous reduction of the apparent grain size. It results in the observed increase in WHR.

Mechanical twins formed during deformation must not be confused with annealing twins. The latter category forms during the recrystallisation of FCC materials. Their formation permits the accommodation of internal stresses inherited from deformation. They are often thicker and with straight and parallel twin boundaries. Moreover, their formation does not result in any shear.

1.1.3. Stage C: limitation of the twinning rate

Stage C begins when the WHR starts to decrease from the strain hardening plateau of stage B. This decrease in WHR has been related to the decrease in twin formation rate^{116,129}. The correlation was observed experimentally on Co-Ni alloys¹³⁰ and on MP35Ni (35Ni-35Co-10Mo-20Cr)¹¹⁶. The reduction in twin formation rate was explained by grain refinement, due to the larger difficulty for twins to form within smaller volumes¹³¹. Two mechanisms result in grain refinement: the formation of deformation domains within grains and the rotation of twins due to slip.

Polycrystalline materials rarely respond homogeneously to external strain^{106,117}. This is true between grains of different crystalline orientations but also within grains¹³². Different slip systems are activated in different parts of grains – called deformation domains or deformation bands. These domains then rotate in different directions, resulting in the development of significant lattice curvatures and misorientations between domains¹³³, reducing the apparent grain size¹¹⁶. As the stress at which twin form increases with decreasing grain size¹³¹, it is expected that deformation banding results in a decrease in twin formation rate.

The second mechanism postulates that twins forming at an early stage of deformation rotate away from their twinning direction, due to the lattice rotations induced by slip. These older twins hence become obstacles for the formation of new mechanical twins because they are no longer parallel to their original $\langle 112 \rangle$ twinning direction. This theory is supported by observations on mechanical twins rotating towards the compression or rolling plane during deformation^{116,134}.

Both mechanisms result in a decrease in the twin formation rate and in its contribution to strain hardening through dynamic Hall-Petch effect. Dynamic recovery processes are hence less counterbalanced resulting in a global decrease in the WHR during stage C. The twin formation rate is however not null, explaining the less steep slope in stage C than in stage III.

1.1.4. Stage D: deformation at large strains

During stage D, grain refinement due to mechanical twinning and deformation banding continues. Additional twinning systems activate resulting in the blockage of dislocation slip on multiple systems¹¹⁶. Twinning becomes also difficult due to the gradual reduction of the apparent grain size. As deformation through dislocation slip and twinning are no longer viable, shear banding activates. Shear bands are highly sheared volumes – that can attain up to 10 times the applied shear stress¹³⁴ – that cross multiple grains. They are widely observed in FCC materials of low SFE^{85,107,134}. Stage D is observed solely at large strains, through compression or plane-strain compression.

To summarize, multiple mechanisms activate during deformation of a polycrystalline FCC material with low SFE. These mechanisms are summarized as follows:

- At the smallest scale, dislocations multiply and glide along their 2D slip systems. Perfect dislocations dissociate into partials. Stacking faults form between leading and trailing partials, impeding cross slip and dynamic recovery. Dislocations or stacking faults interact to create jogs and locks, hindering further dislocation slip.
- Mechanical twins form. Their formation is difficult when grains are too finely refined.
- Grains divide in several smaller volumes called deformation domains, limiting twinning.
- At the largest scale, shear bands form when deformation by dislocation slip and twinning are no longer viable. They cross multiple grains and consist in highly sheared volumes.

The activation and intensity of these multiple mechanisms depend on the local crystallographic orientations, resulting in a heterogeneously deformed microstructure. These discrepancies have a large influence on the activation of softening mechanisms.

1.1.5. The influence of chemical inhomogeneity: from pure metals to MCAs

The material chemistry has an influence on the nature, structure but also behaviour of dislocations¹³⁵. In pure metals, all atoms in the lattice are the same. This results in a regular lattice and a flat energy landscape for dislocations to glide, with a similar amount of energy required for any slip step. In this case, dislocation slip is homogeneous and does not depend on position.

When solute atoms are added, as in conventional alloys such as steels, chemical inhomogeneities arise. Chemical inhomogeneities depend on the number and nature of elements. They remain limited and have low influence on the material behaviour in dilute alloys such as most of conventional alloys. They however become significant when considering MCAs, constituted solely of solute atoms, as observed in CoCrFePdNi¹³⁶. They also depend on the processing method, as they decrease after long-term annealing treatments. They directly impact material parameters such as the SFE which vary depending on the local chemical composition, as observed in the Cantor alloy¹³⁷. Dislocation slip is also impacted by these local variations of chemistry. The flat energy landscape in pure metals becomes rugged, with atomic positions being more or less stable depending on the neighbouring atoms. It results in additional energy costs for dislocations to move and hence in larger material strength, effect called solid solution strengthening. These chemical inhomogeneities can be related to the lattice distortion effect theorised in MCAs⁴.

In addition, interactions arise between solute atoms, but also between solute atoms and dislocations. These interactions are of two types: local chemical ordering and solute drag. Local chemical ordering, also called short-range ordering, consists in the clustering of solute atoms to lower their energy. It could be for example to lower their strain fields. It can occur at the sub-nanometre scale making it very difficult to identify experimentally, especially in the highly concentrated structures of MCAs¹³⁶. This local ordering intensifies chemical inhomogeneity and could become obstacles for dislocation slip. Moreover, it has been proposed that these clusters could help or limit cross-slip depending on their nature and size¹³⁸.

Solute atoms can also migrate towards defects such as grain boundaries or dislocations in order to lower their energy, mainly through the accommodation of their strain fields. These solute atoms then follow these dislocations in their glide. This phenomenon is called solute drag and results in the limitation of the mobility of dislocations or of boundaries. While true experimental proof was not yet given for the presence of solute drag in MCAs, many researchers proposed this concept to explain the observed limitation of recrystallisation or grain growth kinetics in these alloys^{139,140}.

1.2. The theory of recrystallisation

During deformation, metallic materials store defects, mainly in the form of dislocations. Their presence perturbs the stability of the structure, which tends to evolve towards more stable states through the activation of restoration mechanisms. They are of two types: recovery and recrystallisation.

Recovery involves a partial restoration of the structural and mechanical properties to their values before deformation. It does not modify the coarse structure of deformation, i.e. the boundaries of deformed grains remain. It is rather dislocations within deformed grains that organise to form sharp cell walls and create sub-grains. Recovery requires a significant mobility of dislocations within the grains and easy cross slip of dislocations from a slip system to another. As a consequence, its extent is limited in materials with low SFE. Additional information regarding recovery can be found in ¹⁴¹.

On the other hand, recrystallisation involves the nucleation of new grains. These new grains, called recrystallised grains, grow and consume the deformed structure until the material becomes fully recrystallised. In this case, structural and mechanical properties are replaced with those of the newly formed structure. Recrystallisation activates when sufficient thermal energy is provided to a deformed structure, for example during an annealing treatment following deformation. It is then called static recrystallisation (sRX). It also activates during deformation when performed at a sufficiently high temperature. It is then called dynamic recrystallisation (dRX). In the same way, recovery mechanisms might be either static or dynamic. As these last mechanisms are limited in low SFE materials, this section only deals with the two types of recrystallisation.

Both types of recrystallisation, whether static or dynamic, include the nucleation and growth of new grains. These phenomena involve the movement of boundaries, whether it is to form nuclei or for their growth. This topic is hence discussed first. Then, the phenomenology of sRX is described. Finally, the specificities of DRX are scrutinized.

1.2.1. Movement of boundaries

The velocity (v) of a boundary depends on two parameters: its mobility (M) and the net pressure (P_{net}) applied on the boundary. In mathematical terms, it gives:

$$v = M * P_{net} \quad (\text{Eq. 1.2})$$

The mobility of boundaries is strongly related to their misorientation (**Fig. 1.5**) ¹¹⁵. There exist two types of boundaries: low-angle grain boundaries (LAGBs) and high-angle grain boundaries (HAGBs). The transition between the two types of boundaries varies between misorientations of 10 to 15° depending on authors ¹⁴².

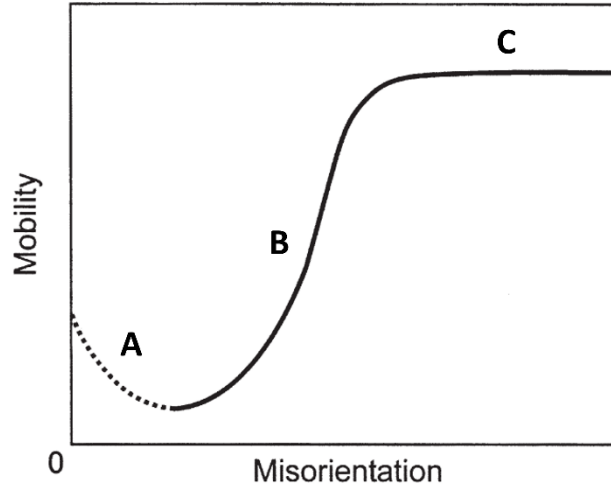


Fig. 1.5 Variation of the mobility of a boundary depending on its misorientation. The letters A-C corresponds to the cases discussed in the text (adapted from ¹¹⁵). [Full-size](#).

LAGBs consist in arrays of dislocations ¹⁴³. The number of dislocations forming the boundary determines their misorientation, which in turn determines their mobility. The boundaries with misorientations lower than 5° (case A in **Fig. 1.5**) consist of dislocations spaced far apart. In such case, the mobility of boundaries is governed by the rate of dislocation climb which is inversely proportional to the boundary misorientation. As a result, their mobility decreases from 0 to 5° ¹¹⁵. On the other hand, the mobility of boundaries presenting misorientations between 5° and 15° (case B in **Fig. 1.5**) is governed by atomic jumps. As the number of dislocations increases in the boundary, along with their misorientation, the diffusion of atoms across the boundary becomes easier. The mobility of this type of LAGBs is hence proportional to its misorientation.

HAGBs does not involve dislocations. It consists in perturbations in the atomic bonds between two lattices rotated for more than 15° (**Fig. 1.5C**) ¹⁴⁴. The mobility of HAGBs is dominated by atom jumps across the boundary. Their mobility is high and is independent of misorientation.

The movement of boundaries is also dependent on the net pressure applied on them. Three types of pressure might be applied on a boundary: the driving pressure (P_D), the pressure related to boundary curvature (P_C) and the Smith-Zener pinning pressure (P_{SZ}). The total pressure P_{net} is obtained as follows:

$$P_{net} = P_D - P_C - P_{SZ} = \frac{\alpha \Delta \rho G b^2}{2} - \frac{2\gamma_b}{R} - \frac{6f_V \gamma_b}{r} \quad (\text{Eq. 1.3})$$

The driving pressure (P_D) depends on the difference in density of dislocations ($\Delta \rho$) between the two sides of a boundary, the shear modulus of the material (G), the Burgers vector (b) and a constant (α) of the order of 1. This pressure drives the growth of the recrystallised grains. As dislocation storage depends on crystallographic orientation, the driving pressure also depends on this parameter.

The pressure associated with boundary curvature depends on the radius of curvature of the boundary (R) and on the energy of a boundary separating two FCC grains (γ_b). This pressure is only significant when the boundary presents a small curvature, i.e. when grains are small. As soon as grains reach a critical size, this term becomes negligible.

Finally, the Smith-Zener pressure relates to the pinning of boundaries by particles, such as precipitates dispersed in the material. This pressure is hence only present when such precipitates are present. It is

otherwise null. This pressure depends on the volume fraction of precipitates (f_V) and of their radius (r). More details will be given on this pressure in the part related to the interactions between precipitation and recrystallisation later on.

A boundary moves if the sum of the pressures applied on it, i.e. P_{net} , is positive. Its velocity depends on the absolute value of P_{net} and of the boundary mobility. A grain with mobile boundaries is in growth configuration and expands.

1.2.2. Static recrystallisation

sRX is heterogeneous and discontinuous. It occurs in two steps: nucleation and growth. Its activation and kinetics depend on the deformed state and on the annealing temperature. Humphreys et al.¹⁴⁵ summarized these dependences as follows:

- a minimum deformation is necessary for recrystallisation to activate;
- larger deformation intensities or annealing temperatures result in faster recrystallisation;
- larger initial grain sizes or deformation temperatures result in slower recrystallisation¹⁴⁶;
- other parameters such as the deformation mode but also the crystallographic texture might influence recrystallisation.

Nucleation describes the development of pre-existing embryos into stable nuclei, meaning with critical size and bounded by HAGBs. As highlighted by Humphreys et al.¹⁴⁵, the term *nucleation* does not truly depict this first step. He proposes the term *initiation* as a better candidate, that better depicts the growth of pre-existing volumes present before the activation of recrystallisation¹⁴⁷. These small volumes present low dislocation contents and are separated from the neighbouring deformed structure by HAGBs. These embryos are also called recrystallisation nuclei.

Nucleation can be either *homogeneous*, when its activation is independent of the location, or *heterogeneous*, when it occurs preferentially at specific locations of the structure. These locations are primarily those with a highly disordered lattice. Examples of heterogeneous nucleation sites are grain boundaries^{148,149}, large second phase particles or inclusions through particle stimulated nucleation (PSN)¹⁵⁰⁻¹⁵³, transition bands – boundaries of deformation bands –^{121,154} and shear bands¹⁵⁴.

While heterogeneous recrystallisation is well understood, the precise mechanisms responsible for the development of homogeneous recrystallisation is still subject of debate. A widely accepted explanation is related to dynamic recovery¹⁵⁵. This mechanism results in the organisation of dislocations into a cell structure. As the deformation intensity increases, the sharpness and misorientation of cell walls increase. It results in the formation of sub-grain boundaries and even reach large mobilities at large strain¹⁵⁶. The sub-grains presenting the more mobile boundaries then grow at the expense of their neighbours¹⁵⁵. This mechanism is called abnormal sub-grain growth¹⁵⁷. These sub-grains then become recrystallisation nuclei. As this mechanism requires the activation of dynamic recovery, it remains limited in FCC materials of low SFE.

Once a nucleus has reached a critical size and became stable, it grows with a velocity dictated by Eq. 1.2. As the stored energy is dependent on crystallographic orientation, growth discrepancies between grains are to be expected.

Both nucleation and growth stages contribute to the development of the recrystallised microstructure. The nucleation stage determines the density of nuclei while growth might favour orientations with highly mobile boundaries. Their respective impact depends on the stored energy. When the stored energy is large, nucleation prevails over growth. A grain presenting a large stored energy develops a large density of nuclei. In this case, their growth is impeded by that of their neighbours resulting in

smaller grain size after completion of recrystallisation (grains 1 and 3 in **Fig. 1.6A** and grains 1, 3 and 5 in **Fig. 1.6B**). At the opposite, a grain with low stored energy provides a low density of nuclei, if any. The growth stage then becomes dominant with the faster development of the orientations with the more mobile boundaries (grain 2 in **Fig. 1.6A** and grains 2 and 4 in **Fig. 1.6B**).

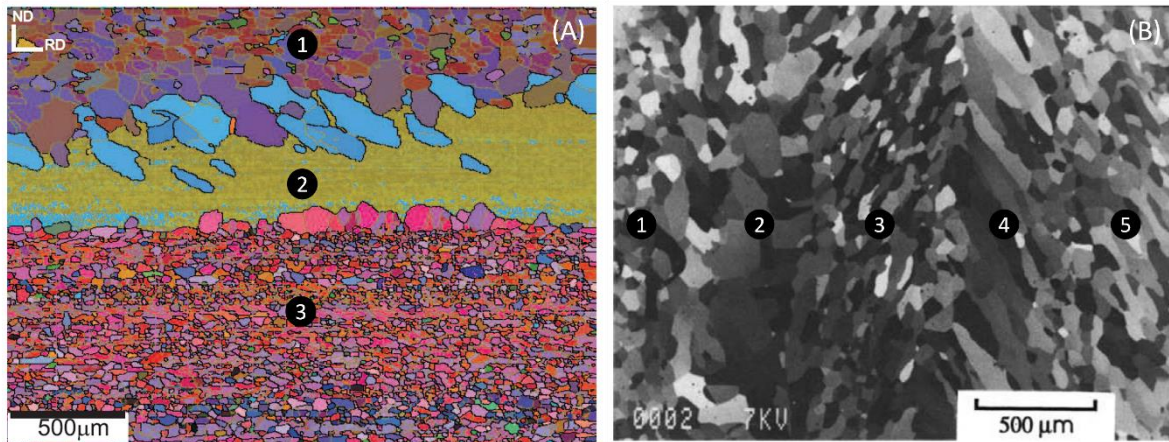


Fig. 1.6 (A) Partially recrystallised microstructure of a cold-rolled single-phase Al-0.3 w.% of Mn. The central grain is Goss-oriented and is not recrystallised ¹⁵⁸. (B) Anisotropic growth observed in high purity aluminium ¹⁵⁹. [Full-size.](#)

1.2.3. Dynamic recrystallisation

Recrystallisation is called *dynamic* when it activates during deformation, as opposed to sRX occurring after deformation. Most of what was explained on sRX applies to dRX. This includes that dRX operates in two steps: nucleation and growth. Moreover, a sufficient temperature is necessary for dRX to activate.

Because deformation and dRX are concomitant, the latter is influenced by deformation conditions, i.e. strain but also temperature and strain rate. Such dependence is summarized in the Zener-Hollomon parameter (Z) which is related to the flow stress as follows:

$$Z = \dot{\epsilon} \exp\left(\frac{Q}{RT}\right) = A(\sinh(\alpha\sigma))^n \quad (\text{Eq. 1.4})$$

where $\dot{\epsilon}$ is the strain rate, Q an activation energy, R the gas constant, T the temperature in Kelvin, σ the flow stress and A , α and n constants. The Zener-Hollomon parameter controls the development of the microstructure, which in turn determines the shape of the stress-strain curve (**Fig. 1.7**). At large values of Z , i.e. large strain rates and low temperatures, a single broad peak is observed. At low values of Z , i.e. low strain rates and high temperatures, multiple peaks with decreasing intensity are observed. Large values of Z also result in larger stresses.

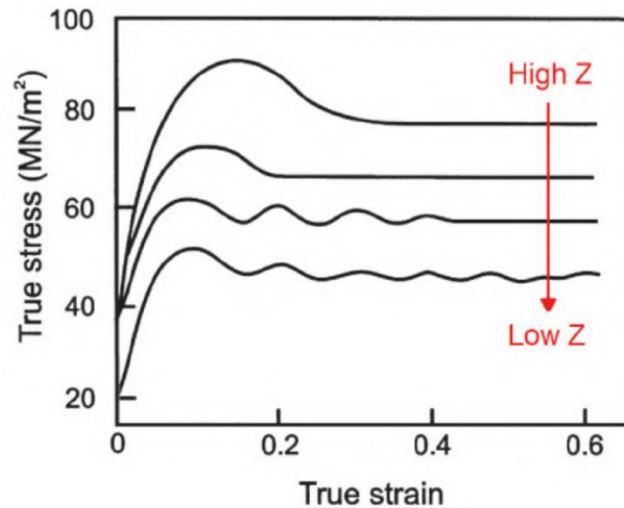


Fig. 1.7 The effect of the Zener-Hollomon parameter on the stress-strain curves during hot deformation (adapted from ¹⁶⁰). [Full-size](#).

At low strain, work-hardening dominates as can be observed by the steep slope of the stress-strain curves. Deforming at such high temperatures results in the simultaneous activation of many slip systems. In addition, dislocations are able to cross-slip and climb easily, even in materials presenting low SFE. It results in large dislocation mobility inducing homogeneous deformation ¹⁶¹. Mechanical twinning, deformation or shear banding are rarely activated at high temperatures.

The multiplication of dislocations and their interactions result in an increase in the driving force for restoration mechanisms. Even in materials presenting low SFE, dRV activates during hot deformation. The extent of dRV remains limited but it helps in the formation of recrystallisation nuclei. dRX then activates at a critical strain before the first peak observed on stress-strain curves ¹⁶⁰. This critical strain corresponds to a sufficient work-hardening, i.e. a sufficient driving force, and to the presence of nuclei. The critical strain decreases with decreasing stress and Z.

During dRX, nucleation is highly heterogeneous. It occurs primarily on the grain boundaries of deformed grains forming necklace structures, as observed in copper (**Fig. 1.8A**) ¹⁶². Nucleation starts along initial grain boundaries (**Fig. 1.8B-C**). Then, the boundaries of newly recrystallized grains also become nucleation sites for dRX (**Fig. 1.8D**). The piling up of layers of recrystallised grains results in the end in the completion of recrystallisation (**Fig. 1.8E**). Heterogeneous nucleation at large second phase particles or inclusions, similar to PSN, was also observed under large Z ¹⁶².

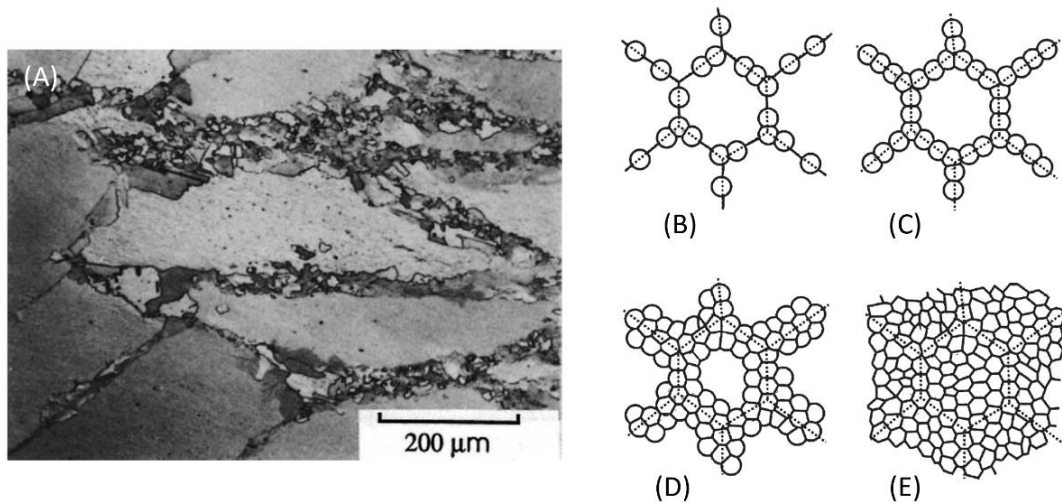


Fig. 1.8 Microstructure evolution resulting from dynamic recrystallisation. (A) Necklace structure observed in polycrystalline copper at 400°C¹⁶². (B-E) Recrystallisation steps of a large grain through dRX¹⁶⁰. [Full-size](#).

While dRX occurs, deformation continues. As a consequence, the newly recrystallised grains work-harden and their driving force for restoration mechanisms increase accordingly. dRX might then activate in previously recrystallised grains resulting in several subsequent and uncompleted cycles of dRX. This occurs under low values of Z depicted by several peaks on the stress-strain curve (**Fig. 1.7**). At large values of Z , a single dRX cycle is observed resulting in a single broad peak (**Fig. 1.7**). Low values of Z result in grain coarsening while large values of Z result in grain refinement¹⁶³. In both cases, a stress steady state is achieved at large strain. At this stage, the hardening produced by dislocation interactions is counterbalanced by the softening due to dRX.

Hot deformation, and more specifically hot rolling, is of paramount importance for industrials. Indeed, deforming at high temperatures lowers the material flow stress by one order of magnitude compared to room temperature. In addition, it is often performed in the fully FCC domain, where the material flow stress is low. Thickness reduction hence requires less energy and is less expensive. Moreover, deforming at high temperatures removes the chemical and structural inhomogeneities as well as the brittle second phases or inclusions of the cast microstructure. Much research was carried out to control the activation of restoration mechanisms throughout the rolling process in order to control the final microstructures and properties^{164,165}.

1.3. Precipitation

Precipitation consists in the local transformation of a phase into another, also called second phase. This new phase presents different chemical composition and/or lattice structure compared to the phase from which it forms. Precipitation of a second phase is governed by both thermodynamics and diffusion. First, thermodynamics determines if a phase is stable in a given system and under given conditions, e.g. temperature, pressure. It also determines the driving force for the formation of this new phase. The kinetics of formation of a stable phase is controlled by both thermodynamics and diffusion.

This section treats first of the phase stability and kinetics of phase transformation. Interactions between recrystallisation and precipitation will then be treated. Finally, the second phases of interest in this work will be detailed along with their influence on strength and work-hardening.

1.3.1. Phase transformation (stability and kinetics)

Thermodynamics

A single component might exist under different states, gas, liquid or solid. In solid state, it might also exist under different crystallographic forms. This is the case of iron that exists as α -iron (BCC), γ -iron (FCC) or δ -iron (BCC). The stable form is that presenting the lowest Gibbs free energy.

When combining elements, for example adding a fraction X^0 of element A to an element B, the resulting free energy does not follow a linear relationship between the energies of pure elements (black dotted straight-line in Fig. 1.9A). In the case where A and B are miscible, the Gibbs free energy decreases, stabilizing the blend over the pure elements (black solid curved line in Fig. 1.9A).

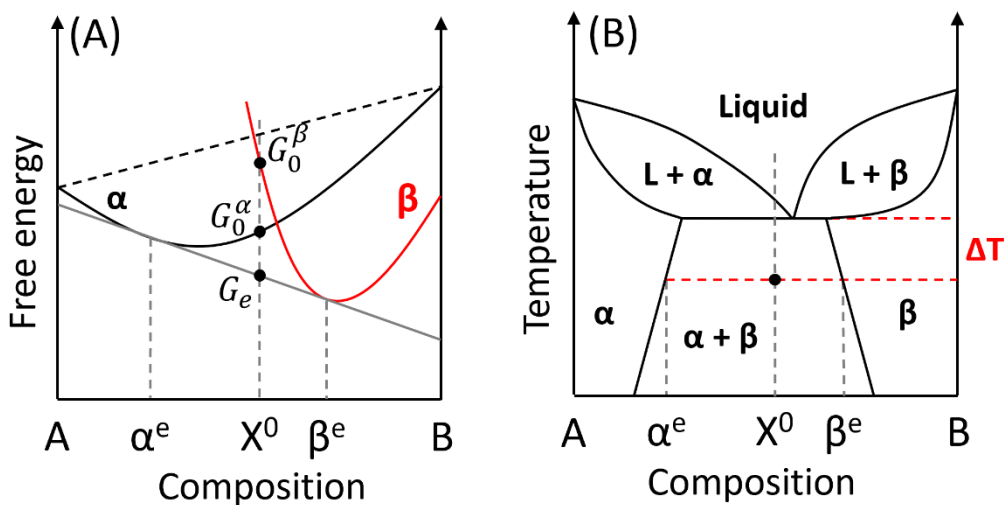


Fig. 1.9 (A) Energy curves of two phases α and β . The total energy of the system is lowered if the β phase forms from the α phase. (B) Schematic phase diagram where stable phases are indicated in function of composition and temperature. The black dot corresponds to the equilibrium found in (A). The driving force for precipitation is related to the temperature difference ΔT . (Adapted from ¹⁶⁶). [Full-size](#).

It is also possible that combinations of elements A and B exist in several forms (α and β on Fig. 1.9A). Following the same reasoning as for single component systems, the lower energy configuration at composition X^0 is G_0^α . There, the system consists in the α phase of composition X^0 . The system might lower its free energy through the reaction $\alpha \rightarrow \alpha + \beta$. The free energy then decreases to G_e where the system consists in the α phase of composition α^e and of the β phase with the composition β^e .

Phase diagrams summarize the stable phases according to temperature and composition (**Fig. 1.9B**). The black solid circle corresponds to the equilibrium of **Fig. 1.9A**. Phase fractions and phase compositions can be extracted from phase diagrams. It also informs on the driving force for transformation which depends on the temperature difference, noted ΔT in **Fig. 1.9B**.

Nowadays, increased interest is given to the numerical calculation of phase diagrams, also called CALPHAD method. This method is based on the extrapolation of experimental data acquired on simple systems. Starting from experimental data, the method calculates the corresponding free energies and extrapolate them to more complex or unstudied compositions. The input experimental data corresponds to binary and ternary compositions, as the influence of compositions above ternaries becomes negligible. In all CALPHAD databases, all binary compositions are fully assessed, while it is the case for only a small fraction of ternaries. The database for multicomponent alloys (MCA), TCHEA, includes more ternaries than others, although it might not be sufficient to cover the wide compositional domain. The CALPHAD method enables to calculate various parameters related to the predicted phases, such as their fractions, compositions and driving force for precipitation. Kinetics and non-equilibrium conditions might also be explored through this method.

Diffusion

Phase transformation might occur through multiple mechanisms: displacive transformation, spinodal or diffusion. In the context of this work, only phase transformation through diffusion occurs. This section describes this phenomenon.

Diffusional transformation involves the modification of the local chemical composition. Such change is carried out by the movement of atoms, also called atomic migration or diffusion. The movement of atoms is driven by a reduction in Gibbs free energy. It acts in the direction of the equilibrium determined by thermodynamics unless a sufficient force is directing the system otherwise. In most cases, i.e. when no phase transformation occurs, diffusion tends to smooth concentration gradients. Diffusion then occurs from locations of large to low concentrations. When phase transformation occurs, diffusion from low to high concentrations occur for elements in which the new phase is enriched. This lowers the energy of the system as it enables the formation of a thermodynamically stable phase.

Diffusion is accelerated along defects, such as grain boundaries or dislocations. In both cases, solute atoms migrate towards these defects to limit the lattice distortion induced by their different chemical composition or lattice structure. Then, the many vacancies present in the disordered structures of grain boundaries ease atomic jumps enabling larger diffusion rates. Solute atoms that migrated to dislocations follow them in their slip, phenomenon also called pipe diffusion.

Transformation in real materials

Phase transformation might occur on defects, i.e. *heterogeneous* nucleation, or in the bulk, i.e. *homogeneous* nucleation. The latter case is treated first.

The Gibbs free energy of a nucleus forming through homogeneous nucleation is composed of three contributions:

1. The formation of a volume V of a stable phase drives the transformation through a negative contribution $-V\Delta G_V$. ΔG_V strongly depends on temperature (related to ΔT in **Fig. 1.9**).
2. The formation of such volume involves the formation of an interface. This limits the transformation by a positive term $+A\gamma_b^{FCC-PCP}$, with A the interface area and $\gamma_b^{FCC-PCP}$ the interfacial energy between the matrix, here FCC, and the new phase or precipitate (PCP).

3. The difference in chemical composition and/or lattice structure induces a positive misfit contribution $+\Delta G_s$ that limits the transformation.

Hence, the total change in energy is:

$$\Delta G = -V\Delta G_V + A\gamma_b^{FCC-PCP} + V\Delta G_s \quad (\text{Eq. 1.5})$$

The energy barrier to overcome for precipitation to activate is defined by applying $d\Delta G/dr = 0$.

While homogeneous nucleation occurs in the bulk, heterogeneous nucleation occurs on defects. The defect removal results in the reduction of the energy of the system by a supplementary contribution $-\Delta G_d$. This new term lowers the energy barrier, easing phase transformation. These defects are, with increasing ΔG_d , vacancies, dislocations, stacking faults, interfaces and free surfaces. Other strategies exist to reduce the energy barrier, such as maximising their volume to boundary area ratio, the reduction of the boundary energy and/or the reduction of the misfit strain.

As soon as nucleation occurred, precipitates start to grow. The growth rate of precipitates depends on the nature of their interfaces. Coherent interfaces present low mobility while incoherent boundaries are highly mobile. The presence of diffusion shortcuts also helps the growth of precipitates. For example, precipitates grow faster when located along grain boundaries.

As precipitates grow, they consume the alloying elements in which they are enriched from their vicinity. It results in local elemental depletion around precipitates. This effect increases with increasing size of precipitates. Concentration gradients hence form from the vicinity of small particles, where the alloying content is still high, to the vicinity of large particles, where it is small. It results in diffusion from the vicinities of small to large particles. This mechanism results in the shrinking of small particles – until their disappearance – at the benefit of large particles that coarsens. During annealing, the number density of precipitates hence decreases while their size increases.

1.3.2. Interactions with recrystallisation

During an annealing treatment or during hot deformation, it is possible that both precipitation and recrystallisation activate. Precipitates may then interfere with recrystallisation. Interactions depend on the size of the precipitates but also on whether or not precipitation occurs before recrystallisation. Three regimes might be separated: precipitation before, during or after recrystallisation. These regimes might cohabit in the same material if the stored energy is not homogeneous. In regions of low stored energy, recrystallisation barely activates and precipitation occurs before its activation or its completion. In regions of high stored energy, recrystallisation completes quickly and recrystallisation only occurs in a second step.

Before recrystallisation

The situation when precipitation occurs before recrystallisation depends on the size of the precipitates.

Small precipitates apply a pinning pressure P_{SZ} to the boundaries that acts against the driving pressure P_D and hence limits their mobility (**Fig. 1.10**). P_{SZ} depends on the ratio f_V/r , with f_V the volume fraction of precipitates and r their radius (Eq. 1.3). A large fraction of small precipitates effectively restricts the movement of boundaries and hence recrystallisation. It also depends on the interphase boundary energy. The pinning effect of incoherent precipitates, with large boundary energy, is larger than that of coherent precipitates. This phenomenon limits both recrystallisation nucleation and growth. Before recrystallisation can proceed, considerable precipitate growth is required. It results in slow recrystallisation as it is not controlled by the mobility of interfaces but by the coarsening of precipitates on the migrating recrystallisation front.

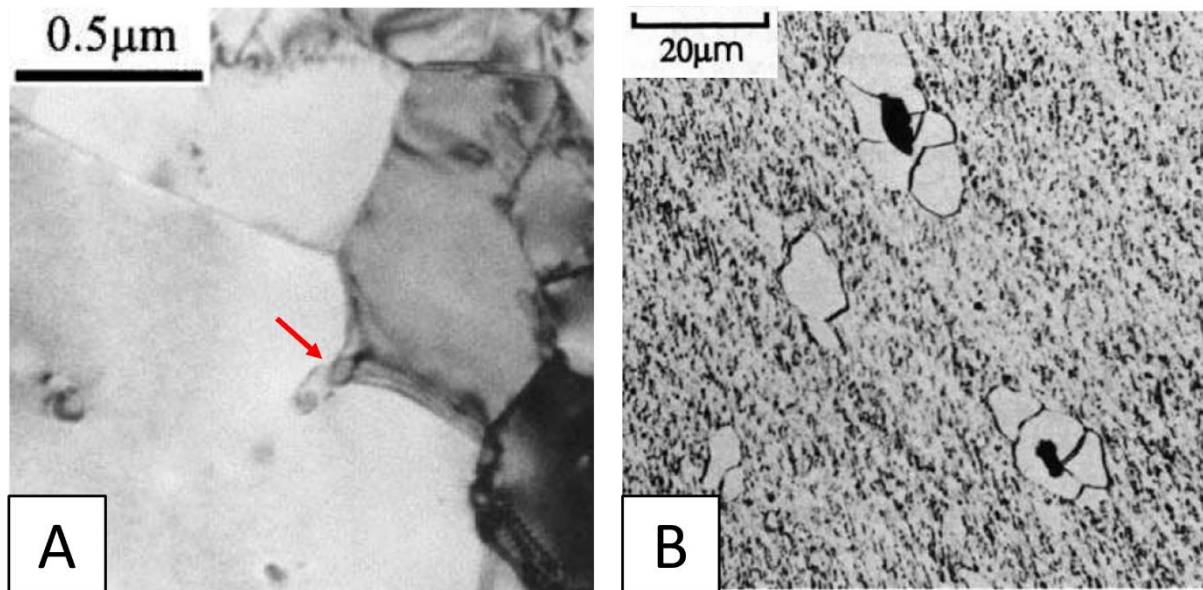


Fig. 1.10 (A) Grain boundary pinned by a precipitate (red arrow) during the recrystallisation of an Al-Mg-Si alloy¹⁶⁷. (B) Particle-stimulated nucleation during annealing of cold-worked iron¹⁶⁸. [Full-size](#).

As the pinning effect decreases with increasing size, large precipitates do not interfere much with boundaries. However, the presence of large precipitates during deformation might result in PSN during subsequent annealing. Due to the difference of intrinsic strength between matrix and precipitates, strain fields form around large precipitates creating local orientation gradients, perfect nucleation sites for recrystallisation (**Fig. 1.10B**).

During recrystallisation

In this regime, recrystallisation begins before significant precipitation occurs but its rate is limited or even stopped before its completion by the formation of precipitates. This regime results in heterogeneous microstructures divided into recrystallised, where the situation is similar to precipitation occurring after recrystallisation, and non-recrystallised regions, similar to precipitation occurring before recrystallisation.

After recrystallisation

When occurring after the completion of recrystallisation, equiaxed precipitates form mainly on the grain boundaries of recrystallised grains.

1.3.3. Strengthening due to second phases

Precipitates do not only interact with restoration mechanisms, through the pinning of boundaries or PSN, they also interfere with the movement of dislocations, and hence induce strengthening. This section focuses on the strengthening propensity of the two second phases of interest in this work: (Ni, Al)-rich B2 and σ phases, when formed in the FCC matrix. After briefly detailing the nature of these two phases, the strengthening induced by their formation is described depending on their nucleation sites. Finally, the influence of precipitates on ductility is studied, as their presence might induce brittleness or result in increased work-hardening.

The **B2 phase** was first defined for binary compounds, such as NiAl. It presents an ordered BCC structure. Nowadays, the concept of *B2 phase* has been widened beyond binary compositions. In the field of MCAs, the name of *B2 phase* is now given to a BCC phase enriched in nickel and aluminium and presenting sublattice reflections on diffraction patterns observed in the TEM. As this designation is

widely used in this field, it is used as well in this manuscript. The B2 phase is harder than the FCC matrix. Joseph *et al.* measured a factor 2.5 in nano-indentation compared to FCC in $\text{Al}_{0.6}\text{CoCrFeNi}$ ¹⁶⁹.

The σ phase is mainly composed of iron and chromium, the latter ranging from 30 to 50 at.%. Its lattice structure is tetragonal, with $P4_2/mnm$ space group. It is present in alloys containing chromium contents over 15 w.%, Fe-Cr and Fe-Cr-Ni alloys ^{170,171}, and stainless steels ^{172,173}. Its formation from the FCC matrix is slow as the FCC/ σ boundary energy is high. It rather forms from BCC structures, such as δ -ferrite, where the boundary energy is lower, the diffusion of chromium faster and the content in chromium and molybdenum larger. Jo *et al.* measured a factor 6 in nano-indentation compared to FCC in a VCoCrFeMnNi alloy ¹⁷⁴.

In addition to the nature of the second phases, their size and location influence their strengthening effect. Two cases are possible: precipitation strengthening and/or strengthening by composite effect.

Precipitation strengthening involves the presence of precipitates within grains. These precipitates are intersecting dislocation slip systems and are hence obstacles for their movement. Dislocations can overcome these obstacles through two mechanisms depending on the nature and size of the precipitates: the shearing mechanism or the bypassing mechanism, also called Orowan looping mechanism. The first mechanism dominates in the case of small and coherent precipitates. In such case, the coherency of their interphase boundary permits dislocations to cut through precipitates. It results in the shearing of the precipitates (**Fig. 1.11A**).

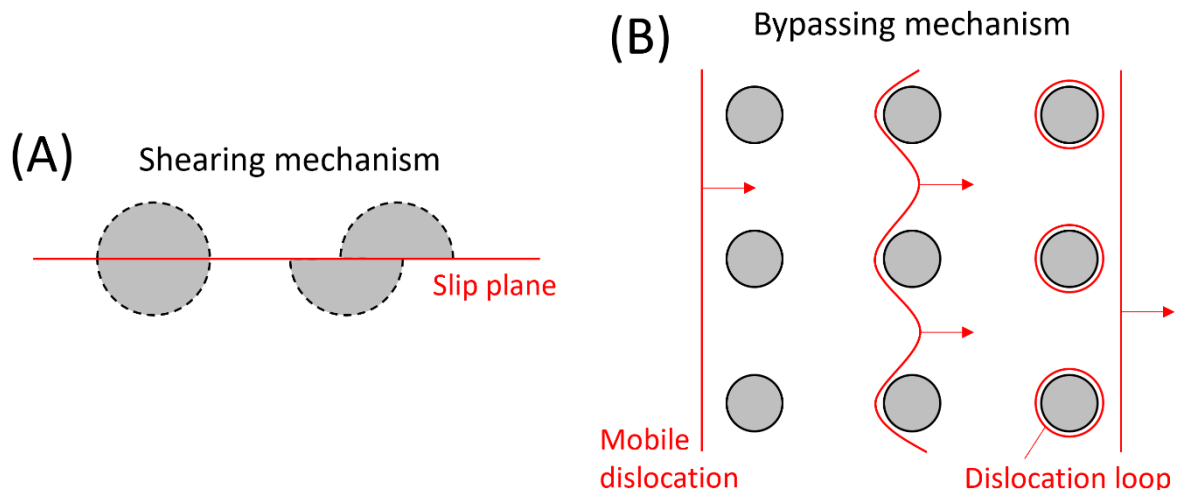


Fig. 1.11 (A) A coherent precipitate (grey circle with dotted perimeter) is cut in two by dislocations gliding on the slip plane. (B) A mobile dislocation front bypasses a line of incoherent precipitates (grey circles with solid perimeters) and leaves dislocation loops around precipitates behind. (Adapted from ¹⁷⁵). [Full-size](#).

The bypassing mechanism dominates when precipitates are large and/or incoherent with the matrix. It is the case of B2 and σ phases which present different lattice structures than the matrix. To explain how the bypassing mechanism works, consider a dislocation front encountering a line of precipitates (**Fig. 1.11B**). Under the applied stress, the dislocation front bows between precipitates, the bowing curvature increasing with stress. At a critical shear stress, τ_{Orowan} , neighbouring bows meet forming loops around precipitates. Beyond τ_{Orowan} , the dislocation front bypasses the line of precipitates and is able to continue letting loops and precipitates behind. The strengthening effect due to this mechanism is maximised for large densities of small precipitates.

The strengthening by **composite effect** applies to microstructures containing different phases presenting similar grain sizes. These microstructures are often the result of grain boundary

precipitation followed by considerable growth of the precipitates. Recrystallised microstructures where precipitation occurred after recrystallisation are good examples. In such case, the strength of the material follows a simple law of mixture, where the total strength is the sum of the products between phase volume fractions and respective strengths. These strengths can be the sum of multiple contributions, such as strengthening due to solid solution or grain boundaries. Precipitation strengthening, as detailed above, can also be a strengthening contribution to consider here.

In addition to strengthening the material, precipitates also contribute to the material work-hardening. In the case where precipitates are large and incoherent with the matrix, this is primarily due to the accumulation of geometrically necessary dislocations (GND) in the form of loops around the precipitates. These GNDs create misorientation gradients that accommodate the different deformation behaviours on each side of interphase boundaries.

The formation of GNDs depends mainly on the interphase boundary area between precipitates and matrix. Hence, many small precipitates result in a larger gain in work-hardening. If considering composite strengthening where precipitates are large, only a small fraction of GNDs are formed. Smaller precipitates located inside the grains offer larger boundary area and hence larger work-hardening capacity. The presence of small coherent precipitates deformed by the shearing mechanism does not result in the formation of GNDs. Nonetheless, they contribute to work-hardening through different mechanisms that are not detailed here. The gain in work-hardening from GNDs delays necking and fracture.

Conclusions

This chapter gathers the current knowledge on the multiple transformations that microstructures experience during thermomechanical treatment (TMT). These transformations are of three types: deformation, restoration and precipitation.

During deformation, defects in the form of dislocations, jogs, locks, mechanical twins and shear bands form, multiply and interact. As strain increases, microstructures refine and complexify as additional deformation mechanisms activate.

Accordingly, the material becomes less stable and tends to reduce the density of defects through the activation of restoration mechanisms. FCC materials with low SFE mainly experience recrystallisation. This mechanism involves the nucleation of defect-free grains and their growth over the deformed matrix. It might activate during deformation, if conducted at large enough temperature, or during an annealing treatment performed after deformation.

Precipitation might also activate if second phases are stable in the explored temperature range. This mechanism involves the transformation of parts of the FCC matrix into another crystallographic structure and/or chemistry. Defects of the microstructures, such as grain boundaries or dislocations, accelerate precipitation. The presence of precipitates impact recrystallisation with consequences depending on the size of the precipitates. It also influences deformation mainly through the formation of GNDs along interphase boundaries. In summary, these three transformations are interconnected and must all be considered in order to correctly interpret experimental observations.

The following chapters focus on different stages of TMT. In each chapter, the specific material characteristics, thermomechanical processes and experimental devices are detailed first. The techniques in common to all chapters are explained at the end of the manuscript in the *materials and methods* chapter (annexe A). Then, results related to the chapter are given. They are linked and compared with literature data in the discussion that follows. The next two chapters directly follow the steps of a conventional TMT: hot rolling and cold rolling. In chapter 2, the behaviour of C+Al when compressed at temperatures between 900 and 1100°C is studied. Then, in chapter 3, its behaviour during cold rolling and subsequent annealing is scrutinized. In both cases, the objective is to understand how microstructures develop in order to predict and optimise microstructures and related tensile properties.

Chapter 2.

EFFECT OF PRECIPITATION ON THE HOT COMPRESSION OF C6AL

Introduction

Hot rolling presents multiple roles. First, it efficiently reduces the thickness of the processed piece. At high temperature, the material flow stress is reduced by one order of magnitude compared to room temperatures. Large strains can be reached with limited applied load. Secondly, it removes the chemical and structural inhomogeneities inherited from casting. Brittle second phases might also dissolve during this processing step. In parallel to these two paramount roles of hot rolling, metallurgists strived to control final microstructures and final properties in order to suppress or limit the need of costly subsequent treatments.

Much research was hence devoted to understand and control the transformations occurring throughout the hot rolling process^{164,165}. These transformations are mainly restoration mechanisms, such as dynamic recrystallisation (dRX) observed in a wide range of alloys mainly with low or medium stacking fault energy (SFE)^{162,176,177} including Cantor's alloy^{97,178}. These mechanisms are influenced by chemical composition, deformation conditions – restoration mechanisms being favoured at large temperatures and low strain rates¹⁶⁰–, and also by the presence of precipitates. Precipitates might be present before deformation. They might also form during deformation. In both cases, precipitates

interact with work-hardening and restoration mechanisms in a way that depends on their size and location. In their review of 1984, McQueen and Jonas list how precipitates might influence dynamic softening ¹⁷⁹:

- Fine coherent precipitates (less than 10 nm in size) pin grain and subgrain boundaries inhibiting the activation of dRX, resulting in very large flow stress;
- Small precipitates (between 10 and 300 nm) limit the extent of dRX by pinning boundaries without fully inhibiting it. It results in the stabilisation of a fine grain structure presenting large flow stress;
- Large and elongated precipitates, for example at grain boundaries, might broke and spheroidize during deformation. Their presence can result in the formation of regions of large strain gradients that could result in particle stimulated nucleation (PSN).

Much research was carried out on the hot rolling of conventional alloys, including steels or stainless steels ^{180–183}. With the recent interest on MCAs, researchers started to focus on their behaviour during hot deformation ^{97,178,183–192}. So far, Cantor's alloys and its derivatives are the most studied, with a particular focus on single phase FCC microstructures ^{97,178,186,190,191}. An increasing interest on eutectic or dual phase microstructures is also to be noted ^{185,189,192}. The studies published so far on Cantor's alloy, with its single-phase FCC microstructure, conclude on its conventional behaviour when submitted to compression at high temperature, with the activation of dislocation slip and dRX during deformation.

This chapter has a double objective. First, it aims to study the behaviour of single-phase FCC C6Al, including 6 at.% of aluminium, when deformed between 900 and 1100°C. Hot compression tests are used to simulate hot rolling. Particular interest will be given to the potential interactions between dRX and precipitation occurring before and/or during deformation. In addition, the same compression experiments are reiterated on an austenitic stainless steel of grade 304L. Among other alloys close to Cantor and C6Al (e.g. nickel-based alloys), this particular alloy was chosen first based on its similarities with Cantor alloy: austenitic matrix, similarity in the elements composing the alloy, similar SFE; but also due to its availability. The comparison between 304L and C6Al will assess how special the MCA is when compared to 304L.

2.1. Materials and methods

2.1.1. Materials

Ingots n°1 of C6Al is used in this chapter. The samples from 304L stainless steel originate from a thick metal sheet bought from a steel manufacturer. The chemical compositions of the two alloys, measured by ICP-OES, are given in **Table 2.1**. A combustion analyser was used to measure their content in light elements, i.e. carbon, nitrogen and oxygen.

Table 2.1 Chemical compositions of the two alloys measured by ICP-OES and combustion analyser for the lighter elements, in atomic percent.

(at.%)	304L	C6Al
Al	0	6.1 ± 0.1
Co	0	18.8 ± 0.1
Cr	18.6 ± 0.1	18.1 ± 0.5
Fe	69.3 ± 0.9	19.2 ± 0.4
Mn	1.6 ± 0.0	19.1 ± 0.2
Ni	9.3 ± 0.0	18.8 ± 0.1
C	0.13 ± 0.01	Not measured
N	0.13 ± 0.02	Not measured
O	0.07 ± 0.01	Not measured
Cu	0.2 ± 0.0	0
Mo	0.1 ± 0.0	0

2.1.2. Processing

The ingot of C6Al was first hot rolled at 1200°C with a thickness reduction of 50% (Von Mises strain equivalent of $\varepsilon_{VM} = 0.8$). Cylinders were machined from the hot rolled bar with a numerical milling machine. Their dimensions are 10 mm in height and 5 or 8 mm in diameter, depending on the deformation temperature. Similar cylinders were machined from the as received 304L bar through electric discharge machining.

The cylinders were submitted to the thermomechanical treatment (TMT) of **Fig. 2.1** with deformation temperatures between 900 and 1100°C and a strain rate of 0.1 or 1/s. Each specimen was deformed to a true strain of 0.6. Due to their respective load and temperature limitations, two compression devices were used to cover the full temperature range. The tests at temperatures of 950 and 1100°C were performed in a dilatometer equipped with a deformation module. Cylinders with a diameter of 5 mm were used. In this case, the temperature was controlled via a thermocouple welded on the surface of the cylinder. No lubrication between the specimens and the quartz heads of the dilatometer was performed.

Tests at temperatures of 900 and 950°C were performed in a MTS Landmark 250 compression-testing machine (CTM) equipped with a tubular furnace from LGTech. Cylinders of 8 mm in diameter were used. In this case, the cylinders were first homogenized at 1200°C in a Carbolite RXF1200 oven placed near the CTM. After 5 minutes, the cylinders were transferred in the CTM preheated at the deformation temperature, i.e. 900 or 950°C. No control of the temperature was performed in this case. The compression curves were not corrected for potential overheating. In this case, boron nitride was pulverized on tools and specimens as lubricant.

In the CTM and in the dilatometer, deformation is performed after a holding time of 5 minutes at the deformation temperature to ensure that the temperature is uniform. The tests performed at 950°C in the dilatometer were successfully compared with what was obtained with the CTM at the same temperature. Only the tests at 950°C using the CTM are shown in this chapter.

Additional specimens were quenched before deformation. They are referred to as blank test samples.

Additional pieces of information on materials, processing and characterisation methods can be found in annexe A at the end of this manuscript.

2.1.3. Nomenclature

The samples are referred to using first the initial of the alloy, i.e. C for C6Al and A for the austenitic stainless steel 304L, and then their deformation conditions. For example, the sample of 304L deformed at 1000°C with a strain rate of 1/s is referred to as A-1000/1. The blank test sample of C6Al annealed at 900°C is referred to as C-900/B.

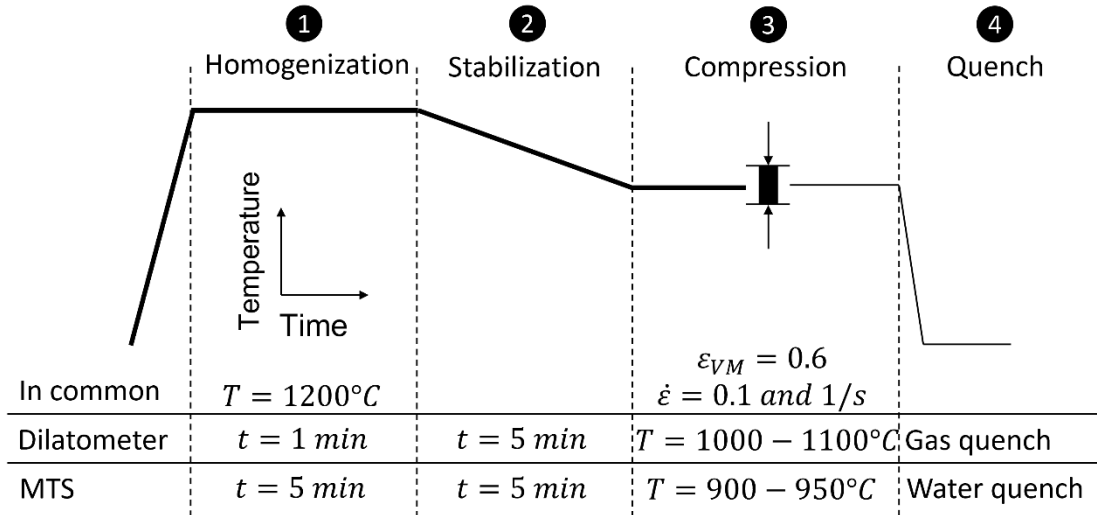


Fig. 2.1 Sketch of the thermomechanical treatment used in this chapter. The processing conditions of each step are given at the bottom depending on the compression device. [Full-size](#).

2.1. Results

Fig. 2.2 presents the phase equilibria of 304L and C6Al calculated using ThermoCalc software with inputs from respectively the TCFE9 and TCHEA4 thermodynamic databases. The homogenisation and deformation temperatures used in this chapter are superimposed on each figure with respectively dashed and dotted black lines. In 304L, the homogenisation and the four deformation temperatures are located in the fully FCC domain. Regarding C6Al, the homogenisation temperature is located in the fully FCC domain. The deformation temperatures of 950, 1000 and 1100°C are located in the FCC+B2 domain, while 900°C is located in the FCC+B2+σ domain.

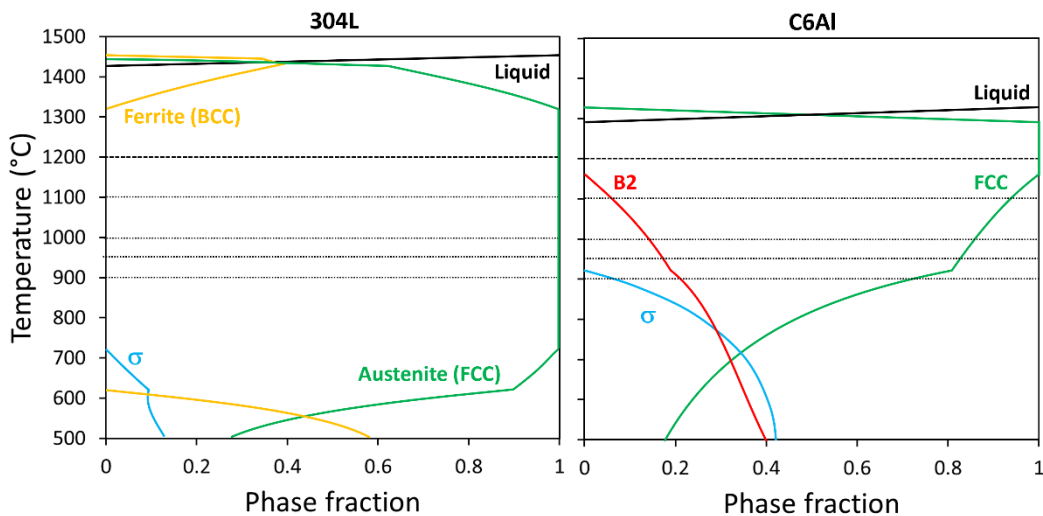


Fig. 2.2 Phase fractions of the two alloys used in this chapter: 304L (left) and C6Al (right). The dashed horizontal line indicates the homogenization temperature of 1200°C. The four dotted horizontal lines indicate the four deformation temperatures considered in this chapter: 900, 950, 1000 and 1100°C. [Full-size](#).

2.1.1. Before compression

Fig. 2.3 presents the microstructures of the compression cylinders before the start of the TMT depicted in **Fig. 2.1**. Both alloys are fully FCC. The grain size of C6Al is $84 \pm 35 \mu\text{m}$ and that of 304L is $73 \pm 28 \mu\text{m}$. Annealing twins are observed in both microstructures.

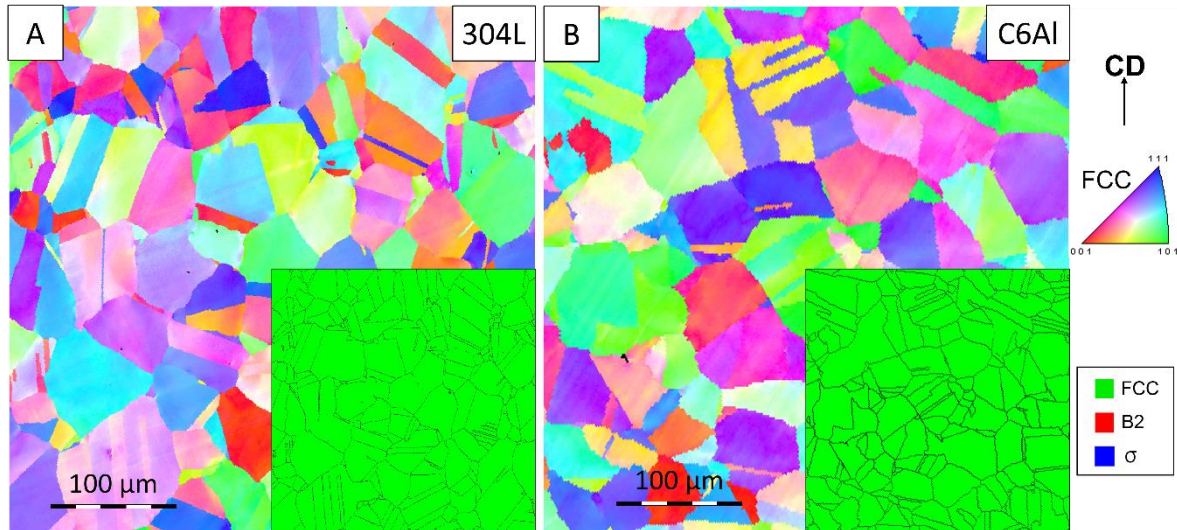


Fig. 2.3 IPF-Z and phase maps of the cylinders used for compression. (A) 304L and (B) C6Al. [Full-size](#).

Blank test specimens of both 304L and C6Al were processed according to the TMT of **Fig. 2.1** but without deformation. These samples were then characterised by XRD and in the SEM in order to identify the presence of second phases before deformation.

Peaks corresponding to the FCC phase are observed in all specimens (**Fig. 2.4A**). No peak corresponding to ferrite or other second phases are observed in **Fig. 2.4A** or in the zoomed view of **Fig. 2.4B**. **Fig. 2.5** presents micrographs taken at grain boundaries. No precipitation is observed there, at least at the scale of observation. These results indicate that 304L is single-phase FCC before deformation.

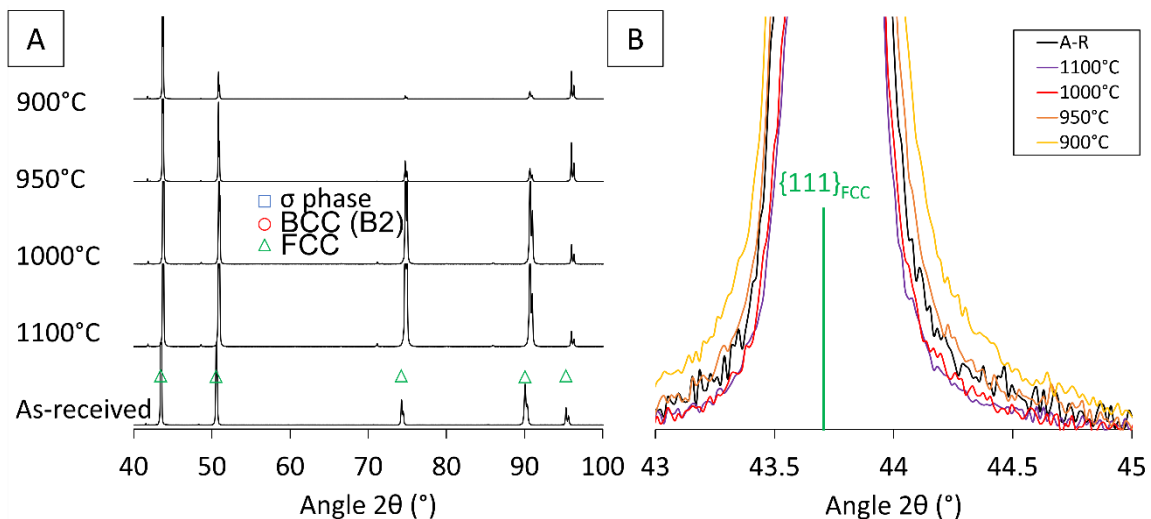


Fig. 2.4 XRD results on the blank test specimens of 304L. (A) Full diffractograms. (B) Zoom on the $\{111\}$ peak of the FCC phase at 43.7° (green vertical line). [Full-size](#).

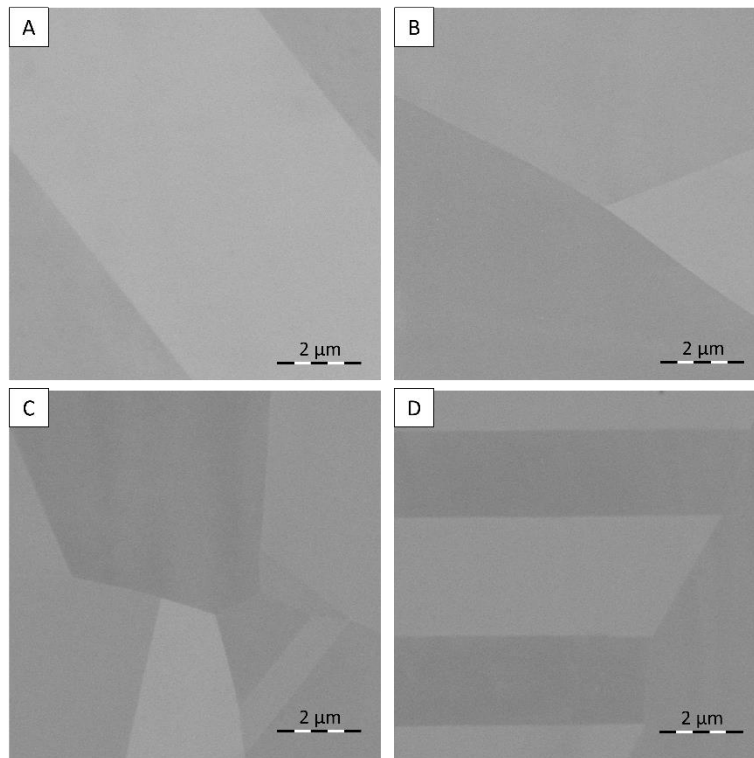


Fig. 2.5 BSE SEM images acquired on the blank test specimens of 304L. (A) 900°C, (B) 950°C, (C) 1000°C and (D) 1100°C. [Full-size](#).

Regarding C6Al before compression, peaks corresponding to the FCC phase are observed at each temperature (**Fig. 2.6A**). A clear shoulder is observed when zooming on the $\{111\}$ FCC peak (**Fig. 2.6B**), indicating the presence of the B2 phase at 900 and 950°C. No peak corresponding to the σ phase was observed at 900°C or at other temperatures. **Fig. 2.7** confirms the presence of precipitates in C-900/B and C-950/B. They are $1.4 \pm 0.9 \mu\text{m}$ in length and $0.3 \pm 0.1 \mu\text{m}$ in width in C-950/B. Precipitates are also observed in C-1000/B. They are elongated and larger than at lower temperatures. All these precipitates are located at grain boundaries. No precipitation is observed in C-1100/B.

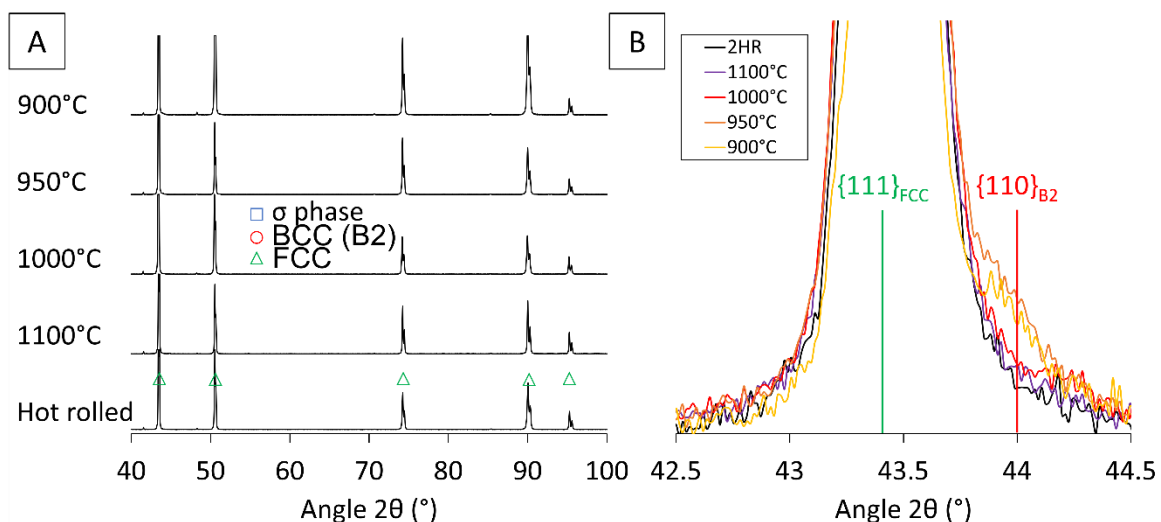


Fig. 2.6 XRD results on the blank test specimens of C6Al. (A) Full diffractograms. (B) Zoom on the $\{111\}$ peak of the FCC phase at 43.4° (green vertical line). The position of the $\{110\}$ peak of the B2 phase is indicated at 44° . [Full-size](#).

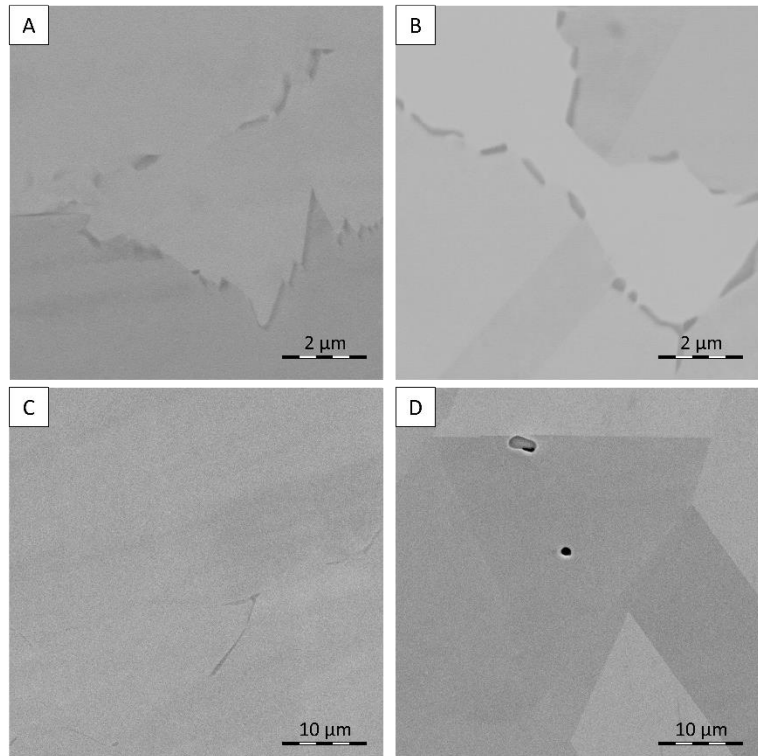


Fig. 2.7 BSE SEM images acquired on the blank test specimens of C6Al. (A) 900°C, (B) 950°C, (C) 1000°C and (D) 1100°C. [Full-size](#).

2.1.2. Compression tests

The true stress – true strain curves of 304L and C6Al are presented in **Fig. 2.8**. All curves present the same shape. It starts with a steep slope that decreases until reaching a peak stress. The flow stress then decreases until a steady state is reached. Only the two curves of 304L deformed at 900°C (in blue in **Fig. 2.8A**) do not present a peak stress nor a stress steady state. Similar stress levels are found at 1000 and 1100°C for C6Al and 304L. For example, at 1000°C and 0.1/s, the maximum stress for 304L is 146 MPa and 137 MPa for C6Al. At lower temperatures, the stress levels reached by C6Al specimens are considerably larger than those of 304L. Moreover, peak stress is reached at lower true strain values in C6Al than in 304L.

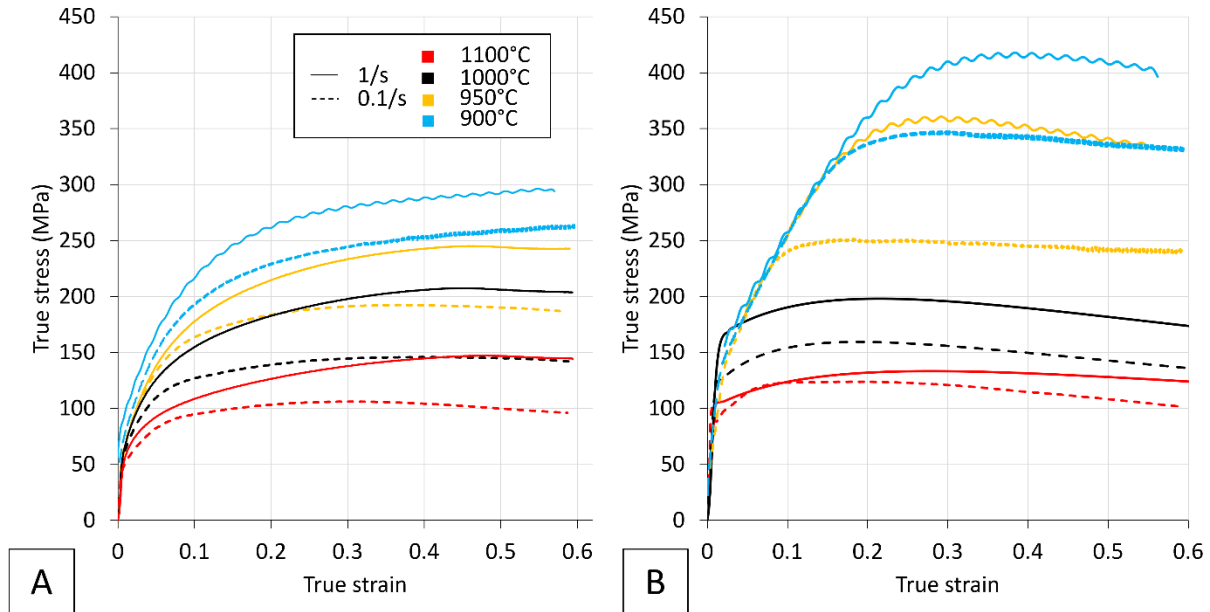


Fig. 2.8 True stress – true strain curves of (A) 304L and (B) C6Al obtained during compression at four temperatures (indicated with colours) and two strain rates (indicated in dotted or solid lines). [Full-size](#).

Fig. 2.9 shows the evolution of WHR versus true stress at 900°C 0.1/s (in blue) and 1000°C 1/s (in black). The two curves of 304L continuously decrease towards zero. In C6Al at 1000°C 1/s, a steep decrease is observed. At 900°C 0.1/s, a transition stage of constant WHR is observed between stress values of 160 and 260 MPa. WHR then decreases towards zero. The two curves of C6Al are shifted by 50 MPa compared to those of 304L.

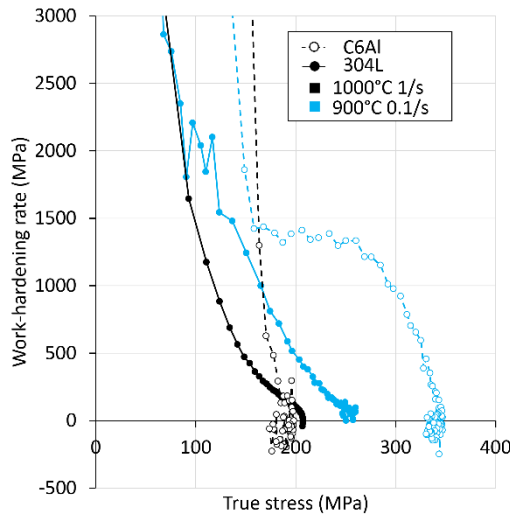


Fig. 2.9 Evolution of WHR versus flow stress. Only the curves at 900°C 0.1/s and 1000°C 1/s are shown for easy reading. The curves of C6Al are shown with dotted lines. [Full-size](#).

Fig. 2.10 shows the link between the logarithm of the Zener-Hollomon parameter (Z) and peak stress for both C6Al and 304L. Z links deformation temperature and strain rate in a single parameter. It is expressed as follows:

$$Z = \dot{\epsilon} \exp\left(\frac{Q}{RT}\right) \quad (\text{Eq. 2.1})$$

with $\dot{\epsilon}$ the strain rate, R the gas constant, T the temperature in Kelvin and Q an activation energy. In this chapter, the value of 350 kJ/mol is used for C6Al, in agreement with the value reported by Eleti *et al.* on Cantor's alloy⁹⁷. For 304L, the value of 386 kJ/mol is used¹⁸².

Peak stress values of 304L are found to follow a linear trend with $\ln Z$. About C6Al, points can be divided in two linear trends: at 900-950°C with the largest slope; and 1000-1100°C. A jump in stress of 50 MPa between the two regimes is also observed. This indicates that an additional strengthening mechanism is present at low temperatures. As will become clear later on, this mechanism is precipitation.

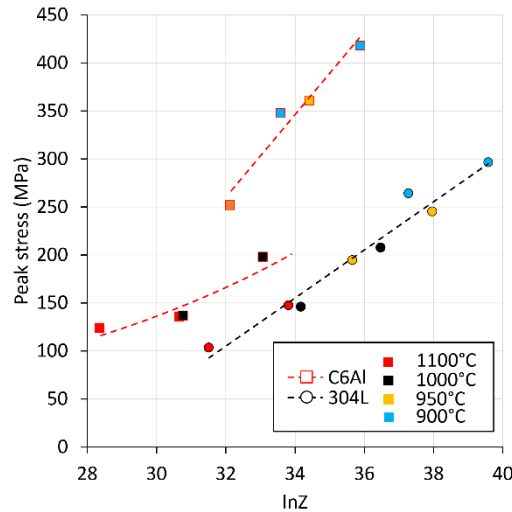


Fig. 2.10 Graph of the logarithm of the Zener-Holomon parameter versus peak stress for 304L (black-edged circles) and C6Al (red-edged squares). The filling colours of the points indicate their deformation temperature. [Full-size.](#)

2.1.3. Microstructures after compression of $\epsilon_{VM} = 0.6$

After compression testing, the microstructure of deformed specimens is characterised in the central parts where the deformation is the largest.

The microstructures after hot compression are given in **Fig. 2.11** as IPF maps. They are partially recrystallised. Recrystallised grains are identified when their grain orientation spread (GOS) is below 4° (see the materials and methods chapter in annexe A for more precision). In some cases, an additional threshold based on the grain aspect ratio was applied due to the low GOS indexes presented by non-recrystallised annealing twins. The non-recrystallised grains appear shaded.

In 304L and C6Al, low deformation temperatures resulted in small recrystallisation fractions and small recrystallised grain sizes. These two parameters increase with an increase in deformation temperature and with a decrease in strain rate. In all cases, recrystallisation occurs along the grain boundaries of the initial FCC grains. Necklace structures form at 1000°C and above. Only FCC was observed.

From these maps (magnification x200), the recrystallisation fraction is extracted. Additional maps acquired at the magnification of x1k on the recrystallised zones (not shown) were used to measure the recrystallised grain size. These parameters are plotted versus peak stress in **Fig. 2.12**. C6Al presents larger recrystallised fractions at 1000-1100°C. Similar fractions are observed at 900-950°C (**Fig. 2.12A**). Similar recrystallised FCC grain sizes are found at all temperatures (**Fig. 2.12B**).

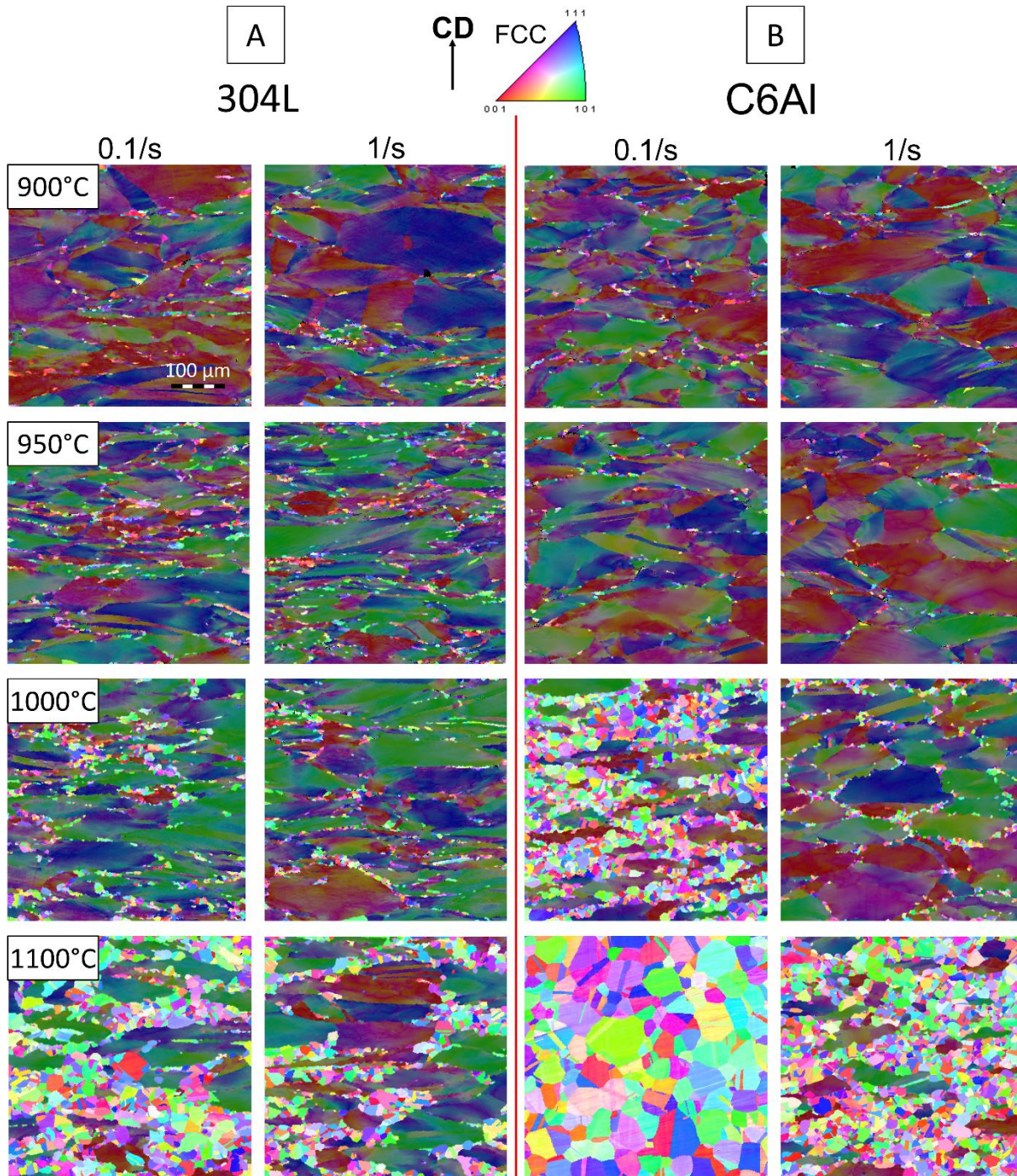


Fig. 2.11 IPF maps after hot compression of the specimens of (A) 304L and (B) C6Al. The colour code indicates the directions parallel to the specimen radial directions. All maps present the same scale. No second phase was observed at this scale in any of these maps. On all maps, the non-recrystallised grains are shaded. The compression direction (CD) is vertical. [Full-size](#).

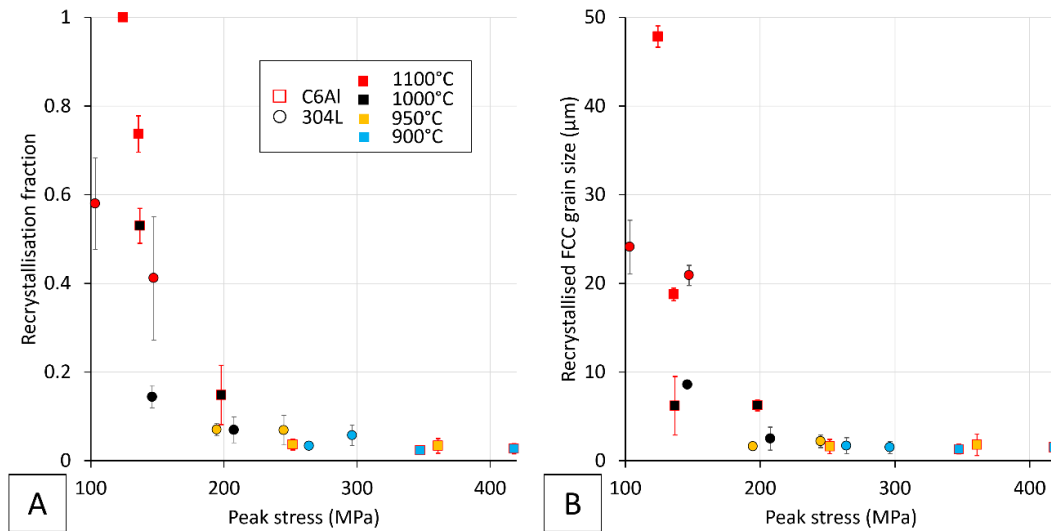


Fig. 2.12 (A) Recrystallisation fraction and (B) recrystallised grain size versus peak stress for 304L (black-edged circles) and C6Al (red-edged squares). The filling colour corresponds to deformation temperatures. [Full-size](#).

Fig. 2.13 shows enlarged views of the microstructures after hot compression in 304L at the strain rate of 0.1/s. No precipitation is observed whatever the deformation temperature, at least at the scale of observation.

In C6Al (**Fig. 2.14**), precipitates are observed after compression between 900 and 1000°C. At the temperatures of 900 and 950°C, a large number of precipitates can be found on the grain boundaries of recrystallised grains. Small and equiaxed precipitates (indicated by red arrows) are located on the newly recrystallised grain boundaries. They are dispersed evenly in the regions where dRX was activated. In C-950/0.1, they measure $0.2 \pm 0.1 \mu\text{m}$ in length and $0.1 \pm 0.1 \mu\text{m}$ in width. At 1000°C, precipitates are rarely found. No precipitates are observed after deformation at 1100°C (**Fig. 2.14D**).

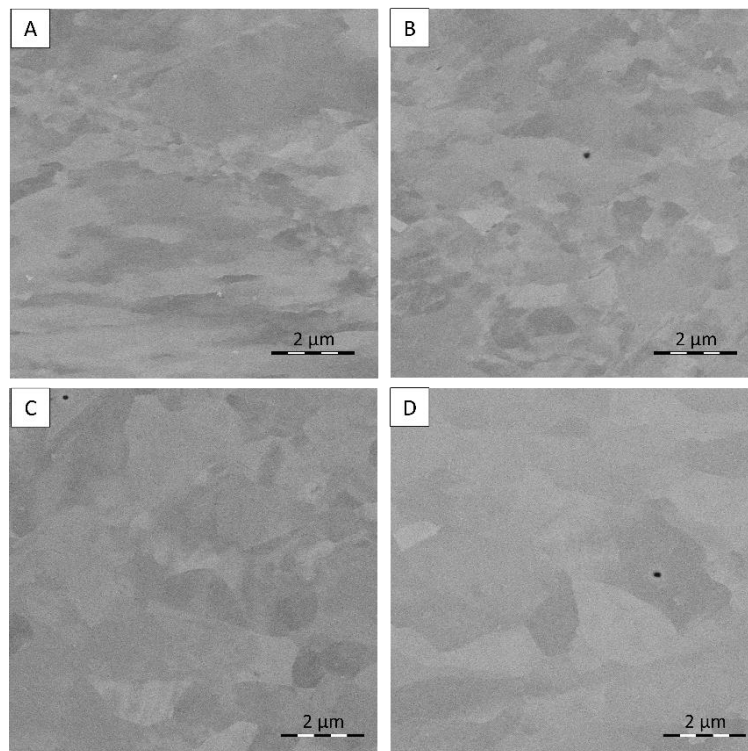


Fig. 2.13 BSE SEM images acquired after hot compression in 304L. (A) A-900/0.1, (B) A-950/0.1, (C) A-1000/0.1 and (D) A-1100/0.1. [Full-size](#).

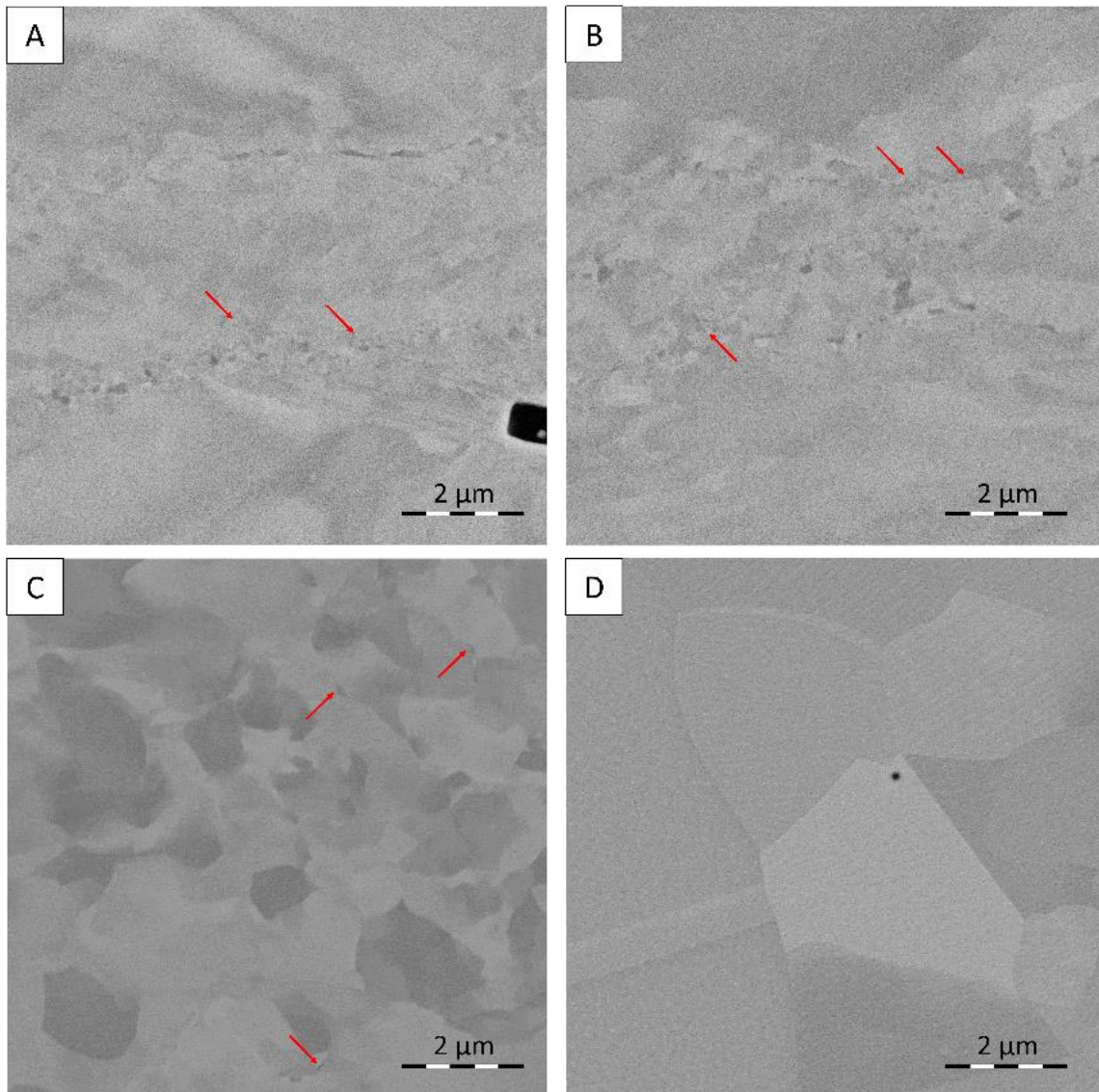


Fig. 2.14 BSE SEM images acquired after hot compression in C6Al. (A) C-900/0.1, (B) C-950/0.1, (C) C-1000/0.1 and (D) C-1100/1. Precipitates are indicated with red arrows. [Full-size](#).

2.2. Discussion

This discussion will first focus on the behaviour of 304L during hot compression. Then, the case of C6Al will be treated, before comparing the two. Finally, process windows for C6Al will be discussed.

2.2.1. Hot compression of 304L

The characterisation of the blank test specimens indicates that 304L is single-phase FCC at all investigated temperatures, at least at the investigated scales of observation (**Fig. 2.4** and **Fig. 2.5**). TEM investigations on grain boundaries would be necessary to confirm this statement. This agrees with the thermodynamic calculations of **Fig. 2.2**. **Fig. 2.13** confirms the absence of strain induced phase transformation in 304L. No martensitic transformation nor precipitation at grain boundaries is observed.

During deformation at 1000 and 1100°C, in the dilatometer, the temperature was controlled via a thermocouple and limited overheating occurred (below 10°C). However, at 900 and 950°C, in the CTM, no such control of the temperature was performed. Overheating of the specimens could then have

occurred. The increase in temperature ΔT due to plastic work can be quantified from the true stress-true strain curve ($\sigma = f(\epsilon)$) by using the following expression ¹⁹³:

$$\Delta T = \frac{k\eta}{\rho C_p} \int_0^\epsilon \sigma d\epsilon \quad (\text{Eq. 2. 2})$$

with $k = 0.95$ the theoretical fraction of mechanical work converted to heat, η the thermal efficiency indicating whether the deformation is adiabatic or not in function of strain rate. For a strain rate $\dot{\epsilon}$ of 0.1/s, $\eta = 0.95 + 0.316 * \log(\dot{\epsilon})$. At 1/s, $\eta = 0.95$ ¹⁹³, ρ the density ($\rho = 7912 \text{ kg.m}^{-3}$ for 304 steel ¹⁹⁴), C_p the specific heat ($C_p = 665 \text{ JK}^{-1}\text{kg}^{-1}$ for 304 steel ¹⁹⁴). It results in a maximum overheating of 25°C at 900°C and of 19°C at 950°C. Stress values at large strains might then be slightly underestimated due to overheating during deformation.

Compression starts with a work-hardening stage where dislocations multiply and interact, resulting in the gradual hardening of the material (steep slopes until 50 MPa in **Fig. 2.8A**). As this process occurs at high temperature, the material SFE is also high, limiting the dissociation of perfect dislocations into partials. It results in easier cross-slipping of dislocations between slip planes. Dislocation climb is also activated. These two elements result in a more homogeneous deformation structure with a lower ability to store defects ¹⁶⁰. Nonetheless, depending on the deformation conditions, the stored energy might become large enough to activate softening mechanisms, such as dRV or dRX. First, dRV activates and results in the decrease of WHR observed at stress larger than 50 MPa, observed in **Fig. 2.9**.

Then, a peak stress is observed in all cases, except at 900°C where stress increases until the true strain of 0.6. The presence of a peak stress indicates the activation of dRX. This is opposed to the observation of a stress steady state without any peak which indicates the activation of solely dRV ¹⁶⁰. The activation of dRX is confirmed in all specimens – including those at 900°C – by the observation of deformed microstructures (**Fig. 2.11B** and **Fig. 2.13**). These observations agree with previous reports on the hot compression of 304L in literature ^{182,183}. Recrystallised grains form on the initial grain boundaries as necklace structures. This is typically observed at 1000°C with recrystallised grains following initial grain boundaries. A peak stress is expected to occur at 900°C if deformed to larger strain levels.

Compression curves present a single stress peak. This type of behaviour, as opposed to the presence of multiple peaks, indicates that a single cycle of recrystallisation is activated during compression. It also indicates grain refinement ¹⁶³, which is confirmed by the observations of deformed microstructures (**Fig. 2.11B** and **Fig. 2.12B**).

Moreover, the observed peak stress values are of the same order of magnitude than what was reported in literature on the hot compression of 304L (**Table 2.2**) ^{182,183}. The evolution of the peak stress of 304L versus temperature (solid green circle) also agrees with that of solid solution alloys such as the austenitic stainless steels of grade 317 (solid black circle) (**Fig. 2.15**) ¹⁷⁹. The deformation conditions also influence the intensity of dRX. This is illustrated through the evolution of recrystallisation fraction and the recrystallised grain size in **Fig. 2.12**. The intensity of dRX increases with increasing temperature and decreasing strain rate, as also observed in literature ¹⁶⁰.

Table 2.2 Comparison of the experimental peak stress values found in this chapter for 304L with those reported in two publications ^{182,183}.

	C+N (w.%)	Initial grain size (μm)	900/0.1 (MPa)	1000/1 (MPa)	Ref.
304L	0.06	73 ± 28	264	208	This study
304L	0.02	60	181	175	¹⁸²
304LN	0.13	27.5	264	229	¹⁸³

In summary, this analysis on 304L reveals that no precipitation or strain induced phase transformation occurs during hot compression. 304L behaves conventionally with an agreement with theory and literature on similar austenitic stainless steels. The next section will focus on the behaviour of C6Al when hot compressed.

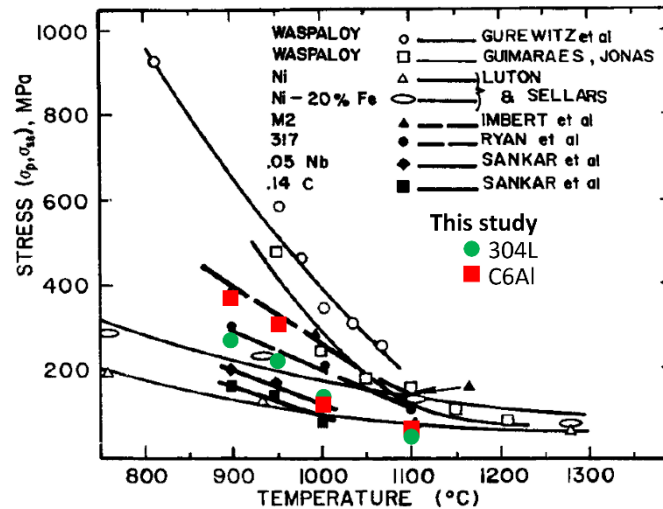


Fig. 2.15 Review of the peak stress values of different alloys during compression between 800 and 1300°C from McQueen and Jonas ¹⁷⁹. [Full-size](#).

2.2.2. Hot compression of C6Al

Precipitates are observed in C6Al before compression between 900 and 1000°C (**Fig. 2.7**). The precipitates at 1000°C revealed larger (**Fig. 2.7C**) but with a lower volume fraction (**Fig. 2.6B**). Even if they exceed that at 1000°C, the fractions of precipitates at 900 and 950°C remain also limited (**Fig. 2.6**). As precipitation is restricted to grain boundaries, these low volume fractions can be attributed to the large grain size presented by C6Al before deformation (**Fig. 2.3**). The presence of precipitates at these temperatures agrees with the phase diagram of **Fig. 2.2** which locates these temperatures in multiphase domains. The σ phase was not observed. No precipitation was observed at 1100°C. The thermodynamic driving force for precipitation must be too low at this temperature to induce the formation of precipitates, due to the proximity of the B2 solvus.

The compression curves of C6Al present similar shapes as those of 304L, with the presence of a peak stress (**Fig. 2.8B**). At 1000 and 1100°C, similar overheating as in 304L (below 10°C) was observed. At 900 and 950°C, the maximum overheating is 34°C at 900°C and 29°C at 950°C. This calculation was performed with $\rho = 7697 \text{ kg} \cdot \text{m}^{-3}$ obtained from a rule of mixture. The specific heat was calculated as $C_p = \sum x_i C_{pi}$, with x_i the atomic fraction of the element i and C_{pi} its specific heat at 900-950°C ¹⁹⁵⁻¹⁹⁷ giving a value of $C_p = 673 \text{ JK}^{-1} \text{ kg}^{-1}$. These overheating values are comparable to those obtained for 304L.

As a consequence, the observed softening at large strain values could be due either to dRX or to the overheating of the sample during deformation. Recrystallised grains were observed after compression in all conditions indicating the activation of dRX in all specimens (**Fig. 2.11B** and **Fig. 2.14**). The presence of precipitates before deformation at 900-1000°C did not suppress dRX.

In all conditions, compression curves start with steep slopes that go up to around 100 MPa, reaching 160 MPa in C-1000/1. At deformation temperatures of 1000 and 1100°C, this first transition is accompanied by a brutal decrease in work-hardening rate. This transition is clearly observed in C-1000/1 (**Fig. 2.8B**). It is also visible on the evolution of WHR that abruptly falls to zero (**Fig. 2.9**). The

large stress at which this transition occurs and its sharpness are the sign of the activation of dRX with limited prior dRV. The limitation of dynamic or static recovery was already observed in MCAs^{198–200}. In these three publications, the authors made the hypothesis of a solute drag effect enhanced by the complex chemical compositions of this family of alloys. It would be strengthened in C6Al with the presence of aluminium with its considerably smaller atomic radius.

At temperatures of 900 and 950°C, larger stress values are observed, up to 420 MPa (**Fig. 2.8**). This strengthening is clearly depicted by the jump in peak stress values observed between 950°C and 1000°C (**Fig. 2.10**). This jump in stress is not a specificity of MCAs but of C6Al, as observed when comparing the peak stress values obtained with C+Al and Cantor^{97,178} (**Table 2.3**). At 1000°C, all three alloys present similar peak stress values. At 900°C, the peak stress of C6Al exceeds for around 100 MPa that of Cantor's alloys.

Table 2.3 Comparison of the experimental peak stress values of C6Al with those reported in two publications^{97,178}.

	Initial grain size (μm)	900/1 (MPa)	1000/1 (MPa)	Ref.
C6Al	84 \pm 35	418	233	This study
Cantor	-	323	232	97
Cantor	12.6	298	233	178

At 900-950°C, the initial steep slopes of the compression curves are followed by a second work-hardening regime of constant WHR (**Fig. 2.9**). Softening is only activated at larger stress values, up to 350 MPa in C-900/1h. As at larger temperatures, the observed softening is due to the activation of dRX. This is confirmed by the SEM micrographs acquired after deformation (**Fig. 2.14**). The limitation of dRX is attributed to the presence of precipitates.

After deformation, precipitates are observed at 1000°C and below (**Fig. 2.14**), as was the case before deformation (**Fig. 2.7**). However, the precipitates before and after deformation do not present the same morphologies and sizes. While precipitates were large and elongated before deformation, they are small and equiaxed after deformation. Their B2 nature is however unchanged, as observed in the phase map of **Fig. 2.16** acquired after deformation. Hence, deformation resulted in the modification of the precipitate populations. These modifications could have happened by the breaking of the initial precipitates and their spheroidization as previously observed in Al alloys²⁰¹ or in steels²⁰². Dissolution and precipitation could have also occurred as suggested by the locations of precipitates at newly formed grain boundaries. A mix of both solutions could also have occurred.

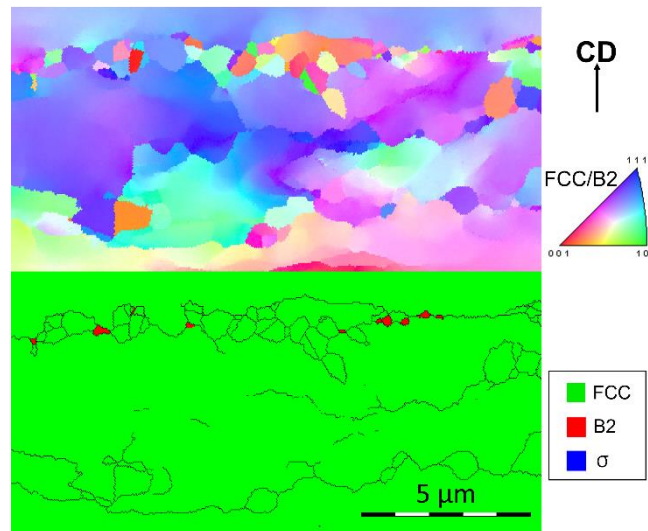


Fig. 2.16 IPF and phase maps acquired along an old grain boundary in C-950/1. The colour code indicates the directions parallel to the specimen radial direction. [Full-size](#).

Interactions between precipitation and dRX have already been observed in a wide range of materials and with different precipitate types^{203–205}. Precipitation, or spheroidization of already present precipitates, is favoured during deformation due to the enhanced diffusion induced mainly by the movement of dislocations. In agreement with McQueen and Jonas¹⁷⁹, such dynamic precipitation results in the limitation of dRX through the Zener pinning effect. Hence, this is most probably the interactions between B2 grains and grain boundaries in C6Al that reduces the extent of dRX, resulting in low dRX fractions and grain sizes at 900 and 950°C. At 1000°C, no limitation of dRX was observed due to the lower fraction and larger size of precipitates.

After deformation, the B2 precipitates are observed only locally in the microstructure, along the initial grain boundaries and in the surrounding zones where dRX activates. Its fraction hence remains limited when considering the overall microstructure with a grain size of around 80 μm . The presence of precipitates in these regions is not expected to result in a significant overall strengthening. Instead, it is the limitation of softening mechanisms, mainly dRX, that results in the strengthening of the material.

As a summary, at 1000°C and above, C6Al can be considered as a solid solution alloy. Nonetheless, its complex chemical composition along with the addition of aluminium results in the limitation of dRV. Instead, dRX activates and results in significant softening. At 900–950°C, interactions between precipitation and grain boundaries limit dRX, resulting in large stress values. This summary is confirmed when comparing the peak stress levels of C6Al with those reviewed by McQueen and Jonas¹⁷⁹, shown in **Fig. 2.15**. At 1000–1100°C, stress levels of C6Al (solid red squares) compare to that of 304L and to solid solution alloys such as 317 stainless steels (solid black circle in **Fig. 2.15**). At 900–950°C, C6Al compares to M2 tool steel exhibiting dynamic precipitation during deformation.

2.2.3. Comparison between 304L and C6Al

As detailed above, dRX activates in both alloys when deformed between 900 and 1100°C (**Fig. 2.8** and **Fig. 2.11**). The extent of dRX was evaluated in both alloys through the measure of the recrystallisation fractions and recrystallised grain sizes. These are plotted in **Fig. 2.12** against peak stress. Two regimes might be distinguished, corresponding to the two regimes already identified for C6Al: at large temperatures (red and black filled points), dRX is more intense in C6Al than in 304L. This is especially visible by comparing recrystallisation fractions (**Fig. 2.12A**). At low temperatures (orange and blue filled points), dRX is slightly less intense in C6Al than in 304L. The same two regimes are observed when

considering peak stress values. At high temperatures, peak stress values are similar, while at low temperatures C6Al presents significantly larger peak stress values.

This comparison must however be considered carefully as the two alloys do not present the same melting points. dRX involves the movement of HAGBs and as such it involves the movement of vacancies and substitutional atoms in the lattice. These events are controlled by diffusion. Experiments on a wide range of materials revealed that diffusion rates were found similar not at equal absolute temperature but at equal homologous temperature (T_H), the latter being the ratio of the former on the material melting point ¹⁶⁶. Differential scanning calorimetry (DSC) experiments were conducted on both alloys to determine their melting temperatures. It was found at 1290°C for C6Al and 1425°C for 304L, close to the values obtained on the calculated phase diagrams (**Fig. 2.2**).

The more intense recrystallisation, observed in C6Al at large temperatures, can then be rationalised by a larger T_H , due to a lower melting point. The larger T_H of C6Al results in larger diffusion rates that in turn induce a more intense dRX. Moreover, it results in the activation of dRX at lower strain values, as observed by the position of stress peaks in **Fig. 2.8**.

When comparing at the constant T_H of 0.77-0.78, i.e. 1000°C for C6Al and 1100°C for 304L (**Table 2.4**), recrystallisation fractions and grain sizes are found lower in C6Al, indicating lower dRX intensity at this T_H . An increase in stress of around 40 MPa is observed in C6Al. This increase in stress is most probably due to the increased solid solution strengthening and increased limitation of dRV observed in C6Al, but also to the more limited dRX. Nonetheless, behaviours are found similar in the two alloys when considering large T_H values.

Table 2.4 Comparison of the recrystallisation fraction and recrystallised grain size between 304L and C6Al at T_H of 0.7 and 0.77-0.78.

T_H	Strain rate (/s)	Peak stress (MPa)	Recrystallisation fraction	Recrystallised grain size (μm)
304L				
0.70	0.1	146	0.14 ± 0.03	8.6 ± 0.4
	1	208	0.07 ± 0.03	2.5 ± 1.3
0.77	0.1	103	0.58 ± 0.10	24.1 ± 3.0
	1	147	0.41 ± 0.14	21.0 ± 1.0
C6Al				
0.70	0.1	347	0.02 ± 0.01	1.3 ± 0.5
	1	418	0.03 ± 0.01	1.5 ± 0.6
0.78	0.1	137	0.53 ± 0.04	6.2 ± 3.3
	1	198	0.15 ± 0.07	6.3 ± 0.6

The situation changes at the homologous temperature of 0.70. Lower dRX fractions and grain sizes are found for C6Al (**Table 2.4**). Moreover, peak stress levels of C6Al exceed that of 304L by around 200 MPa, increasing significantly from the interval of 40 MPa found at the lower T_H of 0.77-0.78. Hence, at low temperature, C6Al differentiates from the conventional behaviour presented by 304L due to precipitation.

This study remains far from the complete industrial process of hot rolling. In the steel industry, rolling is performed on metal slabs of around 250 mm in thickness. Hot rolling then starts with *roughing* where the thickness is reduced to 25-40 mm (Von Mises equivalent ε_{VM} of maximum 2.7). The metal slab starts at 1200°C and ends at around 1000°C. Then *finishing* is performed to achieve thickness of

2-10 mm (ε_{VM} of maximum 2.9). Temperature is then between 800 and 1000°C. Coiling is finally performed after controlled cooling²⁰⁶. Also, strain rates are much larger in industrial rolling, attaining several tens per second, as opposed to the maximum strain rate of 1/s used in this study. The compression tests realised in this chapter with an equivalent strain of 0.6 are closer to a single pass than to the complete industrial hot rolling process.

Nonetheless, process windows of C6Al can be determined based on these results. At deformation temperatures of 1000-1100°C, C6Al behaves as a conventional solid solution alloy. Hence, industrial roughing could be applied to C6Al. Large thickness reductions would then be possible without significant increase in load. An increase in load is still expected due to solid solution strengthening as shown when comparing 304L and C6Al at 1000°C (**Table 2.4**). At 900-1000°C – corresponding to the finishing stage of industrial hot rolling –, precipitation is activated. It has two main consequences.

First, precipitation is interesting as it stabilises structures with small grain sizes. The final metal sheet then presents large strength. Such process was developed for steels with the dynamic precipitation of niobium carbonitrides achieving fine ferritic grain sizes²⁰⁴. The B2 precipitates of C6Al could be used in the same way as they result in recrystallised grain sizes below 2 μm (**Fig. 2.12**).

Secondly, the limitation of dRX by precipitation in C6Al considerably increases the material flow stress. A larger load would then be required for the metal sheet to be deformed to low thicknesses. In conventionally rolled metals, the flow stress does not exceed 300 MPa in the finishing passes of industrial rolling²⁰⁷⁻²⁰⁹. In C6Al, the flow stress reaches 420 MPa in C-900/1, suggesting difficulties to roll this material at 950°C and below.

Conclusions

Specimens of the MCA C6Al and of an austenitic stainless steel of grade 304L were submitted to compression tests between 900 and 1100°C. dRX activates in both alloys in the investigated temperature range. 304L compares well to other solid solution alloys with low stress values even when deformed at low temperatures. C6Al presents a similar behaviour when deformed at high temperatures. Nonetheless, its lower melting point results in more intense dRX than in 304L when compared at equal absolute temperature. The complex chemistry of C6Al also induces solid solution strengthening, as observed when comparing stress values at equal T_H . The grain size of recrystallised grains is also found smaller in C6Al than in 304L at equal T_H . This could be due to solute drag enhanced by the complex chemistry of C6Al although such link was not experimentally attested so far. At deformation temperatures of 900 and 950°C, C6Al exhibits large stress values, that do not follow the evolution drawn at high temperatures. This jump in stress is due to the interactions between B2 precipitates and the newly formed recrystallised grain boundaries, limiting their mobility. The limited fraction of these precipitates, and their location on grain boundaries, indicates that their influence on stress is indirect through the limitation of dRX softening.

From an industrial point of view, the dual behaviour of C6Al is interesting. Indeed, the first steps of hot rolling could be performed in the domain without precipitation to reach large reductions in thickness without significant increase in load. The last steps of hot rolling could then be performed at temperatures where precipitation is present to reach fine grain sizes in the final metal sheet. The significant increase in load at these temperatures is however a problem. This study on the hot behaviour of C6Al assesses the interesting potential of C6Al, closely related to precipitation. A study closer to the industrial conditions would be necessary to conclude on its true potential.

Chapter 3.

COLD ROLLING AND THE INTERACTIONS BETWEEN RECRYSTALLISATION AND PRECIPITATION DURING SUBSEQUENT ANNEALING¹

Introduction

After hot rolling, the next step of conventional thermomechanical treatment (TMT) is cold rolling (CR). Sheet thicknesses below the millimetre are reached with this technique. As developed in chapter 1, multiple deformation mechanisms are activated during deformation. As large strains can be reached with rolling, complex and refined microstructures are formed. These

¹ Most of this chapter was published ²¹⁰.

microstructures present high strength but limited ductility. They however contain a high density of defects that drive the activation of restoration mechanisms, such as recrystallisation, during subsequent annealing treatments. These treatments restore part of the material ductility while tuning its properties to specific needs. As the activation and kinetics of restoration mechanisms depend on the deformed state – and of the mechanisms activated during deformation – this study will first focus on the evolution of the microstructure during rolling. Knowing how C+Al behaves during rolling, annealing treatments at various temperatures are conducted.

The first objective related to annealing is to assess the possibilities of microstructural optimisations in C+Al. This first objective is interested in the *final* microstructures, obtained after completion of TMTs. It echoes with the wide literature interested in final microstructures^{38,58,60–66,68,91,199,211–214}. Notably, the extensive work performed on Al_{0.3}CoCrFeNi, containing 7 at.% of aluminium, proved the many possibilities of microstructures proposed by this composition^{61–66,91}. Yield strengths ranging from 160 MPa to 1800 MPa were obtained depending on the thermal history after CR⁶⁶. This type of studies often use large deformation levels, e.g. CR reductions of 90%^{63,65}, in order to reach in the shortest annealing times the desired microstructures and to ensure their homogeneity.

In addition to this first objective, the second is to understand what happens *during* the annealing treatment. Focus will be given to understand the interactions between the two mechanisms activated during annealing: recrystallisation and precipitation. To reach this objective, a TMT route with a CR thickness reduction of 60% is used. This first route results in slow rates of transformations. The mechanisms involved are identified based on this route, and their sequence of activation discussed. Finally, the influence of the CR intensity is analysed through the implementation of a second route with CR thickness reductions up to 92%.

3.1. Materials and methods

3.1.1. Materials

In this chapter, ingots n°1 and 2 of C6Al are used. Their compositions are given in **Table 3.1**. As will become clear, each ingot will be submitted to different thermomechanical routes (denoted H-CR and CR for ingots n°1 and 2, respectively).

Table 3.1 Chemical compositions of the two ingots used in this chapter, in atomic percent.

Ingot n°	1	2
Al	6.1 ± 0.1	5.8 ± 0.1
Co	18.8 ± 0.1	19.1 ± 0.2
Cr	18.1 ± 0.5	17.9 ± 0.1
Fe	19.2 ± 0.4	18.8 ± 0.1
Mn	19.1 ± 0.2	19.1 ± 0.2
Ni	18.8 ± 0.1	19.3 ± 0.1
C	Not measured	0.12 ± 0.03
N	Not measured	0.10 ± 0.03
O	Not measured	0.02 ± 0.00

3.1.2. Processing

The material was submitted to the processing routes presented in **Fig. 3.1** consisting first of a hot rolling step at 1200°C for a total reduction of 70% (true Von Mises strain of $\varepsilon_{VM} = 1.4$)

followed by water quenching. The first route consisted of a homogenization step at 1200°C for 24 hours and of cold rolling for a total reduction of 58% ($\varepsilon_{VM} = 1.0$). This route is called “H-CR”, related to the presence of a homogenisation step. The material was then annealed at various temperatures ranging from 620 to 1000°C for 50 hours. At the annealing temperature of 900°C, additional annealing times from 5 minutes to 750 hours have also been investigated. The second route does not contain any homogenisation. CR is performed directly after HR with reductions up to 92% ($\varepsilon_{VM} = 3.0$). It is referred to as route “CR”. Samples were cut from the rolled sheet at every 20% of thickness reduction. Annealing treatments at 900°C for times ranging for 5 minutes to 750 hours were performed after rolling reductions of 80% ($\varepsilon_{VM} = 1.9$) and 92% ($\varepsilon_{VM} = 3.0$). All the annealing steps were performed under argon atmosphere and followed by air cooling.

Additional pieces of information on materials, processing and characterisation methods can be found in annexe A at the end of this manuscript.

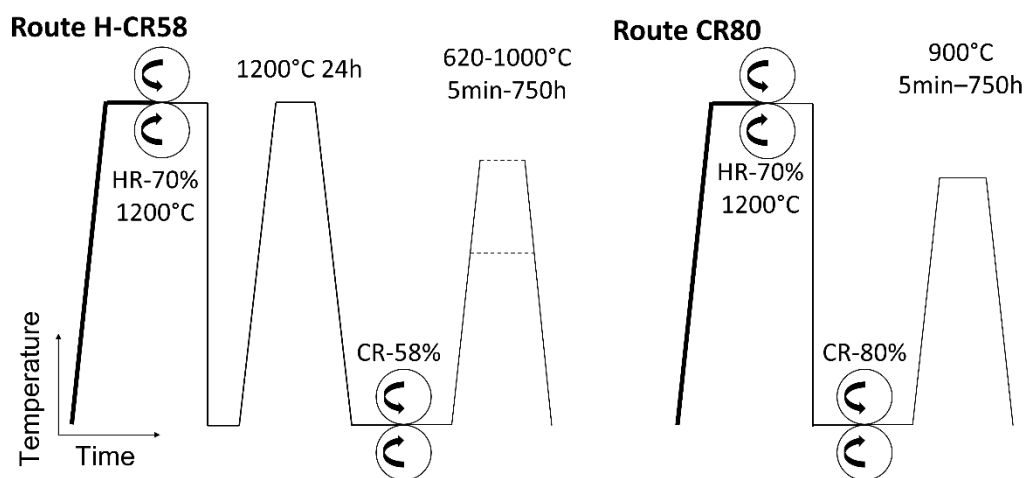


Fig. 3.1 Schematics of the two thermomechanical schedules chosen for processing of C6Al. [Full-size](#).

3.1.3. Nomenclature

In what follows, the different samples are referred to using their thermomechanical schedule. For example, the sample submitted to route H-CR with a CR reduction of 58% and an additional annealing treatment at 900°C for 50 hours is referred to as H-CR58-900°C/50h. A sample submitted to route CR with a rolling reduction of 80% and an additional annealing treatment at 900°C of 1 hour is referred to as CR80-900°C/1h

We will now turn to the results. First, the results corresponding to the CR step in route CR are presented. Then, we will focus on the heat-treatments conducted in route H-CR58. The results on the larger rolling reductions of 80% and 92% will then be presented.

3.2. Results

Fig. 3.2 presents the $Al_{0.32}CoCrFeMnNi$ isopleth phase diagram calculated from TCHEA4. The temperatures used in this chapter are depicted with circles. They are aligned vertically with the aluminium content of C6Al of 6 at.% of aluminium. The hot rolling temperature of 1200°C is predicted in the single-phase FCC domain (solid circle), in agreement with the necessity of performing severe deformation by rolling. The annealing temperature of 1000°C is located in the FCC+B2 domain, while 900 and 620°C are located in the FCC+B2+ σ domain (open circles).

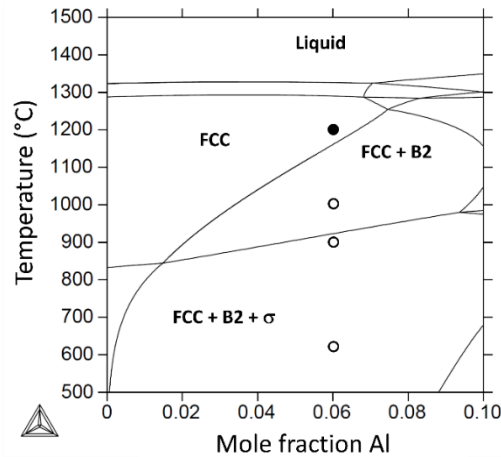


Fig. 3.2 CoCrFeMnNi + Al phase diagram. The studied composition C6Al corresponds to an addition of 6 at.% of aluminium. The solid circle indicates the hot rolling temperature of 1200°C. The open circles indicate the three annealing temperatures considered in this study : 620, 900 and 1000°C. [Full-size](#).

3.2.1. Development of the microstructure during rolling

Influence of the CR reduction

Fig. 3.3 presents the microstructure before cold rolling in route CR. It is composed of equiaxed grains with a profusion of annealing twins. The grain size is $125 \pm 70 \mu\text{m}$. The material is fully FCC at this stage.

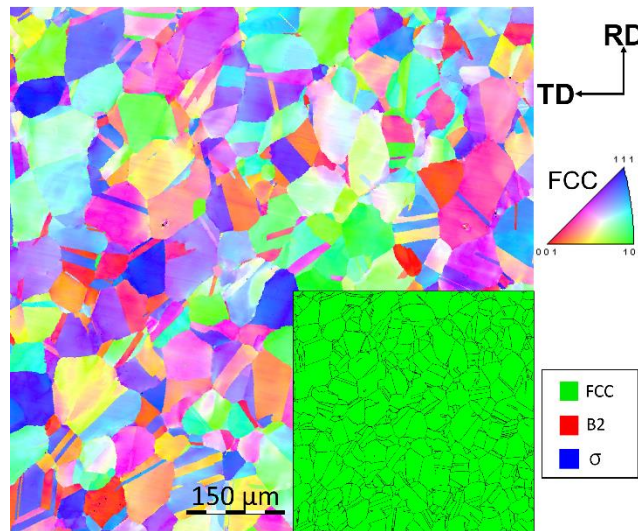


Fig. 3.3 IPF-Z and phase maps before CR in route CR. [Full-size](#).

Fig. 3.4A shows the microstructure of CR60. Grains are elongated in the rolling direction and present intragranular orientation gradients. Deformation twins are observed. They are characterized by 60° rotation angles at their boundaries, as shown on the misorientation profile measured along the black arrow. The hardness is $345 \pm 9 \text{HV}0.5$.

The crystallographic texture is measured during CR with XRD from a different sample. From these measurements, an orientation density figure (ODF) is calculated for each studied rolling reduction. **Fig. 3.4B** presents the ODF corresponding to a rolling reduction of 60%. The crystallographic texture consists in the α -fibre with the $\langle 110 \rangle$ direction parallel to ND with major Brass (Bs) and Goss (G) texture components (TC). Minor Copper TC (Cu) is also present. The

crystallographic texture exhibits a maximum at $\phi_1 = 60^\circ$ and $\phi = 90^\circ$ with a value of 4.6 times random.

From the set of ODFs obtained, it is possible to plot texture indices along the β -fibre (Fig. 3.4C), going from Brass to Copper through S (ϕ_2 is not constant), and along the α -fibre (Fig. 3.4D) at constant $\phi = 90^\circ$ and $\phi_2 = 45^\circ$. Both are plotted versus the angle ϕ_1 . Fig. 3.4C shows a constant increase of the Brass TC ($\phi_1 = 35^\circ$) through rolling. While the Copper TC ($\phi_1 = 90^\circ$) is 0.9 after hot rolling, its index increases to 1.8 and remains constant between 20 and 60% of rolling reduction. At larger reductions, it decreases to 0.6 at 92%. Fig. 3.4D confirms the strengthening of the Brass component during rolling. It is accompanied with a strengthening of the full α -fibre spreading from Brass TC to Goss TC ($\phi_1 = 90^\circ$). The peak of texture intensity is reached at $\phi_1 = 65^\circ$.

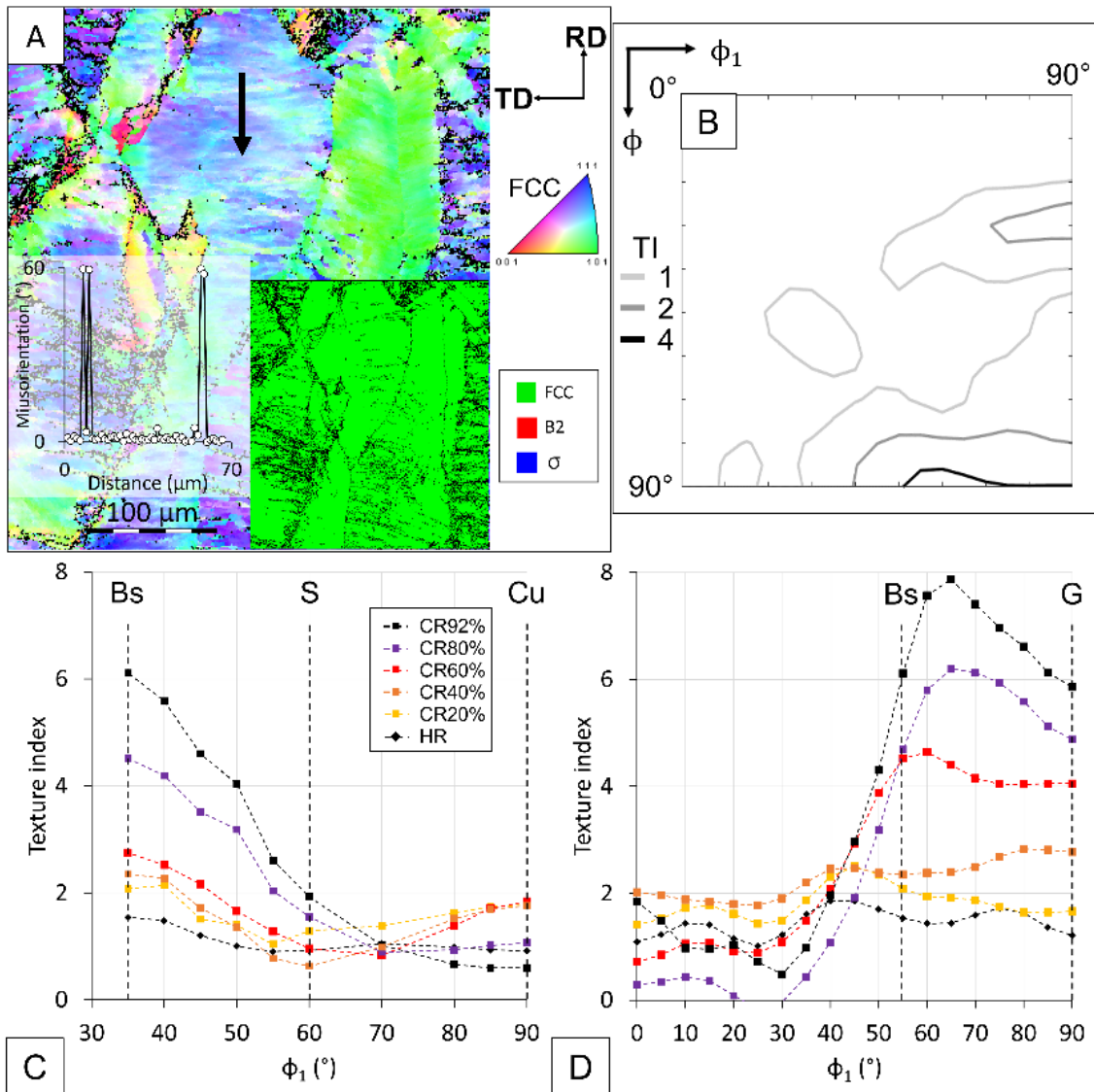


Fig. 3.4 Influence of rolling on microstructures and crystallographic texture in route CR. (A) Microstructure after CR60% presented with IPF and phase maps. The misorientation profile along the black arrow is also given. (B) ODF section at $\phi_2 = 45^\circ$ of the material after CR60. (C) Texture indices along the β -fibre throughout rolling. (D) Texture indices along the α -fibre. [Full-size](#).

Table 3.2 gives the evolution of dislocation density in C6Al during CR, measured by XRD. The dislocation densities increase with the increase in CR intensity. The dislocation density of twinning induced plasticity (TWIP) steel, measured by XRD, is also given ²¹⁵.

Table 3.2 Dislocation densities measured with XRD during CR of C6Al. The data measured in a TWIP steel are also given ²¹⁵.

Alloy	Reference	Dislocation densities ($10^{14} / \text{m}^2$)				
		CR20	CR40	CR60	CR80	CR92
C6Al	This study	2.7	6.8	9.2	11.6	17.7
		CR25	CR45	CR65	CR80	
TWIP	²¹⁵	3.1	5.3	7.5	12.3	

Influence of the initial grain size: CR60 vs H-CR58

The microstructure before CR in route H-CR is homogeneous and consists of equiaxed grains containing annealing twins (**Fig. 3.5**). The grain size is $410 \pm 150 \mu\text{m}$. The material is fully FCC.

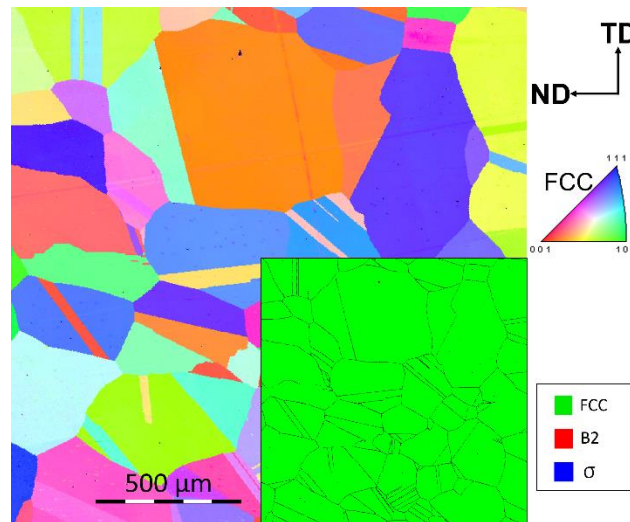


Fig. 3.5 IPF-Z and phase maps before CR in route H-CR58. [Full-size](#).

After H-CR58, the material presents elongated grains as long as 1 millimetre in length. Intragranular orientation gradients are observable with strong colour gradients on the IPF map (**Fig. 3.6A**). The hardness is $341 \pm 12 \text{HV0.5}$. Deformation twins are observed, as shown on the misorientation profile measured along the black arrow in **Fig. 3.6A**. The microstructure of the alloy is a single-phase solid solution with FCC structure. **Fig. 3.6B** presents the $\phi_2 = 45^\circ$ section of the ODF. The crystallographic texture consists of the α fibre spreading from Goss ($\phi_1 = 90^\circ$) to A ($\phi_1 = 40^\circ$) TCs. It exhibits a maximum for the Goss component with a value of 5.7 times random.

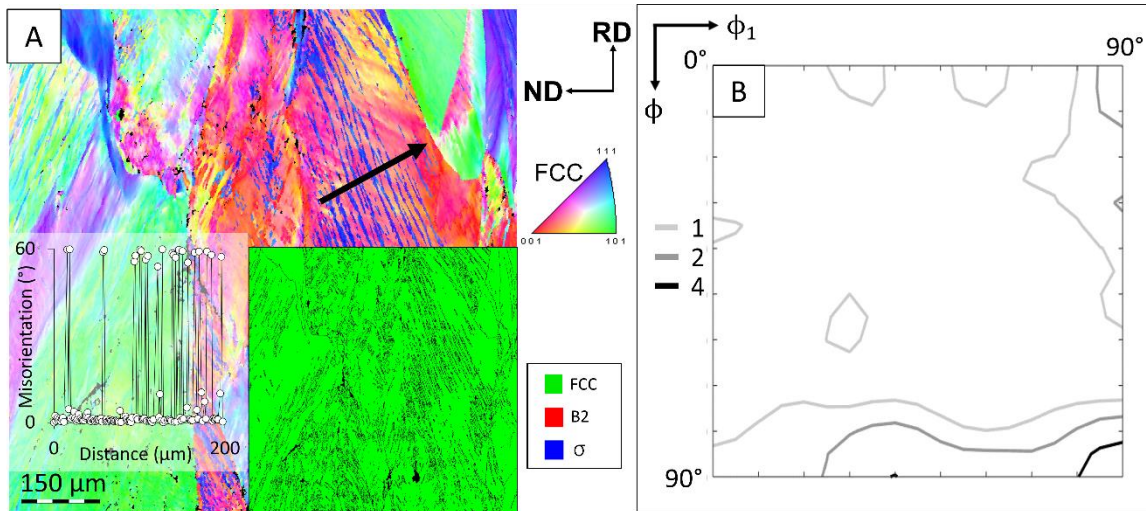


Fig. 3.6 H-CR58. (A) IPF-Z and phase maps, (B) deformation texture, $\phi_2 = 45^\circ$ ODF section. [Full-size](#).

3.2.2. Annealing treatments after H-CR58

The following results will focus first on the microstructures obtained after annealing treatments at 900°C for 50 hours and then for shorter times. The microstructures obtained after annealing treatments at 620°C for 50 hours and 1000°C for 15 minutes will be detailed next.

The sample H-CR58- $900^\circ\text{C}/50\text{h}$ consists of two zones with distinct microstructures (**Fig. 3.7**). First, the region located in the middle of the EBSD maps is composed of equiaxed and strain free FCC, BCC and σ grains. As will become clear later, the BCC phase is the B2 phase, consistent with the calculated phase diagram. The mean grain sizes are 8 ± 0.3 and $1.5 \pm 0.3 \mu\text{m}$ for the FCC and the second phases, respectively. The second phases are mainly present at grain boundaries. Interestingly, the σ grains are always located next to at least one B2 grain.

Secondly, on the sides of the maps, larger FCC grains are present with occasional deformation twins inherited from CR. Precipitation of elongated B2 grains is observable within this zone. These B2 grains show a mean length of $1 \pm 0.5 \mu\text{m}$ for a width of $0.3 \pm 0.1 \mu\text{m}$. **Fig. 3.7C** presents a BSE SEM image of a similar region. Part of these intragranular B2 precipitates formed on twin boundaries (precipitates aligned vertically on the sides of the image) while the rest formed in the bulk and are aligned in different directions (centre of the image). The zoomed view shown in **Fig. 3.7B** highlights the alignment of these latter B2 needles with the $\{111\}$ plane traces depicted by the 4 black lines. In addition, the intragranular B2 precipitates present most of their FCC/B2 interfaces respecting the Kurdjumov-Sachs (K-S) orientation relationship (OR), as highlighted in yellow in **Fig. 3.7B**. The K-S OR corresponds to the orientation relationship $\{111\}_{\text{FCC}} // (011)_{\text{BCC}}$ & $\langle \bar{1}01 \rangle_{\text{FCC}} // \langle \bar{1}\bar{1}1 \rangle_{\text{BCC}}$. Unlike intragranular B2 grains, the B2 grains formed on recrystallised FCC grain boundaries present a K-S OR with only one of their FCC neighbours.

The centre region containing equiaxed grains will be called recrystallised zones (RXZs) as opposed to the non-recrystallised zones (nRXZs) consisting of the larger FCC and elongated B2 grains. The RXZs and nRXZs present hardness values of $250 \pm 6 \text{HV}0.5$ and $281 \pm 5 \text{HV}0.5$, respectively.

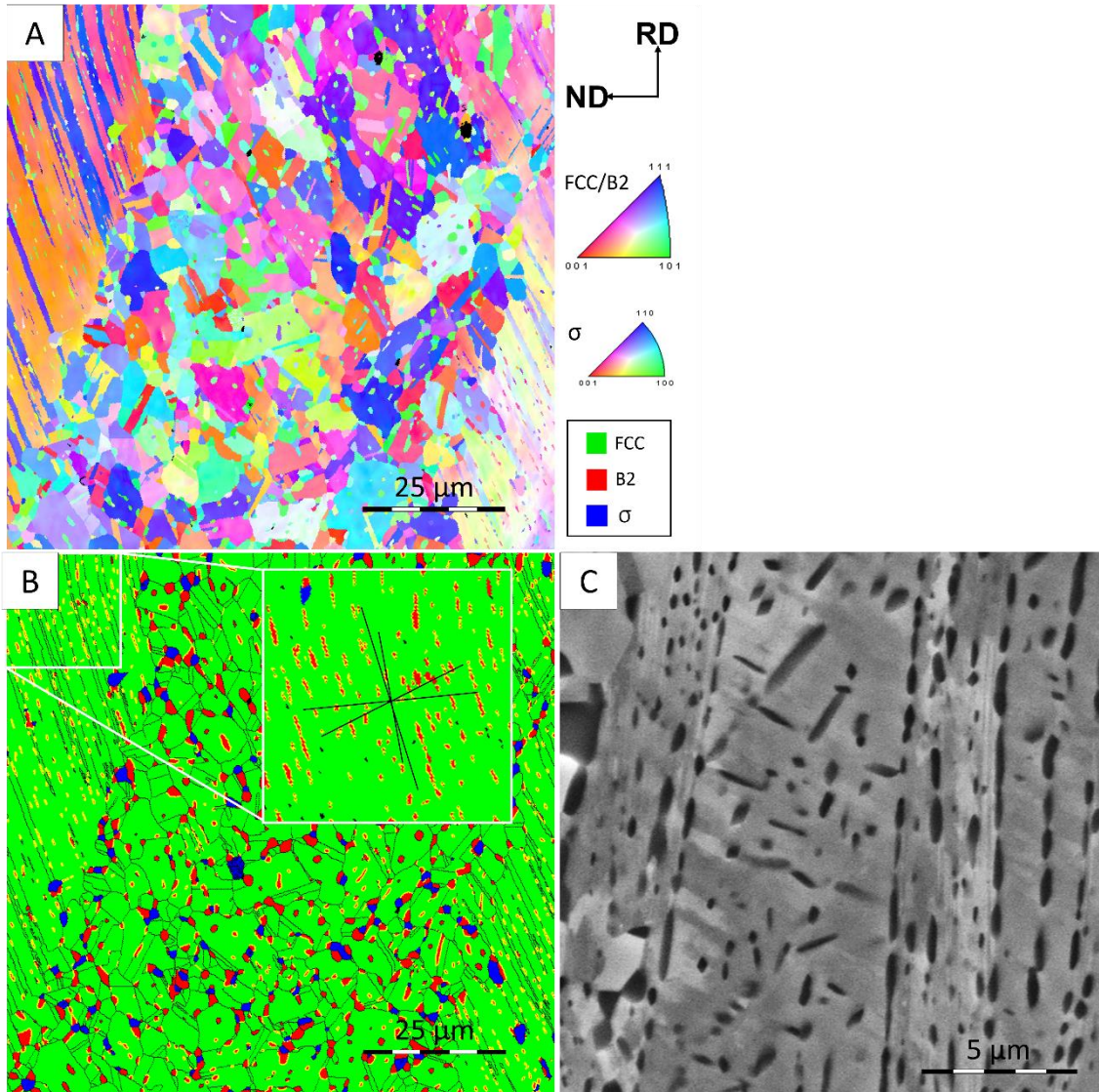


Fig. 3.7 H-CR58-900°C/50h. (A) IPF-Z map, (B) phase map. The black lines on the phase map correspond to grain boundaries with misorientation angles larger than 15°. The yellow lines correspond to the grain boundaries respecting K-S OR. (C) BSE SEM image of a nRXZ with precipitation of the B2 phase on twin boundaries (on the sides) and in the bulk (in the centre). [Full-size](#).

Two regions have been analysed by TEM in order to precise the nature of, first, the B2 and FCC phases (**Fig. 3.8A**) and of the σ phase (**Fig. 3.8B**). **Fig. 3.8C-E** presents the corresponding diffraction patterns. The B2 phase is ordered as shown by the sublattice spots encircled in yellow in **Fig. 3.8C**. This is the B2 phase in agreement with CALPHAD predictions. The matrix corresponds to a FCC lattice structure (**Fig. 3.8D**). The diffraction pattern of **Fig. 3.8E** corresponds to primitive tetragonal which corresponds to the lattice structure of the σ phase. The chemical compositions of these three phases were measured by averaging 10 EDS data points (**Table 3.3**).

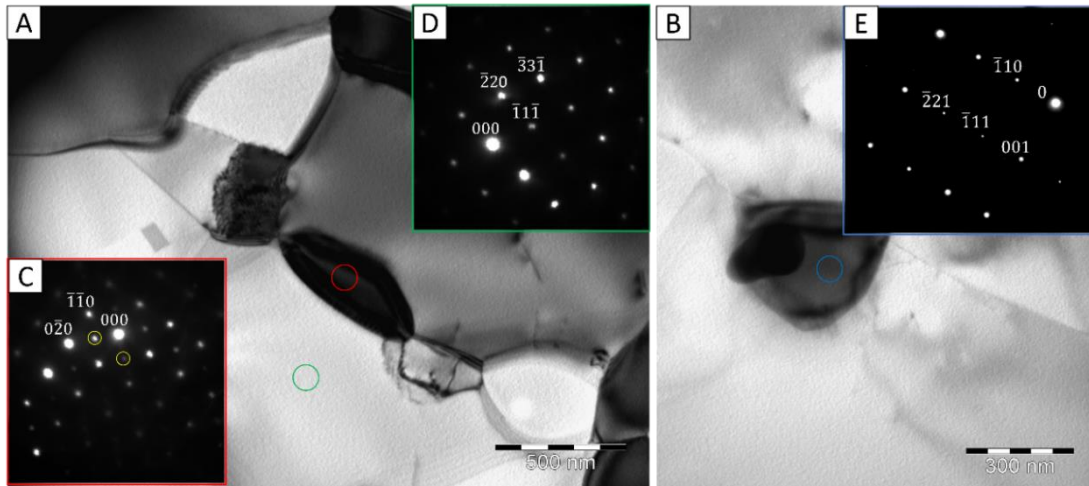


Fig. 3.8 TEM observations of a recrystallised zone. (A-B) bright field images, (C-E) diffraction patterns recorded in (C) a B2 grain (red circle) with sublattice spots encircled in yellow ([001] zone axis), (D) a FCC grain (green circle) ([011] zone axis), (E) a σ grain (blue circle) ([110] zone axis). [Full-size](#).

Table 3.3 Chemical compositions measured by EDS of the phases present after 50 hours at 900°C, in atomic percent.

	Al (at.%)	Co (at.%)	Cr (at.%)	Fe (at.%)	Mn (at.%)	Ni (at.%)
FCC	5 ± 1	19 ± 1	20 ± 1	20 ± 1	20 ± 1	17 ± 1
B2	22 ± 2	13 ± 1	7 ± 3	8 ± 2	20 ± 1	31 ± 3
σ	2 ± 2	17 ± 1	41 ± 3	19 ± 1	16 ± 1	6 ± 2

BSE SEM micrographs of H-CR58-900°C/5min and H-CR58-900°C/15min samples are presented in **Fig. 3.9**. The microstructure of H-CR58-900°C/5min is divided between RXZs and deformed grains (**Fig. 3.9A**). The RXZs are located mostly on the right-hand side and composed of equiaxed FCC grains in grey with a mean grain size of $1 \pm 0.3 \mu\text{m}$. The B2 grains in black and σ grains in white present a similar mean grain size of $0.5 \pm 0.3 \mu\text{m}$. The deformed grains are composed of deformed FCC grains in shades of grey. When the annealing time is increased to 15 minutes, black needles of B2 lattice structure appear in the deformed grains located on the left-hand side of **Fig. 3.9B**. These needles present a length of $130 \pm 70 \text{ nm}$ and a width of $60 \pm 20 \text{ nm}$.

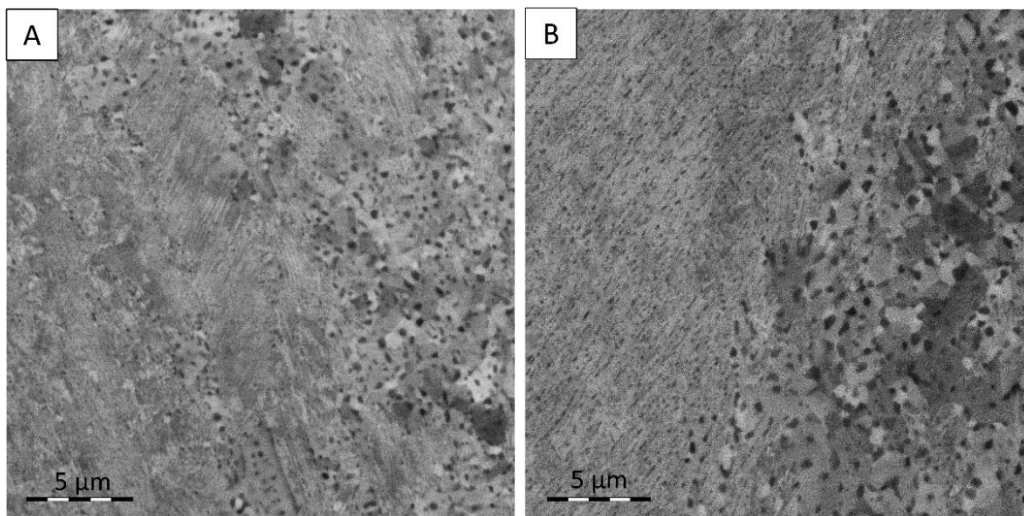


Fig. 3.9 BSE SEM micrographs acquired after annealing treatments at 900°C for (A) 5 minutes and (B) 15 minutes. [Full-size](#).

The microstructure of H-CR58-620°C/50h is also composed of both RXZs and nRXZs (**Fig. 3.10A-B**). nRXZs consist of elongated FCC grains longer than the height of the scan. RXZs consist of equiaxed grains organized in bands spread heterogeneously in the sample (**Fig. 3.10A**). Two of these bands are depicted in the zoomed view in **Fig. 3.10B**. The grains contained in these bands are FCC, B2 or the σ phase. The mean grain size of the FCC grains is $1.2 \pm 0.3 \mu\text{m}$ while it is $0.5 \pm 0.3 \mu\text{m}$ for the two second phases. The hardness was measured to be $486 \pm 14 \text{ HV0.5}$ – compared to the hardness of $341 \pm 12 \text{ HV0.5}$ after CR –, accounting mainly for the nRXZs because of the small size and proportion of the RXZs.

The microstructure of H-CR58-1000°C/15min is composed of strain free FCC grains with a mean grain diameter of $10 \pm 5 \mu\text{m}$ (**Fig. 3.10C-D**). A small proportion (1%) of B2 precipitates is spread randomly in the material. Those B2 grains are much smaller than the FCC grains with an average diameter of $0.50 \pm 0.08 \mu\text{m}$. The σ phase does not form at this annealing temperature. The hardness level is $168 \pm 10 \text{ HV0.5}$.

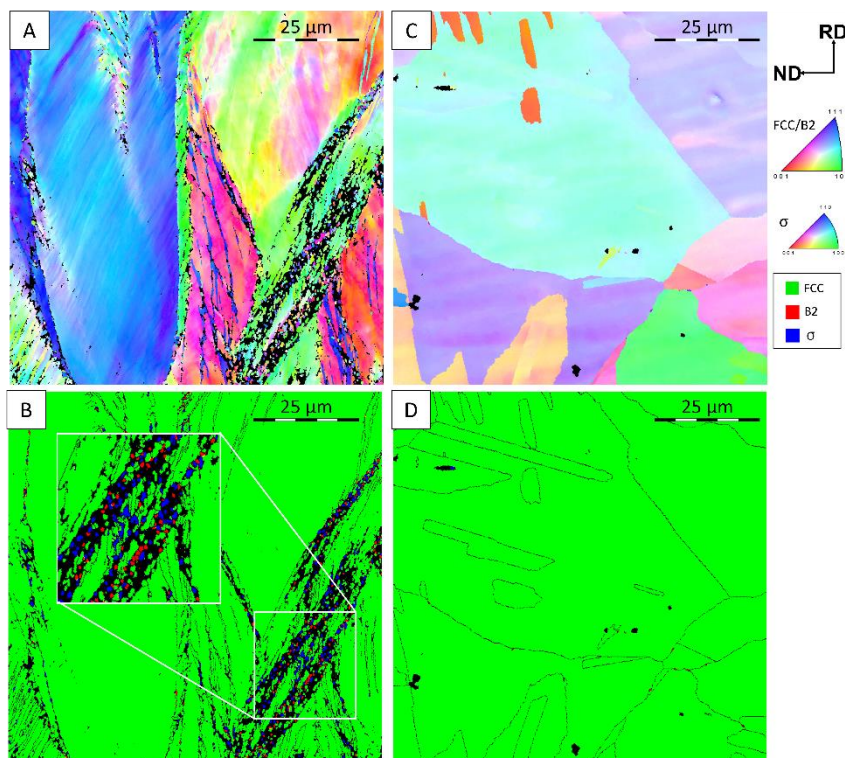


Fig. 3.10 EBSD maps. (A, C) are IPF-Z maps and (B, D) phase maps measured on H-CR58-620°C/50h (A-B) and H-CR58-1000°C/15min (C-D). The black lines on phase maps correspond to grain boundaries with misorientation angles larger than 15°. [Full-size](#).

Fig. 3.11A presents the evolution of the volume fraction of recrystallised FCC grains with annealing temperature, for a constant annealing time of 50 hours. Annealing temperatures of 620, 700, 800, 900 and 1000°C were studied. The recrystallised fraction is 14% after 50 hours at 620°C and then increases with the annealing temperature until reaching complete recrystallisation after 50 hours at 1000°C. **Fig. 3.11B** shows four XRD diffractograms measured after CR and further annealing treatments at 620, 900 and 1000°C for 50 hours. The FCC phase is present in all samples. A BCC phase appears during annealing treatments at 620°C and 900°C. This phase is identified as the B2 phase as was observed by TEM. The peaks corresponding to the σ phase are also present under these two annealing conditions. **Fig. 3.11C** presents the volume fractions of the B2 and σ phases quantified with Topas software after annealing

treatments of 50 hours at 620, 700, 800, 900 and 1000°C. The second phase fractions calculated using ThermoCalc are also shown. The fractions of the B2 and σ phases reach the maxima of 28% and 5% after annealing treatments at 700°C and 800°C, respectively. It is interesting to note that the evolution of B2 fraction agrees well with thermodynamic calculations whereas it is not the case for the σ phase.

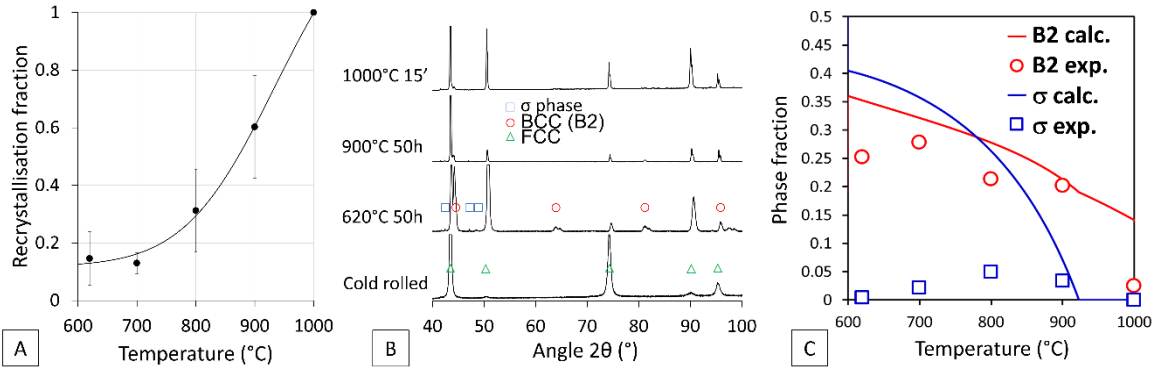


Fig. 3.11 Measurements performed after annealing treatments of 50 hours at various temperatures. (A) Evolution of the recrystallised FCC fraction. (B) XRD diffractograms. (C) Experimental and calculated evolutions of the volume fractions of the B2 and σ phases. [Full-size](#).

3.2.3. Effect of CR intensity

The evolution of the recrystallised volume fraction during annealing treatments at 900°C is reported in **Fig. 3.12** after H-CR58, CR80 and CR92. It is clear that the recrystallisation kinetics is much faster after CR80 than after H-CR58. A slight increase in kinetics is observed when the rolling reduction is increased to 92%. For example, 50% of the microstructure is recrystallised after 20 hours for H-CR58 specimens while it takes less than 5 minutes for CR80 specimens. Complete recrystallisation is achieved in CR80 after 20 hours of annealing while it is not reached for H-CR58 even after 744 hours of annealing. It is attained after about 6 hours in CR92.

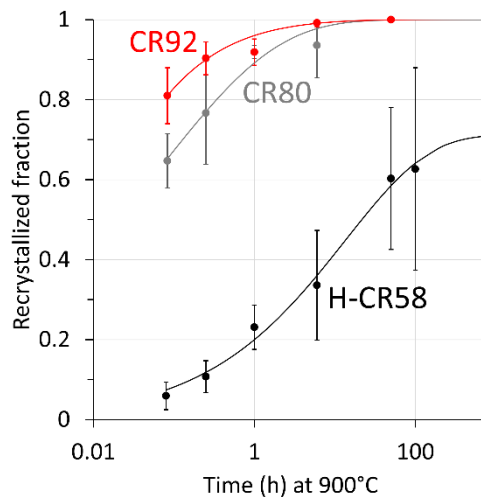


Fig. 3.12 Recrystallisation fractions versus annealing time at 900°C after H-CR58 and CR80 and CR92. [Full-size](#).

The microstructure of CR80-900°C/50h is composed of recrystallised and equiaxed FCC grains along with equiaxed B2 and σ grains (**Fig. 3.13**). The mean grain sizes are $5 \pm 0.3 \mu\text{m}$ and $1.4 \pm 0.3 \mu\text{m}$ for the FCC and the second phases, respectively. The hardness is $227 \pm 3 \text{HV}0.5$.

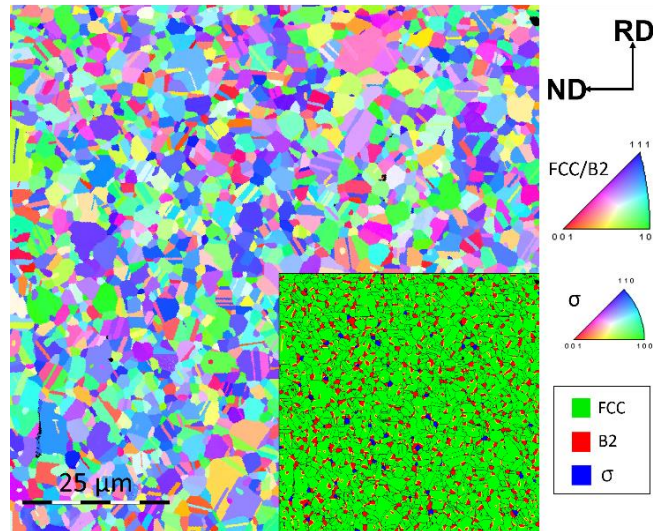


Fig. 3.13 IPF-Z and phase maps of CR80-900°C/50h. [Full-size](#).

Fig. 3.14a presents the microstructure of CR80-900°C/5min. Fig. 3.14A is divided in two partitions corresponding to RXZs (Fig. 3.14C) and deformed grains (Fig. 3.14E). These partitions are separated according to their GOS. In each grain, this index calculates the intensity of the deviation in orientation from its mean orientation. When this index is larger than 4°, the corresponding grain is considered as non-recrystallised. Fig. 3.14B, D and F present the crystallographic textures ($\varphi_2 = 45^\circ$ ODF sections) calculated for the whole microstructure, for the RXZs (more than 30,000 grains) and nRXZs (400 grains), respectively. All three textures are similar with maxima close to Goss and Brass. The corresponding maximum intensities are 10.8, 7.5 and 48.0. The texture of deformed grains is six times stronger than the texture of RXZs.

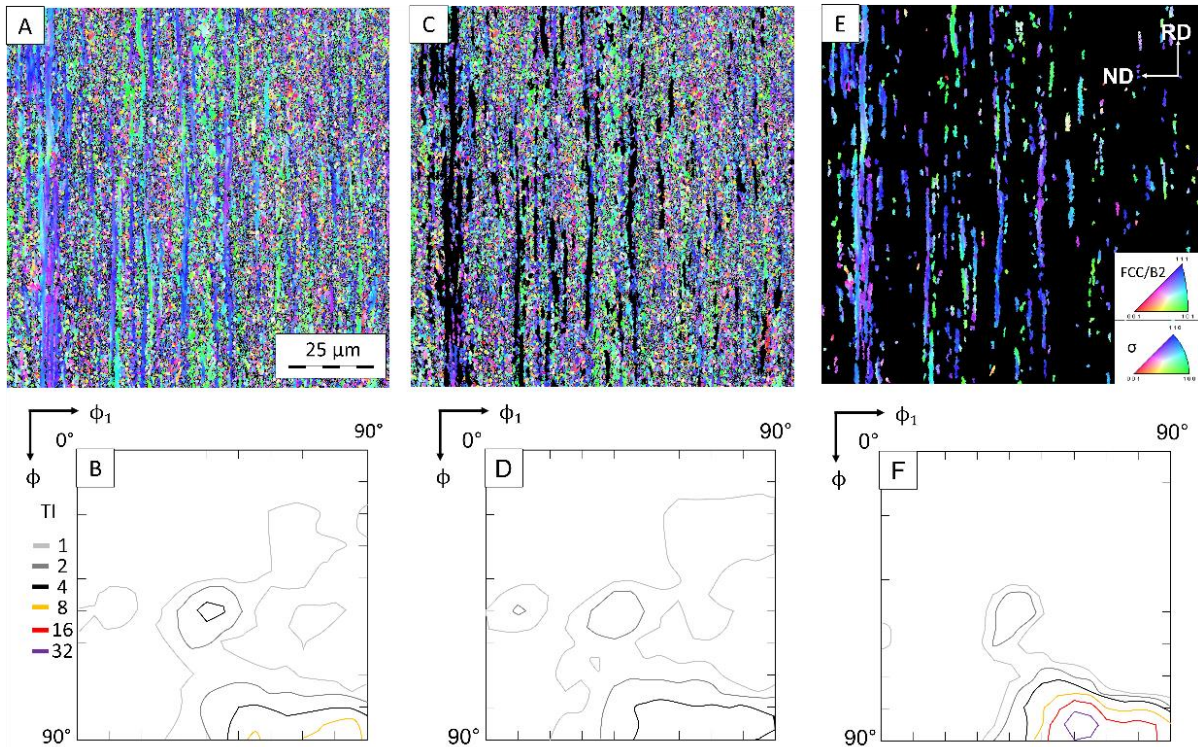


Fig. 3.14 CR80-900°C/5min. (A-B) correspond to the whole microstructure. (C-D) are limited to RXZs. (E-F) are limited to deformed regions (with the threshold GOS>4°). (A, C and F) IPF-Z maps, (B, D and F) crystallographic textures, Phi2=45° ODF section. [Full-size](#).

3.3. Discussion

3.3.1. Deformed state

Evolution of the microstructure during rolling

The microstructure after CR for a thickness reduction of 60% in route CR (**Fig. 3.4A**) consists of elongated grains presenting (i) large orientation gradients and (ii) mechanical twins.

The formation of orientation gradients is typical of materials deforming by dislocation glide. The activation of dislocation glide is confirmed by the increase in dislocation density measured by XRD (**Table 3.2**). Although the exact nature and structure of dislocations in HEA is still the topic of fundamental research¹³⁵, it is natural to compare the present alloy to austenitic stainless steels, especially in view of its chromium content and its FCC structure^{216,217}. Unlike most austenitic stainless steels, C6Al does not undergo strain-induced martensitic transformation (phase maps in **Fig. 3.4B** and **Fig. 3.6B**).

The analysis of crystallographic texture is used to follow the evolution of the microstructures during deformation and to identify the activated deformation mechanisms. This topic has been recently reviewed by Sathiaraj *et al.*²¹⁸. As described in chapter 1, the deformation texture is the result of the local rotations of the lattice due to dislocation slip. The final texture determines the anisotropy of mechanical properties, an aspect of primary interest for industrials. Hence, considerable work has been achieved to control and understand the development of deformation textures^{219,220}. In the case of the rolling of FCC materials, Copper-type or Brass-type deformation textures might develop. The Copper-type texture is dominated by Copper – {112}<111> aligned with the rolling direction – and S – {123}<634> – with minor Goss – {110}<001> – components. FCC materials with large SFE present such deformation texture after deformation by rolling. The Brass type texture consists in major Brass – {110}<112> – with minor Goss components. It is present in FCC materials of low SFE.

It is now believed that at low strain the Copper-type texture develops whatever the SFE of the material²²¹. The activation of additional mechanisms of deformation, such as mechanical twinning, results in the transition from Copper-type to Brass-type deformation textures. Mechanical twinning is involved in two ways. First, it transforms orientations in the material into new ones – the orientation of the twins – that might not belong to the same type of texture. This is the case of the twinned Copper orientation (Cu-T), with orientation {552}<115> close to the Goss component and hence belonging to the Brass-type texture. Moreover, the presence of twins also acts on the grain stability under deformation. It was observed in single crystals that the presence of mechanical twins destabilizes Copper-oriented or S-oriented grains²²² which then tend to rotate towards more stable orientations such as Brass TC. The transition from Copper-type to Brass-type texture is also observed in materials that do not exhibit mechanical twinning²²³. It is then explained by the activation of shear banding.

In C6Al, the significative dislocation activity (**Table 3.2**) results in the presence of the Copper-type texture at low rolling reductions. This is supported by the increase in the intensity of the Copper TC (**Fig. 3.4C**). In parallel, the Brass-type texture, with Brass and Goss TCs, continuously increase (**Fig. 3.4D**). This is due to the activation of mechanical twinning, observed since CR reductions of 20% (**Fig. 3.15A-B**). This makes the present alloy comparable to TWIP steels²¹⁵. This comparison is reinforced by similar dislocation activities during rolling (**Table 3.2**). At reductions larger than 60%, the Copper-type texture progressively disappears. This decrease

coincides with the first observations of shear bands at a reduction of 60% (**Fig. 3.15C**). It might also be due to an intensification of mechanical twinning.

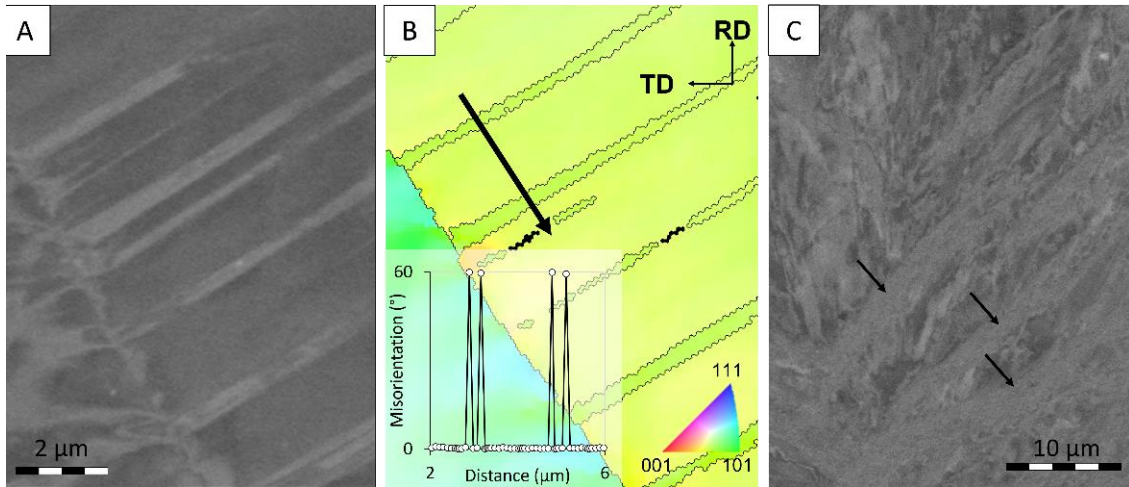


Fig. 3.15 (A-B) Mechanical twins in CR20. (A) BSE SEM micrograph. (B) IPF-Z map corresponding to the region shown in (A). In inset is given the misorientation profile along the black arrow. (C) Presence of shear bands in CR60 (indicated by black arrows). [Full-size](#).

Both ODF sections acquired in H-CR58 (**Fig. 3.6B**) and in CR60 (**Fig. 3.4B**) are similar, with the development of the α -fibre in both cases. The copper TC is however absent of the former case. This could be explained by the easier formation of mechanical twins in larger grains ¹³¹.

The rolling texture observed in C6Al are commonly reported in both austenitic stainless steels ²¹⁷ and TWIP steels ^{215,224}. Moreover, the comparison between H-CR58 and CR60 confirms the low influence of the initial grain size on the behaviour during deformation. The same mechanisms of deformation are activated, even if there is a factor 3 between grain sizes. Nonetheless, the initial grain size is expected to result in variations in recrystallisation kinetics. Indeed, grain boundaries are favoured nucleation sites for recrystallisation due to the large orientation gradients present in their vicinity ¹⁴⁸. The variation in grain size also influences the intensity of mechanical twinning which only modifies slightly the material behaviour.

Evaluation of the SFE of C6Al

The activation of mechanical twinning is commonly linked to a low SFE – even if other factors need to be considered such as the content in interstitial elements ^{124,125} –, as it is the case in TWIP steels ²²⁵. In those steels, SFE values ranging between 20 and 50 mJ/m² are often reported ^{125,226}. In the case of Cantor's alloy, Zaddach *et al.* calculated using *ab initio* calculations a SFE between 18 and 27 mJ/m² ⁹⁴ while the presence of twins after deformation was also confirmed experimentally ²⁵.

The influence of aluminium content on the SFE of Al_xCoCrFeMnNi alloys can be calculated based on the thermodynamic modelling approach proposed by Olson and Cohen ¹¹⁴ and adopted by several authors ^{227,228}. In this model, the SFE represents the Gibbs energy required to create two layers of hexagonal close-packed (ϵ_{HCP}) phase separated from the face-centred cubic (γ_{FCC}) matrix by two interfaces:

$$\gamma_{\infty} = 2\rho\Delta G^{\gamma \rightarrow \epsilon} + 2\sigma_{\frac{\gamma}{\epsilon}} \quad (\text{Eq. 3.1})$$

where γ_{∞} is the ideal SFE (mJ/m²), ρ is the surface density of atoms in the {111} planes, $\sigma_{\frac{\gamma}{\epsilon}}$ is the surface energy of the interface γ/ϵ , and $\Delta G^{\gamma \rightarrow \epsilon}$ is the difference in Gibbs free energy of the

FCC and HCP phases. The term $\Delta G^{\gamma \rightarrow \epsilon}$ can be calculated from the Gibbs energy descriptions of the involved phases using the TCHEA4 database. However, large extrapolations from the thermodynamic models in the central region of the compositional space (e.g. CoCrFeMnNi) may lead to inaccurate evaluations of the Gibbs energies¹⁷. To overcome this problem, the present study utilizes the SFE value determined by Zaddach *et al.* for the CoCrFeMnNi alloy as a reference to adjust the estimate from CALPHAD for C6Al. The result of the calculation suggests that aluminium addition increases the SFE by 60% for C6Al (~30-40 mJ/m²) as compared to the Cantor alloy (18-27 mJ/m²).

Liu *et al.* measured experimentally the SFE of another alloy close to CoCrFeMnNi: Al_{0.1}CoCrFeNi. He reported a value around 30 mJ/m²²²⁹ which is slightly larger than the SFE of CoCrFeNi reported at 28 mJ/m²⁹⁴. The authors linked the presence of deformation twins after CR with this low SFE²²⁹. This experimental result agrees with the calculation performed above on C6Al about the increase in SFE due to the addition of aluminium. Nevertheless, the addition of aluminium in CoCrFeMnNi, until at least 6 at.%, does not seem sufficient to suppress mechanical twinning during rolling at ambient temperature.

3.3.2. Microstructure evolution during annealing

A bird's eye view

Three situations can be observed according to the annealing temperature. Below 900°C, the microstructure evolution is governed by precipitation. At 900°C, precipitation and recrystallisation occur simultaneously. Above 900°C, recrystallisation is the main phenomenon taking place.

Below 900°C, precipitation is governing the microstructure evolution of the material. In H-CR58-620°C/50h, the precipitation fraction was measured at 25%, close to the value predicted by CALPHAD (**Fig. 3.11C**). Precipitation is coupled to a limited recrystallisation. In the same sample, the recrystallisation fraction is below 20% after 50 hours of annealing treatment (**Fig. 3.11A**). Recrystallisation happens where the stored energy is the largest, i.e. along grain boundaries and shear bands (**Fig. 3.10A**). Co-precipitation of B2 and σ phases is also observed there (**Fig. 3.10B**). The overall precipitation fraction, exceeding the recrystallised fraction, suggests that a large fraction of B2 grains is present inside nRXZs. However, most likely due to their small size, they were not observed with SEM.

The limited recrystallisation coupled to the precipitation of fine B2 grains in nRXZs result in a hardening of 145 HV compared to the cold rolled state.

Above 900°C, recrystallisation is the main phenomenon taking place. Compared to lower annealing temperatures where 50 hours is not sufficient to recrystallise completely the material (**Fig. 3.11A**), it is completed after less than 15 minutes at 1000°C (**Fig. 3.10C**). This increased rate can be correlated to the negligible precipitation (**Fig. 3.10D**). The B2 fraction was measured by both EBSD and XRD to be below 3% after 50 hours of annealing (**Fig. 3.11C**). The negligible precipitation also results in significant grain growth inducing a decrease of the hardness level of about 170 HV after 15 minutes at 1000°C compared to the cold rolled state.

At 900°C, both recrystallisation and precipitation are activated. The microstructure sequence can be summarized in three steps: (i) recrystallisation, (ii) precipitation and (iii) interactions between these two phenomena. As both mechanisms activate and interact, the description of this microstructure sequence at 900°C is more complex. It is studied in detail in the next section.

Recrystallisation and precipitation behaviour at 900°C

We will focus first on recrystallisation.

Recrystallisation is activated first where the stored energy is the highest, i.e. along grain boundaries²³⁰ and shear bands¹³⁴. Recrystallised grains form in bands following these defects as observed after 5 minutes of annealing in **Fig. 3.9A**.

After recrystallisation occurred on these defects, it activates inside grains. **Fig. 3.16** shows that GOS and Taylor factors (M) are correlated. Grains can be divided in two groups: those presenting large Taylor factors that efficiently stored energy during rolling and hence present large GOS; and those with low Taylor factors that did not store energy during rolling and hence present low GOS. At short annealing times, the deformed grains combine these two groups (top right of the graph). During the annealing treatment, the grains from the first group recrystallise and become RXZs. In the end, there remains only the grains of the second group that do not recrystallise and become nRXZs (bottom left of the graph).

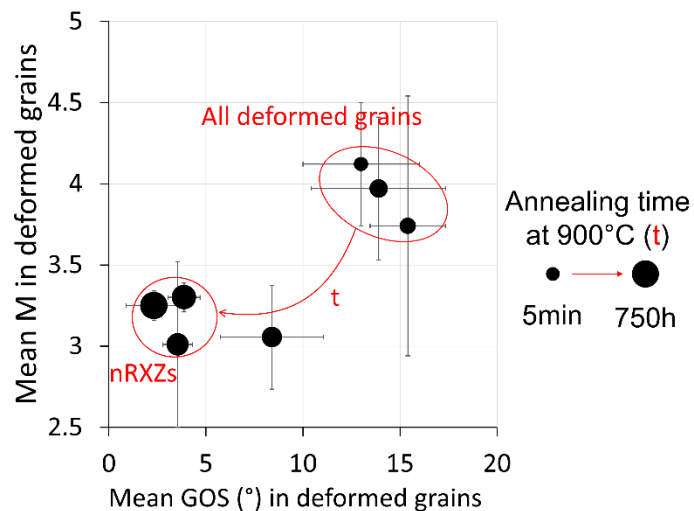


Fig. 3.16 Correlation between Taylor factor and GOS during the annealing treatment at 900°C. [Full-size](#).

The measure of crystallographic textures of **Fig. 3.14** indicates that the grains that did not yet recrystallise (**Fig. 3.14E**) present orientations spreading from Goss to Brass (**Fig. 3.14F**). According to literature, these orientations correspond to low values of M , i.e. 2.4 – 3.3^{231,232}. This is consistent with the results of **Fig. 3.16**. Grains presenting orientations between Goss and Brass present a delay or an absence of recrystallisation.

Interestingly, although their intensities differ in a large way, the deformed (**Fig. 3.14F**) and recrystallised (**Fig. 3.14D**) textures are very similar. This is consistent with literature on MCAs presenting low SFE, such as Cantor's alloy⁹⁹ and CoCrFeNi¹⁰⁰, as well as in TWIP steels²³³. These similarities were attributed to the absence of preferential nucleation and growth during recrystallisation.

We will now turn to precipitation. It occurs in two steps.

First, precipitates form in RXZs on the new recrystallised grain boundaries. This precipitation on grain boundaries is observed after 5 minutes of annealing (**Fig. 3.9A**). The precipitates consist of equiaxed B2 and σ grains, the latter sharing a boundary with at least one B2 grain (**Fig. 3.7B**).

To rationalize the difference in precipitation sequence between the RXZs and nRXZs we will now discuss the driving forces for nucleation. Driving forces are the main factor that affects nucleation kinetics and can be calculated if the Gibbs free energies of the phases are known. The onset driving forces for nucleation (ODFN) associated with the beginning of the precipitation of a given precipitate phase (here B2 and σ) from a supersaturated solid solution (here FCC) is the difference in chemical potentials between the tangent hyperplane to the Gibbs free energy hypersurface of the supersaturated solid solution at instant composition and the parallel tangent hyperplane to the Gibbs free energy hypersurface of the precipitate phase. Positive values of ODFN indicate that precipitation is thermodynamically possible. The ODFN from the supersaturated FCC solid solution of both B2 (red line) and σ (blue line) phases were calculated using the CALPHAD method (**Fig. 3.17A**).

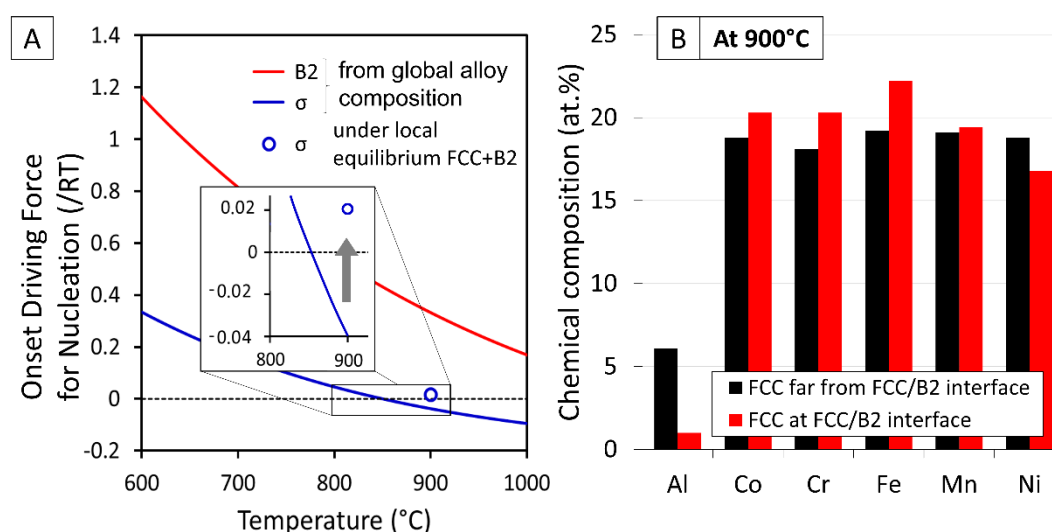


Fig. 3.17 (A) ODFN calculated with CALPHAD from the supersaturated FCC matrix of composition $Al_{0.32}CoCrFeMnNi$ for the B2 (red line) and σ (blue line) phases. The open circle corresponds to the ODFN of the σ phase under the local chemical equilibrium in the FCC matrix at the B2 interface. (B) Local equilibrium chemical compositions of the FCC phase far from FCC/B2 interfaces (in black) and at FCC/B2 interfaces (in red) calculated with ThermoCalc. [Full-size](#).

At 900°C, the B2 phase has the highest driving force (**Fig. 3.17A**) which shows that it is the more likely to precipitate first from the supersaturated FCC solid solution. In contrast, the calculation indicates that the driving force of the σ phase is close to null. This suggests that its formation in the RXZs cannot be explained by assuming homogeneous nucleation. This explains the large discrepancy between measured and calculated fractions of σ phase under equilibrium conditions, given in **Fig. 3.11C**.

Fig. 3.17B presents the local equilibrium chemical conditions in the FCC matrix at FCC/B2 interfaces (in red) in comparison to that far from FCC/B2 interfaces (in black), i.e. the nominal composition of the alloy (ingot n°1 in **Table 3.1**). Near FCC/B2 interfaces, the FCC matrix is depleted in aluminium and nickel. This agrees with the enrichment of the B2 phase in these two elements (**Table 3.3**). Furthermore, the FCC matrix near the B2 interface is enriched in chromium, iron and cobalt. The local enrichment in chromium, in which the σ phase is enriched (**Table 3.3**), results in a local increase in the ODFN of the σ phase (inset in **Fig. 3.17A**), facilitating its formation there. This explains well the fact that σ is observed always in contact with B2.

There is also a kinetic advantage of the two phases forming to side to side. Indeed, it decreases the diffusion distance necessary for both phases to form - aluminium and nickel going to B2, and

chromium going into the other direction to the σ phase. By forming together, both can grow faster. Experimental proofs of this chromium enrichment at FCC/B2 interfaces, e.g. by local EDS measurements in TEM, would be necessary to truly assess its influence on the formation of the σ phase.

Such coupling was already reported in austenitic stainless steels where the σ phase appears much faster, by almost two orders of magnitude, from δ -ferrite (which is BCC as is B2) than from austenite (or γ which is FCC as is the supersaturated matrix of C6Al)^{173,234}. Such phenomenon is attributed to the large surface energy of the γ/σ interface, to the slow diffusion of substitutional elements – such as chromium – in γ but also to the enrichment in chromium and molybdenum of the δ -ferrite²³⁵. Consequently, several studies identified the δ/γ interfaces as beneficial sites for heterogeneous nucleation of the σ phase^{236,237}. In the present case, the B2 phase is depleted in chromium. The two first elements, lower surface energy and larger diffusion rates of chromium, contribute to the faster formation of the σ phase from B2.

Interestingly, the size of B2 in RXZs is about 10 times larger than in nRXZs. This suggests an enhancement of the diffusion at grain boundary benefiting to both B2 and σ phases. In summary, the σ phase needs both thermodynamic (local ODFN at the B2/FCC interface) and kinetic (short circuit diffusion of chromium in the migrating grain boundaries) to precipitate which explains why it is not observed in the nRXZs. Furthermore, it was observed in duplex stainless steels that the σ phase is less prone to form on boundaries presenting specific orientation relationships, especially K-S^{172,238}. As shown by the zoomed view in **Fig. 3.7B**, most of the B2 precipitates in deformed grains formed with K-S ORs on all their boundaries. This could also contribute to the absence of the σ phase from nRXZs.

In a second step, precipitation occurs inside deformed grains. In these regions, precipitates form both on twin boundaries (sides of **Fig. 3.7C**) and in the bulk (centre of **Fig. 3.7C**). The formation of precipitates on twin boundaries is not surprising as mechanical twins were widely observed after cold rolling for 58% (**Fig. 3.5A**). In parallel, the precipitates that formed in the bulk are aligned with the $\{111\}$ directions of their parent FCC grain (inset in **Fig. 3.7B**). This indicates that they formed on dislocations introduced by cold rolling. As these grains are not recrystallised, dislocations formed during rolling serve as preferential nucleation sites for the B2 precipitates.

Although recrystallisation and precipitation were detailed separately, they do not occur subsequently. Their simultaneous activations result in interactions that will be detailed here.

Intragranular precipitation occurs in non-recrystallised regions after 15 minutes of annealing (**Fig. 3.9B**). Yet, at this stage of the annealing treatment, only 7% of the material is recrystallised compared to 71% after 744 hours (**Fig. 3.12**). Hence, 64% of the material recrystallised while containing intragranular B2 precipitates. The small size of these precipitates results most probably in the pinning of grain boundaries. A significative coarsening of the precipitates is then needed to decrease the pinning pressure exerted by precipitates and allow the movement of grain boundaries. This coarsening happens via the Ostwald ripening mechanism: the growth of B2 grains being linked to a decrease in the precipitate density. As previously observed during the recrystallisation of aluminium alloys, this process can be accompanied by a spheroidization of precipitates¹⁶⁷. These modifications in the B2 grain size, density and shape are observed when comparing RXZs and nRXZs, as in **Fig. 3.7B** for example. Because recrystallisation rate is determined by the precipitation coarsening rate, generally considered slower than boundary

migration rate, this phenomenon results in the slow recrystallisation kinetics observed in C6Al (**Fig. 3.12**).

While recrystallisation proceeds, grain growth is activated within RXZs. However, the co-precipitation of B2 and σ phases on recrystallised grain boundaries limits the growth of recrystallised grains, which is also limiting the recrystallisation kinetics.

3.3.3. Influence of rolling intensity

The recrystallisation kinetics are directly linked to the strain level applied by CR as highlighted in **Fig. 3.12**. It is observed from the same figure that recrystallisation is not completed after 744 hours at 900°C in H-CR58 while it is the case after 50 hours CR80. Indeed, when the applied strain is larger, even the grains with lower M would have a sufficient stored energy to recrystallise, limiting the fraction of nRXZs. Nonetheless, 50 hours are required to achieve complete recrystallisation after a 80% CR reduction. As a matter of comparison, Cantor's alloy, remaining FCC during annealing, is completely recrystallised after 5 minutes at 900°C following a CR for 80% as detailed in chapter 6. De la Cuevas *et al.* reported that a 22% Mn-0.6% C (in weight %) TWIP steel recrystallises entirely in one second at 900°C after CR for 60% and above²³⁹. These comparisons confirm the slow recrystallisation kinetics of the present C6Al alloy. The presence of interstitial elements, such as carbon and nitrogen (**Table 3.1**), can also contribute to the limitation of recrystallisation kinetics through solute drag.

Apart from the difference in kinetics, the two thermomechanical routes result in similar microstructures. It is highlighted when comparing the RXZs obtained after the two routes including the same annealing treatment at 900°C for 50 hours (**Fig. 3.7** and **Fig. 3.13**). Both present equiaxed FCC, B2 and σ grains. The grain sizes after route CR80 are smaller due to a larger nucleation rate. These similarities confirm that the microstructure formation sequence detailed above remains valid whatever the CR reduction. The slower kinetics induced by the lower CR reduction allowed the different mechanisms and their interactions to be clearly identified in the present study.

Fig. 3.18 summarizes with sketches the microstructure evolution at annealing temperatures of 620, 900 and 1000°C after CR reduction of 58% and at 900°C after CR reduction of 80%.

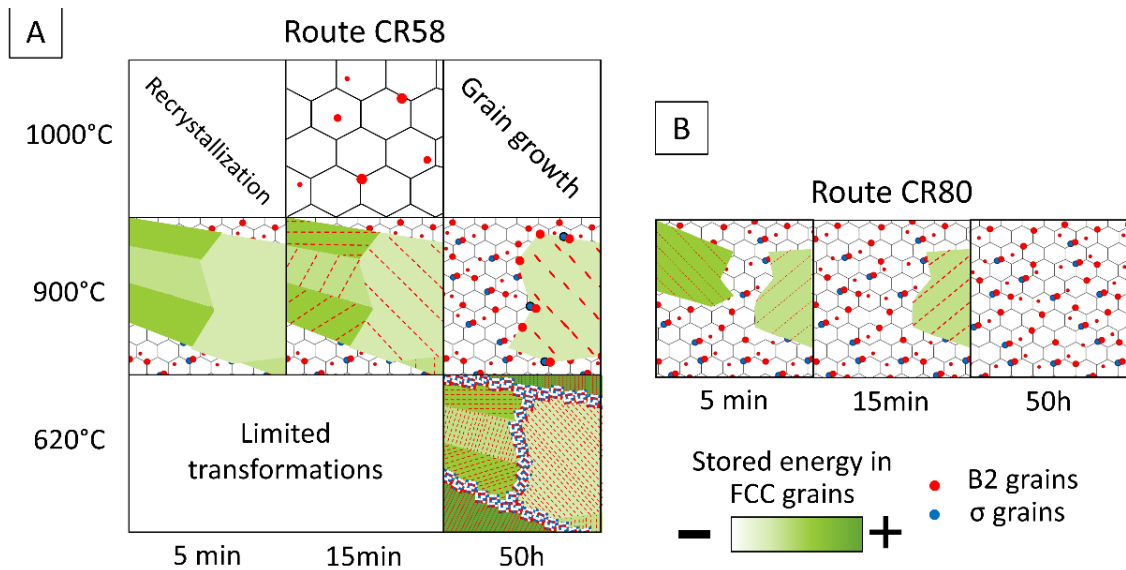


Fig. 3.18 Matrixes summarizing the microstructure evolutions after CR reductions of (A) 58% with annealing at 620, 900 and 1000°C, and of (B) 80% with annealing at 900°C. The local stored energy in the FCC phase is depicted with shades of green. The darkest green indicates the largest stored energy while the recrystallised strain free grains are depicted in white. The second phases are shown in red for the B2 phase and blue for the σ phase. [Full-size.](#)

Conclusions

The composition C6Al was submitted to CR and annealing. Focus was given on two CR reduction levels. Small rolling reduction (58%) resulted in slow microstructure transformation rates allowing the different mechanisms involved to be decorrelated. The annealing temperature is shown to be the key parameter determining the governing microstructure transformations.

At annealing temperatures below 900°C, precipitation is the main phenomenon taking place. Above 900°C, recrystallisation is governing the evolution of the microstructure. At 900°C, both mechanisms are occurring simultaneously. The energy stored in grains is then the main parameter influencing the microstructure transformations. It determines where recrystallisation occurs. In recrystallised regions, B2 and σ grains precipitate on newly formed grain boundaries. As previously reported in austenitic stainless steels, a coupling between the nucleation of these two phases was observed. The formation of the σ phase was explained by a local chromium enrichment at the B2/FCC interface. This was confirmed by thermodynamic calculations. Where recrystallisation does not occur, fine intragranular B2 grains are observed. It was shown that these precipitates do not suppress recrystallisation but delay it. After considerable annealing times, only the grains presenting the lowest stored energy, i.e. the grains with orientations close to Goss and Brass TCs, do not recrystallise. Moreover, it was shown that this microstructure sequence remains valid with an increase of the CR reduction. Larger CR reductions result in accelerated recrystallisation rates and enables a complete recrystallisation of the material. Nonetheless, 6 hours are necessary to fully recrystallise C6Al at 900°C after CR92 suggesting that interactions between recrystallisation and precipitation are not suppressed with increased rolling intensity.

These results give a new understanding of the microstructure sequence occurring after CR in C6Al. It also gives an overview of the wide range of microstructures and hardness values that can be achieved from this single chemical composition by adapting the thermomechanical route.

Chapter 4.

A WIDE RANGE OF TENSILE PROPERTIES FROM THE SINGLE ALLOY C6Al

Introduction

Chapter 3 showed the wide range of microstructures that can be obtained from the single chemical composition C6Al. Depending mainly on the annealing temperature, it is possible to choose the phases present, their sizes and fractions. These results proved in general agreement with the phase diagram calculated with ThermoCalc software. In chapter 3, the mechanisms governing the formation of the microstructures were also identified along with their respective kinetics. Based on this new understanding, three microstructures, representative of the wide range observed, were designed with the aim of characterizing them in tension. These three microstructures assess the properties of the single-phase FCC solid solution but also the role of precipitation and of non-recrystallised zones (nRXZ).

This chapter focuses on the identification and quantification of the multiple strengthening and deformation mechanisms. First, the three yield strength values (YS) are modelled according to the formalism of Kocks²⁴⁰ in order to identify the microstructural features contributing the most. Then, the deformation mechanisms are identified based on the work-hardening rate (WHR) curves and on post-mortem observations. Cantor's alloy, from which C6Al is derived, was

reported to present twinning during deformation at room temperature, granting its large work-hardening capacity (WHC) and ductility ^{31,98}. Particular attention will be given to the identification of mechanical twinning in C6Al.

4.1. Materials and methods

4.1.1. Material composition

Ingot n°2 of C6Al is used in this chapter. Its chemical composition is given in **Table 4.1**.

Table 4.1 Chemical composition of the ingot used in this chapter, in atomic percent.

Ingot n°	2
Al	5.8 ± 0.1
Co	19.1 ± 0.2
Cr	17.9 ± 0.1
Fe	18.8 ± 0.1
Mn	19.1 ± 0.2
Ni	19.3 ± 0.1
C	0.12 ± 0.03
N	0.10 ± 0.03
O	0.02 ± 0.00

4.1.2. Processing

The thermomechanical schedule used in this chapter is schematized in **Fig. 4.1**. It corresponds to the route CR defined in chapter 3. Ingots are first hot rolled at 1200°C for a thickness reduction of 70% (corresponding to a Von Mises strain equivalent $\varepsilon_{VM} = 1.4$). Then cold rolling (CR) is performed for a thickness reduction of 80% ($\varepsilon_{VM} = 1.9$). Finally, three different annealing treatments are performed: 2 minutes at 1200°C; 5 minutes and 6 hours at 900°C. These annealing treatments were all performed in sealed quartz capsules filled with argon and followed by air cooling.

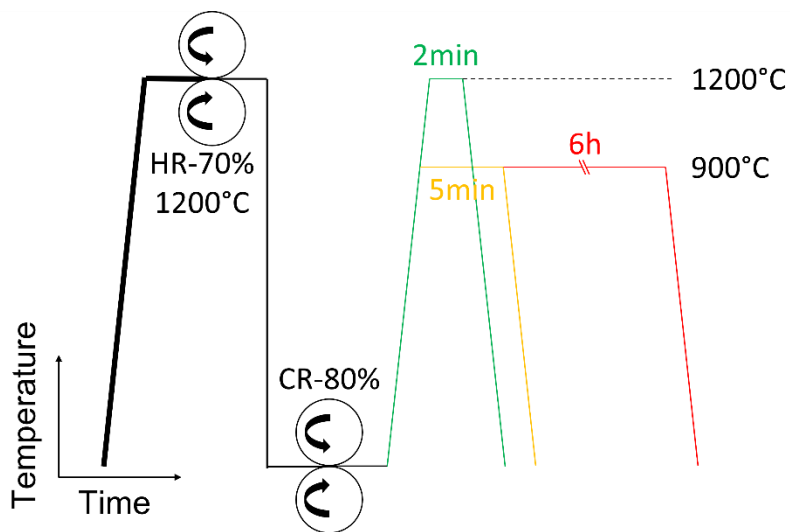


Fig. 4.1 Sketch of the thermomechanical schedule followed in this study. [Full-size](#).

Additional pieces of information on materials, processing and characterisation methods can be found in annexe A at the end of this manuscript.

4.1.3. Nomenclature

In this chapter, the nomenclature of chapter 3 is also used. As an example, the samples submitted to the annealing treatment at 1200°C for 2 minutes are referred to as CR80-1200/2min.

4.2. Results

4.2.1. Microstructures

Fig. 4.2 presents the microstructures of the three microstructural states selected for tensile testing.

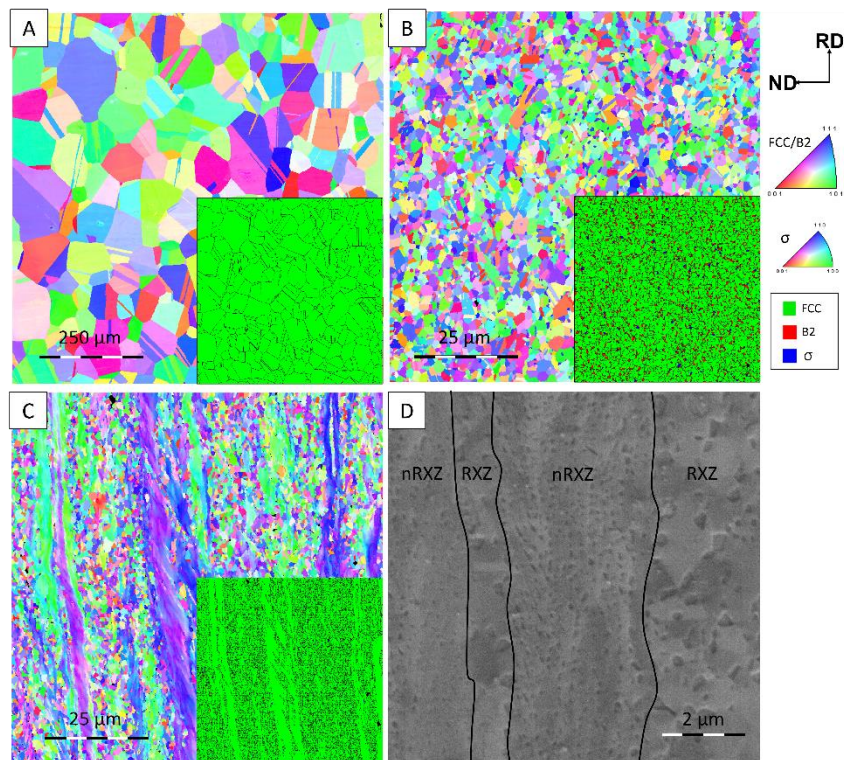


Fig. 4.2 Microstructures of the three microstructural states selected for tensile testing. (A-C) IPF-Z and phase maps obtained after respectively 2 minutes at 1200°C, 6 hours and 5 minutes at 900°C. (D) Enlarged BSE SEM micrograph obtained after 5 minutes at 900°C. [Full-size](#).

CR80-1200/2min is single-phase FCC (**Fig. 4.2A**) with a mean grain size of $95 \pm 30 \mu\text{m}$. Annealing twins are present in most of the grains.

CR80-900/6h consists of FCC, B2 and σ grains (**Fig. 4.2B**). The FCC grain size is $3.7 \pm 1.9 \mu\text{m}$. Second phases present grain sizes of $0.9 \pm 0.2 \mu\text{m}$. The material is recrystallised at $94 \pm 6 \%$. This value was measured from optical micrographs with the procedure detailed in the *materials and methods* section. It is considered as fully recrystallised.

CR80-900/5min is partially recrystallised (**Fig. 4.2C-D**) with a recrystallisation fraction of $65 \pm 7 \%$. The recrystallised zones (RXZ) are composed of FCC, B2 and σ grains (**Fig. 4.2C**). The

FCC grain size is of $1.2 \pm 0.6 \mu\text{m}$ and that of second phases of $0.5 \pm 0.1 \mu\text{m}$. The phase volume fractions in the RXZs were measured on EBSD datasets acquired at a larger magnification: 9% for B2 and 1% for σ .

The nRXZs are composed of elongated FCC grains (visible on the IPF and phase maps of **Fig. 4.2C**). Their dimensions measured from EBSD are $5 \pm 2 \mu\text{m}$ in their short axis and $40 \pm 45 \mu\text{m}$ in their long axis. Their intragranular colour gradients (IPF map of **Fig. 4.2C**) suggest that they are work hardened. They contain fine and elongated precipitates. These precipitates are clearly visible in the BSE SEM micrograph of **Fig. 4.2D**. Their dark colour indicates that they are lighter than the FCC matrix and hence contain more aluminium. This suggests that they are B2 as presented in chapter 3. They also present a similar colour than the B2 grains located in the RXZs confirming this hypothesis.

Additional images, acquired at larger magnifications, were used to measure the precipitate dimensions. These observations permit to measure the small and long axes of the precipitates observed in 2D (w and l), which are projections or sections of the 3D precipitates. Based on the observations of **Fig. 4.2D** and at larger magnifications, the 3D precipitates are considered as elongated cylinders. As illustrated in **Fig. 4.3** in the case of a projection, the dimensions measured in 2D might considerably differ from the dimensions in 3D. Consequently, the dimensions of 3D precipitates are determined as follows ²⁴¹:

$$W = \text{avg}(w) \text{ and } L = \max(l) \quad (\text{Eq. 2})$$

with W the cross-section diameter and L the long axis of 3D precipitates. In CR80-900/5min, the cross-section diameter W is $50 \pm 20 \text{ nm}$ and the long axis L is $450 \pm 70 \text{ nm}$.

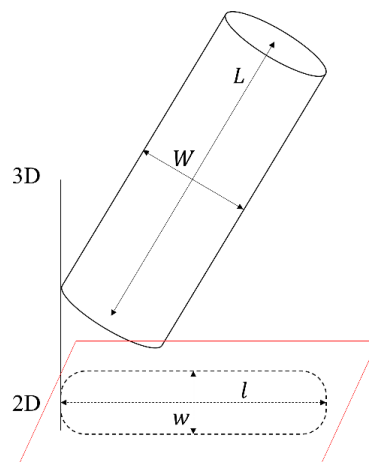


Fig. 4.3 Schematic of the projection in 2D of a 3D cylinder. W and L indicate the small and long axes of the 3D precipitate, w and l of the projection. [Full-size](#).

Hardness was evaluated respectively at 356 ± 5 and $371 \pm 11 \text{ HV0.05}$ in RXZs and nRXZs with a load of 50 grams.

Fig. 4.4 presents the XRD diffractograms of the material after CR80 and of the three selected microstructures. The materials after CR80 and after CR80-1200/2min are confirmed to be single-phase FCC. Peaks corresponding to a BCC phase (B2 phase) and to the σ phase appear when annealing is performed at 900°C . These peaks are more intense after 6 hours of annealing. The volume fractions of the second phases were quantified from the XRD diffractograms with the Topas software. In CR80-900/6h, they are of 15% for B2 and 5% for σ . In CR80-900/5min, they are of 12% for B2 and 1% for σ .

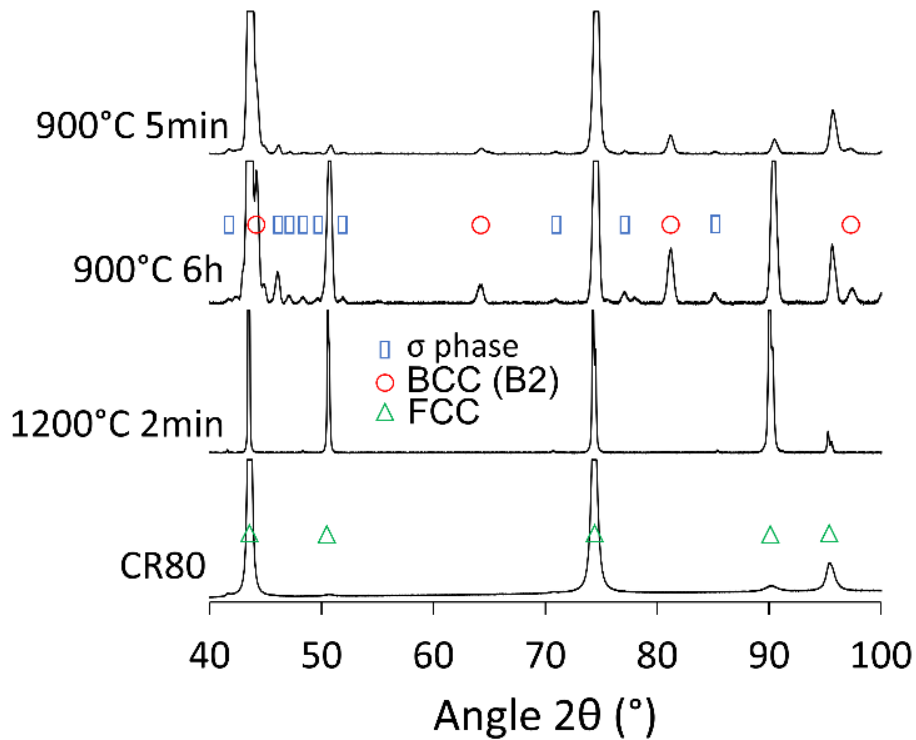


Fig. 4.4 XRD diffractograms measured after CR80, CR80-1200/2min, CR80-900/6h and CR80-900/5min. [Full-size.](#)

4.2.2. Tensile properties

Fig. 4.5 presents the tensile curves for the three selected microstructures of C6Al. The true stress – true strain curves are given in solid lines while the WHR are shown in dotted lines. The corresponding microstructural features are given in **Table 4.2** along with the corresponding tensile properties.

The green curve corresponds to CR80-1200/2min. It presents the largest uniform elongation of 61% and the lowest YS of 300 MPa. It presents a WHC – difference between tensile and yield stress levels – of 850 MPa. Its WHR does not steadily decrease during tensile testing but stabilizes and even increases before decreasing until necking. The red curve presents a uniform elongation of 19% with a YS of 650 MPa. Its WHC is 410 MPa. Its WHR steadily decreases until necking. The orange curve presents a uniform elongation of 7%, a YS of 1050 MPa and a WHC of 250 MPa. As for the red curve, the WHR constantly decreases during plastic deformation until failure.

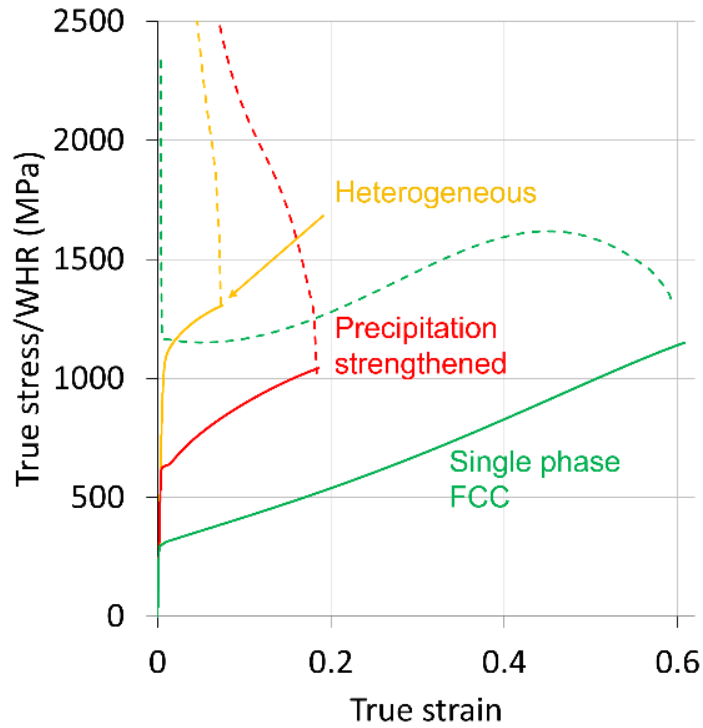
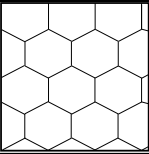
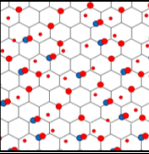
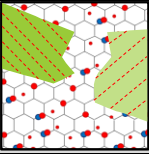


Fig. 4.5 Tensile curves for the three selected microstructures of C6Al. The true stress – true strain curves are shown in solid lines while the WHR curves are given with dotted lines. The green curves correspond to CR80-1200/2min. The red curves correspond to CR80-900/6h. The orange curves correspond to CR80-900/5min. The reader is referred to **Table 4.2** for further details on the corresponding microstructure features and tensile properties. [Full-size](#).

Table 4.2 Microstructure features of the three selected microstructures of C6Al. The tensile properties of each state are also given.

Microstructure	RXZ fraction	Volume fractions		RXZ FCC grain size (μm)	Yield strength (YS) (MPa)	Maximum tensile stress (MPa)	Uniform elongation
		B2	σ				
CR80-1200/2min - Single phase microstructure (blue curve)							
	1	0	0	95 ± 30	300	1150	0.61
CR80-900/6h - Precipitation strengthened microstructure (red curve)							
	0.94 ± 0.06	0.15	0.05	3.7 ± 1.9	630	1040	0.19
CR80-900/5min - Heterogeneous microstructure (orange curve)							
	0.65 ± 0.07	0.12	0.01	1.2 ± 0.6	1050	1300	0.07

Microstructural characterization was performed after tensile testing until failure on the three specimens. The presence of gradients of grey in CR80-1200/2min (**Fig. 4.6A**) indicates that deformation is governed by dislocation slip. In addition, mechanical twins are observed. **Fig. 4.6B** reveals the presence of twins intersecting each other. The typical 60° misorientation highlighted on the misorientation profile shown in inset, confirms their nature.

In **Fig. 4.6C**, gradients of grey are also present and are localised in the FCC phase, in grey. This suggests that deformation is governed by dislocation slip in the FCC phase. Precipitates, that appear darker and whiter, do not seem to deform plastically. Voids are present at the FCC/B2 or B2/ σ boundaries (indicated by white arrows).

Fig. 4.6D presents the microstructure after tensile testing of CR80-900/5min. No sign of plastic deformation is visible at this scale.

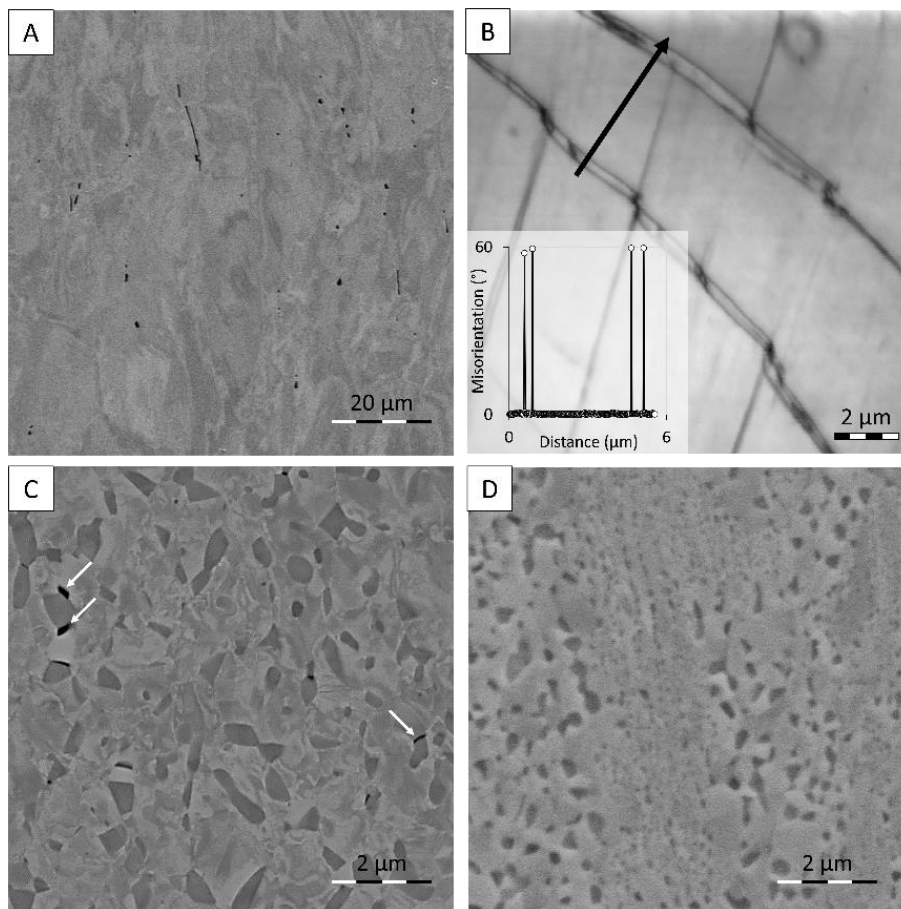


Fig. 4.6 Microstructures after tensile testing until failure. (A-B) CR80-1200/2min with SEM BSE micrograph in (A) and IQ map showing the presence of mechanical twins with their typical 60° boundary misorientation in (B). (C) SEM BSE image of CR80-900/6h. (D) SEM BSE image of CR80-900/5min. [Full-size.](#)

4.3. Discussion

4.3.1. Strengthening contributions

Fig. 4.5 shows the wide range of tensile properties that can be achieved through thermomechanical treatment (TMT) from the single chemical composition C6Al. YS from 300 to 1050 MPa were recorded (**Table 4.2**). This wide range of YS results from the large variety of

microstructures, with different number of phases, presenting different morphologies and sizes. In order to decorrelate the different contributions resulting from the different microstructural features, YS are modelled.

According to Kocks ²⁴⁰, the material YS σ_{YS} can be expressed as a rule of mixture, being the sum of the strength of each constituent σ_{YS}^i weighted by its volume fraction f^i .

$$\sigma_{YS} = \sum_i \sigma_{YS}^i * f^i \quad (\text{Eq. 4.3})$$

A *constituent* can be an homogeneous phase, as the FCC matrix of CR80-1200/2min or the second phases when located at grain boundaries, as in CR80-900/6h. In this case, the YS is the sum of its intrinsic strength σ_0 – including solid solution strengthening – and of its grain boundary strength σ_{GB} expressed with the Hall-Petch relationship. It gives :

$$\sigma_{YS}^i = \sigma_0^i + \sigma_{GB}^i = \sigma_0^i + \frac{K}{\sqrt{d_i}} \quad (\text{Eq. 4.4})$$

with K the Hall-Petch constant and d the grain size. No grain boundary strengthening is considered for second phases in this model, in agreement with Gwalani *et al.* ²⁴².

A *constituent* can also be more complex such as the nRXZs of CR80-900/5min which are work-hardened and contain intragranular B2 precipitates. The isotropic contribution σ_{ISO} resulting from the presence of dislocations before tensile testing is expressed using the Taylor equation:

$$\sigma_{ISO} = \alpha M G b \sqrt{\rho} \quad (\text{Eq. 4.5})$$

with α the Taylor constant, M the Taylor factor, G the material shear modulus, b the Burgers vector and ρ the dislocation density. The dislocation density of nRXZs could not be assessed from XRD due to the presence of RXZs. Instead, two extremum values were measured. The dislocation density after CR80 of $11.6 * 10^{14} / \text{m}^2$ is the upper bound. The lower bound is measured on CR80-900/5min (considering both RXZs and nRXZs). It gives a value of $3.6 * 10^{14} / \text{m}^2$.

Moreover, these nRXZs also contain intragranular precipitates. The strengthening depends first on the nucleation sites, being partly twin boundaries and dislocations as shown in chapter 3. For simplicity's sake, it is chosen in this calculation that the precipitates in the nRXZs cannot be circumvented by dislocations and hence answer a simple law of mixtures, following Eq. 4.3.

As an example, the YS of CR80-900/5min can be expressed as:

$$\begin{aligned} \sigma_{YS} = & f_{RXZ} \left(f_{RXZ}^{FCC} \left(\sigma_0^{FCC} + \frac{K^{FCC}}{\sqrt{d_{RXZ}^{FCC}}} \right) + f_{RXZ}^{B2} \sigma_0^{B2} + f_{RXZ}^{\sigma} \sigma_0^{\sigma} \right) \\ & + f_{nRXZ} \left(f_{nRXZ}^{FCC} \left(\sigma_0^{FCC} + \frac{K^{FCC}}{\sqrt{d_{nRXZ}^{FCC}}} + \alpha M G b \sqrt{\rho} \right) + f_{nRXZ}^{B2} \sigma_0^{B2} \right) \end{aligned} \quad (\text{Eq. 4.6})$$

Table 4.3 gathers the constants and variables used in the simulation. The corresponding references or characterisation technics used are also given.

Table 4.3 Parameters used in the simulation of the YS of C6Al.

Symbol	Parameters	Value	Source
All specimens			
α	Taylor constant	0.25	113
M	Taylor factor	3.063	
G	Shear modulus	81 GPa	243
b	Burgers vector	0.254 nm	XRD
σ_0^{FCC}	FCC intrinsic strength	172 MPa	244
K^{FCC}	FCC Hall-Petch coefficient	730 MPa. $\sqrt{\mu\text{m}}$	244
d_i^{FCC}	Grain size	See section 4.2.1	EBSD, ²⁴⁵
σ_0^{B2}	B2 intrinsic strength	1800 MPa	242
σ_0^σ	σ intrinsic strength	240 MPa	242
f^i	Phase volume fractions	See section 4.2.1	XRD, EBSD
Specific to CR80-900/5min			
ρ_{MAX}	Dislocation density (CR80)	$11.7 \cdot 10^{14} / \text{m}^2$	XRD
ρ_{MIN}	Dislocation density (CR80-900/5min)	$3.6 \cdot 10^{14} / \text{m}^2$	XRD

The results of the calculation are given in **Fig. 4.7**. The simulated YS of the two first specimens are in good agreement with the measured values. CR80-900/5min presents however a large deviation of 175 MPa. This discrepancy is mainly attributed to the absence of a grain size dependence of the second phase strengthening. As the B2 grains in nRXZs are smaller than in RXZs, it is expected that their strengthening would be larger than those in RXZs at equal volume fraction. The deviation between calculation and measured values could be also due to consider all precipitates in nRXZs as non-circumventable. The detailed values of each contribution can be found in **Table 4.4**.

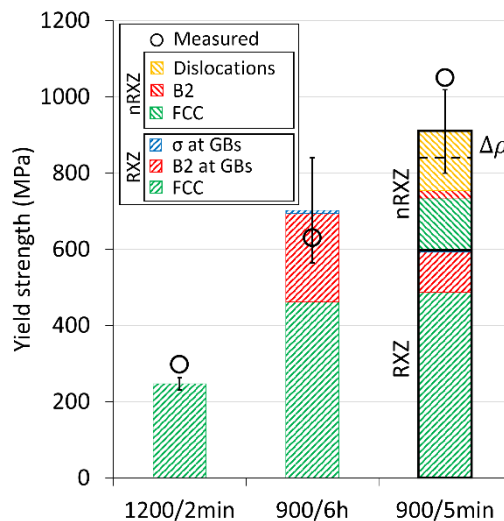


Fig. 4.7 Simulation of the YS of the three selected microstructures. The contributions corresponding to the strain free FCC phases appear in green, to the isotropic strengthening due to dislocations in orange, to the B2 phase in red and to the σ phase in blue. For CR80-900/5min, the contributions corresponding to RXZs and nRXZs are indicated. For nRXZs, the uncertainty in dislocation density results in an uncertainty in the isotropic contribution, indicated by $\Delta\rho$. [Full-size](#).

Table 4.4 Numerical results of the simulation.

Contributions	CR80-1200/2min	CR80-900/6h	CR80-900/5min
RXZ			
FCC	247	439	488
B2	-	276	105
σ	-	12	4
nRXZ			
FCC	-	-	167
Dislocations MAX	-	-	189
Dislocations MIN	-	-	105
Intragranular B2	-	-	19
Total	248	727	840-909
Error	16	131	109
Measured	300	630	1050

The simulation reveals that the FCC phase contributes the most to the YS. It contributes respectively for 60% and 67% in CR80-900/6h and CR80-900/5min when considering FCC phases in both RXZs and nRXZs. This results directly from the Hall-Petch relationship chosen with a value of K^{FCC} at 730 MPa. $\sqrt{\mu\text{m}}$. This value is surprisingly large when compared to values around 400 MPa. $\sqrt{\mu\text{m}}$ found in the literature for TWIP steels²⁴⁶. However, other studies on multicomponent alloys reported similar values, with 824 MPa. $\sqrt{\mu\text{m}}$ for Gwalani *et al.*²⁴² and even 970 MPa. $\sqrt{\mu\text{m}}$ depending on the points considered for Annasamy *et al.*²⁴⁷, both on Al_{0.3}CoCrFeNi. These large values of K^{FCC} could be a specificity of multicomponent alloys.

In CR80-900/5min, nRXZs contribute for 34% of the total YS, while consisting of 35% of the material. The strength from RXZs results for 80% from the FCC phase, the 20% remaining coming from B2 grains. In nRXZs, the FCC phase and dislocations contribute similarly while the B2 phase presents a contribution almost ten times lower. This result supports that their contribution is underestimated by the model and could explain the large deviation between calculation and measured values.

In CR80-900/6h, the B2 phase contributes to 38% of the YS. Even located at grain boundaries, the large volume fraction of the B2 phase results in a significant strengthening of 276 MPa. Due to the lower intrinsic strength of the σ phase found by Gwalani *et al.*²⁴², it does not contribute much to the YS. This is surprising in regard of its large hardness, as found experimentally through nano-indentation experiments (see **Table A.4** in the materials and methods chapter). Its contribution would have been in all cases limited due to its low volume fraction.

4.3.2. Work-hardening

In C6Al, deformation is governed by dislocation slip in the FCC phase. This is indicated by the gradients of grey observed in CR80-1200/2min and CR80-900/6h (**Fig. 4.6A** and C). These gradients are signs of the presence of orientation gradients within grains, typically observed after dislocation slip. However, no sign of these gradients is observed in CR80-900/5min after tensile testing (**Fig. 4.6D**). Orientation gradients did not develop due to the low uniform elongation of this specimen. No sign of deformation is observed in the B2 phase (**Fig. 4.6C**) due to its larger hardness compared to the surrounding FCC matrix.

Microstructural observations performed after tensile testing revealed the presence of mechanical twins in CR80-1200/2min, with their 60° rotation at their boundaries (**Fig. 4.6B**). The activation of mechanical twinning is not surprising in C6Al when considering its SFE. It was evaluated in chapter 3 between 30-40 mJ/m². The activation of mechanical twinning during straining results in a grain in WHR²²⁵, that can be observed in **Fig. 4.5**.

However, the work-hardening behaviour of this specimen is peculiar with the concave plastic part of the tensile curve and the large peak in WHR, observed at the large strain of 0.45. The true reason for this behaviour is unknown. Microstructural observations performed after tensile testing did not reveal the activation of a third deformation mechanism – such as the TRIP effect. An hypothesis could be related to the presence of carbon and of aluminium in C6Al.

Bouaziz *et al.* proposed that interstitial carbon in TWIP steels, in addition to increasing the SFE, also decreases the critical resolved shear stress for twinning¹²⁵. As a consequence, the addition of a low carbon content might favour twinning. This theory is mainly based on the work of Allain *et al.* who compared two Fe-Mn alloys with similar SFE but only one containing carbon¹²³. After tensile testing, mechanical twins were only observed in the alloy containing carbon. This theory is also confirmed by the results obtained by Chen *et al.* on carbon-containing Cantor's alloys³². At carbon contents lower than 2 at.%, mechanical twins were observed, resulting in increased strength and ductility compared to Cantor's alloy without carbon. At larger carbon contents, mechanical twins were hardly found and ductility dropped. The presence of carbon in C6Al could hence contribute to the activation of mechanical twinning, but the low carbon content of C6Al – 0.12 at.% – makes it unlikely. Recent results seem to indicate that interstitial nitrogen present a similar effect on mechanical twinning than carbon¹²⁶.

Mishra *et al.* proposed that aluminium could have a similar effect on mechanical twinning than carbon, due to its influence on lattice distortion²⁴⁸. The increase in SFE resulting from the presence of aluminium in C6Al would delay the activation of mechanical twinning – WHR peak observed at a large strain – but the lattice distortion would then permit an increased twinning activity. This theory would require additional work to be confirmed, such as a study of the influence of aluminium content on twinning activity.

In the two specimens annealed at 900°C, the WHR curves only present a slight increase in slope. This is also attributed to the activation of mechanical twinning during deformation while of lower intensity than in CR80-1200/2min. Mechanical twins were observed in CR80-900/6h after tensile testing until rupture, as shown in **Fig. 4.8**. No twins could be observed in CR80-900/5min most probably due to the low FCC grain size.

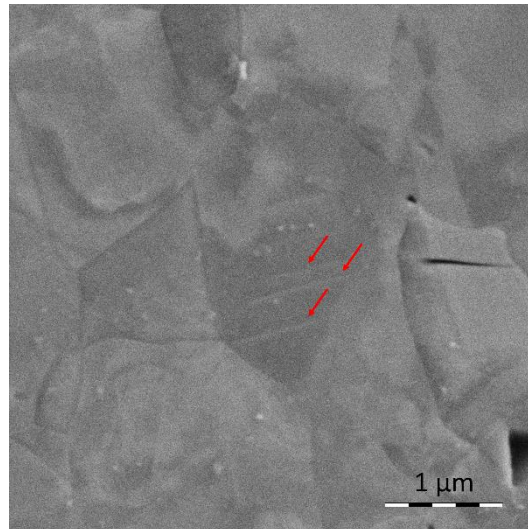


Fig. 4.8 SEM BSE micrograph showing the presence of mechanical twins (indicated by red arrows) in C6Al CR80-900/6h. [Full-size](#).

It is surprising that mechanical twinning activates in such small FCC grains as the reduction in grain size is often coupled to a limitation of twinning¹³¹. The presence of carbon and aluminium in C6Al could contribute to the activation of twinning in small FCC grains.

Work-hardening is also influenced by the presence of second phases, present in CR80-900/6h and CR80-900/5min. As detailed in section 4.3.1, gliding dislocations in the FCC phase interact with intragranular precipitates through the Orowan looping mechanism. During deformation, dislocation bypass precipitates by leaving dislocation loops around them (c.f. section 1.3.3. of chapter 1). This mechanism results in an additional work-hardening contribution, called kinematic hardening σ_{KIN} by Fribourg *et al.*²⁴⁹. It is expressed by:

$$\sigma_{KIN} = \frac{f}{1-f} E_p \frac{bn}{2r_p M} \quad (\text{Eq. 4.7})$$

with E_p the Young's modulus of precipitates. The value of $E_p = 200 \text{ GPa}$ is used (from a B2 shear modulus of 80 GPa²⁵⁰ and a Poisson's ratio of 0.25²⁵¹). The parameter n is the number of loops stored around precipitates. The value $n = 9$ is used in agreement with the value reported by Fribourg *et al.*²⁴⁹ where precipitates present similar volume fraction and equivalent radius but a lower aspect ratio of around 3 (9 in this study).

In the case of the nRXZs of CR80-900/5min, it gives a value of 268 MPa. When applied to RXZs, this formula gives strengthening contributions of 30 MPa for both CR80-900/6h and CR80-900/5min. These two last values should be even decreased due to the lower number of dislocation loops that could be stored around such large precipitates. This simple calculation indicates that grain boundary precipitates do not contribute much to work-hardening. Their influence on tensile properties is mainly on YS through composite strengthening.

However, the formation of intragranular precipitates might result in significative hardening, as is shown by the value of 268 MPa obtained in the nRXZs of CR80-900/5min. However, the experimental WHC for this sample is 250 MPa (**Table 4.2**), smaller than the previous value. The limitation of the work-hardening induced by the presence of intragranular precipitates is attributed to the work-hardened state of the FCC matrix in nRXZs (**Fig. 4.2C**). This last feature

limits the movement of dislocations, limiting the potential hardening from precipitates. Moreover, cracks were observed at second phase interfaces (white arrows in **Fig. 4.6C**). These contribute to the decrease in ductility in multiphase specimen and also to their limited WHC.

Conclusions

A wide range of tensile properties was achieved through TMT from the single chemical composition C6Al. YS from 300 to 1050 MPa were recorded along with uniform elongations from 7 to 61%.

The modelling of YS values reveals that the FCC phase contributes most in the three specimens. The B2 phase contribute to a lesser extent, mainly depending on its volume fraction. The σ grains do not contribute much due to their low volume fraction and location on grain boundaries. Ductility levels are strongly correlated to strength levels with ductility decreasing as strength increases. Hence, these three specimens, obtained through conventional processing, follow the well-known strength-ductility trade-off.

Nonetheless, this first approach permitted to identify the different strengthening mechanisms and to evaluate their contributions. Deformation mechanisms were also identified based on the evolution of WHR and on post-mortem examinations. Mechanical twinning was shown to activate in single-phase FCC microstructures with grains of 100 μm and of 4 μm . In the former case, it contributes significantly to work-hardening. Finally, the presence of intragranular precipitates in CR80-900/5min was shown to induce an increase in work-hardening. However, this phenomenon cannot develop at its full potential due to the work-hardened state of the FCC matrix and to the formation of cracks at interphase boundaries.

Chapter 5.

DEVELOPMENT OF MICROSTRUCTURES WITH INCREASED WORK-HARDENING THROUGH INTRAGRANULAR PRECIPITATION

Introduction

Chapter 4 showed that a large range of tensile properties can be obtained from the chemical composition C6Al. Indeed, yield strength levels (YS) ranging from 300 to 1050 MPa were obtained. This was permitted by the variety of microstructures obtained after thermomechanical treatment (TMT) with different number of phases, different morphologies, different grain sizes... The activation of different deformation mechanisms also contributed to this wide range of properties, i.e. dislocation glide and mechanical twinning. Intragranular precipitation also proved to contribute to work-hardening though in a lesser extent. However, the work-hardened state of the FCC matrix, due to the prior rolling, did not permit to take full advantage of this effect. These results echo those obtained on $Al_{0.3}CoCrFeNi$ where YS from 160 to 1080 MPa were obtained depending on the microstructures⁶⁶. However, these results show a strong correlation between increased strength and decreased ductility, also known as the strength-ductility trade-off. This chapter goes forward in the development of microstructures presenting strength-ductility synergy.

The development of strength-ductility synergy, as opposed to strength-ductility trade-off, is and has been of great metallurgical interest, as it results in materials with both large levels of strength and

ductility. Multiple strategies were proposed to overcome this trade-off, often involving the activation of new deformation mechanisms during deformation. These additional deformation mechanisms maintain work-hardening at a high-level, postponing necking and permitting to achieve large tensile strength. Two examples are mechanical twinning or deformation driven phase transformation activated respectively in TWIP and transformation induced plasticity (TRIP) ^{225,252} steels or complex concentrated alloys (CCA) ^{31,42}. However, these two strategies often present low YS, around 400 MPa ^{225,252}. A third possibility is to benefit from the presence of second phases with different intrinsic strength than the surrounding matrix. In addition to precipitation strengthening, increasing YS, local strain incompatibility at interphase boundaries results in increased work-hardening. Such effect was observed in a wide range of alloys, such as aluminium, high strength steels or titanium alloys ^{249,253}. This new contribution to work-hardening is directly dependent on the interphase surface area. Close control of the microstructure is hence required in order to benefit the most from this effect.

The present work aims at reconciling intragranular precipitation with large work-hardening capacity. A new thermomechanical route is developed. It includes an intermediate cold rolling step with a moderate thickness reduction. The microstructures throughout this new processing route are scrutinized. The final microstructures with and without intermediate cold rolling step are compared. Then, the tensile properties are discussed. The work-hardening behaviour is modelled in order to shed some light on the respective contributions of the different hardening mechanisms. The role of intragranular precipitates is discussed.

5.1. Materials and methods

5.1.1. Materials

In this chapter, the ingots n°2 (C6Al) and n°3 (C5.3Al) of C+Al are used. Their chemical compositions are given in **Table 5.1**.

Table 5.1 Chemical compositions of the two ingots used in this chapter, in atomic percent.

Ingot n°	2 (C6Al)	3 (C5.3Al)
Al	5.8 ± 0.1	5.3 ± 0.1
Co	19.1 ± 0.2	19.0 ± 0.1
Cr	17.9 ± 0.1	17.9 ± 0.3
Fe	18.8 ± 0.1	19.8 ± 0.4
Mn	19.1 ± 0.2	19.6 ± 0.2
Ni	19.3 ± 0.1	18.2 ± 0.2
C	0.12 ± 0.03	0.14 ± 0.00
N	0.10 ± 0.03	0.08 ± 0.02
O	0.02 ± 0.00	0.05 ± 0.02

ThermoCalc software with inputs from the TCHEA4 thermodynamic database was used to predict the phase equilibria in Cantor's alloy as a function of aluminium addition (**Fig. 5.1**). The two circles indicate the two temperatures of interest during TMT: the recrystallisation temperature of 1100°C (solid circle) and the aging temperature of 800°C (open circle).

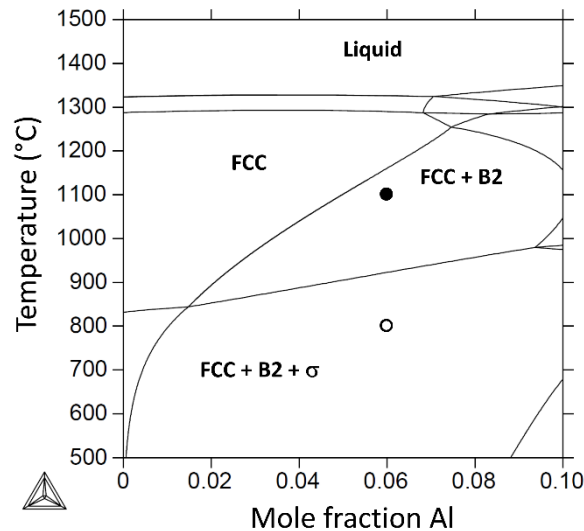


Fig. 5.1 CoCrFeMnNi + Al phase diagram. The 2 circles indicate the two temperatures of interest during TMT of C6Al. The solid circle indicates the recrystallisation temperature. The open circle indicates the aging temperature of 800°C. [Full-size](#).

5.1.2. Processing

The material was submitted to the processing route presented in **Fig. 5.2**. The first two steps are similar to the beginning of the route CR presented in chapter 3: i.e. hot rolling at 1200°C for a thickness reduction of 70% ($\epsilon_{VM} = 1.4$); and cold rolling for a total thickness reduction of 80% ($\epsilon_{VM} = 1.9$).

The material is then submitted to a recrystallisation stage (RX) at 1100°C for 2 minutes, followed by water quenching. This stage aims at recrystallising completely the material in a short time while limiting grain growth. It is performed in the dual phase (**Fig. 5.1**) domain but, as shown in section 5.2.1, no precipitation was observed.

A second cold rolling step follows with a thickness reduction of 15% ($\epsilon_{VM} = 0.2$). This step aims at forming dislocations inside the FCC grains of the matrix that will serve as intragranular nucleation sites during aging.

Finally, the material is aged at 800°C for durations ranging from 15 minutes to 50 hours, followed by air cooling. The temperature of 800°C was chosen in order to form a significant volume fraction of intragranular precipitates while limiting their coarsening.

Both the recrystallisation and aging steps were performed in quartz sealed capsules under argon atmosphere.

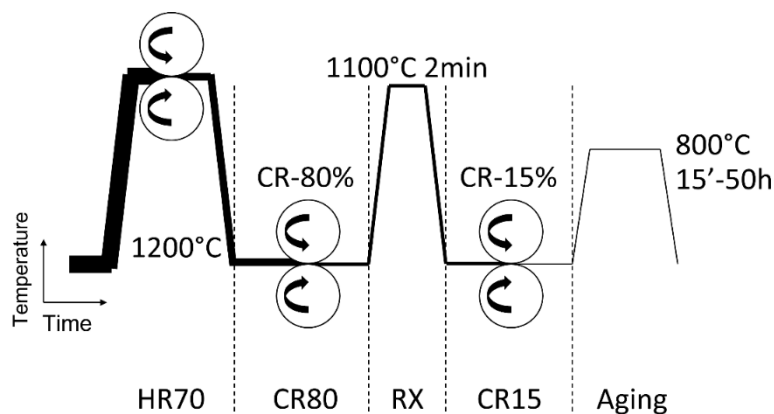


Fig. 5.2 Schematics of the thermomechanical schedule chosen for processing of C+Al. [Full-size](#).

Additional pieces of information on materials, processing and characterisation methods can be found in annexe A at the end of this manuscript.

5.1.3. Nomenclature

In what follows, the different samples are referred to using the steps of the thermomechanical schedule they were submitted to. For example, the sample submitted to the complete processing route with an aging step of 1 hour at 800°C is referred to as RX+CR+800/1h. The sample submitted to the recrystallisation step directly followed by the same aging step, i.e. without the intermediate CR step, is referred to as RX+800/1h.

5.2. Results

5.2.1. Microstructures after RX and RX+CR

The microstructure after RX consists in equiaxed grains containing annealing twins (**Fig. 5.3A**). Grains are strain free as indicated by the absence of colour gradients. The mean grain size is $32 \pm 5 \mu\text{m}$. The material is fully FCC.

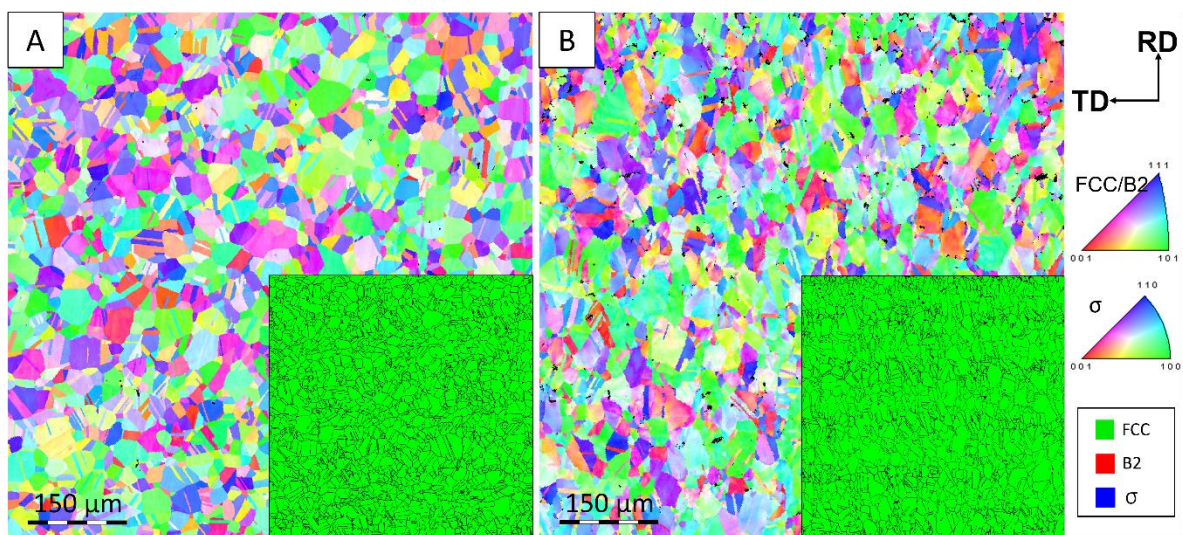


Fig. 5.3 IPF-Z and phase maps acquired after (A) RX and (B) RX+CR. [Full-size](#).

The microstructure after RX+CR presents grains slightly elongated in the rolling direction (**Fig. 5.3B**). Grains present intragranular misorientations as indicated by colour gradients. The grain size is unchanged. The material is fully FCC.

5.2.2. Comparison between RX+800°C and RX+CR+800°C

The following results will focus on the comparison of the microstructures of RX+800°C, i.e. *without* the second cold rolling stage, and RX+CR+800°C, i.e. *including* the second cold rolling stage.

The microstructure of the sample RX+800/1h consists in FCC grains, with very few intragranular precipitates (**Fig. 5.4A**). Precipitates formed mainly at grain boundaries (indicated by black arrows in **Fig. 5.4A**). There, precipitates of the B2 and σ phases are present (**Fig. 5.4B**). The microstructure of RX+CR+800/1h is composed of FCC grains in which thin elongated precipitates formed (indicated by white arrows in **Fig. 5.4C**). Some of these precipitates formed along twin boundaries as observed in

chapter 3 but the main part formed in the bulk. Precipitates also formed on grain boundaries (indicated by black arrows in **Fig. 5.4C**). These precipitates are of the B2 and σ phases, as shown in **Fig. 5.4D**.

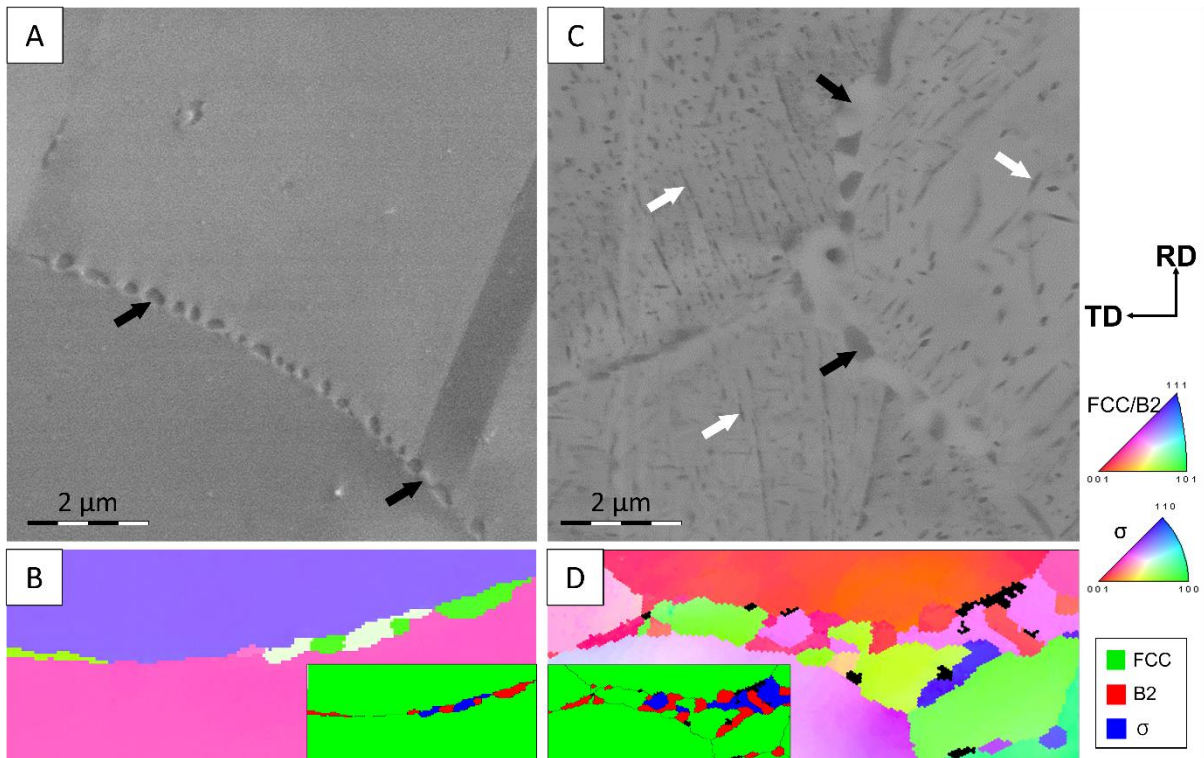


Fig. 5.4 Comparison between the microstructures of (A-B) RX+800/1h and (C-D) RX+CR+800/1h. (A and C) BSE SEM micrographs. Intergranular and intragranular precipitates are indicated with black and white arrows, respectively. (B and D) IPF-Z and phase maps acquired on grain boundaries in the two materials. The scale bars of the BSE micrographs and of the IPF-Z maps are identical. [Full-size](#).

The two samples RX+800/1h and RX+CR+800/1h were analysed by TEM in order to precise the presence and dimensions of intragranular precipitates. TEM observations confirmed the absence of intragranular precipitation in RX+800/1h (**Fig. 5.5A**). In RX+CR+800/1h, intragranular precipitates were widely observed throughout the material (**Fig. 5.5B**). Precipitation was observed mainly in the bulk.

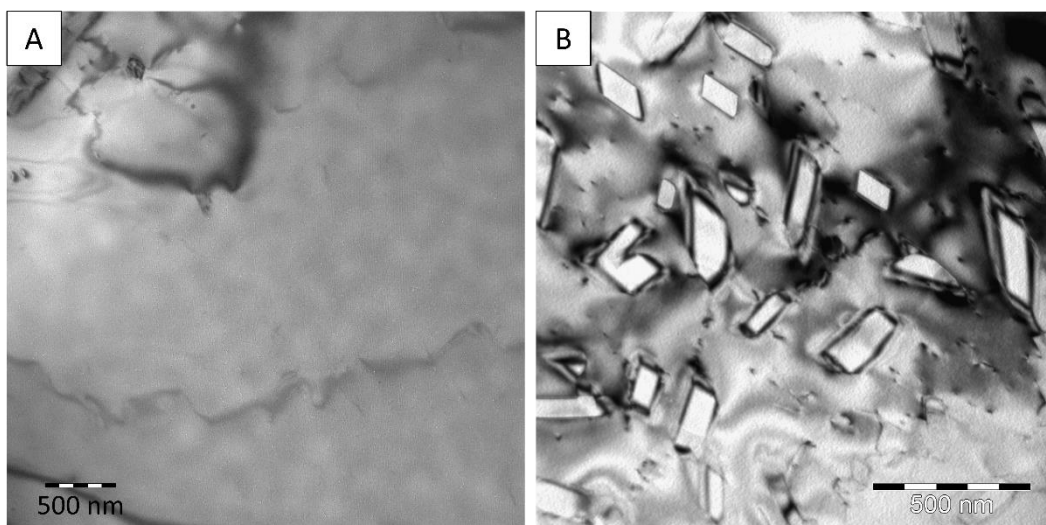


Fig. 5.5 Bright field TEM observations of intragranular regions. (A) RX+800/1h and (B) RX+CR+800/1h. [Full-size](#).

Several additional images were acquired in different grains of RX+CR+800/1h in order to measure the precipitate dimensions. As detailed in chapter 4, the observed dimensions in 2D (w and l) were used to determine the dimensions of the precipitates in 3D (W and L). The same equations are used :

$$W = \text{avg}(w) \text{ and } L = \text{max}(l) \quad (\text{Eq. 5.1})$$

W was calculated at 70 ± 30 nm and L at 630 ± 10 nm.

In order to precise the nature of the intragranular precipitates, TEM observations were performed on larger intragranular precipitates in RX+CR+800/50h (**Fig. 5.6**). The bright-field image of **Fig. 5.6A** shows several intragranular precipitates. The EDS maps (**Fig. 5.6D**) show that they are enriched in nickel and aluminium. Diffraction patterns were recorded to determine the nature of the precipitates. The intragranular precipitates are confirmed to be of the B2 phase, as indicated by the presence of sublattice spots (encircled in yellow in **Fig. 5.6C**). The matrix is confirmed to be FCC (**Fig. 5.6B**). The chemical compositions of the FCC matrix and of intragranular precipitates are reported in **Table 5.2**.

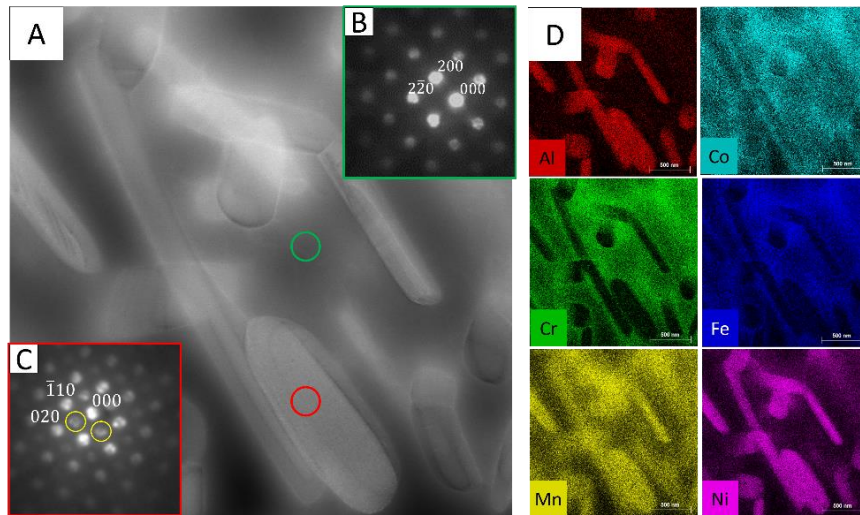


Fig. 5.6 TEM observation of intragranular precipitates in RX+CR+800/50h. (A) Bright field image, (B-C) diffraction patterns recorded in (B) a FCC grain (green circle) ([001] zone axis), (C) a B2 grain with sublattice spots encircled in yellow (red circle) ([001] zone axis). (D) STEM-EDS maps for the six elements composing C5.3Al. [Full-size](#).

Table 5.2 Chemical compositions measured with STEM-EDS of the different phases present in RX+CR+800/50h, in atomic percent.

	Al (at.%)	Co (at.%)	Cr (at.%)	Fe (at.%)	Mn (at.%)	Ni (at.%)
FCC	2 ± 1	21 ± 1	21 ± 1	25 ± 1	19 ± 1	11 ± 1
B2	18 ± 1	14 ± 1	4 ± 1	7 ± 1	26 ± 1	31 ± 2

Fig. 5.7 presents the results of XRD measurements. Four diffractograms corresponding to the conditions RX, RX+800/1h, RX+CR and RX+CR+800/1h are shown in **Fig. 5.7A**. The FCC phase is present in all samples. The B2 and σ phases appear in samples submitted to aging and are more intense in RX+CR+800/1h. Based on the diffractograms recorded on RX+800°C and RX+CR+800°C with aging times from 15 minutes to 50 hours, the volume fractions of the B2 and σ phases (**Fig. 5.7B**) were calculated. The formation of the B2 phase is significantly accelerated in samples submitted to CR15 (in red). For example, a B2 fraction of 10% is reached in 20 minutes or in 6 hours at 800°C with and without CR15, respectively. The volume fractions of the σ phase are similar with and without CR15.

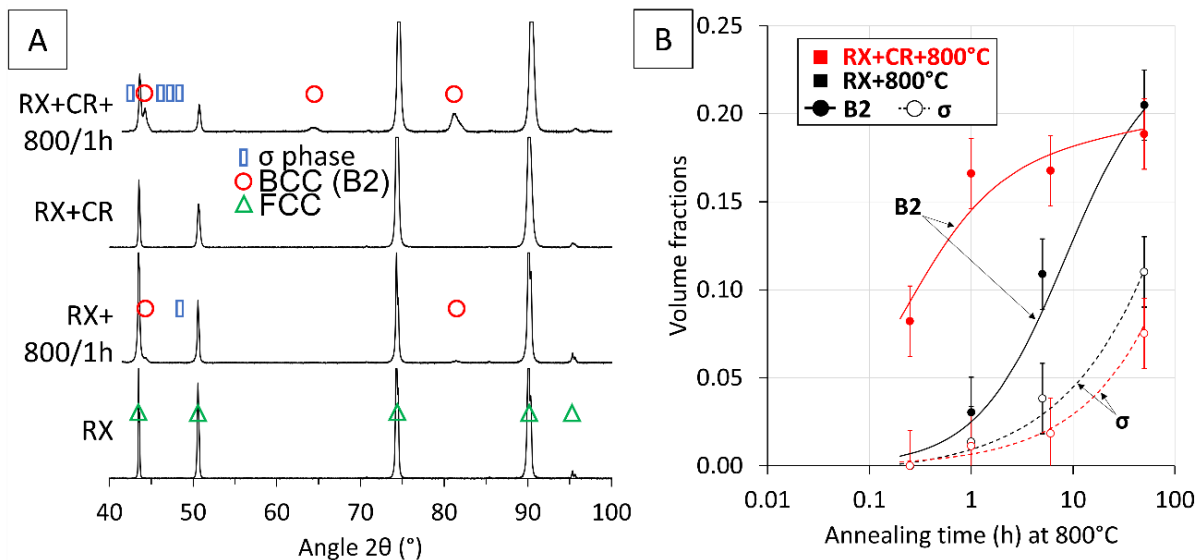


Fig. 5.7 (A) XRD diffractograms measured after RX, RX+800/1h, RX+CR and RX+CR+800/1h. (B) Volume fractions of the B2 phase and σ phase in RX+800°C (in black) and of RX+CR+800°C (in red), calculated from the XRD diffractograms after annealing durations ranging from 15 minutes to 50 hours. [Full-size](#).

5.2.3. Tensile properties

Fig. 5.8 presents the tensile curves at four stages of the processing route. The true stress – true strain curves are given in solid lines in **Fig. 5.8A** and **Fig. 5.8B**. WHR is shown in dotted lines in **Fig. 5.8B**. The features of the corresponding microstructures are given in **Table 5.3** along with the corresponding tensile properties.

The RX material (in grey) presents a low YS of 380 MPa but considerable work-hardening capacity (WHR, which is the difference between maximum tensile stress and YS) and uniform elongation of 560 MPa and 24%, respectively. Tensile properties remain unchanged with the addition of the aging step of 1 hour at 800°C (RX+800/1h).

The material after RX+CR (in orange) presents an increased YS of 760 MPa but with decreased WHR and ductility, i.e. 110 MPa and 13%. Finally, the RX+CR+800/1h condition presents a YS of 880 MPa coupled to a work-hardening capacity of 560 MPa and a uniform elongation of 15%.

Chapter 5 – DEVELOPMENT OF MICROSTRUCTURES WITH INCREASED WORK-HARDENING
THROUGH INTRAGRANULAR PRECIPITATION

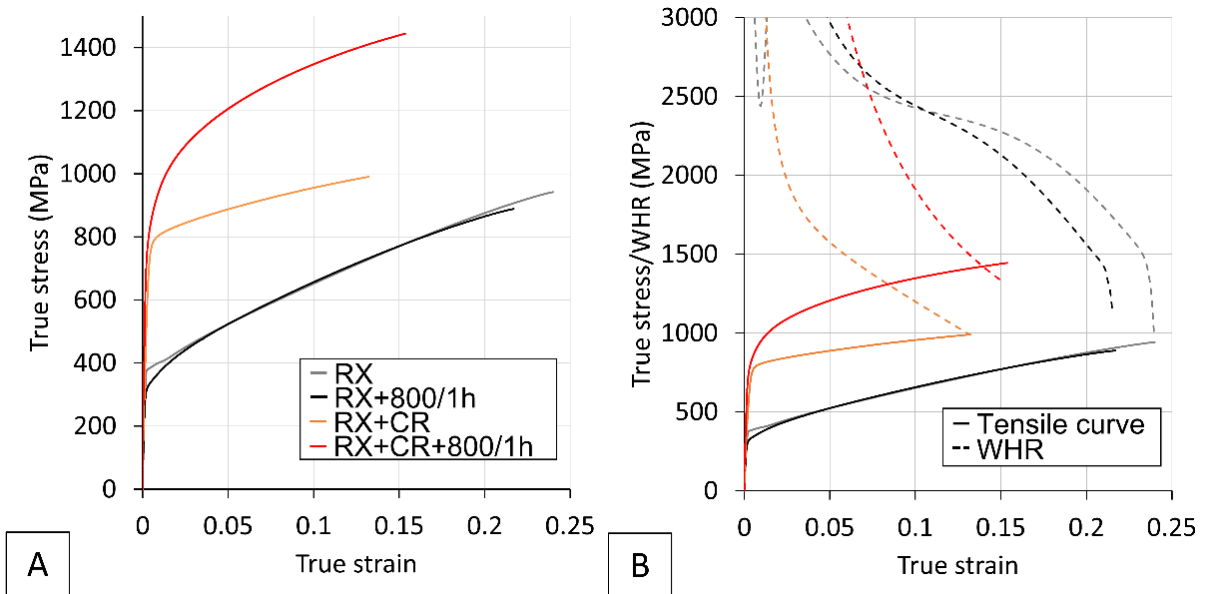


Fig. 5.8 Tensile properties of RX (in grey), RX+800/1h (in black), RX+CR (in orange) and RX+CR+800/1h (in red). (A) True stress – true strain curves (solid lines). (B) The curves of WHR are superimposed (dotted lines). The reader is referred to **Table 5.3** for further details on the corresponding microstructural features and tensile properties. [Full-size](#).

Table 5.3 Microstructural features of the four microstructure states of C+Al characterized in tension. The tensile properties of each state are also given.

Microstructure	Volume fractions		Yield strength (YS) (MPa)	Maximum tensile stress (MPa)	Uniform elongation	WHC (MPa)
	B2	σ				
RX (grey curve)	0	0	380	940	0.24	560
RX+800/1h (black curve)	0.03	0.01	330	890	0.22	560
RX+CR (orange curve)	0	0	755	990	0.13	235
RX+CR+800/1h (red curve)	0.17	0.01	880	1440	0.15	560

We will now turn to the discussion. It is divided into two parts. The first part deals with precipitation. It focuses on the intragranular precipitates, their formation, their chemistry and nature. The second part treats of the work-hardening behaviour of RX+800/1h and then of RX+CR+800/1h. The work-hardening behaviour of RX+CR+800/1h is modelled in order to understand the contributions of the different hardening mechanisms.

5.3. Discussion

5.3.1. Precipitation

The distinguishing feature of the microstructure of C6Al induced when a second cold rolling step (CR15) is applied between RX and precipitation aging (RX+CR+800/1h), is that it contains a fine distribution of needle shaped precipitates inside the FCC grains. These intragranular precipitates add to the B2 and σ precipitates located at grain boundaries which also form when aging is performed directly after recrystallization (RX+800/1h). The activation of intragranular precipitation in RX+CR+800/1h echoes with the accelerated precipitation of the B2 phase (**Fig. 5.7B**). Indeed, volume fractions larger than 10% are reached after 20 minutes in RX+CR+800°C, while more than 6 hours – 18 times more – are required without CR15. Diffraction and EDS analyses in the TEM showed that these intragranular precipitates are B2 (**Fig. 5.6**) in agreement with the calculated phase diagram (**Fig. 5.1**). Furthermore, the preferred distribution of the intragranular precipitates along specific directions in the deformed FCC microstructure (**Fig. 5.4C**) suggests their heterogeneous nucleation on dislocations⁹².

In addition, few B2 precipitates formed on twin boundaries. In the new TMT developed in this chapter, the cold rolling step preceding aging presents a thickness reduction of 15%, compared to 80% in chapter 3. It results in a much smaller twinning activity (if any) during rolling. Hence, most of the intragranular B2 precipitates formed on dislocations in the bulk as illustrated by **Fig. 5.4C** and **Fig. 5.5B**.

The fractions of the σ phase obtained by XRD (**Fig. 5.7B**) show a radically different evolution compared to that of the B2 phase. This suggests that the σ phase does not form on dislocations, as confirmed by TEM observations (**Fig. 5.6**), but is restrained to grain boundaries (**Fig. 5.4**). Gwalani *et al.*⁶⁵ rationalized this behaviour in Al_{0.3}CoCrFeNi by invoking the higher energy barrier for the nucleation of σ from the supersaturated FCC matrix in comparison to B2. Moreover, according to CALPHAD calculations, a lower onset driving force for nucleation from the supersaturated FCC phase of composition C6Al is observed for the σ phase (**Fig. 5.9**). These two elements confirm that the formation of the σ phase is restrained to grain boundaries. It is confirmed when comparing its fractions measured in RX+800/1h or RX+CR+800/1h (**Fig. 5.7B**) with those obtained when the aging step is performed directly after cold rolling – without RX –, as was performed in chapter 3. In the latter case, interactions between recrystallisation and precipitation during aging result in FCC grain sizes below 5 μm (c.f. **Fig. 3.7**). The larger boundary area results in an increase in the formation kinetics of the σ phase, with a fraction 10 times larger after 1 hour at 800°C. Because of the lower grain boundary area in RX+CR+800/1h – FCC grain size of 32 μm –, a slowdown of the precipitation kinetics of the σ phase is observed.

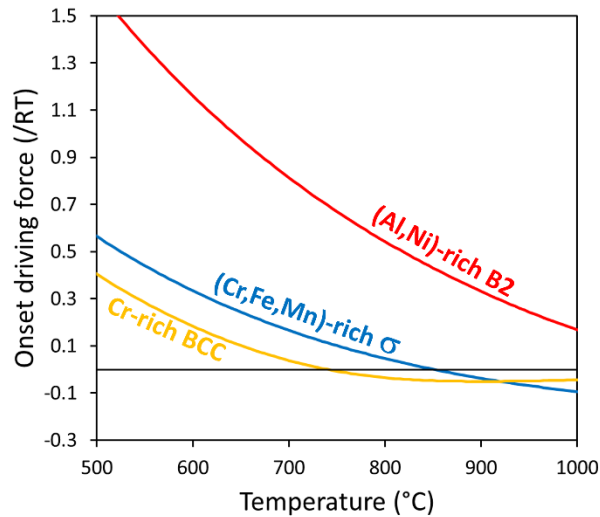


Fig. 5.9 Normalized onset driving forces for the nucleation of various phases from the FCC matrix in C6Al, calculated using ThermoCalc and the TCHEA4 thermodynamic database. [Full-size](#).

The kinetics of precipitation of B2 and σ can be qualitatively captured on the calculated isothermal transformation diagram (or TTT diagram) shown in **Fig. 5.10**. The two solid C-shaped curves represent the time required at each temperature for the initiation of the bulk precipitation of B2 and grain boundary precipitation of σ . The formation of B2 is favoured at high temperatures, while the precipitation of σ occurs at lower temperatures. There is a large overlap of the B2 and σ curves at intermediate temperatures (in purple) delimiting a temperature-time region where the precipitations of both phases are concurrent. The thermal treatment at 800°C for 1h applied on C6Al in the present work falls right in that region which explains why we observed both the precipitation of B2 and σ . Moreover, **Fig. 5.10** illustrates the effects of the number of nucleation sites on the transformation kinetics. When the number of bulk nucleation sites (e.g. the density of dislocations) is lowered (red arrow), the intragranular precipitation of B2 requires longer time to begin. Likewise, the time necessary for the σ grain boundary precipitation to start is slowdown when the grain size of the FCC supersaturated solid solution is increased (blue arrow).

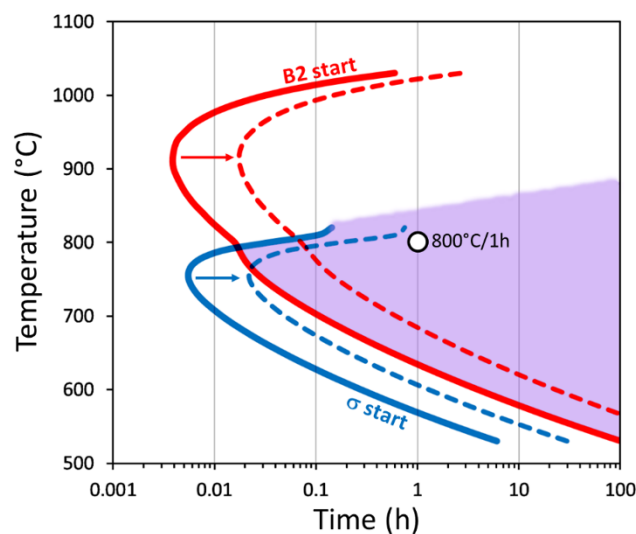


Fig. 5.10 Isothermal transformation diagram for the concurrent precipitation of B2 in bulk and σ at the grain boundaries from the supersaturated FCC C6Al, calculated using the TCHEA4 thermodynamic database and the MOBHEA2 mobility database. The solid red and blue C-shaped curves represent temperature-time combinations for the beginning of precipitation of B2 and σ , respectively. The purple-coloured area shows the temperature-

time combinations for concurrent precipitation of B2 and σ . The discontinuous curves show the slowdown of the kinetics of the bulk precipitation of B2 and the grain boundaries precipitation of σ with decreasing the number of bulk nucleation sites (e.g. dislocation density) and increasing the grain size, respectively. [Full-size](#).

Chromium enriched BCC is another microstructural product that might form in C6Al (**Fig. 5.9**) but that is not revealed by the simulation of the precipitation processes in **Fig. 5.10** nor in the phase diagram of **Fig. 5.1**. Its presence was assessed in $\text{Al}_{0.3}\text{CoCrFeNi}$ after annealing treatments performed between 550°C and 900°C ^{66,254}.

In C6Al, it was not experimentally observed after 1 hour at 800°C. Instead, it was experimentally observed with atom probe tomography (**Fig. 5.11B**) in a sample of C6Al annealed for 1 hour at 700°C (RX+CR+700/1h). This phase contains 80 at.% of chromium (**Fig. 5.11D**). Such high chromium content does not correspond to the σ phase which typically contains 30-50 at.% of chromium ^{65,237}. Instead, it corresponds to the chromium contents measured in the BCC phase enriched in chromium observed in $\text{Al}_{0.3}\text{CoCrFeNi}$ ^{66,254}. Its formation at 700°C but not at 800°C in C6Al agrees with the calculation of its onset driving force for nucleation (**Fig. 5.9**) indicating a positive driving force below 740°C. This phase could be an intermediate phase between σ and B2.

Moreover, these results confirm the presence of the B2 phase (**Fig. 5.11A and C**) as its composition matches that of previously reported B2 grains ^{65,92}. There is no sign of an enrichment in chromium in the FCC phase at the FCC/B2 interface that would support the explanation of the formation of σ phase given in chapter 3. The APT measurement were performed after annealing at 700°C, different from the 900°C used in chapter, which could explain this discrepancy.

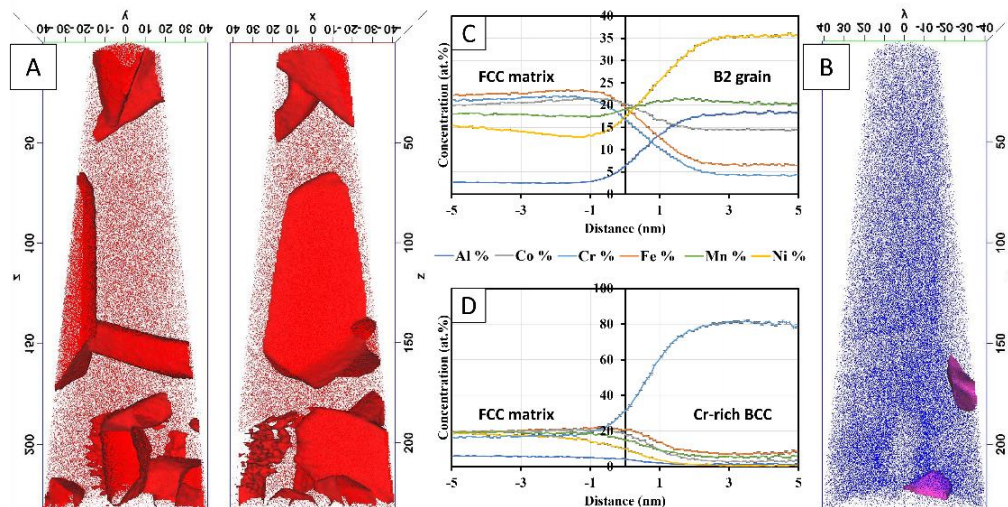


Fig. 5.11 Results from atom probe tomography showing the 3D reconstructions of (A) Al and (B) Cr ions. (C-D) give the composition profiles across B2 and a Cr-rich BCC interfaces, respectively. [Full-size](#).

5.3.2. Work-hardening behaviour

The tensile properties measured on the four conditions (**Fig. 5.8A**) evidence the large work-hardening capacities that are attained by RX, RX+800/1h and RX+CR+800/1h despite different microstructures. Interestingly, their work-hardening capacities are similar, i.e. around 560 MPa. However, the WHR of RX and RX+800/1h differ from that of RX+CR+800/1h (**Fig. 5.8B**), suggesting different deformation mechanisms.

RX and RX+800/1h

The observation of a plateau on the WHR curves of RX and RX+800/1h is typical from the activation of an additional deformation mechanism during tensile testing ¹¹⁶. In order to precise the nature of this additional mechanism, microstructural characterisation in SEM was performed on RX, RX+800/1h and RX+CR+800/1h specimens after tensile testing until fracture (**Fig. 5.12**). It revealed the presence of mechanical twins in RX and RX+800/1h (indicated by red arrows in **Fig. 5.12A-B**) but none in RX+CR+800/1h (**Fig. 5.12C**). The activation of mechanical twinning was already observed after tensile testing in similar materials, such as CoCrFeMnNi ^{31,48}, and after rolling and tensile testing of C+Al (c.f. chapters 3 and 4) ²¹⁰, both at room temperature. It is hence not surprising to observe the activation of mechanical twinning after tensile testing in RX and RX+800/1h.

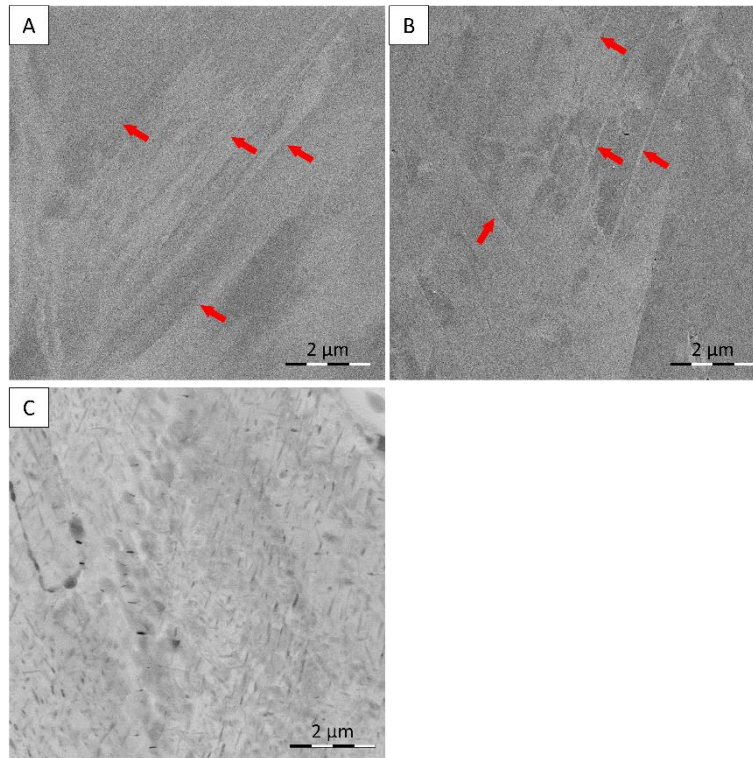


Fig. 5.12 BSE SEM image revealing the presence of mechanical twins after tensile testing of (A) RX and (B) RX+800/1h. Red arrows indicate mechanical twins. [Full-size](#).

RX+CR+800/1h

RX+CR+800/1h presents a YS of 880 MPa, 2.7 times larger than that of RX+800/1h. Despite this significant increase in YS, the same level of WHC, i.e. 560 MPa, is maintained. It is unlikely that this WHC is due to the activation of mechanical twinning, as it is the case for RX+800/1h, as the typical plateau in WHR is not observed (dotted red curve in **Fig. 5.8**) ²²⁵. Moreover, no mechanical twin was observed after tensile testing until fracture (**Fig. 5.12C**). This is not surprising as the length scale over which twins can form is greatly reduced by the presence of intragranular precipitates. It is clearly illustrated by the comparison between **Fig. 5.12A-B** and **Fig. 5.12C**. Mechanical twins are known to form more difficulty as the grain size decreases ¹³¹.

The direct comparison between the tensile curves of RX+CR (in orange) and of RX+CR+800/1h (in red) (**Fig. 5.8A**) evidences a large gain in WHR, WHC and in maximum tensile stress, all due to the aging step at 800°C. These evolutions result from the combination of two mechanisms: the partial recovery of the FCC matrix and the intragranular precipitation inside the FCC matrix. The effect of precipitation on grain boundaries is considered negligible as it changes only slightly the tensile behaviour of RX+800/1h

(in black) compared to RX (in grey). Moreover, as shown in chapter 4, the strengthening effect due to grain boundary precipitates is strongly related to their volume fraction. In the case of RX+CR+800/1h, it is found at 3%, if considered equal to that measured in RX+800/1h. It is considered low enough to be neglected.

In order to understand the respective roles of static recovery and intragranular precipitation and to identify the different contributions to work-hardening, the flow stress of RX+CR+800/1h is modelled. The model is based on the formalism of Kocks²⁴⁰ presented in chapter 4 and is extended to non-zero plastic strain based on the publication from Fribourg *et al.*²⁴⁹.

It includes microstructural features such as the initial dislocation density and its evolution, the precipitate volume fraction and dimensions. Only intragranular precipitates are considered. As they are incoherent with the matrix and formed mainly in the bulk on dislocations, the model will focus on precipitation strengthening due to the Orowan looping mechanism. This mechanism involves the multiplication of geometrically necessary dislocations (GND) around precipitates and their organisation as loops. The mathematical background of the model is presented below. It is then applied to RX+CR+800/1h.

In presence of intragranular precipitates in FCC grains, the flow stress σ_f can be approached by the sum of the following contributions²⁴⁰:

$$\sigma_f = \sigma_{FCC} + \sigma_{KIN} + (\sigma_{ISO}^m + \sigma_{PPT}^m)^{\frac{1}{m}} \quad (\text{Eq. 5.2})$$

As dislocations and precipitates present similar strength but different densities, the parameter m takes the value of 2 according to the theory established by Kocks^{240,255}.

(1) The contribution due to the FCC matrix σ_{FCC} includes the intrinsic strength of the matrix, the solid solution strengthening, both included in σ_0 , and the Hall-Petch strengthening related to the grain size of the FCC matrix d_{FCC} . σ_{FCC} is given below with K_{FCC} the Hall-Petch constant:

$$\sigma_{FCC} = \sigma_0 + \frac{K_{FCC}}{\sqrt{d_{FCC}}} \quad (\text{Eq. 5.3})$$

(2) The kinematic contribution σ_{KIN} corresponds to the back-stress resulting from the presence of loops around the precipitates. It is expressed as a composite law with the precipitate volume fraction f_V . The stress induced by the presence of loops is given as a Hooke's law²⁵⁶. It gives:

$$\sigma_{KIN} = \frac{f_V}{1 - f_V} E_P \varepsilon_*^P = \frac{f_V}{1 - f_V} E_P \frac{bn}{2rM} \quad (\text{Eq. 5.4})$$

with E_P the Young's modulus of the precipitates, ε_*^P the unrelaxed plastic strain associated with the formation of Orowan loops, n the number of loops stored around each precipitate, b the norm of the Burgers vector, r the precipitate radius, and M the Taylor factor. It must be noted that the expression from²⁴⁹ was normalized by a factor $(1 - f_V)$ due to the large value of f_V , i.e. $(1 - f_V)$ significantly different from 1.

The number of loops stored around precipitates is defined by, with ε^P the true plastic strain²⁵⁶:

$$n = n^* \left(1 - \exp \left(- \frac{2rM}{bn^*} \varepsilon^P \right) \right) \quad (\text{Eq. 5.5})$$

The number of loops saturates at the value n^* at large strain.

(3) The isotropic contribution σ_{ISO} includes the interactions between dislocations. It is based on the Taylor relation $\sigma = \alpha G_M b M \sqrt{\rho}$, with α the Taylor constant and ρ the density of dislocations. In the present case, two distinct dislocation densities must be considered: the density of SSDs ρ_S and the density of GNDs ρ_P .

In the case of spherical precipitates, ρ_P is expressed as the product of the precipitate density $3f_V/4\pi r^3$, the length of a loop $2\pi r$ and the number of loops around a precipitate n .

$$\rho_P = \frac{3f_V}{2r^2} n \quad (\text{Eq. 5. 6})$$

The evolution of the density of SSDs ρ_S in function of true plastic strain ε^P in a material without precipitates is given by:

$$\frac{\partial \rho_S}{\partial \varepsilon^P} = M(k_1 \sqrt{\rho_S} - k_2 \rho_S) \quad (\text{Eq. 5. 7})$$

with k_1 a constant associated with the rate of dislocation generation and k_2 a constant associated with the rate of dynamic recovery (DRV). In a precipitation-free material, this relation, along with the Taylor relation, allows to deduce the equation of the WHR ($\theta = d\sigma/d\varepsilon^P$):

$$\theta = \frac{M^2 \alpha G_M b k_1}{2} - \frac{M k_2}{2} (\sigma_f - \sigma_Y) \quad (\text{Eq. 5. 8})$$

with σ_f the flow stress and σ_Y the YS. In presence of precipitates, it remains valid at large values of $(\sigma_f - \sigma_Y)$ where the number of loops stored around precipitates saturates. In this case, the parameter k_2 is however changed to k_2^0 . As will become clear below, the parameter k_2 is split in two in presence of precipitates.

In the presence of precipitates, dislocation loops influence DRV. Indeed, if the lattice is strongly strained by the presence of a precipitate, the stress fields of the loops would help dislocations to cross-slip, resulting in enhanced DRV²⁴⁹. This is implemented by including in k_2 the probability that two dislocations annihilate without being helped by a dislocation loop. This probability equals $\exp(-l_0/\lambda_P)$ with l_0 the distance between two mobile dislocations which equals $\rho_S^{-0.5}$ and λ_P the inter-precipitate distance given by $\lambda_P = 2r(\sqrt{\pi/4f_V} - 1)$ ²⁵⁷. The parameter k_2 then becomes:

$$k_2 = k_2^0 \exp\left(-\frac{l_0}{\lambda_P}\right) + k_2^P \left(1 - \exp\left(-\frac{l_0}{\lambda_P}\right)\right) \quad (\text{Eq. 5. 9})$$

The evolution of ρ_S is hence the solution of the differential equation Eq. 5.7 coupled to Eq. 5.9. It takes as initial condition ρ_0 at $\varepsilon^P = 0$ which corresponds to the density of dislocations introduced by the intermediate cold rolling state and partially restored during aging.

(4) The strengthening contribution due to intragranular precipitates σ_{PPT} is computed from the measured yield strength σ_Y and Eq. 3 at $\varepsilon^P = 0$ ²⁴⁹.

$$\sigma_{PPT} = \sqrt{(\sigma_Y - \sigma_{FCC})^2 - \sigma_{ISO}^2} \quad (\text{Eq. 5. 10})$$

This mode of calculation was chosen to limit the errors coming from the coupling of models and such that the simulation of the flow stress starts at the experimental value of the YS.

This finally gives the following relation for the flow stress:

$$\begin{aligned}\sigma_f &= \sigma_{FCC} + \sigma_{KIN} + \sqrt{\sigma_{ISO}^2 + \sigma_{PPT}^2} \\ &= \sigma_0 + \frac{K_{FCC}}{\sqrt{d_{FCC}}} + \frac{f_V}{1-f_V} E_P \frac{bn}{2rM} + \sqrt{\left(\alpha G_M b M \sqrt{\rho_S + \frac{3f_V}{2r^2} n} \right)^2 + \sigma_{PPT}^2}\end{aligned}\quad (\text{Eq. 5.11})$$

To summarize, intragranular precipitates influence work-hardening in three ways:

- i. Dislocation loops result in a back-stress in the surrounding FCC matrix inducing a kinematic contribution to the flow stress;
- ii. GNDs interact and induce a new isotropic contribution;
- iii. The loop stress fields influence dRV.

The constants used to model the flow stress of RX+CR+800/1h are given in **Table 5.4**. Several precisions are needed regarding these parameters.

- The Young's modulus of the intragranular B2 precipitates is calculated from their shear modulus with the relation $E_P = 2G_P(1 + \nu_P)$, with ν_P the Poisson's ratio of the precipitates considered equal to that of the FCC matrix.
- The model takes as input the volume fraction of intragranular precipitates, f_V . It is determined as the subtraction of the volume fraction of B2 phase at grain boundaries, assumed equal to that in RX+800/1h, from the total volume fraction of B2 phase in RX+CR+800/1h. Both are measured from XRD (**Fig. 5.7B**).
- The elongated intragranular precipitates are considered as cylindrical. Their equivalent radius is given by $r = l/2 * \sqrt[3]{3L/2l}$, with l and L the short and long axes of the 3D precipitates ²⁴⁵.
- The parameters k_1 and k_2^0 are determined from Eq. 5.8 on the experimental plot WHR versus true plastic stress at large stress values.
- The parameters k_2^P and n^* are determined by applying a root mean square (RMS) routine to the experimental tensile curve using Matlab software. Ranges of these two parameters are scanned, starting with large ranges and low resolution, and reducing ranges and increasing resolution as the deviation between the experimental and modelled curves becomes smaller.

Table 5.4 List of the parameters used in the model.

Symbol	Parameter	Value	Origin
σ_0	Intrinsic strength of the FCC matrix (Al _{0.3} CoCrFeNi)	172 MPa	244
K_{FCC}	Hall-Petch constant (Al _{0.3} CoCrFeNi)	730 MPa.√μm	244
d_{FCC}	Mean grain size of the FCC matrix	32 ± 5 μm	EBSD
G_P	Shear modulus of the precipitates	80 MPa	250
G_M	Shear modulus of the FCC matrix	81 GPa	243
f_V	Volume fraction of intragranular precipitates	14 ± 2%	XRD
r	Mean radius of the precipitates	80 ± 10 nm	TEM
λ_P	Inter-precipitate distance	230 ± 45 nm	257
ρ_0	Initial dislocation density	4.5 ± 0.5 10 ¹⁴ /m ²	XRD
b	Norm of the Burgers vector	0.2540 ± 0.0005 nm	XRD
ν	Poisson's ratio	0.25	251
M	Taylor's factor	3.063	
α	Taylor's constant	0.25	113
k_1	Constant related to the generation of dislocations	2.5*10 ⁸ /m	Fit
k_2^0	Constant related to dRV without help from loops	5.2	Fit
k_2^P	Constant related to dRV with help from loops	-55	RMS
n^*	Maximum number of loops around a precipitate	10	RMS

We will now turn to the application of the model to RX+CR+800/1h. First, a focus is given to the YS to evaluate the influence of the multiple strengthening mechanisms. Then, work-hardening will be discussed.

Table 5.5 gives the contributions of the different strengthening mechanisms to the YS, i.e. at $\varepsilon^P = 0$, and at uniform elongation. The error range of the model is calculated from the standard deviations of the measured parameters (**Table 5.4**).

Table 5.5 Contributions from the strengthening mechanisms in RX+CR+800/1h calculated with the model at plastic true strains of 0, i.e. at yield stress, and at maximum plastic true strain. The contributions corresponding to the model computed without including precipitates are also added.

Precipitation ε^P	With		Without
	0	0.15	0.15
FCC	297	297	297
KIN	0	158	-
ISO	334	861	619
PPT	480	480	-
Total	882	1442	916
Error	140	-	-
Measured	882	1445	-

The results of the modelling approach applied to RX+CR+800/1h are presented in **Fig. 5.13**, along with the experimental data (in black). The model is applied in two ways: with and without including precipitates, in red and green, respectively. These two variations are referred to as respectively “w/ Pcp” and “w/o Pcp” on the figure. The former case corresponds to Eq. 5.11, while in the latter case, the model reduces to $\sigma_f = \sigma_{FCC} + \sigma_{ISO}$. The same constants are used in both cases (**Table 5.4**).

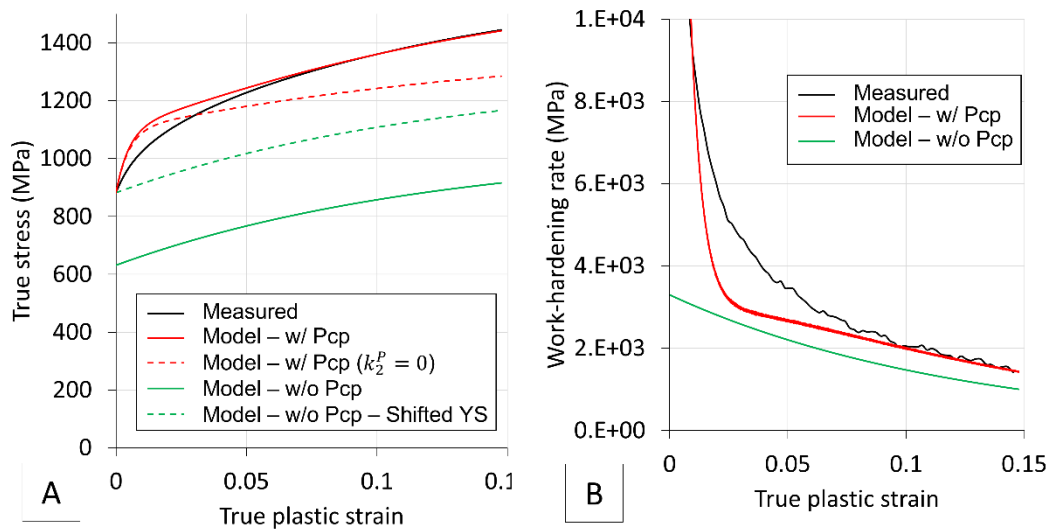


Fig. 5.13 Results of the model for RX+CR+800/1h. (A) True stress-true strain curves. The measured curve is given in black and the model including precipitates in red (w/ Pcp). In dotted red is given the model including precipitates but with the constant $k_2^P = 0$. The solid green line corresponds to the same model without considering precipitates (w/o Pcp). For comparison purposes, the dotted green line is shifted compared to the solid green line such that its YS matches that of the red curve. (B) WHR curves. [Full-size](#).

The tensile curve obtained with the model including precipitates (solid red curve) agrees well with the experimental tensile curve (solid black curve) (**Fig. 5.13A**). This good agreement between model and experiment is also found on the WHR curves (**Fig. 5.13B**). In **Fig. 5.13A**, the direct comparison between the solid red and the dotted green curves suggests the large influence of precipitates on the work-hardening behaviour of RX+CR+800/1h. The WHC without including precipitates is 282 MPa compared to 560 MPa as measured experimentally. Hence, half of the WHC of the material is attributed to the presence of intragranular precipitates. Moreover, the WHC of RX+CR is 236 MPa (**Fig. 5.13A**). Hence, static recovery results in a gain in WHC of 46 MPa. The influence of intragranular precipitates on work-hardening is definitely larger than that from static recovery. The influence of precipitates can be decomposed in three contributions discussed next: the influence of precipitates on dRV, the formation of GNDs and the kinematic contribution.

The model first gives insight on the balance between the generation of SSDs and dRV in RX+CR+800/1h through the constants, k_1 , k_2^0 , k_2^P . The two first constants are similar to those reported by Fribourg *et al.*²⁴⁹ from which the model is inspired. This suggests that, without considering precipitation, AA7449 alloy and Al_{0.3}CoCrFeMnNi present a similar balance between generation of SSDs and dRV.

The sign of k_2^P is however different. In the study by Fribourg *et al.*, it is positive with a value of +70. This was correlated to the strong stress fields associated to dislocation loops around precipitates that favour cross-slip and hence dRV. In the present case, k_2^P is negative with a value of -55. This value indicates that the dislocation loops do not favour cross-slip but “capture” mobile dislocations in their tangles, limiting dRV. This can be correlated to stress fields of lower intensity created by dislocation loops around precipitates. Their intensity depends on the difference in shear moduli ΔG between matrix and precipitate. The value of ΔG is three times larger in²⁴⁹ compared to this study suggesting larger stress fields, agreeing with a larger value of k_2^P in²⁴⁹.

At the author best knowledge, nothing alike was reported before in conventional nor multicomponent alloys. To better highlight the influence of this negative k_2^P on the tensile curve, the model was iterated with the same constants except from a $k_2^P = 0$. The result is a much lower WHC than the model with a negative value of k_2^P (comparison between dotted and solid red lines in **Fig. 5.13**). This is due to the

direct influence of the negative value of k_2^P on the density of SSDs ρ_S as observed in **Fig. 5.14** when comparing solid red and green curves. The presence of precipitates results in the doubling of the density of SSDs at maximum tensile stress that reaches $2.7 \cdot 10^{15} / \text{m}^2$. Even if this value seems rather high, it is highly dependent on the choice of the parameters of the Taylor equation, i.e. the Taylor constant α , the shear modulus of the matrix G_M and the Taylor factor. These parameters were chosen in agreement with literature but the values chosen might not reflect the exact behaviour of C+Al. The important point here is the relative analysis of dislocation densities with an increase of the density of SSDs with the presence of precipitates.

More than the precise value of k_2^P , this comparison indicates the activation of a mechanism – different from conventional dislocation glide – providing a constant work-hardening during the deformation of RX+CR+800/1h. This mechanism is certainly related to the intragranular precipitates as no sign of it was observed in RX nor in RX+800/1h. Hence, it seems not linked to the multicomponent structure of C6Al, as confirmed by the standard values found for the constants k_1 and k_2^0 . Additional tests, such as Bauschinger tests, should be performed in order to precise the true nature of this mechanism.

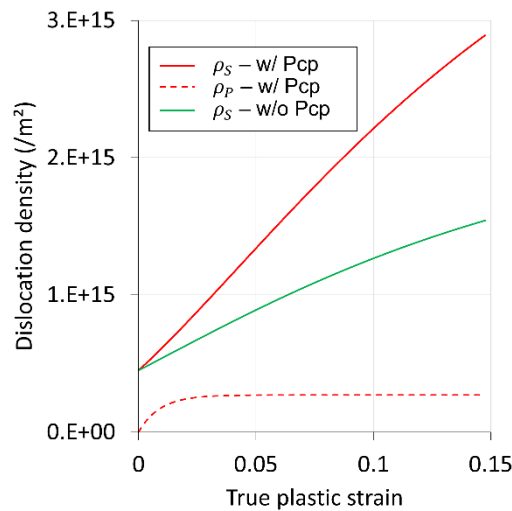


Fig. 5.14 Evolution of dislocation densities versus true plastic strain. The solid red line corresponds to the evolution of ρ_S in the model including precipitates and the dotted red line to the evolution of ρ_P . The green curve gives the evolution of ρ_S without considering precipitates. [Full-size](#).

The model also allows the isotropic contribution from GNDs to be estimated. This phenomenon is implemented in the model through the additional dislocation density ρ_P , which depends on the precipitate dimensions and volume fraction and on the mean number of loops stored around each precipitate, represented by n . A value of 10 for the maximum number of loops n^* was found in this study. This value is slightly larger than that of 9 reported by Fribourg *et al.*²⁴⁹ and considerably lower than that of 60 reported in²⁵⁶. The capacity of precipitates to store dislocation loops depends primarily on their aspect ratio, being larger for more elongated precipitates. A n^* value of 60 was indeed reported for precipitates with an aspect ratio of 45 whereas the value of 9 was reported for an aspect ratio around 3. In this study, the aspect ratio of 9 would suggest a n^* value of 16 larger from the value of 10 found. The larger size of B2 precipitates could be a limiting factor.

This n^* value translates in a GND density nine times lower than that of SSDs at maximum tensile stress (**Fig. 5.14**). The coupling of SSDs and GNDs results in an isotropic contribution of 527 MPa at maximum tensile stress compared to 285 MPa without including precipitates (**Table 5.5**).

Finally, the model sheds some light on the intensity of the back-stress applied by the dislocation loops on the FCC matrix. It contributes to 158 MPa of the total flow stress at maximum tensile stress.

This assessment highlights the relative intensities of the three strengthening mechanisms due to precipitation. The increase in the density of SSDs contributes most, while the interactions between GNDs and SSDs contribute less. Their sum is however non negligible and represents half of the WHC of the material, emphasizing the important influence of precipitation on work-hardening behaviour in RX+CR+800/1h. To conclude, the presence of intragranular precipitates in RX+CR+800/1h permits to free from the paradigm stating that WHC decreases as the YS increases. Indeed, the same level of WHC is maintained in RX+CR+800/1h compared to RX+800/1h although the YS is multiplied by 2.7.

Conclusions

An innovative thermomechanical route was developed in the aim of increasing work-hardening through the activation of intragranular precipitation. It includes an intermediate cold rolling step between the recrystallisation treatment and the aging step. It is applied to C+Al. The addition of this intermediate cold rolling step results in the heterogeneous nucleation of elongated precipitates on dislocations, inside the FCC grains of the matrix. These precipitates were shown to be B2 in agreement with the calculated phase diagram. The σ phase is also present but is restricted to FCC grain boundaries. The presence of intragranular precipitates results in both significant strengthening and work-hardening capacity, respectively 880 MPa and 560 MPa after aging at 800°C for 1 hour. Its flow stress evolution and work-hardening behaviour were modelled in order to decorelate the different contributions of the various strengthening mechanisms. Interestingly, intragranular precipitates contribute to 30% of yield strength and to 50% of the work-hardening capacity at ultimate tensile stress. Even if the precise mechanisms at the origin of this interesting behaviour remain to be discovered, kinematic hardening along with interactions between precipitates and dislocations could be involved.

These results show the beneficial effect of the addition of an intermediate cold rolling step during TMT of C+Al. It also gives a new understanding of the role of intragranular precipitates on tensile properties through the implementation of an analytical model.

Chapter 6.

WHAT MAKES CANTOR AND C6AL SO SPECIAL (OR NOT)

Introduction

Since the first developments of multicomponent alloys (MCA) in 2005^{3,5}, more and more interest has been drawn to this new field. The four core effects from Yeh et al.⁴ attribute to MCAs specific – and theoretical – features that would result in their superior properties compared to conventional alloys. In practice, specific MCAs proved equal or even superior to conventional alloys, but no consensus has been drawn so far on the true originality of MCAs⁸. Few studies proposed to compare conventional and MCAs in order to assess the influence of the complex chemistry of the latter^{74,198,200}. These studies conclude, when comparing MCAs of various complexity to pure nickel, that the chemical complexity of alloys has an influence on multiple properties, such as strength, thermal and electrical resistance, etc.⁴, most probably through lattice distortion. However, there is no direct link between the number of elements and properties. The choice of the elements more than their number influences these properties¹¹.

Going forward from pure nickel, this study proposes to compare Cantor's alloy to an austenitic stainless steel of grade 304L, widely known and used in industry. This last material was chosen due to its similar chemical composition, i.e. presence of chromium, iron, manganese and nickel; similar microstructure, both of them being single-phase FCC in a wide temperature range; similar stacking fault energy (SFE); but also due to its availability in the lab. Other alloys meeting these criteria such as nickel-based alloys could also have been chosen. More than assessing the effect of chemical complexity, this study aims to evaluate the relative performances of Cantor's alloy when compared to a widely known reference.

Cantor's alloy has been widely studied since the development of MCAs. This is partly due to its single-phase FCC microstructure²⁵. More recently, it was used as a base alloy for further chemical optimisation, in the same way as iron and nickel were used to develop steels or nickel-based alloys. Two promising alloying strategies proved to be the addition of carbon^{83,85}, similarly as in steels, or of aluminium^{39,65}, similarly as in Ni-Al compounds. This second option is widely discussed in the previous chapters of this manuscript with the compositions C+Al. In order to assess the influence of these two alloying strategies, C6Al and a carbon-containing Cantor's alloys are also compared.

In this chapter, 304L, Cantor's alloy, C6Al and a carbon and nitrogen-enriched Cantor alloys are compared. This comparison treats of the deformation mechanisms during rolling and tensile testing along with recrystallisation and grain growth kinetics.

6.1. Materials and methods

6.1.1. Materials

Four materials with distinct chemical compositions are studied:

- An austenitic stainless steel of grade 304L. It will be referred to as 304L.
- CoCrFeMnNi, called Cantor alloy and referred to as Cantor.
- C6Al with the ingot n°2.
- Cantor alloy with addition of carbon and nitrogen. It is referred to as C+C.

Ingots of the MCAs were cast in a vacuum induction furnace in the facilities of the IMAP laboratory of the *Université catholique de Louvain*. Different ferromanganese alloys were used for casting of Cantor, C6Al and C+C resulting in different carbon and nitrogen contents. The samples from 304L originate from a bar bought from a steel manufacturer.

The chemical composition of the four materials were measured by ICP-OES (**Table 6.1**). The lighter elements, i.e. carbon, nitrogen and oxygen, were quantified using a combustion analyser. The four materials contain similar fractions of small elements except from the large oxygen content of the Cantor alloy and the considerable carbon and nitrogen content of C+C.

Table 6.1 Chemical compositions of the four studied materials, in atomic percent.

(at.%)	304L	Cantor	C6Al	C+C
Al	0	0	5.8 ± 0.1	0
Co	0	19.7 ± 1.0	19.1 ± 0.2	19.7 ± 0.0
Cr	18.6 ± 0.1	18.7 ± 0.5	17.9 ± 0.1	18.7 ± 0.2
Fe	69.3 ± 0.9	20.8 ± 0.3	18.8 ± 0.1	21.8 ± 0.5
Mn	1.6 ± 0.0	18.8 ± 1.3	19.1 ± 0.2	18.3 ± 0.3
Ni	9.3 ± 0.0	21.6 ± 1.3	19.3 ± 0.1	20.3 ± 0.0
C	0.13 ± 0.01	0.14 ± 0.03	0.12 ± 0.03	0.70 ± 0.30
N	0.13 ± 0.02	0.03 ± 0.01	0.10 ± 0.03	0.52 ± 0.20
O	0.07 ± 0.01	0.49 ± 0.10	0.02 ± 0.00	0.07 ± 0.01
Cu	0.2 ± 0.0	0	0	0
Mo	0.1 ± 0.0	0	0	0

6.1.2. Processing

Materials were processed according to the route CR detailed in chapter 3. Cold rolling (CR) was performed at room temperature for the Cantor alloy, C+C and C6Al for a thickness reduction of 80%. It was performed at 200°C for 304L. The increase of the rolling temperature for 304L limits the phase transformation to martensite during deformation. Annealing treatments were then performed at temperatures ranging from 700 to 1200°C with annealing times between 2 minutes to 50 hours, depending on temperature and alloy. Annealing treatments were performed in sealed quartz capsules filled with argon gas. They were always followed by air cooling, except for the 304L samples that were water quenched to ensure that no second phase form during cooling.

Because alloys do not present the same melting temperatures, their comparison is based on homologous temperatures, noted T_h . These are defined as the ratios between annealing and melting temperatures. The latter was determined experimentally by using differential scanning calorimetry (DSC). The melting and homologous temperatures of the four studied materials are given in **Table 6.2**. Cantor, C6Al and C+C present the same melting temperature, and hence the same T_h . Similar T_h is found for 304L at an absolute temperature increased by 100°C.

Table 6.2 Melting and homologous temperatures at the annealing temperatures of 700 to 1000°C. Similar homologous temperatures are highlighted in colours.

Annealing temperature (°C)	T_f (°C)	T_h (°C)			
		700	800	900	1000
304L	1425	0.49	0.56	0.63	0.7
Cantor / C+C / C6Al	1290	0.54	0.62	0.7	0.78

Additional pieces of information on materials, processing and characterisation methods can be found in annexe A at the end of this manuscript.

6.1.3. Nomenclature

The samples are referred to using first the name of the alloy and then the conditions of their annealing treatment. For example, the sample of 304L annealed for 1 hour at 900°C is referred to as 304L-900/1h. Samples cold rolled are referred to with the letters “CR” in place of the annealing treatment conditions.

In the sections 6.2.3 and 6.3.3 about tensile testing, microstructures are gathered according to their grain sizes. Microstructures with grain sizes between 3 and 5 μm will be referred to as s-GS (for small grain size). Those with grain sizes around 100 μm will be referred to as l-GS (for large grain size).

6.2. Results

6.2.1. Cold rolling step

Fig. 6.1 presents BSE SEM micrographs acquired on the four materials after CR for 80%. The four microstructures are similar. They all present shades of grey, indicating the presence of orientation gradients. Shear bands are also visible with an angle of around 30° with the rolling direction (aligned vertically). Examples are indicated by black arrows. In insets are given the orientation density figure (ODF) sections at $\phi_2 = 45^\circ$ measured after cold rolling. All deformation textures are similar with a strong α -fibre spreading from Goss to Brass texture components (TC). C+C is the most textured with an overall texture index of 3.0, then follows C6Al (2.7), 304L (2.5) and finally Cantor alloy (2.3).

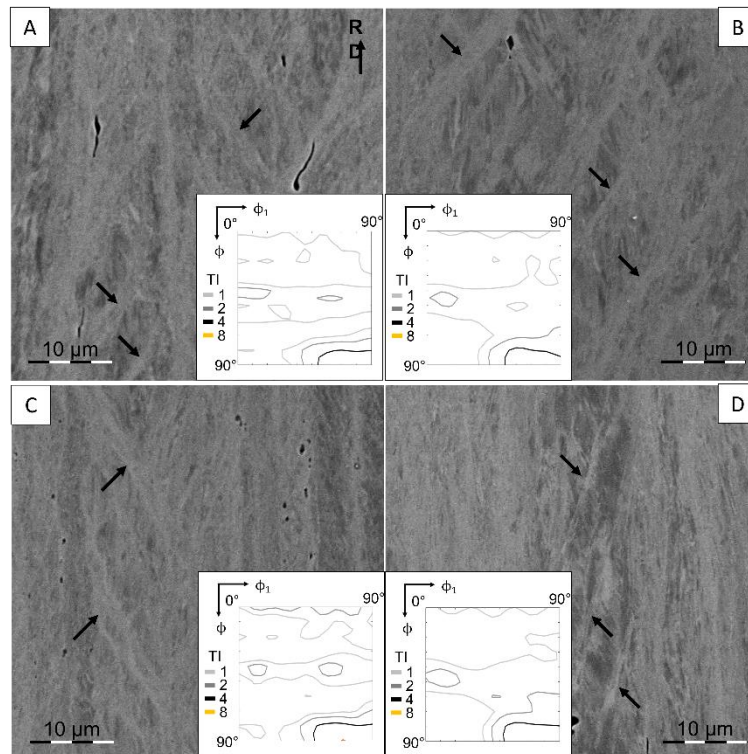


Fig. 6.1 BSE SEM micrographs after CR for 80%. Examples of shear bands are indicated by black arrows. In inset are given the ODF sections at $\phi_2 = 45^\circ$. (A-D) correspond to respectively 304L, Cantor, C+C and C6Al. [Full-size](#).

Fig. 6.2 presents the XRD diffractograms of the four materials after CR80. They are all single-phase FCC.

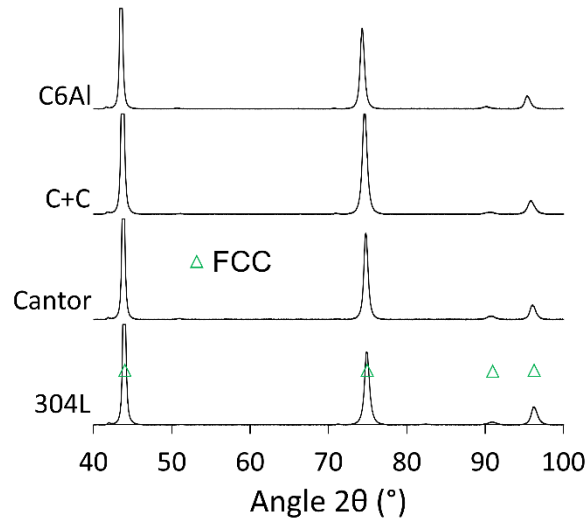


Fig. 6.2 XRD diffractograms measured after CR. [Full-size](#).

The dislocation densities were measured after CR for 80% from XRD diffractograms (**Fig. 6.2**). The results are gathered in **Table 6.3**. The four materials present similar dislocation densities, i.e. between 11 and $17 \cdot 10^{14}/m^2$.

Table 6.3 Dislocation densities measured from XRD diffractograms.

	304L	Cantor	C6Al	C+C
ρ ($10^{14}/m^2$)	16.3 ± 0.5	11.9 ± 0.5	11.6 ± 0.5	16.9 ± 0.5

6.2.2. Annealing treatments

Annealing treatments are performed on the deformed microstructures at temperatures ranging from 700 to 1200°C for 2 minutes to 50 hours, depending on the material. The phases present were identified by XRD (Fig. 6.3A). Fig. 6.3B summarizes the phases observed in function of the annealing temperature. 304L and the Cantor alloy are single-phase FCC in the full range of studied annealing temperatures and durations. Nonetheless, the large oxygen content in the Cantor alloy (Table 6.1) results in the formation of oxides enriched in chromium and manganese that were observed in the SEM (not shown). No peaks corresponding to these oxides are detected with XRD suggesting their limited volume fraction. Moreover, the large diameter of around 2 μm of these inclusions limits their pinning effect on boundary and their influence on mechanical properties. As a consequence, these inclusions are not considered in this chapter.

Peaks corresponding to carbides of type $M_{23}C_6$ were identified in C+C below 1100°C. In C6Al, peaks corresponding to the B2 phase appear below 1000°C and those corresponding to the σ phase are observed at 900°C and below.

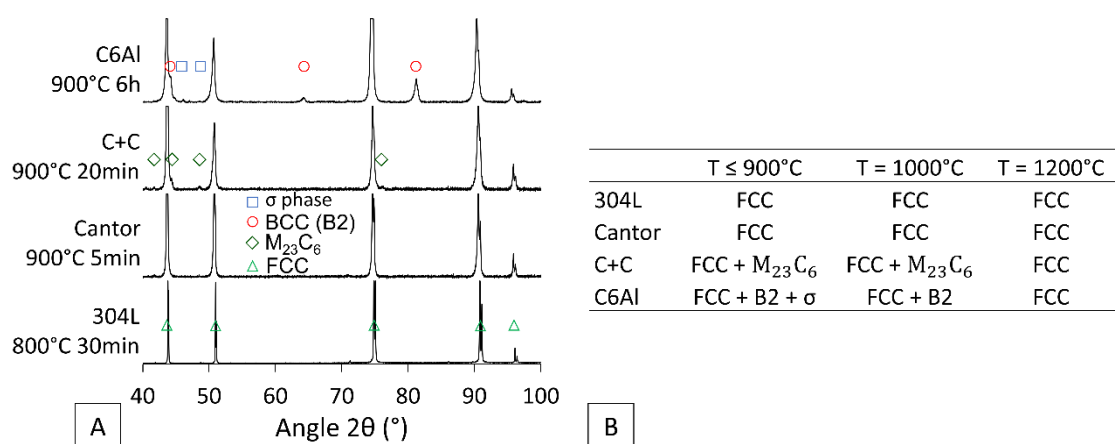


Fig. 6.3 (A) XRD diffractograms highlighting the different phases observed after annealing. (B) Table summarizing the phases observed in the studied annealing temperature/duration range. [Full-size](#).

Different annealing times at 700 to 900°C were used to follow the evolution of the recrystallisation fractions. These fractions were determined by EBSD for all materials, except for C6Al. The grains presenting a grain orientation spread (GOS) index smaller than 4° are considered recrystallised. An example is given in Fig. 6.4A for 304L annealed at 700°C for 3 hours. The grains with GOS larger than 4° are shaded. The recrystallisation fraction is then defined as the ratio between the number of pixels with GOS < 4° over the total number of pixels presenting a confidence index larger than 0.1. These fractions are used to plot the recrystallisation fraction versus annealing time, as in the example given in Fig. 6.4B for 304L. Similar graphs were plotted for the three other materials. For C6Al, the determination of the recrystallisation fraction is performed using optical microscopy and systematic manual point counting. The reader is referred to the *materials and methods* chapter for more details.

Fig. 6.4C presents the annealing times necessary to reach a recrystallisation fraction of 90% at the two homologous temperatures of 0.55 and 0.62. These values were extracted from the recrystallisation fraction vs time curves, e.g. Fig. 6.4B for 304L. 304L and the Cantor alloy present similar recrystallisation kinetics : 9 minutes are necessary to recrystallise 90% of the materials at $T_h = 0.55$. This duration increases to 1 hour in the case of C+C and to 100 hours in the case of C6Al.

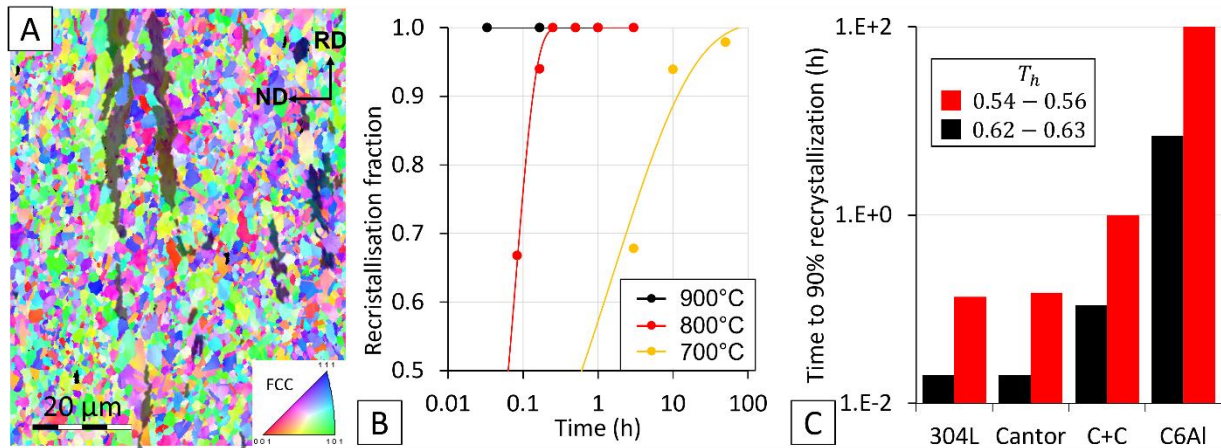


Fig. 6.4 Recrystallisation kinetics of the four materials. (A) IPF-Z map acquired after 3 hours at 700°C in 304L. The shaded areas correspond to non-recrystallised grains. (B) Recrystallisation kinetics at 700, 800 and 900°C for 304L. (C) Annealing times to attain recrystallisation fractions of 90% for the four studied materials. [Full-size](#).

6.2.3. Tensile tests

Two groups of fully recrystallised microstructures with similar grain sizes were obtained for tensile testing. The first group presents grain sizes of few micrometres, called s-GS, while the second around 100 μm , called l-GS. The microstructures of s-GS are presented in **Fig. 6.5**. 304L (**Fig. 6.5A**) and the Cantor alloy (**Fig. 6.5B**) present single-phase FCC microstructures. C+C (**Fig. 6.5C**) contains carbides of type M_{23}C_6 (in dark green) and M_7C_3 (in yellow). C6Al (**Fig. 6.5D**) contains grains of the B2 phase (in red) and σ phase (in blue). The microstructures of l-GS were obtained during annealing treatments at 1200°C. As indicated in **Fig. 6.3B**, the four materials were found single-phase FCC.

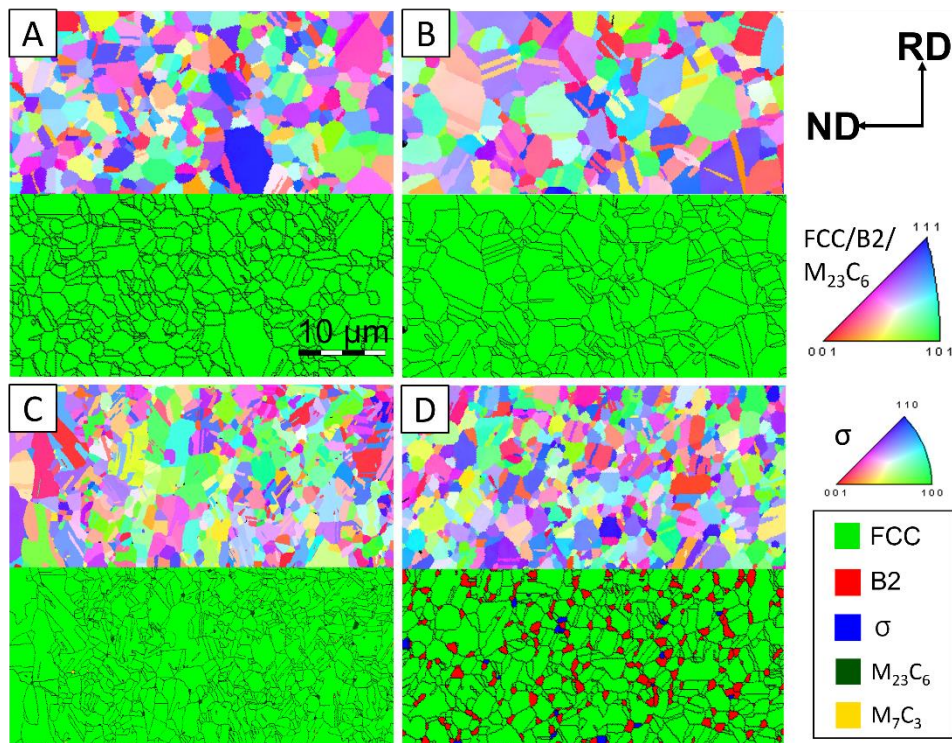


Fig. 6.5 Fully recrystallized microstructures with grain sizes of few micrometres (s-GS). (A-D) correspond respectively to 304L, Cantor, C+C and C6Al. Both IPF-Z and phase maps are shown. All maps present the same scale. [Full-size](#).

The eight microstructures of the two groups were tensile tested at room temperature. The corresponding tensile curves and work-hardening rate (WHR) curves are shown in **Fig. 6.6**. The corresponding microstructural features along with yield strengths (YS), ultimate tensile strengths (UTS) and uniform elongations are given in **Table 6.4**. YS are ranked in the same order at l-GS and s-GS. 304L presents the lowest YS, then Cantor, C6Al and C+C the largest. Regarding work-hardening behaviour, curves present similar shapes in each group. In s-GS, they decrease continuously (**Fig. 6.6C**). In l-GS (**Fig. 6.6D**), the WHR curves do not present a monotonic trend. An increase in the WHR slope is observed for the four materials. It is more intense in C6Al and C+C.

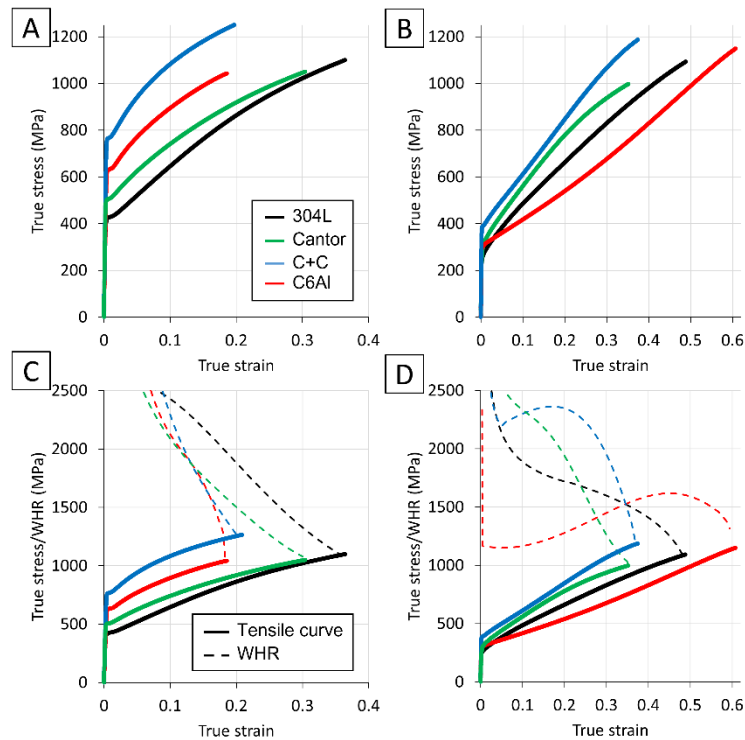


Fig. 6.6 (A-B) Tensile curves. (C-D) Tensile and WHR curves. (A and C) correspond to grain sizes between 3-5 μm (s-GS) and (B and D) of around 100 μm (l-GS) for the four materials. [Full-size](#).

Table 6.4 Microstructural features of the eight microstructures characterized in tension. The tensile properties of each state are also given.

Material	FCC grain size	Precipitate fraction	Yield strength (MPa)	Tensile strength (MPa)	Uniform elongation
	(μm)				
s-GS: grain sizes of few micrometres					
304L (black)	3.2 ± 1.5	0	420	1100	0.36
Cantor (green)	5.2 ± 2.2	0	500	1050	0.3
C+C (blue)	4.8 ± 3.0	0.04 ± 0.02	760	1260	0.21
C6Al (red)	3.7 ± 1.9	0.20 ± 0.02	630	1040	0.19
l-GS: grain sizes of around 100 μm					
304L (black)	110 ± 54	0	250	1090	0.49
Cantor (green)	100 ± 40	0	290	1000	0.35
C+C (blue)	110 ± 45	0	390	1190	0.37
C6Al (red)	95 ± 30	0	300	1150	0.61

Microstructural observations were performed on the I-GS tensile tested specimens of 304L, Cantor and C+C (**Fig. 6.7**). In 304L, no deformation driven phase transformation was observed as indicated by the phase map in inset of **Fig. 6.7A**. **Fig. 6.7B** gives the misorientation profile along the black arrows. Mechanical twins are identified by their typical 60° rotation angle at their boundaries. The twins crossed by the profile are indicated with red arrows. They appear darker in the IQ map of **Fig. 6.7A**. Mechanical twins were observed in Cantor and C+C (**Fig. 6.7C-D**). Examples of twins are indicated by red arrows.

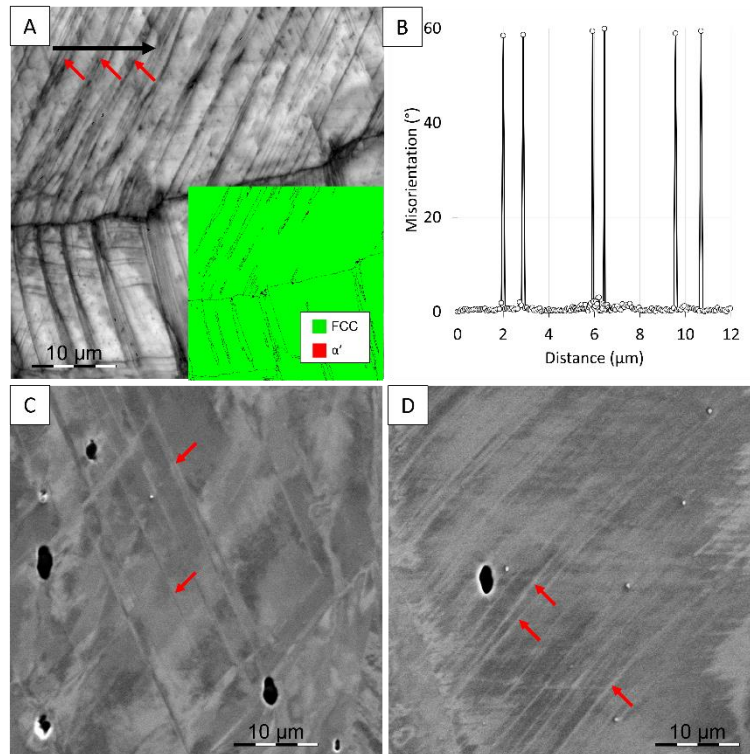


Fig. 6.7 (A) IQ map of the tensile tested I-GS specimen of 304L. In insets are given the corresponding phase map and the misorientation profile measured along the black arrow. (B-C) BSE SEM micrographs of respectively Cantor and C+C tensile specimens in I-GS after tensile testing. Examples of mechanical twins are indicated by red arrows. [Full-size.](#)

6.3. Discussion

6.3.1. Deformed state

The microstructures after CR of 304L, the Cantor alloy and C+C (**Fig. 6.1**) are similar to that of C6Al detailed in chapter 3. They present significant intragranular orientation gradients indicating that they deform primarily by dislocation slip. The measured dislocation densities (**Table 6.3**) suggest similar dislocation activities in all four materials.

Moreover, shear bands are observed (indicated by black arrows in **Fig. 6.1**). They are rotated of around 30° to the rolling direction, close to the value of 35° reported after heavy rolling of many FCC metals²⁵⁸. Mechanical twins are not observed on these micrographs. However, their presence after tensile testing (**Fig. 6.7**) most probably indicates their presence after rolling for 80%. Their presence is however less favoured in 304L due to the larger rolling temperature of 200°C. In addition, the four materials present similar deformation textures consisting of the α -fibre (insets in **Fig. 6.1**). As was discussed for C6Al in chapter 3, this type of texture is explained by the activation of twinning and shear banding during rolling.

All these features are typically observed after deformation in FCC materials with low SFE, such as TWIP steels^{215,224} or austenitic stainless steels²¹¹. However, the latter might also present phase transformation during deformation. In the current study, phase transformation in 304L was inhibited by the increased rolling temperature of 200°C (**Fig. 6.2**).

The SFEs of the four materials were determined based on literature or on thermodynamic calculations. The following calculations are performed on the nominal compositions of the alloys, meaning when they are single-phase. They hence do not consider potential change of the chemical composition of the matrix with the occurrence of precipitation. Precise measurements of chemical compositions in presence of second phases, through atom probe tomography for example, would be necessary to calculate the SFEs of the alloys when multiphase.

First, the SFE of the currently studied 304L is determined based on the formula proposed by Meric de Bellefon *et al.*²⁵⁹. It gives a SFE of 23 mJ/m². This value agrees with the experimental values previously reported for 304L²⁵⁹. The SFE of the Cantor alloy was reported at 18-27 mJ/m² by Zaddach *et al.*⁹⁴. As detailed in the beginning of the discussion of chapter 3, the addition of 6 at.% of aluminium in Cantor results in an increase in SFE of 40%. It gives a SFE for C6Al between 30 and 40 mJ/m². About C+C, it was reported that the addition of carbon in the Cantor alloy results in an increase in its SFE¹¹², as it is the case for TWIP steels¹²⁵. This increase was quantified by *ab initio* calculations at 7 mJ/m² per atomic percent of carbon¹¹², resulting in a value of 23-32 mJ/m² for C+C. Following the same reasoning, an additional increase should result from the enrichment in nitrogen of C+C.

Overall, the four materials present similar SFE values between 18 and 40 mJ/m². This finding confirms the similar behaviours presented by the four materials during CR. Moreover, mechanical twinning was reported to activate in steels at SFE between 20 and 40 mJ/m²¹²². All the studied alloys fall in this range explaining the observations of mechanical twins after tensile testing. Hence, at this stage, not much difference can be established between MCAs and 304L, as well as between the three MCAs.

6.3.2. Recrystallisation kinetics

Starting from similar deformed microstructures, and with similar stored energies (**Table 6.3**) – implying similar driving forces for recrystallisation –, annealing treatments were performed between 700 and 900°C to assess the differences in recrystallisation kinetics between the four materials.

The results, presented in **Fig. 6.4C**, indicate that 304L and the Cantor alloy present similar recrystallisation kinetics. They both require around 9 minutes at $T_h \sim 0.55$ to reach 90% of recrystallisation. These similar and quick recrystallisation kinetics are attributed to their single-phase FCC microstructures, confirmed by XRD (**Fig. 6.3A**). It suggests that the chemical complexity of the MCAs does not influence much recrystallisation.

On the other hand, C+C and C6Al require annealing times of respectively 1 and 100 hours at the same homologous temperature (**Fig. 6.4C**). This considerable slowing down of recrystallisation is attributed to the presence of second phases in these two materials. Indeed, $M_{23}C_6$ and M_7C_3 carbides were observed in C+C, and B2 and σ phases in C6Al after annealing at 700-900°C (**Fig. 6.3B**). As these second phases are not present after deformation (**Fig. 6.2**), they must have formed during annealing in parallel with recrystallisation. Interactions between the two phenomena might hence be at the origin of the limitation of the recrystallisation kinetics.

Precipitates interact with recrystallisation by limiting the mobility of boundaries. The pinning pressure exerted by precipitates on boundaries, or Smith-Zener pressure P_{SZ} , is given by:

$$P_{SZ} = \frac{6f_V\gamma_b}{r} \quad (\text{Eq. 6.1})$$

with f_V and r the volume fraction and radius of precipitates, and γ_b the energy of a boundary separating two FCC grains. As precipitates form during annealing, in parallel to recrystallisation, they are expected to be small and that whatever their nature. The decisive parameters are hence the precipitate volume fraction and the interphase boundary energy. It is important to note that, as detailed in chapter 3, the σ phase forms from B2 grains. As a consequence, its influence on recrystallisation is expected to be negligible. Moreover, the M_7C_3 carbides are not detected in XRD (**Fig. 6.3A**) suggesting low volume fractions. The following reasoning will hence focus on $M_{23}C_6$ carbides in C+C and on B2 grains in C6Al.

XRD measurements were performed on C6Al and C+C in order to calculate the volume fractions of precipitates during annealing. The results are shown in **Fig. 6.8**. Volume fractions of B2 phase in C6Al are considerably larger than that of $M_{23}C_6$ in C+C. For example, after an annealing treatment of 1 hour at 800°C, the volume fraction of $M_{23}C_6$ is 4% in C+C, whereas in C6Al it is 15% for the B2 phase. The lower volume fraction of carbides in C+C induces a lower pinning pressure exerted on boundaries and hence a lower impact on recrystallisation. This explains the large gap in recrystallisation kinetics between the two multiphase materials.

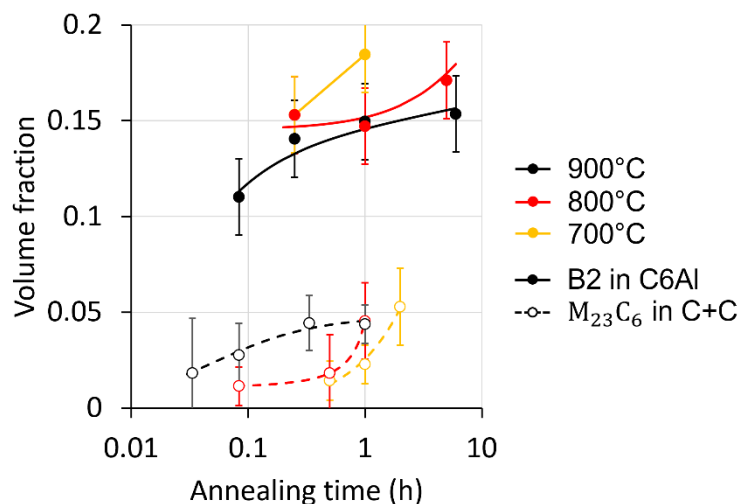


Fig. 6.8 Volume fractions of the B2 phase in C6Al (solid lines and circles) and of $M_{23}C_6$ in C+C (dashed lines and empty circles) at 700°C (in orange), 800°C (in red) and 900°C (in black). [Full-size](#).

The results of **Fig. 6.4C** highlight (i) the primary role of precipitation on recrystallisation kinetics and (ii) the similarity between austenitic stainless steels and high-entropy alloys when single-phase FCC. This second statement is partially reconsidered when considering grain growth kinetics. The FCC grain size was measured at $T_h = 0.7$ in the four alloys (**Fig. 6.9**). The FCC grain size of 304L increases faster than that of Cantor. The slow grain growth kinetics of Cantor or of its subset CoCrFeNi was already reported when compared to pure nickel^{198,200}. The complex chemistry of the Cantor alloy could be at the origin of these slow kinetics, most probably through solute drag. Moreover, **Fig. 6.9** shows lower grain sizes for C+C and C6Al. These results indicate that precipitation also limits boundary mobility during grain growth.

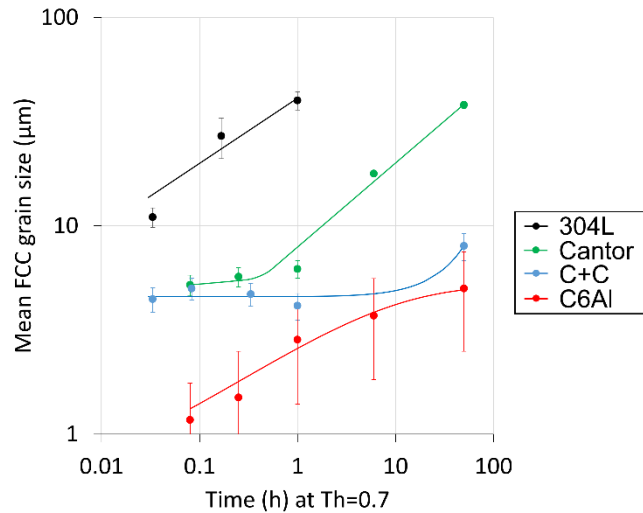


Fig. 6.9 Evolution of the FCC grain size of the four materials during annealing at $T_h = 0.7$. [Full-size](#).

6.3.3. Tensile properties

The discussion of tensile properties is divided in two parts. First, the strengthening mechanisms are identified based on chemistry and microstructural observations. This first part focuses on YS. In a second step, WHR and post-mortem observations will be used to determine the mechanisms activated during deformation.

Strengthening mechanisms

As detailed in chapters 4 and 5, the YS can be calculated with a rule of mixture between the different phases present. The strength of a phase is the sum of the contributions from its different strengthening mechanisms, such as intrinsic strengthening, Hall-Petch strengthening, precipitation strengthening...

In I-GS (**Fig. 6.6B**), all materials are fully FCC (**Table 6.4**). As the four microstructures present similar FCC grain sizes – similar Hall-Petch strengthening – and are not work-hardened, the differences in YS come from differences in solid solution strengthening. This strengthening contribution is related to the atomic size misfit (δ)^{260,261}, defined as follows²⁶²:

$$\delta = \sqrt{\sum_i x_i \left(1 - \frac{r_i}{\bar{r}}\right)^2} \quad (\text{Eq. 6.2})$$

with x_i and r_i the volume fraction and radius of the substitutional element i and \bar{r} the averaged radius. Based on the chemical compositions of the four materials (**Table 6.1**) and on the atomic radii reported in²⁶³, the atomic size misfits are calculated. They are given along with the averaged radii in **Table 6.5**.

Table 6.5 Averaged radii and atomic size misfits for the four studied materials.

	304L	Cantor	C6Al	C+C
\bar{r} (nm)	0.124	0.127	0.128	0.125
δ (%)	1.4	3.2	4.3	3.5

304L presents the smallest atomic size misfit. It agrees with its chemical composition, mainly constituted of iron atoms. The larger misfit values for the three other materials agree with the lattice distortion effect proposed for MCAs⁴. The presence of aluminium in C6Al, with its larger atomic radius of 0.143 nm, results in an increased atomic size misfit. This reasoning explains the ranking in YS of 304L, the Cantor alloy and then C6Al, which only contain elements in substitution.

The reasoning on atomic misfit, based on substitutional atoms, is not sufficient to explain the larger YS of C+C (**Fig. 6.6B**). C+C contains larger fractions of carbon and nitrogen than the three other alloys (**Table 6.1**). These atoms, of much smaller radii, occupy the interstitial sites between substitutional atoms, resulting in considerable strengthening. The largest YS of C+C is due to the combination of solid solution strengthening and interstitial strengthening.

In s-GS (**Fig. 6.6A**), solid solution and interstitial strengthening are complemented by the presence of second phases in C6Al and C+C. These second phases are harder than the matrix. Their presence hence results in an additional strengthening contribution. In both materials, precipitates formed on FCC grain boundaries (**Fig. 6.5C-D**). These microstructures can be considered as a “composite” of FCC and second phase grains. The strengthening corresponding to the two phases can then be added as a simple rule of mixture. The smaller grain size of carbides (**Fig. 6.5**) and their lower volume fraction (**Fig. 6.8**) are expected to result in a smaller strengthening contribution in C+C than from B2 and σ grains in C6Al. However, less precipitation of carbides also means more carbon atoms remaining in solid solution and hence a larger contribution from interstitial strengthening in FCC grains. The increase in YS from l-GS to s-GS in C+C is hence mainly due to the decrease in grain size, and only in a lesser extent to the formation of carbides.

It appears from **Table 6.4** that the YS of both Cantor and 304L are multiplied by 1.7 from l-GS to s-GS. This increase is due to the decrease in grain size also known as Hall-Petch strengthening. A factor of 1.9 is found for C+C indicating a low influence of precipitation on strength. In the case of C6Al, a factor of 2.1 is found indicating a larger strengthening effect of precipitates. This is confirmed in chapter 4 by the YS simulation of CR80-900/6h (corresponding to the C6Al specimen of s-GS). Precipitates proved to contribute for 38% of the total YS.

Work-hardening behaviour

Focus is first given to the case of l-GS. As observed in **Fig. 6.6D**, the four materials present WHRs that do not continuously decrease during deformation. The increase in WHR during deformation is typical of the activation of an additional deformation mechanism¹¹⁶, supplementary to dislocation slip. As discussed in chapters 4 and 5, this behaviour is attributed to the activation of mechanical twinning in the case of C6Al. Mechanical twins were also observed in Cantor and C+C after tensile testing until fracture (**Fig. 6.7C-D**). The observation of mechanical twins in these three materials is not surprising when considering their SFEs evaluated between 18 and 40 mJ/m².

In the case of 304L, Shen *et al.* reported that both mechanical twinning and transformation-induced plasticity (TRIP) effect, with the formation of α' martensite, activate during tensile testing²⁶⁴. In the present case, the phase map shown in inset of **Fig. 6.7A** shows the absence of phase transformation during tensile testing. Mechanical twins are observed as shown by their 60° twinning angle on the misorientation profile (along the black arrow) presented in inset. In steels, it is commonly reported that the TRIP effect activates at SFEs between 10 and 20 mJ/m² depending on the material^{122,125}. The SFE of the present 304L was evaluated at 23 mJ/m² which agrees with the absence of TRIP effect. This feature confirms the choice of this particular 304L as a good candidate for comparison with FCC MCAs that do not undergo phase transformation during deformation.

From the three MCAs, two stand out for different reasons. First, C+C presents larger strength and similar elongation compared to Cantor. Similarly as discussed in chapter 4 for C6Al, these interesting tensile properties are attributed to the presence of carbon. This addition favours mechanical twinning and in turn delay necking. As shown by Chen *et al.*⁸², at carbon contents below 2 at.%, mechanical twinning is favoured. The presence of 0.7 at.% of carbon in C+C is hence expected to present the same effect.

Moreover, C6Al stands out due to its exceptional work-hardening capacity (WHC) and ductility. While the two other MCAs do not exceed uniform elongations of 0.4, it is 0.61 for C6Al. As detailed in chapter 4, this behaviour could be explained by an intensification of twinning due to the presence of carbon and aluminium in C6Al. The role of aluminium in this phenomenon is supported by the larger intensity of the WHR peak in C6Al and by its shift in strain when compared to that of the Cantor alloy, as both alloys contain a similar carbon content.

At s-GS, the four materials present similar work-hardening behaviours (**Fig. 6.6A**), with WHR decreasing continuously towards Considere's criterion (**Fig. 6.6C**). This behaviour is typically observed when deformation is governed by dislocation slip¹¹⁸. It indicates that mechanical twinning is not activated or not significantly activated in these cases. This is explained based on the important decrease in FCC grain size, from 100 to 3-5 μm . Indeed, twinning activity was reported to decrease as grain size decreases¹³¹. Nonetheless, large variations in uniform elongations are observed. These can be rationalised based on the precipitation contents. Indeed, due to the difference in hardness between precipitate and matrix, interphase boundaries act as nucleation sites for voids that in turn coalesce and result in fracture. This is observed in **Fig. 4.6C** of chapter 4 (indicated by white arrows) in the case of C6Al. The larger precipitate fraction in C6Al result in lower uniform elongation than C+C. The comparison is even clearer when comparing with single-phase Cantor or 304L.

Conclusions

Three MCAs, i.e. the Cantor alloy and its counterparts with addition of aluminium or carbon, were compared to an austenitic stainless steel of grade 304L. The comparison focused on deformation by rolling, subsequent annealing treatments and tensile properties.

This study shows that when single phase FCC, multicomponent and conventional alloys behave similarly. The same mechanisms were activated when deformed by rolling or during tensile testing, i.e. dislocation glide, mechanical twinning and shear banding. Moreover, when annealed at equal homologous temperature, 304L and Cantor present similar recrystallisation kinetics. The two families of alloys still differentiate due to the complex chemistry of MCAs. Indeed, grain growth was observed to be slower in MCAs, most probably due to solute drag. Moreover, MCAs present larger YS than 304L, related to larger solid solution strengthening.

This study also showed the paramount role of precipitation in the limitation of recrystallisation and grain growth kinetics. However, its influence on tensile properties, when precipitates are located on grain boundaries, is significant only when their volume fractions are significative. This result indicates that the comparison of C6Al with a conventional multiphase alloy, such as dual phase steels for example could also be interesting. Finally, the interstitial-containing Cantor alloy showed interesting tensile properties. It seems that the addition of a small fraction of carbon in MCAs results in the coupling of high YS, through interstitial strengthening, and of large ductility, through more intense mechanical twinning. Finally, C6Al was found to present an exceptional WHC that could be related to the presence of aluminium.

7. GLOBAL SUMMARY, CONCLUSIONS AND PERSPECTIVES

7.1. Summary and conclusions

In the young family of multicomponent alloys, Cantor's alloy stood out due to its single-phase FCC structure and to the activation of mechanical twinning during deformation. These two features grant Cantor's alloy interesting mechanical properties at ambient and cryogenic temperatures. As such, Cantor's alloy became a base alloy for further chemical or microstructural optimisation. Multiple alloying strategies were tested with a particular interest for the addition of aluminium that induces the stabilisation of the harder B2 second phase. By choosing aluminium contents below 7 at.%, a single-phase FCC domain is maintained at high temperatures permitting easy forming, while significant B2 fractions, up to 40%, can be formed at lower temperatures. Based on these two results, the choice was made to focus on the $\text{Al}_{0.3}\text{CoCrFeMnNi}$ complex concentrated alloy, with aluminium contents around 5.6 at.%, called C+Al.

This work first aimed at assessing how this alloy behaves when submitted to conventional processing steps used in industry. The chapters 2 and 3 focus on the behaviour of C+Al when submitted respectively to hot rolling, and cold rolling with subsequent annealing treatments.

Hot rolling is simulated in chapter 2 by compression tests between 900 and 1100°C. As expected in a FCC alloy of low stacking fault energy, discontinuous dynamic recrystallisation activates during deformation at all four investigated temperatures. At 1000-1100°C, C+Al behaves as a solid solution alloy, as confirmed by the comparison with a conventional austenitic stainless steel of grade 304L. Larger stress values were observed in C+Al due to its enhanced solid solution strengthening. Solute drag might also be present and would limit recrystallised grain sizes. Nonetheless, important recrystallisation fractions and grain sizes are observed at these temperatures, mainly due to the low melting temperature of C+Al. Complete recrystallisation is even reached after deformation at 1100°C with a rate of 0.1/s for an equivalent strain of 0.6. At 900-950°C, precipitation of the B2 phase at grain boundaries limits the extent of dynamic recrystallisation. This results in a significant increase in stress coupled to low recrystallisation fractions and grain sizes. The hot deformation of C+Al hence largely depends on deformation temperatures. At 1000-1100°C, where C+Al remains single-phase FCC, large reductions in thickness would be possible without excessive increase in load. At the opposite, hot rolling seems difficult between 900-950°C where stress reaches up to 420 MPa due to the limitation of dynamic recrystallisation by precipitation.

The first part of chapter 3 focuses on the behaviour of C+Al when deformed by cold rolling in the single-phase FCC domain until a thickness reduction of 92%. The analysis of microstructures revealed that deformation is controlled by dislocation slip. In addition, mechanical twinning activates since the reduction of 20%. The activation of mechanical twinning in C+Al is not surprising in regard of its low stacking fault energy. Moreover, shear bands appear after reductions of 60%. The evolution of crystallographic texture, followed during cold rolling by XRD, confirms this sequence of event. When fully FCC, the behaviour of C+Al during cold rolling is comparable to other FCC metallic materials presenting low stacking fault energies, such as austenitic stainless steels or TWIP steels. The absence

of strain induced phase transformation and the observation of mechanical twins make it closer to TWIP steels.

In the second part of chapter 3, microstructural transformations were found to depend mainly on the deformation temperature. Below 800°C, precipitation governs the evolution of microstructures, resulting in a recovered material containing a fine dispersion of precipitates inside the grains and larger precipitates at grain boundaries. At 1000°C and above, static recrystallisation is prevailing. Complete recrystallisation is reached quickly and rare precipitates are observed at grain boundaries. In between, both phenomena are significantly activated, inducing strong interactions. In this last case, the local stored energy determines whether a region of the microstructure recrystallises first and then experiences precipitation on newly formed grain boundaries, or whether precipitates form first inside the deformed grains delaying recrystallisation. It results in composite microstructures with grain sizes below 5 μm but with full recrystallisation obtained after several tens of hours. The increase in cold rolling reduction was found to accelerate recrystallisation kinetics.

On the basis of the comprehension of microstructural transformations in C+Al acquired in the second part of chapter 3, three microstructures were selected for tensile testing. These microstructures were selected to represent the full scope of microstructures that can be obtained after annealing in C+Al. Tensile properties of these three microstructures are detailed in chapter 4. A large range of tensile properties is observed with yield strengths ranging from 300 to 1050 MPa and uniform elongations from 7 to 61%. These tensile properties are located on the Ashby map presented in the introduction of this manuscript (black circles on **Fig. 7.1**). They cover a wide region of the Al-Co-Cr-Fe-Mn-Ni property range but follow the well-known strength-ductility trade-off (materialised with a black dotted line).

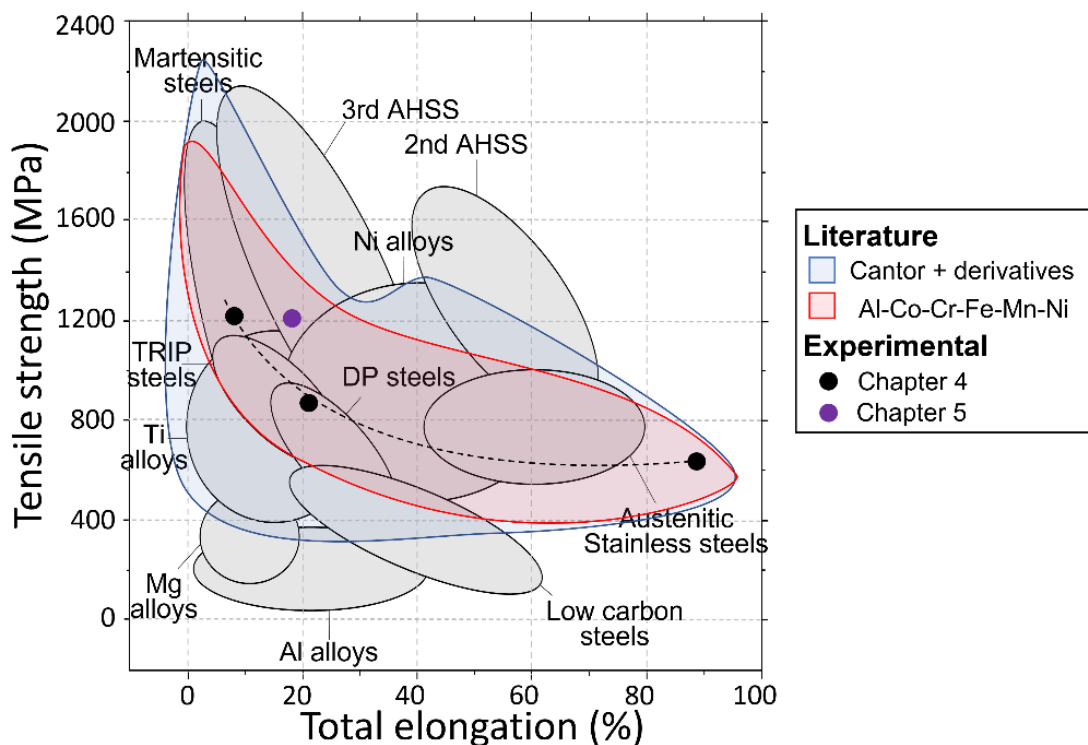


Fig. 7.1 Ashby map of the engineering ultimate tensile strength (UTS) vs total elongation. The blue envelope corresponds to Cantor's alloy and its derivatives. The red envelope corresponds to the Al-Co-Cr-Fe-Mn-Ni family. These envelopes were built based on the analysis of 62 articles (see the introduction of this manuscript for more details). In background are reported the properties shown by various families of conventional alloys. 2nd and 3rd AHSS stand for the two generations of advanced high-strength steels, DP steels for dual-phase steels. [Full-size](#).

The strengthening mechanisms contributing the most were identified with the simulation of yield strength values. The FCC phase contributes for at least half of the total yield strengths, mainly due to the small grain sizes of the two specimens annealed at 900°C. Moreover, intragranular B2 precipitation revealed more efficient than B2 precipitation at grain boundaries. The analysis of work-hardening behaviours revealed that mechanical twinning activates during tensile testing of single-phase FCC C+Al with a grain size of 100 µm. Precipitates at grain boundaries do not contribute much to work-hardening. At the opposite, intragranular precipitates contribute to work-hardening through the Orowan looping mechanism. However, the work-hardened state of the FCC matrix and the formation of voids at interphase boundaries limit this effect.

Chapter 5 focuses on the development of microstructures coupling large yield strength and large work-hardening capacity. A new thermomechanical route was developed in order to maximise the fraction of intragranular precipitation and hence maximise their contribution to work-hardening. This new route includes a second cold rolling step in between a recrystallisation step and a precipitation aging stage. During the recrystallisation stage at large temperature, complete recrystallisation is reached quickly – in several minutes compared to several tens of hours at lower temperatures. During the second cold rolling step, dislocations are stored inside the grains and then serve as nucleation sites for precipitates during aging. It results in a homogeneous microstructure consisting of large FCC grains containing intragranular precipitates. Precipitates at grain boundaries are also present. This microstructure couples the large yield strength of 880 MPa and the large work-hardening capacity of 560 MPa. The yield strength and flow stress were simulated in order to decorrelate their multiple contributions. The simulation of the flow stress permitted to determine that intragranular precipitates increase the work-hardening capacity in three ways: back-stress induced by the dislocation loops stored around intragranular precipitates, increase in the densities of statistically stored and geometrically necessary dislocations.

Finally, in chapter 6, C+Al is compared to three FCC alloys presenting low stacking fault energies and similar chemical compositions: an austenitic stainless steel of grade 304L, Cantor's alloy and a carbon containing Cantor's alloy. As a summary, multicomponent alloys behave similarly as conventional alloys, except that their large solute content induces increased solid solution strengthening and limit grain growth. Both the addition of carbon and of aluminium seem interesting but for different reasons: intensification of mechanical twinning for carbon; and versatility of microstructures for aluminium. The potential coupling of these two alloying strategies could be an interesting perspective for further research.

When comparing the tensile properties of C+Al obtained in this work (**Fig. 7.1**), an improvement can be observed from chapter 4 to chapter 5. The tensile properties obtained with the new thermomechanical strategy implemented in chapter 5 break from the strength-ductility trade-off of chapter 4 (dotted black line). Nonetheless, when compared to literature (grey envelopes in the background), the strategies implemented in chapter 4 and 5 do not challenge the best 2nd or 3rd generations of advanced high-strength steels (AHSS) nor the best nickel alloys. In addition, when compared to conventional alloys, C+Al is more costly – with large contents of expensive elements such as cobalt and nickel – ²⁶⁵; contain a large fraction of cobalt whose availability risk is high and mining conditions often miserable ²⁶⁵; and its adaptation to industrial production lines is not straightforward and would require investments. Overall, this work concludes that the tensile properties of C+Al are not sufficient to justify its further development.

Nonetheless, this work explores only tensile testing at room temperature as an indicator of its worth. As previously shown in Cantor's alloy, it is when tensile tested at cryogenic temperatures that it really

stands out²⁵. It might be the same for C+Al which could reveal interesting through other mechanical or structural properties, or through interesting combinations of them.

To conclude, thermodynamic calculations were used in most of the chapters to compute phase diagrams, stacking fault energies or onset driving forces for nucleation. These calculations were performed using the TCHEA4 database, developed specifically for multicomponent alloys by ThermoCalc software. Globally, the results described well the studied systems. For example, the phases predicted by the calculations were observed experimentally, i.e. FCC, B2 and the σ phase. In some cases, these calculations even proved to be quantitatively accurate as for the B2 fractions in chapter 3. The calculations of stacking fault energies and onset driving forces for nucleation proved qualitatively relevant with trends matching what was observed experimentally. For example, the computed stacking fault energies agreed with the activation of mechanical twinning during deformation.

However, deviations between calculations and experiments were also observed, questioning the reliability of this method. This topic is not new but became increasingly relevant with the development of multicomponent alloys where thermodynamic calculations became necessary to avoid long and tedious experimental screening¹⁷. In this work, quantitative deviations were observed for example in chapter 5 with the recrystallisation temperature of 1100°C. According to the calculated phase diagram, this temperature falls in the duplex domain FCC + B2, while no B2 was observed experimentally.

Hence, thermodynamic calculations remain a great tool to quickly gather information on new alloying compositions. It permits to correctly evaluate trends but care must be taken when considering quantitative outputs. These conclusions apply to the Cantor alloy and its close derivatives as they are well assessed in thermodynamic databases and their number of phases relatively low. In more complex and unexplored systems, the reliability of these calculations should be even more questioned.

7.2. Perspectives

Going further, four axes of perspectives are proposed. The first three focus on the composition C+Al with suggestions of experiments that could be performed to complete the understanding of this alloy. The fourth axis gives guidelines for future alloy design.

The first axis focuses on the tensile behaviour of C+Al when submitted to the new thermomechanical strategy detailed in chapter 5. This new strategy is interesting as it permits to control independently different parameters of the microstructures by playing on each processing step. So far, only one set of microstructural parameters was studied. The recrystallisation step could be used to tune the grain size of the FCC matrix. The intermediate cold rolling step could be used to vary the density of intragranular nucleation sites for precipitates. The aging step could also be used to tune the number density and size of the intragranular and grain boundary precipitates. By finely controlling these multiple levers simultaneously, it might be possible to go forward in the coupling of large strength and large work-hardening capacity.

In term of mechanical characterisation, this work is restricted to tensile testing which could give a biased view of how interesting C+Al could be. The second axis of perspectives is the focus on other types of mechanical tests, such as Bauschinger experiments. A study of the rupture of C+Al with and without precipitates could also be an interesting subject of future research.

The third axis of perspectives is the study of mechanical properties at cryogenic temperatures. C+Al was derived from Cantor's alloy, which presents an intensification of mechanical twinning as the testing temperature decreases. This work focused on the tensile properties at room temperature.

While intense twinning was observed in single-phase FCC microstructures of large grain size, only rare, if any, mechanical twins were observed in microstructures of smaller FCC grain sizes and/or containing precipitates. This is most probably due to the limitation of the length scale over which twins can form. At cryogenic temperatures, mechanical twinning activates more widely and could maybe combine with precipitation to push further back the strength-ductility trade-off and challenge the last generations of AHSS.

Finally, the fourth axis of perspectives is the optimisation of chemical composition. The presence of aluminium in Cantor revealed interesting as a large variety of microstructures can be achieved through the activation of precipitation below 1100°C. Even if a single-phase FCC domain is maintained at high temperature, it revealed narrow, as shown in chapter 2. If considering a conventional steel rolling schedule, precipitation in C+Al would occur before the end of hot rolling inducing a significative increase in load that cannot be sustained by commonly used rolling mills. Decreasing the aluminium content in C+Al would lower the temperature at which precipitation occurs permitting easier processing. This decrease should not have an important effect on tensile properties as second cold rolling thickness or aging temperature and duration could be adapted. Moreover, the decrease in aluminium content in C+Al also decreases the fractions of σ phase. Even if no true link was made here between its presence and brittleness, it was often shown detrimental for mechanical properties.

Moreover, the presence of carbon was observed twice in this work to result in more intense twinning activity (C6Al in chapter 4 and carbon containing Cantor's alloy in chapter 6). The addition of a small fraction of carbon in multicomponent alloys could be interesting to keep in mind for the future developments of new multicomponent alloys.

A. MATERIALS AND METHODS

A.1. From raw materials to samples

A.1.1. Casting

Material casting was performed in a vacuum induction furnace in the facilities of the IMAP laboratory of the *Université catholique de Louvain* (UCL). The raw materials were bought from Strem Chemicals Inc[®], except from the ferromanganese alloys. Details on these products are given in **Table A.1**.

Table A.1 Details on the raw materials used for casting.

	Al	Co	Cr	Fe	Ni
Elemental form	Rod	Piece	Flake	Lump	Pellet
Purity (%)	99+	99.9+	99.3	99.98	99.9
CAS Number	7429-90-5	7440-48-4	7440-47-3	7439-89-6	7440-02-0

Three ingots of 1.1 kg were cast. The two first ingots were cast with a ferromanganese alloy from UCL. The ingot n°3 was cast with a ferromanganese alloy bought from American Elements. The chemical compositions of these two ferromanganese alloys are given in **Table A.2**.

Table A.2 Chemical compositions of the ferromanganese alloys used for casting, in atomic percent.

Ingot n°1-2		Mn	Si	C	P	S	Fe
	UCL	94.4	0.8	0.4	0.10	0.02	Balance
Ingot n°3		Mn	Si	Se	P		Fe
	American Elements	75.00	0.005	0.03	0.001		Balance

The chemical compositions of the three ingots were analysed in several locations by inductively coupled plasma linked to optical emission spectroscopy (ICP-OES). The presence of light elements was quantified with a combustion analyser. The results are reported in **Table 3.1** together with the targeted composition. The chapters in which the ingots are used are also specified. Ingots n°1-2 is referred to as C6Al while ingot n°3 as C5.3Al. The denomination C+Al includes both.

Table A.3 Chemical compositions of the three cast ingots measured with ICP-OES along with the targeted composition, in atomic percent. A combustion analyser is used for quantifying the presence of light elements.

Ingot n°	1	2	3	Targeted composition
Chapter(s)	2, 3	3, 4, 5, 6	5	
Al	6.1 ± 0.1	5.8 ± 0.1	5.3 ± 0.1	6
Co	18.8 ± 0.1	19.1 ± 0.2	19.0 ± 0.1	18.8
Cr	18.1 ± 0.5	17.9 ± 0.1	17.9 ± 0.3	18.8
Fe	19.2 ± 0.4	18.8 ± 0.1	19.8 ± 0.4	18.8
Mn	19.1 ± 0.2	19.1 ± 0.2	19.6 ± 0.2	18.8
Ni	18.8 ± 0.1	19.3 ± 0.1	18.2 ± 0.2	18.8
C	Not measured	0.12 ± 0.03	0.14 ± 0.00	0
N	Not measured	0.10 ± 0.03	0.08 ± 0.02	0
O	Not measured	0.02 ± 0.00	0.05 ± 0.02	0

The three ingots were cast with the objective of attaining the targeted composition given in the right of **Table A.3**. The observed deviations from the targeted composition come from the casting process. Despite its slightly lower aluminium content, the ingot n°3 was shown experimentally to match ingots n°1 and 2 in term of microstructures and hardness when submitted to given thermomechanical treatments. Moreover, the light elements were not intentionally introduced but come from the raw materials or the casting process. As ingots n°1 and 2 were cast with the exact same raw materials, similar levels of light elements are probable. Furthermore, ingots 2 and 3 present similar levels of light elements making them potentially comparable.

A.1.2. Processing

These three ingots were submitted to different processing routes. These will be presented in more details at the beginning of each chapter. This section aims to present the processing steps shared by multiple processing routes, along with the devices used.

Rolling is performed in the facilities of the 4MAT lab in the *université libre de Bruxelles* starting from an ingot thickness of 27 mm. After casting, ingots are always hot rolled at 1200°C in order to break the casting structure and to chemically homogenise the material. The hot rolling is performed as follows:

- an oven is positioned near the rolling mill and heated at 1200°C;
- the piece is put in the oven for 30 minutes;
- for each pass, the piece is taken out of the oven using long jaws, rolled and put back into the oven as fast as possible in order to limit the heat loss in the piece. Each pass corresponds to a thickness reduction of 1 mm. The oven is closed during the rolling pass.
- the piece is left in the oven for at least 5 minutes to heat up before starting the next pass;
- the thickness of the piece is controlled by comparing it to a thickness standard chosen according to the desired final thickness.
- when the thickness is judged satisfactory, the piece is put in the oven at 1200°C for 15 minutes to ensure its single-phase FCC microstructure. It is then water cooled.

The thickness reduction varies from 50 to 70%, corresponding to a Von Mises strain equivalents (ϵ_{VM}) of 0.8 to 1.4. The same procedure is used for the warm rolling of 304L at 200°C (c.f. chapter 6).

Rolling is also performed at ambient temperature, called cold rolling (CR). In this case, each pass corresponds to a thickness reduction of 0.1 mm. The final thickness reduction varies from 15 to 92% (ϵ_{VM} from 0.2 to 3). Most of the results presented in this word were acquired on pieces cold rolled for 80% ($\epsilon_{VM} = 1.9$).

The metal sheets obtained after rolling were cut using a Setocom-15 cutting machine from Struers®. 10S15 cutting blades for non-ferrous materials were used. In most cases, samples were cut as squares of 1x1 mm. Subsequently, samples requiring an annealing treatment were encapsulated in quartz tubes under argon atmosphere. A homemade device was used for such process. The sample is inserted in the quartz tube. Vacuum is then drawn with a vacuum pump. Three argon flushes are performed to remove residual oxygen. Finally, argon is introduced in the system with a pressure slightly lower than atmospheric pressure. The system is then put in rotation and locally heated with a welding torch until the tube seals.

Annealing, aging and recrystallisation treatments were performed in two ovens: Nabertherm® HTCT equipped with P330 controller up to 1400°C and Carbolite® AAF heating up to 1100°C. In each case, a

thermocouple was inserted inside the chamber of the oven such that its extremity falls about where samples are located. The setpoint temperature of the oven was adjusted in function of the value given by the thermocouple. In all cases, the oven was pre-heated to the targeted temperature before the sample was inserted. The targeted temperature is maintained until the sample is taken out of the oven. In the context of this work, samples were annealed for a wide range of temperatures, between 620 to 1200°C, and durations, between 1 minute to 1 month. Most of the annealing steps were followed by air cooling.

A.1.3. Sample preparation

All the consumables cited in this sub-section were bought from Struers®.

Before polishing, samples are hot mounted in a LABO-PRESS-3 mounting press with Polyfast resin. This type of resin is used because it is hard enough to endure hardness measurements and conductive to enable characterization in the scanning electron microscope (SEM).

Samples are then polished using silicon carbide papers of grain sizes FEPA P320, P500, P1200 and P2000, corresponding to grain sizes from 46 to 7 µm. Then samples are polished using diamond paste DP-Paste P with particle diameters of 3 µm on a DP-DUR polishing cloth. The final step of polishing is performed with OP-U NonDry solution containing a colloidal silica suspension, particle diameters of 40 nm, on a MD-Chem polishing cloth for 30 minutes.

A.2. Characterisation

A.2.1. Analysis by X-ray diffraction

The theory of X-ray diffraction (XRD) on crystals was established by W. H. Bragg in the beginning of the 20th century²⁶⁶. One family of crystallographic planes diffracts if it fulfils the following condition :

$$2d_{hkl}\sin\theta = \lambda \quad (\text{Eq. A. 1})$$

with d_{hkl} the interplanar spacing of the $\{hkl\}$ family of planes, θ the angle between the sample surface and the incoming beam and λ the incoming wavelength. With a known incoming wavelength, it is hence possible by varying the diffraction angle to determine the families of planes that a crystal contains. It then permits to identify the corresponding crystal lattice.

XRD was performed on a Bruker® D8 Advance Eco equipped with a X-ray source composed of a tungsten filament and a copper $K\alpha$ anode, resulting in a X-ray wavelength of $\lambda_{Cu}^{K\alpha} = 1.5405 \text{ \AA}$. The aging of the X-ray source results in the deposition of tungsten near the anode. This tungsten deposit also emits X-rays but at the different wavelength of the $L\alpha$ of tungsten at $\lambda_W^{L\alpha} = 1.4764 \text{ \AA}$. This results in the presence of additional peaks on the diffractograms.

Fig. A.1 gives an example of diffractogram measured on a fully FCC C6Al sample (from chapter 2). The typical peaks observed for the FCC phase with the copper source are present (green open triangle). Shifted towards lower diffraction angles, an additional series of peaks is also observed (solid purple diamond). This series comes from the diffraction of the X-rays emitted by the tungsten deposit on the same FCC lattice. They are significantly less intense and as such they cannot be mistaken with the peaks of the FCC matrix from the copper source. However, they could be mistaken with peaks coming from second phases.

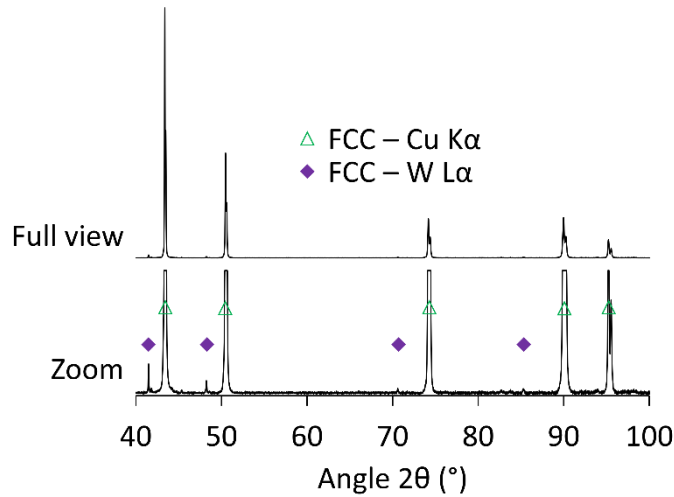


Fig. A.1 Diffractogram of the C6Al blank test specimen annealed at 1000°C extracted from chapter 2. It presents two series of FCC peaks from the copper and tungsten sources. [Full-size](#).

Phase identification was performed with the software Bruker® DiffraC.Eva. Phase quantification was performed by Rietveld refinement with the software Bruker® DiffraC.Topas. Spherical harmonics of order 8 were used for FCC, B2 and σ phases. When negative peaks appeared for the σ phase in the fitted diffractogram, the order of spherical harmonics for this phase was decreased until these peaks disappeared.

XRD was also used to measure dislocation densities via the widening of diffraction peaks. The following formula was used ²⁶⁷:

$$\rho = \frac{3\sqrt{2\pi}\langle\varepsilon^2\rangle^{0.5}}{Db} \quad (\text{Eq. A. 2})$$

with $\langle\varepsilon^2\rangle^{0.5}$ the averaged microstrain, D the crystallite size and b the intensity of the Burgers vector. The crystallite size was fitted on the FCC peaks by a Lorentzian-type approach. The parameter *LVol-IB* was used, in accordance with the technical manual of the software. To calculate the microstrain, a strain contribution of Gaussian-type was added to the FCC fit. The microstrain then corresponds to the parameter e_0 given by Topas.

Finally, the crystallographic texture of the FCC matrix was measured by XRD. The crystallographic texture relates to the orientation of crystals. Each crystal, which could be a grain or part of a grain, presents a lattice that might be rotated from its neighbours. Its specific orientation is then defined as the 3D rotation required to rotate a reference axis system to match the orientation of the grain. This rotation can be decomposed in three rotations around the three axes of the reference system. The three corresponding rotation angles are called the Euler angles. Crystallographic texture is the measure of the distribution in orientation in the sample. It is plotted against random texture where all orientations are present in equal proportion, corresponding to a texture index of 1. A specific orientation presenting a texture index of 2 is present twice more than another orientation belonging to the random texture.

Different ways exist to plot crystallographic texture, e.g. pole figures (PF), inverse pole figures (IPF) or orientation density figures (ODF). In this work, ODF was chosen to present texture, as it permits in a single figure to inform on the global texture of the specimen, where several PFs or IPFs would be necessary. For cubic lattices, including FCC, an ODF can be seen as a cube. Its three axes correspond to

the Euler angles, from 0 to 90°. The orientation of any crystal can be represented in the ODF by a point with coordinates equal to its Euler angles. Some of these orientations are commonly found in FCC lattice and might be indicative of the material state. These are called texture components (TC). For example, the Cube TC is observed after recrystallisation of aluminium alloys, whereas copper and S TCs are indicative of a FCC material with high SFE deformed by cold rolling.

An ODF is often cut into sections along the ϕ_2 direction. The most commonly used section is that at 45° as it gathers most common TCs observed in FCC lattice (**Fig. A.2**).

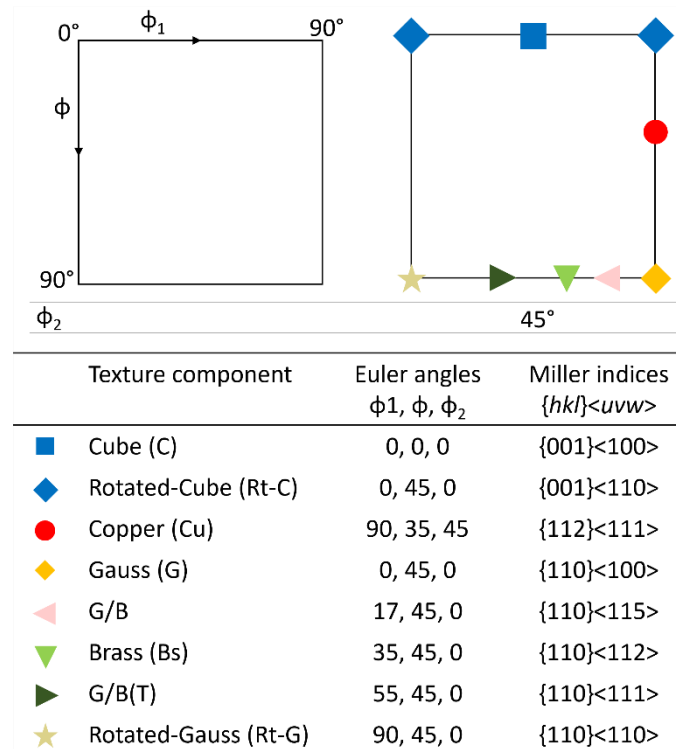


Fig. A.2 Schematic representations of the section at $\phi_2 = 45^\circ$ of the ODF. The most common TCs are superimposed on this section. The table on the right indicates the corresponding Euler angles and Miller indices. [Full-size](#).

Measures of the crystallographic texture were performed on a Bruker® D5000 using a molybdenum K_α source of wavelength $\lambda = 0.7093 \text{ \AA}$. At least the (111), (220) and (331) pole figures were measured. The (200) pole figure was added when the corresponding peak was sufficiently intense. The software Diffrac.Texture was used to treat the data and to plot the ODFs. The rank 18 of the harmonic expansion is used.

A.2.2. Microstructural characterization

This part describes the several types of microscopy used in this work, and their specific uses.

Optical microscopy was performed on an Olympus® DSX510. This microscope permits observations in bright field (e.g. **Fig. A.3A**), where the brightest elements in the sample appear white in the image, and in dark field (e.g. **Fig. A.3B**), where the brightest elements appear black. This last imaging mode reveals precipitates (appearing bright) with a better contrast, as can be observed by comparing **Fig. A.3A** and B. As precipitate populations are not the same in recrystallised and non-recrystallised zones, dark field imaging was used to measure recrystallisation fraction by systematic manual point counting²⁶⁸. This method consists in superimposing a grid on the image to characterize. Then, the intersections located

in recrystallised regions, or in non-recrystallised regions, are counted. The recrystallisation fraction is the number of intersections falling in recrystallised regions divided by the total number of intersections (e.g. 10/25 in **Fig. A.3C**). In this work, grids of 19x19 intersections are used, i.e. 361 intersections. A minimum of ten images were acquired for each set of processing parameters in order to get a satisfactory statistic.

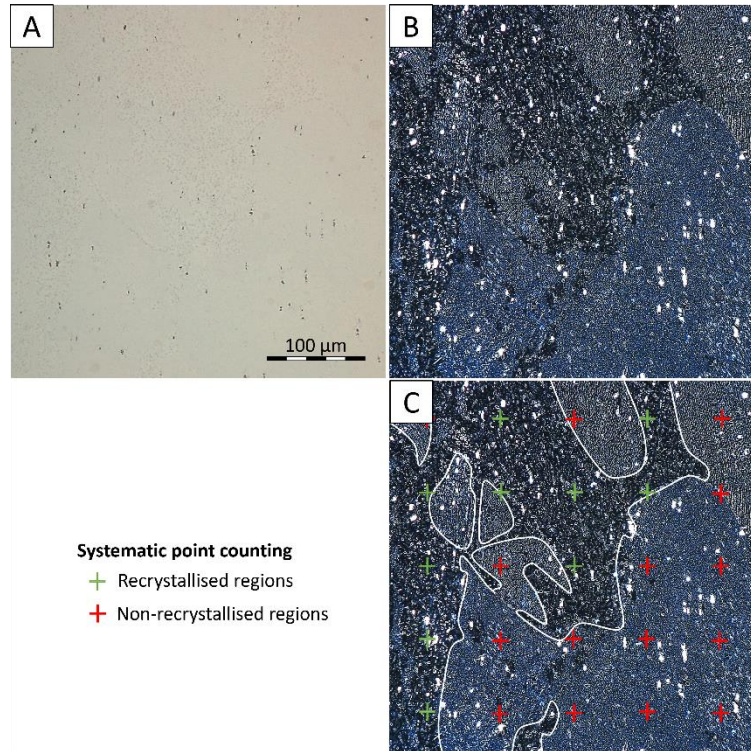


Fig. A.3 Optical microscopy of a sample cold rolled for 58% and annealed for 50 hours at 900°C (c.f. H-CR58-900°C/50h in chapter 3). (A) Bright field image. (B) Dark field image. (C) Dark field image with systematic point counting superimposed. The green and red intersections are located in recrystallised and non-recrystallised regions, respectively. The white line indicates the separation between these two regions. [Full-size](#).

Scanning electron microscopy (SEM) characterization was conducted using a Hitachi SU70 FEG-SEM equipped with two detectors collecting two types of electrons: secondary electrons (SE) and backscattered electrons (BSE). SEs inform on the topography of the sample, while BSEs inform on the local atomic weight. Observations from magnifications of 50 to 20k were performed with operating voltages between 5 and 20 kV. Most micrographs presented in this work were acquired using the BSE detector.

This microscope is coupled to an energy dispersive spectroscopy (EDS) detector from Edax®. EDS permits to measure local chemical compositions. As electrons are focused locally on the sample surface, they transfer part of their energy to electrons of the analysed material, which tend to become excited. Their transition back to their ground state releases X-rays. The energy of these X-rays depends on the nature of the excited chemical element, permitting their identification. EDS measurements were always performed at a working distance of 15 mm and at an operating voltage of 15 kV.

Electron backscattered diffraction (EBSD) has also been used in the same microscope. EBSD is based on the diffraction of BSEs. The sample is first rotated of 70° from its initial horizontal position to maximise the diffraction intensity. The diffraction of electrons by crystallographic $\{hkl\}$ planes, when Braggs conditions for diffraction are fulfilled²⁶⁶, creates two diffraction cones (green in **Fig. A.4**). The orientation of the cones depends on the orientation of the $\{hkl\}$ planes. Their intersections with the

detectors, a flat surface, are hence seen as straight lines, also called Kikuchi lines. The superposition on the detector of the Kikuchi lines of all the diffracting families of planes creates the Kikuchi diagram. The EBSD software then compares this diagram with known diagrams in order to determine the nature of the analysed crystal and its crystallographic orientation. The acquisitions and comparisons of Kikuchi diagrams are performed in real time while the electron beam scans the sample surface.

The step of the scanning, i.e. the distance between two subsequent acquisitions, is an important parameter. It determines the resolution of the EBSD dataset but is also directly linked to the duration of the acquisition. It must be adjusted according to the size of the scanned region.

After the acquisition of the full EBSD dataset, it is possible to visualise on colourful maps the local nature of grains and their orientations. Orientation is often presented with IPF maps which present the local crystallographic directions aligned with a known macroscopic direction.

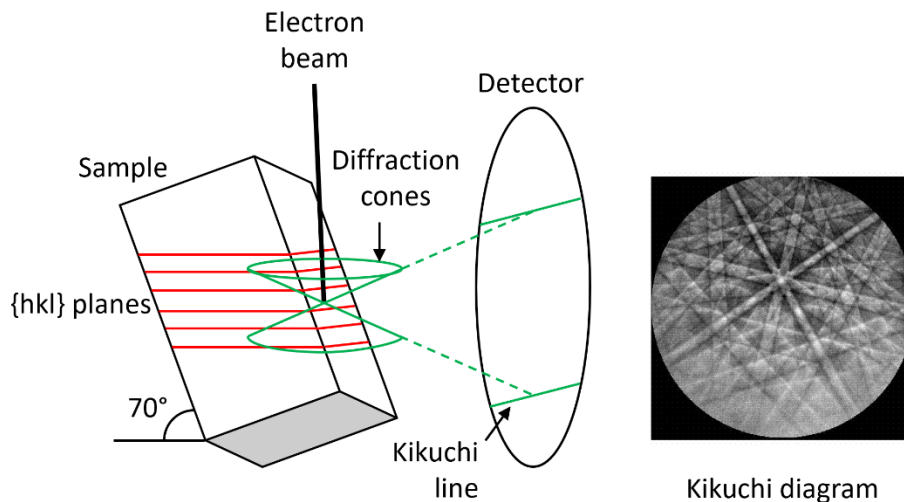


Fig. A.4 How EBSD works. Adapted from ²⁶⁹. [Full-size](#).

In the context of this work, EBSD datasets were recorded with an Hikari® CCD camera, at operating voltages of 15 or 20 kV. The scanning step was adjusted in function of the size of the scan, ranging from 50 nm to 3 μm . Depending on the clarity of the Kikuchi diagrams, the scanning speed was adjusted from 10 to 200 frames per second. Usually, a small step requires a low scanning speed.

All the EBSD datasets acquired during this work were cleaned with TSL® OIM Analysis™ software before being analysed or presented. The cleaning procedure is as follows:

- a grain dilation step was conducted with a grain tolerance angle of 5° and a minimum grain size of 5 pixels;
- a confidence index standardisation was then applied with the same parameters;
- the grains presenting a confidence index lower than 0.1 were removed. They appear black on the maps.

The analysis of the EBSD datasets was then performed with the same software. Crystallographic orientations are presented as IPF-Z maps. The macroscopic direction Z is then defined as the perpendicular direction of the section analysed. For example, if the IPF of a section RD-TD is presented, the crystallographic directions given on the map are parallel with the ND direction. In order to identify the three main phases of interest, FCC, B2 and σ , the files corresponding to phases present in steels: austenite, ferrite and the σ phase, are used. These three phase files gave satisfactory results on the

alloys considered in this work. FCC, B2 and σ phases always appear respectively green, red and blue on phase maps.

From EBSD datasets, it is also possible to measure grain sizes. This is typically performed on large areas where a large number of grains are observed. To calculate the grain size, the annealing twins are first excluded from grain boundaries. Then, the grain size is determined by using the formula below:

$$\bar{d} = \frac{\sum A_i d_i}{\sum A_i} \quad (\text{Eq. A. 3})$$

where A_i and d_i are the area and diameter of grain i . This type of weighted average is used to better represent microstructures with heterogeneous distributions of grain sizes.

EBSD also permits to divide between recrystallised and non-recrystallised grains based on their grain orientation spread (GOS). The GOS index calculates the standard deviation in orientation in a grain. Hence, a recrystallised grain presents a low GOS while a deformed grain presents a large GOS²⁷⁰. The threshold of 4° was chosen based on cases where the identification of the recrystallised and non-recrystallised regions was easy, as in **Fig. A.5**.

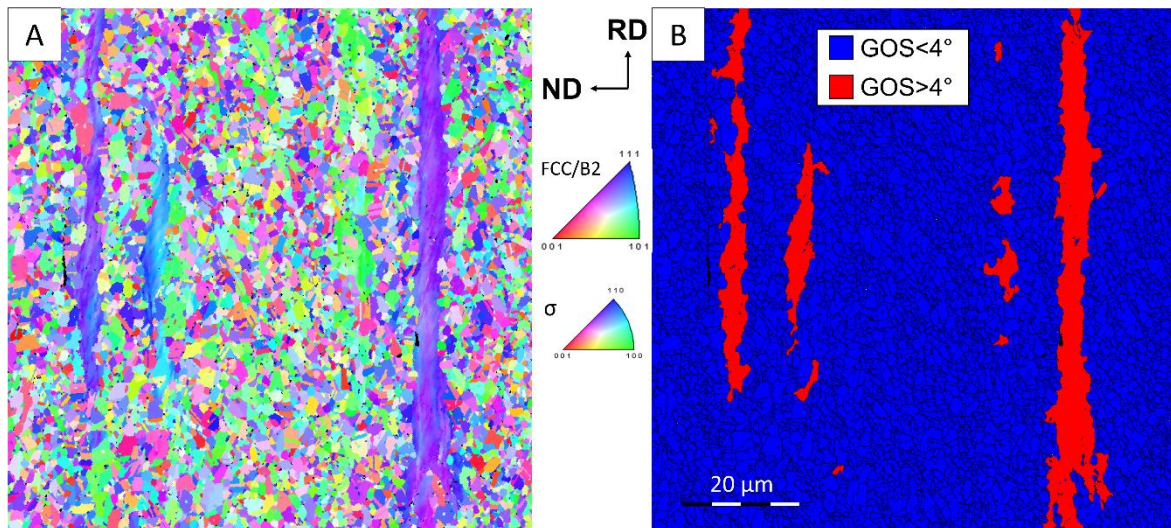


Fig. A.5 EBSD dataset acquired on a partially recrystallised sample processed with route CR with a rolling thickness reduction of 80% and annealed at 900°C for 1 hour. (A) IPF-Z map. (B) On this map, the grains presenting a GOS index below 4° are coloured in blue and those with a GOS larger than 4° in red. [Full-size](#).

Crystallographic textures were also calculated from EBSD datasets acquired on large areas. At smaller scales, EBSD was used to study the populations of precipitates and to confirm the presence of deformation twins.

Transmission electron microscopy (TEM) was used to determine the local morphology, structure and chemistry of the material at large magnifications, up to 150k. This technique is based on the interaction of an electron beam of high energy with a thin sample. The collection and analysis of transmitted electrons permit to inform on the analysed sample. TEM works in two modes: imaging and diffraction (**Fig. A.6**).

- The imaging mode permits to acquire micrographs of the analysed sample. It informs on its morphology. In this mode, the object plane of the intermediate lens is aligned with the image plane of the objective lens.

- The diffraction mode permits to acquire diffraction patterns. It informs on the lattice structure of the analysed material. A diaphragm is used to limit the diffracting region to a single diffracting crystal. In this mode, the object plane of the intermediate lens is aligned with the focal plane of the intermediate lens.

Switching between the modes is performed by modifying the focalisation of the intermediate lens.

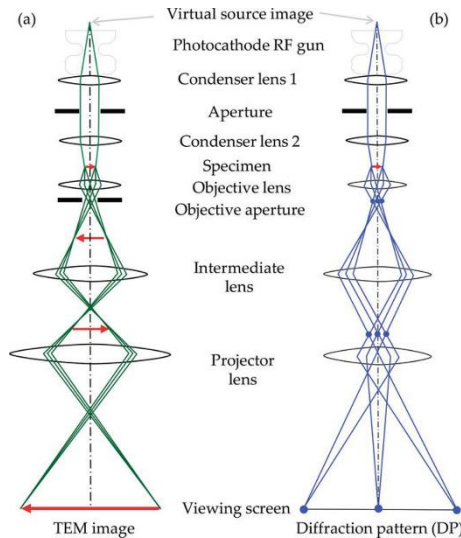


Fig. A.6 The two operation modes of TEM. (A) Imaging mode. (B) Diffraction mode. From ²⁷¹. [Full-size](#).

Two transmission electron microscopes were used during this work: a JEOL 2000 EX for structure and morphology determination, and Tecnai G2 20 S-TWIN TEM equipped with a Xflash® 6T | 60 BRUKER® EDS detector for chemical analyses. Samples studied in TEM were thinned first mechanically to approximately 100 μm and then electrochemically by a twinjet electropolisher. The electrolytical thinning process was performed by immersing the samples in a mixture of 10 vol.% perchloric acid in acetic acid at 30 V and 15°C.

A.2.3. Mechanical characterization

Mechanical characterization was performed first by hardness measurements. This technique permitted to get a quick overview of the influence of processing parameters on strength. Hardness measurements were performed on an Innovatest® Falcon 500. At least 10 indents were performed on each specimen. The indentations were performed with a pyramidal Vickers indenter and a load of 500g.

Nano-indentation was used to measure the intrinsic strength of the FCC, B2 and σ phases. These measurements were performed on the Hysitron Inc. Triboindenter equipped with a Berkovitch tip. This device is also equipped with a scanning probe microscope permitting to image the sample surface. Measurements were performed on two samples. The first sample was annealed for 50 hours at 900°C directly after hot rolling in order to form large precipitates. The second sample was cold rolled for 58% and then annealing for 50 hours at 900°C (corresponding to H-CR58-900°C/50h), resulting in a microstructure closer from those studied in this work. The measurements on both samples gave similar values. A target load of 3 mN was used. At least 4 nano-indentations were performed on each phase.

Tensile properties were measured at room temperature on a Zwick Roell Z100. Dog-bone-shaped tensile specimens with gauge length of 30 mm and width of 6 mm were machined from the rolled sheets. The precise dimensions are given in **Fig. A.7**. Both sides of specimens were ground using SiC

paper P2000 to ensure the absence of oxides or defects on the surface. Final thickness between 0.6 and 1.4 mm were achieved. Annealing treatments were performed on the machined specimens encapsulated in quartz capsules after polishing. Tensile tests were performed at an engineering strain rate of $2 \cdot 10^{-3} \text{ s}^{-1}$.

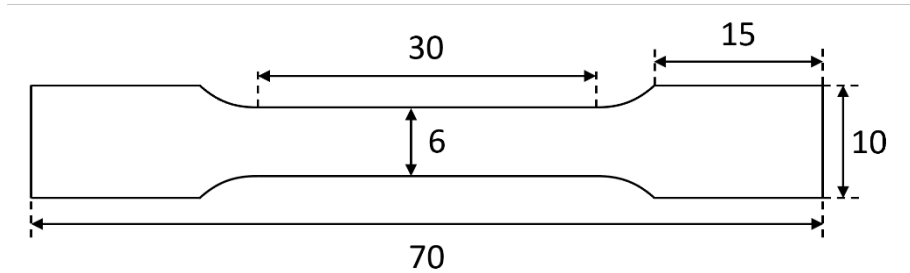


Fig. A.7 Dimensions of the tensile specimens used. [Full-size](#).

After tension, data treatment was performed with Microsoft® Excel software. Engineering stress σ_E , and strain ε_E , provided by the tensile machine, were converted to true strain ε_T , and true stress σ_T , by using the following formulae.

$$\varepsilon_T = \ln(1 + \varepsilon_E) \quad (\text{Eq. A. 4})$$

$$\sigma_T = \sigma_E * (1 + \varepsilon_E) \quad (\text{Eq. A. 5})$$

A Visual Basics for Application (VBA) macro was written to compute the work-hardening rate. The slope of the true stress-true strain curve is computed on intervals of 100 experimental points.

A.3. Phases of interest in C+Al

A.3.1. The FCC phase

The FCC phase of C+Al is a supersaturated solid solution of six chemical elements. Chemical homogeneity was verified by EDS on the ingot n°1 (C6Al) after hot rolling for a thickness reduction of 70% (**Fig. A.8**). The six chemical elements composing C6Al are homogeneously distributed in the material as shown by the six EDS mappings. The material is hence considered chemically homogeneous after hot rolling, at least at the resolution of the EDS in the SEM ($1 \mu\text{m}$). As the same hot rolling procedure was applied to the two other ingots, they are expected to be chemically homogeneous.

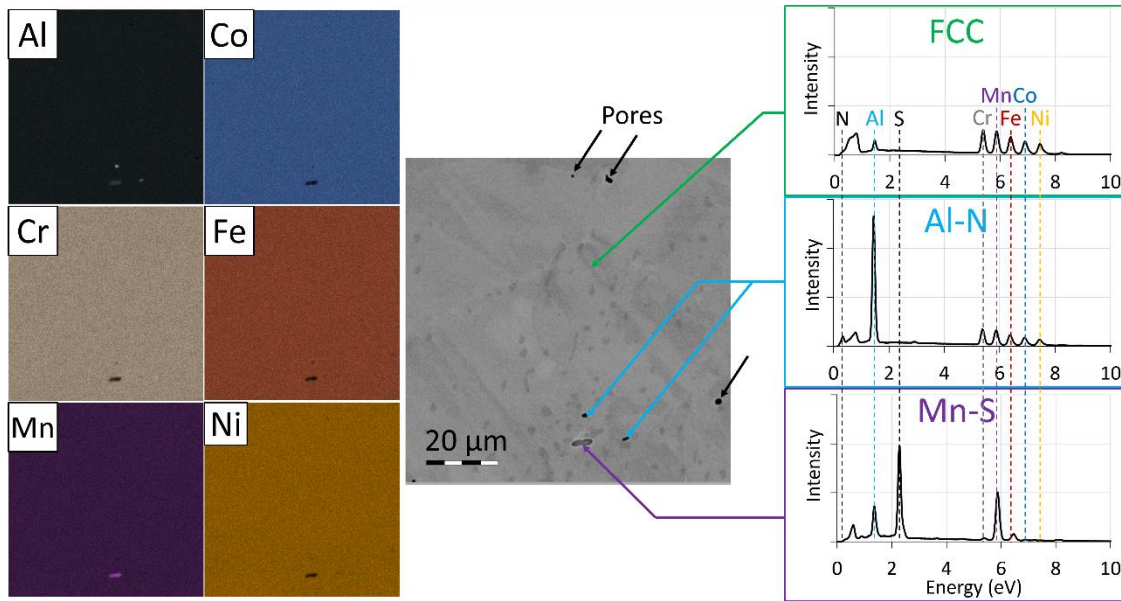


Fig. A.8 Verification of the chemical homogeneity of the ingot n°1 of C6Al. The BSE SEM image of the analysed zone is given in the middle. On the left are the EDS mappings corresponding to the six elements composing C6Al. On the right are shown the EDS energy plots obtained on the locations indicated by the arrows. The vertical scales of the three graphs are the same. [Full-size](#).

As shown in the right of **Fig. A.8**, inclusions are present. They are of two types: (Al, N) and (Mn, S). In addition, (Mn, S) inclusions in C5.3Al were found to contain selenium. Pores are also present in all ingots. All these inclusions and cavities are inherited from casting. They are found whatever the subsequent processing steps. Their fractions remain limited as they are not detected with XRD.

A.3.2. The second phases

ThermoCalc software with inputs from the TCHEA4 thermodynamic database was used to predict the phase equilibria in Cantor's alloy as a function of aluminium addition (**Fig. A.9A**). The calculated isopleth shows that the addition of 6 at.% of aluminium results in the stabilisation of the B2 phase below 1150°C. The σ phase is also predicted to form below 920°C. In addition, the composition allows a full FCC field to be maintained between 1150 and 1290°C. This is consistent with the need to carry out hot working in the FCC phase. **Fig. A.9B** presents the phase volume fractions of C6Al.

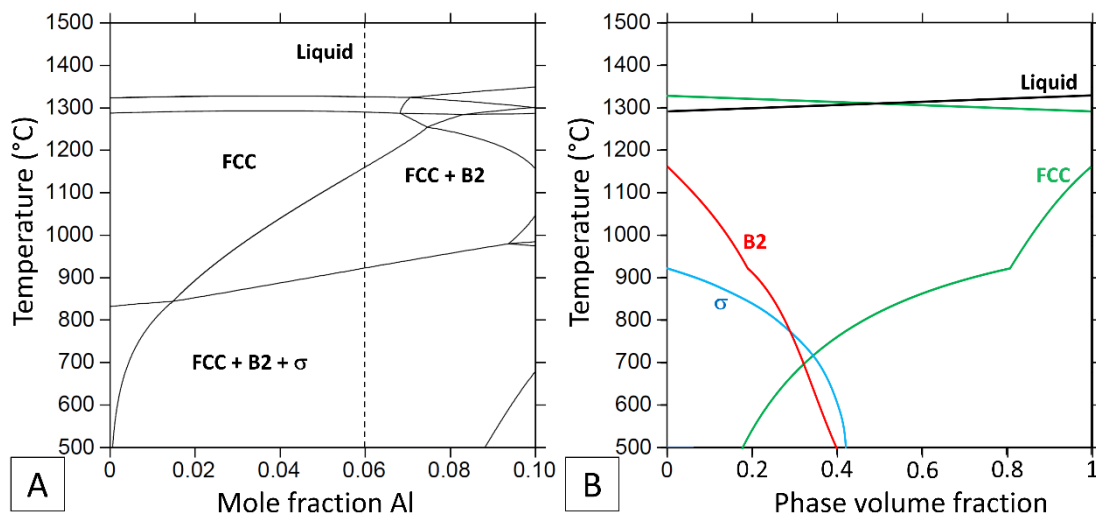


Fig. A.9 (A) CoCrFeMnNi + Al phase diagram. The dashed line corresponds to C+Al with 6 at.% of aluminium. (B) Volume fractions of the stable phases in the composition C6Al. [Full-size](#).

MATERIALS AND METHODS

Nano-indentation testing was performed on the FCC, B2 and σ phases with a load of 3 mN. The results are given in **Table A.4**. As expected based on their natures and on literature, the σ phase is the hardest. The FCC is the softest. These measurements confirm the strengthening capacity of B2 and σ phases when precipitating in the FCC matrix of C+Al.

Table A.4 Hardness of the phases stable in C+Al measured by nano-indentation with a load of 3mN.

Phase	FCC	B2	σ
H (GPa)	3.7 ± 0.7	5.9 ± 0.7	14.3 ± 0.3

B. RÉSUMÉ SUBSTANTIEL [FR]

Introduction

De nos fourchettes aux applications les plus high-tech, les matériaux métalliques sont partout dans notre société actuelle. Ces matériaux sont rarement composés d'un seul élément chimique. La plupart sont des mélanges, appelés alliages, composés d'une combinaison de nombreux éléments chimiques. Jusqu'à récemment, ces alliages étaient développés selon la même stratégie. Un alliage est basé sur un élément chimique principal qui représente plus de 60% du matériau. Par exemple, le fer est l'élément principal des aciers. De petites quantités d'autres éléments, e.g. carbone, chrome, nickel, etc..., sont ensuite ajoutées pour optimiser les propriétés de l'alliage à ses applications.

En s'affranchissant de cette stratégie conventionnelle, un nouveau type d'alliages a été développé. Ces alliages – désignés comme multi-composants ou à plusieurs éléments principaux – se basent sur la combinaison de plusieurs éléments chimiques dans des proportions similaires. Ce qui attira l'attention sur les alliages multi-composants fut que certains de ces alliages sont formés d'un faible nombre de phases, certains étant même monophasés. La formation de ces microstructures simples fut attribuée à leur entropie configurationnelle élevée, aussi appelé *effet haute entropie*. De plus, leurs chimies complexes devaient leur conférer un réseau métallique distordu, une diffusion chimique ralentie et la possibilité de combiner des propriétés jugées jusque-là opposées – aussi appelé *effet cocktail*. De plus amples recherches montrèrent que ces effets étaient reliés non pas à la complexité de la chimie mais au choix des éléments, et ne sont donc pas reliés intrinsèquement aux alliages multi-composants.

Parmi cette jeune famille des alliages multi-composants, l'alliage de Cantor, de composition équimolaire CoCrFeMnNi, sortit du lot du fait de sa structure monophasée cubique face centrée (FCC) mais aussi de l'activation du maclage pendant la déformation. Ces deux éléments procurent à cet alliage des propriétés mécaniques intéressantes à température ambiante et cryogénique. Ainsi, l'alliage de Cantor devint un alliage de base pour des optimisations chimiques ou microstructurales supplémentaires. De nombreuses stratégies ont été essayées avec un intérêt particulier pour l'ajout d'aluminium qui induit la stabilisation de la phase B2 (à cristallographie cubique centrée (BCC) ordonnée), plus dure que la matrice FCC. De plus, à des taux d'aluminium inférieurs à 7 at.%, un domaine monophasé FCC est maintenu à haute température permettant une mise en forme facilitée. Dans ce manuscrit, il a été choisi d'étudier l'alliage de Cantor auquel 5-6 at.% d'aluminium a été ajouté, alliage appelé C+Al dans la suite.

Chapitre 1. Etat de l'art

Le premier chapitre se penche sur la théorie. Il est divisé en trois parties concernant la déformation d'un alliage FCC à faible énergie de faute d'empilement (SFE), la recristallisation et la précipitation.

Les alliages FCC à faible SFE se déforment principalement par glissement de dislocations. Sous l'effet de la contrainte appliquée, les dislocations se multiplient et interagissent, durcissant le matériau. Une contrainte supérieure est alors nécessaire pour poursuivre la déformation, phénomène appelé écrouissage. Ce phénomène est opposé à la restauration dynamique qui adoucit le matériau par l'annihilation ou l'organisation des dislocations.

Le taux d'écrouissage, i.e. la pente de la partie plastique de la courbe contrainte-déformation, est utilisé pour étudier le comportement d'un matériau lorsque soumis à une contrainte. Son évolution

renseigne sur la balance entre écrouissage et restauration, ou sur l'activation de mécanismes de déformation supplémentaires.

Dans les alliages FCC à faible SFE, le maclage peut être activé et induit alors une augmentation du taux d'écrouissage. De même, des bandes de cisaillement peuvent se former lorsque l'élongation est importante. Elles induisent le même effet. Cette description s'applique aux aciers inoxydables austénitiques, aux aciers TWIP ou à l'alliage de Cantor.

L'ensemble des défauts stockés dans la microstructure pendant la déformation, principalement sous forme de dislocations, constitue la force motrice de phénomènes d'adoucissement tels que les restaurations et recristallisations statiques ou dynamiques. Ces mécanismes requièrent un apport énergétique pour être activés, à l'exception de la restauration dynamique qui est active à température ambiante. À la suite de la déformation, un recuit peut être utilisé pour provoquer l'activation de ces phénomènes.

Dans les alliages FCC à faible SFE, la restauration est limitée. Le principal mécanisme d'adoucissement activé est la recristallisation. La recristallisation est composée de deux étapes : nucléation et croissance. Lors de la nucléation, des volumes dénués de dislocations présents après déformation se développent jusqu'à atteindre la taille critique de stabilité. De tels volumes se forment notamment proche de défauts tels que les joints de grain, les interfaces avec des inclusions ou précipités... Ensuite, ces germes croissent en consommant la matrice déformée alentour. La forme et la taille des grains recristallisés dépendent des conditions de recuit mais aussi des conditions de déformation.

Un autre phénomène pouvant être activé pendant un recuit est la précipitation. La précipitation est la transformation d'un volume d'une phase en une autre dont la nature et/ou la chimie diffère. La précipitation est déterminée par la thermodynamique, régissant la force motrice de précipitation, et la diffusion, contrôlant les mouvements des différents éléments chimiques dans l'alliage. La première est maximale à température faible alors que la deuxième l'est à température élevée. Il en résulte que le taux de nucléation de précipités est maximal aux températures intermédiaires, températures définies selon les phases en présence et le matériau.

La présence de précipités entraîne des interactions avec la recristallisation. Premièrement, si les précipités sont suffisamment fins, ils peuvent épingler les joints de grain, limitant ainsi la recristallisation (**Erreur ! Source du renvoi introuvable.**A). Deuxièmement, si les précipités sont suffisamment gros et sont présents avant déformation, de forts champs de contrainte se développent autour de ces précipités pendant la déformation. Il en résulte la nucléation de germes recristallisés préférentiellement autour des précipités. Ce phénomène est appelé nucléation stimulée par précipitation (PSN).

Pour finir, la présence de précipités dans les microstructures finales entraîne un durcissement. Ce durcissement est différent selon la localisation et la forme des précipités. Lorsque formés aux joints de grain, le durcissement est dit composite. Les résistances des phases composant la microstructure sont ajoutées selon une loi des mélanges. Les paramètres importants ici sont les fractions de phase. Si les précipités sont présents à l'intérieur des grains, deux cas peuvent survenir. Si les précipités sont fins et cohérents, ils sont cisailés par les dislocations. Dans le cas contraire, les dislocations bouclent autour des précipités. Dans C+Al, les précipités ne sont pas cohérents et correspondent donc au deuxième cas. Le renforcement est maximal pour de fins précipités peu espacés.

Ce travail vise d'abord à évaluer le comportement de cet alliage lorsque soumis aux étapes de traitement utilisées conventionnellement dans l'industrie. Les chapitres 2 et 3 se concentrent sur le comportement de C+Al lorsque soumis au laminage à chaud, et au laminage à froid suivi de recuits.

Chapitre 2. Effet de la précipitation sur la compression à chaud de C+Al

Le laminage à chaud est simulé dans le chapitre 2 par des essais de compression entre 900 et 1100°C. Comme prévu dans un alliage FCC de faible SFE, la recristallisation dynamique est activée pendant la déformation aux quatre températures étudiées.

L'activation de la recristallisation dynamique est observée clairement sur les courbes contrainte-déformation avec la présence de pics de contrainte. À 1000-1100°C, C+Al se comporte comme un alliage à solution solide, comme le confirme sa proximité avec un acier inoxydable austénitique conventionnel de grade 304L. Des valeurs de contrainte supérieures ont toutefois été observées pour C+Al en raison d'un renforcement par solution solide plus important. La traînée de soluté (*solute drag*) pourrait également être présente et serait à l'origine des tailles de grains recristallisés plus faibles observées dans C+Al. A 900-950°C, les niveaux de force présentés par C+Al excèdent largement ceux présentés par l'acier 304L. Cela est couplé à une chute de l'intensité de la recristallisation dynamique dans C+Al. A ces températures, la précipitation de la phase B2 épingle les joints de grains recristallisés limitant l'intensité de la recristallisation dynamique.

La déformation à chaud de C+Al dépend donc largement des températures de déformation. À 1000-1100°C, où C+Al reste monophasé FCC, de grandes réductions d'épaisseur seraient possibles sans augmentation excessive de la charge. A l'inverse, le laminage à chaud semble difficile entre 900-950°C où la contrainte atteint jusqu'à 450 MPa en raison de la limitation de la recristallisation dynamique par la précipitation.

Chapitre 3. Laminage à froid et interactions entre recristallisation et précipitation pendant les recuits ultérieurs

La première partie du chapitre 3 se concentre sur le comportement de C+Al lorsque déformé par laminage à froid dans le domaine monophasé FCC jusqu'à une réduction d'épaisseur de 92%. L'analyse des microstructures révèle que la déformation est contrôlée par le glissement des dislocations (gradients de couleur sur **Erreur ! Source du renvoi introuvable.**A). De plus, le maillage mécanique s'active dès 20% de réduction d'épaisseur. L'activation du maillage mécanique dans C+Al n'est pas surprenante au regard de sa faible SFE. De plus, des bandes de cisaillement apparaissent à des réductions supérieures à 60%. L'évolution de la texture cristallographique, suivie pendant le laminage à froid par XRD, confirme cette séquence d'événements. Lorsqu'il est entièrement FCC, le comportement du C+Al pendant le laminage à froid est comparable à celui d'autres matériaux métalliques FCC à faible SFE, tels que les aciers inoxydables austénitiques ou les aciers TWIP. L'absence de transformation de phase induite par la déformation et l'observation de macles mécaniques le rapprochent des aciers TWIP.

La deuxième partie du chapitre 3 s'intéresse aux recuits suivant le laminage à froid. Les transformations microstructurales dépendent principalement de la température de déformation. En dessous de 800°C, la précipitation gouverne l'évolution des microstructures, résultant en un matériau restauré contenant une fine dispersion de précipités à l'intérieur des grains et des précipités plus gros aux joints de grains. À 1000°C et plus, c'est la recristallisation statique qui prévaut. La recristallisation complète est atteinte rapidement et de rares précipités sont observés. Entre les deux, précipitation et recristallisation sont significativement activées, induisant de fortes interactions. Dans ce dernier cas, l'énergie stockée détermine si une région de la microstructure recristallise en premier et subit ensuite une précipitation aux joints de grains nouvellement formés, ou si des précipités se forment d'abord à l'intérieur des grains déformés, retardant ainsi la recristallisation. Il en résulte des microstructures composites avec

des tailles de grain inférieures à 5 μm mais avec une recristallisation complète obtenue après plusieurs dizaines d'heures. Un laminage à froid plus intense accélère les cinétiques de recristallisation.

Chapitre 4. Une large gamme de propriétés en traction à partir de la seule composition C+Al

Sur base de la compréhension des transformations microstructurales dans C+Al acquise dans la deuxième partie du chapitre 3, trois microstructures ont été sélectionnées pour les essais de traction. Ces microstructures ont été choisies pour représenter toute l'étendue des microstructures qui peuvent être obtenues après recuit avec une microstructure monophasée FCC à gros grains, une microstructure complètement recristallisée et triphasée FCC/B₂/ σ , et une microstructure partiellement recristallisée et triphasée FCC/B₂/ σ .

Les propriétés en traction de ces trois microstructures sont détaillées au chapitre 4. Une large gamme de propriétés de traction est observée avec des limites d'élasticité allant de 300 à 1050 MPa et des allongements uniformes allant de 4 à 61%.

Les mécanismes de renforcement contribuant le plus ont été identifiés par la simulation analytique des limites élastiques. La phase FCC contribue pour au moins la moitié des limites d'élasticité totales, principalement en raison des petites tailles de grain des deux microstructures triphasées. De plus, la précipitation intragranulaire de B₂ s'est révélée plus efficace que la précipitation de B₂ aux joints de grains.

L'analyse des comportements d'érouissage a révélé que le maclage mécanique est activé pendant la déformation de l'échantillon monophasé. Dans les microstructures multi-phasées, la déformation est localisée dans la matrice FCC. La ductilité est limitée par la faible taille des grains et par la présence importante d'interfaces.

Chapitre 5. Développement de microstructures à érouissage amélioré par précipitation intragranulaire

Le chapitre 5 s'intéresse au développement de microstructures associant une grande limite d'élasticité et une capacité importante de durcissement par érouissage (WHC). Une nouvelle voie thermomécanique est développée afin de maximiser la fraction de précipitation intragranulaire et donc de maximiser le durcissement cinématique. Cette nouvelle voie comprend quatre étapes : laminage à froid avec une réduction d'épaisseur de 80% (CR80), une étape de recristallisation (RX), une deuxième étape de laminage à froid de 15% (CR15) et une étape de vieillissement de 1 heure à 800°C. Pendant l'étape de recristallisation à haute température, la recristallisation complète est atteinte rapidement – en quelques minutes par rapport à plusieurs dizaines d'heures à des températures plus basses. Pendant la deuxième étape de laminage à froid, des dislocations sont stockées à l'intérieur des grains et servent ensuite de sites de nucléation pour les précipités pendant le vieillissement. Il en résulte une microstructure homogène constituée de gros grains FCC contenant de fins précipités B₂ intragranulaires. Des précipités B₂ et σ sont également présents aux joints de grains. Sans la deuxième étape de laminage à froid, seuls les précipités aux joints de grain se forment.

Les propriétés en traction ont été mesurées après RX, RX+800/1h (sans CR15), RX+CR15 et RX+CR15+800/1h. Les propriétés en traction après RX et RX+800/1h sont similaires avec une limite d'élasticité faible, autour de 300 MPa, et une WHC élevée, de 560 MPa. Le maclage est alors activé pendant la traction. Après, RX+CR15, la limite d'élasticité augmente mais avec une chute de WHC.

RX+CR15+800/1h présente une augmentation de limite élastique, à 880 MPa, et de WHC, à 560 MPa, par rapport à RX+CR15. Or, cette WHC élevée n'est pas due à l'activation du maclage comme dans RX et RX+800/1h. La précipitation intragranulaire est à l'origine de ces deux augmentations.

La contrainte d'écoulement a été simulée analytiquement afin de décorréler ses multiples contributions. Cela a permis de déterminer que les précipités intragranulaires augmentent la capacité d'écrouissage de trois manières : contrainte en retour induite par les boucles de dislocation stockées autour des précipités intragranulaires, augmentation des densités de dislocations statistiquement stockées et géométriquement nécessaires.

Chapitre 6. Ce qui rend C+Al et l'alliage de Cantor si *spéciaux* (ou pas)

Enfin, dans le chapitre 6, C+Al est comparé à trois alliages FCC présentant de faibles SFE et des compositions chimiques similaires : un acier inoxydable austénitique de grade 304L, l'alliage de Cantor et un alliage de Cantor contenant du carbone (C+C). La comparaison porte sur les mécanismes de déformation lors du laminage à froid, les cinétiques de recristallisation et de croissance de grains, et les propriétés de traction.

Lorsque monophasés FCC, les alliages multi-composants se comportent de manière très similaire à l'acier 304L. Ils présentent les mêmes mécanismes de déformation, i.e. glissement de dislocation, maclage et formation de bandes de cisaillement. L'alliage de Cantor, monophasé FCC à toutes les températures explorées, présente aussi des cinétiques de recristallisation similaires. Cependant, l'alliage de Cantor présente une croissance de grain plus lente que 304L. Il présente aussi des contraintes plus élevées en traction. Ces deux effets sont attribués à la chimie complexe de Cantor via un renforcement par solution solide accru et une diffusion possiblement ralentie par trainée de soluté (*solute drag*). Il en va de même pour C+Al lorsque monophasé FCC. La présence d'aluminium accroît toutefois l'effet solution solide. C+C est aussi renforcé par la présence d'atomes de carbone occupant les sites interstitiels. Tous les alliages monophasés FCC présentent l'activation du maclage pendant la déformation, particulièrement C+C pour lequel la présence de carbone semble augmenter cet effet.

Lorsque recuits à des températures inférieures à 1000°C, des précipités se forment dans C+Al et C+C. Ce sont des précipités B2 et σ dans le cas de C+Al, et des carbures dans celui de C+C. La présence de ces précipités limite considérablement les cinétiques de recristallisation et de croissance de grain. De plus, un renforcement est observé sur leurs courbes de traction. Ce renforcement est le plus important pour C+Al qui présente une fraction volumique de précipités plus importante.

En résumé, les alliages multi-composants se comportent de la même manière que les alliages conventionnels, à l'exception d'un renforcement par solution solide accru et d'une croissance de grain limitée, dus à leurs teneurs élevées en soluté. L'ajout de carbone et d'aluminium semble intéressants mais pour des raisons différentes : intensification du maclage mécanique pour le carbone ; et polyvalence des microstructures pour l'aluminium. Le couplage potentiel de ces deux stratégies d'alliage pourrait être une perspective intéressante pour des recherches ultérieures.

Ce manuscrit se termine par une conclusion générale et quatre axes de perspectives. Les matériaux et méthodes utilisés sont présentés en annexe A.

REFERENCES

1. Gooch, J. W. Metal Alloying. in *Encyclopedic Dictionary of Polymers* (2011).
2. Li, Z. & Raabe, D. Strong and Ductile Non-equiatomic High-Entropy Alloys: Design, Processing, Microstructure, and Mechanical Properties. *JOM* **69**, 2099–2106 (2017).
3. Cantor, B., Chang, I. T. H., Knight, P. & Vincent, A. J. B. Microstructural development in equiatomic multicomponent alloys. *Materials Science and Engineering: A* **375–377**, 213–218 (2004).
4. Yeh, J.-W. Recent progress in high-entropy alloys. *European Journal of Control* **31**, 633–648 (2006).
5. Yeh, J.-W. *et al.* Nanostructured High-Entropy Alloys with Multiple Principal Elements: Novel Alloy Design Concepts and Outcomes. *Adv. Eng. Mater.* **6**, 299–303 (2004).
6. Otto, F., Yang, Y., Bei, H. & George, E. P. Relative effects of enthalpy and entropy on the phase stability of equiatomic high-entropy alloys. *Acta Materialia* **61**, 2628–2638 (2013).
7. Ma, D., Grabowski, B., Körmann, F., Neugebauer, J. & Raabe, D. Ab initio thermodynamics of the CoCrFeMnNi high entropy alloy: Importance of entropy contributions beyond the configurational one. *Acta Materialia* **100**, 90–97 (2015).
8. Miracle, D. B. High-Entropy Alloys: A Current Evaluation of Founding Ideas and Core Effects and Exploring “Nonlinear Alloys”. *JOM* **69**, 2130–2136 (2017).
9. Murty, B. S., Yeh, J. W. & Ranganathan, S. *High-Entropy Alloys*. (2014).
10. Varvenne, C., Luque, A. & Curtin, W. A. Theory of strengthening in fcc high entropy alloys. *Acta Materialia* **118**, 164–176 (2016).
11. Varvenne, C., Leyson, G. P. M., Ghazisaeidi, M. & Curtin, W. A. Solute strengthening in random alloys. *Acta Materialia* **124**, 660–683 (2017).
12. Dong, W. *et al.* Applications of High-Pressure Technology for High-Entropy Alloys: A Review. *Metals* **9**, 867 (2019).
13. Miracle, D. B. Critical Assessment 14: High entropy alloys and their development as structural materials. *Materials Science and Technology* **31**, 1142–1147 (2015).
14. Miracle, D. B. & Senkov, O. N. A critical review of high entropy alloys and related concepts. *Acta Materialia* **122**, 448–511 (2017).
15. Senkov, O. N., Miller, J. D., Miracle, D. B. & Woodward, C. Accelerated exploration of multi-principal element alloys with solid solution phases. *Nature Communications* **6**, 1–10 (2015).
16. Gorsse, S. & Tancret, F. Current and emerging practices of CALPHAD toward the development of high entropy alloys and complex concentrated alloys. *Journal of Materials Research* **33**, 2899–2923 (2018).
17. Gorsse, S. & Senkov, O. N. About the Reliability of CALPHAD Predictions in Multicomponent Systems. *Entropy* **20**, 899 (2018).

18. Gorsse, S., Miracle, D. B. & Senkov, O. N. Mapping the world of complex concentrated alloys. *Acta Materialia* **135**, 177–187 (2017).
19. Gorsse, S., Couzinié, J.-P. & Miracle, D. B. From high-entropy alloys to complex concentrated alloys. *Comptes Rendus Physique* **19**, 721–736 (2018).
20. Senkov, O. N., Senkova, S. V., Dimiduk, D. M., Woodward, C. & Miracle, D. B. Oxidation behavior of a refractory NbCrMo_{0.5}Ta_{0.5}TiZr alloy. *J Mater Sci* **47**, 6522–6534 (2012).
21. Liu, C. M., Wang, H. M., Zhang, S. Q., Tang, H. B. & Zhang, A. L. Microstructure and oxidation behavior of new refractory high entropy alloys. *Journal of Alloys and Compounds* **583**, 162–169 (2014).
22. Liaw, P. K., Egami, T., Zhang, C., Zhang, F. & Zhang, Y. *Radiation behavior of high-entropy alloys for advanced reactors. Final report.* <https://www.osti.gov/biblio/1214790> (2015) doi:10.2172/1214790.
23. Xia, S., Wang, Z., Yang, T. & Zhang, Y. Irradiation Behavior in High Entropy Alloys. *Journal of Iron and Steel Research, International* **22**, 879–884 (2015).
24. Lu, C. *et al.* Enhancing radiation tolerance by controlling defect mobility and migration pathways in multicomponent single-phase alloys. *Nature Communications* **7**, 13564 (2016).
25. Gludovatz, B. *et al.* A fracture-resistant high-entropy alloy for cryogenic applications. *Science* **345**, 1153–1158 (2014).
26. Gludovatz, B. *et al.* Exceptional damage-tolerance of a medium-entropy alloy CrCoNi at cryogenic temperatures. *Nature Communications* **7**, ncomms10602 (2016).
27. Li, D. *et al.* High-entropy Al_{0.3}CoCrFeNi alloy fibers with high tensile strength and ductility at ambient and cryogenic temperatures. *Acta Materialia* **123**, 285–294 (2017).
28. Syn, C. K., Morris, J. W. & Jin, S. Cryogenic fracture toughness of 9Ni steel enhanced through grain refinement. *MTA* **7**, 1827–1832 (1976).
29. Kim, J. I., Syn, C. K. & Morris, J. W. Microstructural sources of toughness in QLT-Treated 5.5Ni cryogenic steel. *MTA* **14**, 93–103 (1983).
30. Sohn, S. S. *et al.* Effects of Mn and Al contents on cryogenic-temperature tensile and Charpy impact properties in four austenitic high-Mn steels. *Acta Materialia* **100**, 39–52 (2015).
31. Laplanche, G., Kostka, A., Horst, O. M., Eggeler, G. & George, E. P. Microstructure evolution and critical stress for twinning in the CrMnFeCoNi high-entropy alloy. *Acta Materialia* **118**, 152–163 (2016).
32. Chen, J. *et al.* Effect of C content on microstructure and tensile properties of as-cast CoCrFeMnNi high entropy alloy. *Materials Chemistry and Physics* **210**, 136–145 (2017).
33. Stepanov, N. D., Yurchenko, N. Yu., Tikhonovsky, M. A. & Salishchev, G. A. Effect of carbon content and annealing on structure and hardness of the CoCrFeNiMn-based high entropy alloys. *Journal of Alloys and Compounds* **687**, 59–71 (2016).
34. Wang, Z., Baker, I., Guo, W. & Poplawsky, J. D. The effect of carbon on the microstructures, mechanical properties, and deformation mechanisms of thermo-mechanically treated Fe_{40.4}Ni_{11.3}Mn_{34.8}Al_{7.5}Cr₆ high entropy alloys. *Acta Materialia* **126**, 346–360 (2017).
35. Wu, Z., Parish, C. M. & Bei, H. Nano-twin mediated plasticity in carbon-containing FeNiCoCrMn high entropy alloys. *Journal of Alloys and Compounds* **647**, 815–822 (2015).

36. Seol, J. B. *et al.* Boron doped ultrastrong and ductile high-entropy alloys. *Acta Materialia* **151**, 366–376 (2018).
37. Shahmir, H., Nili-Ahmadabadi, M., Shafiee, A. & Langdon, T. G. Effect of a minor titanium addition on the superplastic properties of a CoCrFeNiMn high-entropy alloy processed by high-pressure torsion. *Materials Science and Engineering: A* **718**, 468–476 (2018).
38. Gwalani, B. *et al.* Role of copper on L12 precipitation strengthened fcc based high entropy alloy. *Materialia* **6**, (2019).
39. He, J. Y. *et al.* Effects of Al addition on structural evolution and tensile properties of the FeCoNiCrMn high-entropy alloy system. *Acta Materialia* **62**, 105–113 (2014).
40. Sun, S. J. *et al.* Enhanced strength and ductility of bulk CoCrFeMnNi high entropy alloy having fully recrystallized ultrafine-grained structure. *Materials & Design* **133**, 122–127 (2017).
41. Diao, H. *et al.* Novel NiAl-strengthened high entropy alloys with balanced tensile strength and ductility. *Materials Science and Engineering: A* **742**, 636–647 (2019).
42. Li, Z., Tasan, C. C., Pradeep, K. G. & Raabe, D. A TRIP-assisted dual-phase high-entropy alloy: Grain size and phase fraction effects on deformation behavior. *Acta Materialia* **131**, 323–335 (2017).
43. Liu, K., Komarasamy, M., Gwalani, B., Shukla, S. & Mishra, R. S. Fatigue behavior of ultrafine grained triplex Al_{0.3}CoCrFeNi high entropy alloy. *Scripta Materialia* **158**, 116–120 (2019).
44. Lu, Y. *et al.* A Promising New Class of High-Temperature Alloys: Eutectic High-Entropy Alloys. *Scientific Reports* **4**, 6200 (2014).
45. Lu, Y. *et al.* Directly cast bulk eutectic and near-eutectic high entropy alloys with balanced strength and ductility in a wide temperature range. *Acta Materialia* **124**, 143–150 (2017).
46. Ma, Y. *et al.* Controlled formation of coherent cuboidal nanoprecipitates in body-centered cubic high-entropy alloys based on Al₂(Ni,Co,Fe,Cr)₁₄ compositions. *Acta Materialia* **147**, 213–225 (2018).
47. Yasuda, H. Y., Miyamoto, H., Cho, K. & Nagase, T. Formation of ultrafine-grained microstructure in Al_{0.3}CoCrFeNi high entropy alloys with grain boundary precipitates. *Materials Letters* **199**, 120–123 (2017).
48. Joo, S.-H. *et al.* Tensile deformation behavior and deformation twinning of an equimolar CoCrFeMnNi high-entropy alloy. *Materials Science and Engineering: A* **689**, 122–133 (2017).
49. Gu, J., Ni, S., Liu, Y. & Song, M. Regulating the strength and ductility of a cold rolled FeCrCoMnNi high-entropy alloy via annealing treatment. *Materials Science and Engineering: A* **755**, 289–294 (2019).
50. Li, Z. *et al.* Effect of Annealing Temperature on Microstructure and Mechanical Properties of a Severe Cold-Rolled FeCoCrNiMn High-Entropy Alloy. *Metall and Mat Trans A* (2019) doi:10.1007/s11661-019-05231-y.
51. Shahmir, H., He, J., Lu, Z., Kawasaki, M. & Langdon, T. G. Effect of annealing on mechanical properties of a nanocrystalline CoCrFeNiMn high-entropy alloy processed by high-pressure torsion. *Materials Science and Engineering: A* **676**, 294–303 (2016).
52. Kang, M., Won, J. W., Kwon, J. B. & Na, Y. S. Intermediate strain rate deformation behavior of a CoCrFeMnNi high-entropy alloy. *Materials Science and Engineering: A* **707**, 16–21 (2017).

53. Kim, S.-W. & Kim, J. H. In-situ observations of deformation twins and crack propagation in a CoCrFeNiMn high-entropy alloy. *Materials Science and Engineering: A* **718**, 321–325 (2018).
54. Otto, F. *et al.* The influences of temperature and microstructure on the tensile properties of a CoCrFeMnNi high-entropy alloy. *Acta Materialia* **61**, 5743–5755 (2013).
55. Stepanov, N. *et al.* Effect of cryo-deformation on structure and properties of CoCrFeNiMn high-entropy alloy. *Intermetallics* **59**, 8–17 (2015).
56. Park, J. M. *et al.* Effect of annealing heat treatment on microstructural evolution and tensile behavior of Al_{0.5}CoCrFeMnNi high-entropy alloy. *Materials Science and Engineering: A* **728**, 251–258 (2018).
57. Park, J. M. *et al.* Role of BCC phase on tensile behavior of dual-phase Al_{0.5}CoCrFeMnNi high-entropy alloy at cryogenic temperature. *Materials Science and Engineering: A* **746**, 443–447 (2019).
58. Dasari, S. *et al.* Engineering multi-scale B2 precipitation in a heterogeneous FCC based microstructure to enhance the mechanical properties of a Al_{0.5}Co_{1.5}CrFeNi_{1.5} high entropy alloy. *Journal of Alloys and Compounds* **830**, 154707 (2020).
59. Dasari, S. *et al.* Hierarchical Eutectoid Nano-lamellar Decomposition in an Al_{0.3}CoFeNi Complex Concentrated Alloy. *Scientific Reports* **10**, 1–15 (2020).
60. Guo, T. *et al.* Microstructure and properties of bulk Al_{0.5}CoCrFeNi high-entropy alloy by cold rolling and subsequent annealing. *Materials Science and Engineering: A* **729**, 141–148 (2018).
61. Gangireddy, S., Gwalani, B., Soni, V., Banerjee, R. & Mishra, R. S. Contrasting mechanical behavior in precipitation hardenable Al₁CoCrFeNi high entropy alloy microstructures: Single phase FCC vs. dual phase FCC-BCC. *Materials Science and Engineering: A* **739**, 158–166 (2019).
62. Gwalani, B. *et al.* Optimizing the coupled effects of Hall-Petch and precipitation strengthening in a Al_{0.3}CoCrFeNi high entropy alloy. *Materials & Design* **121**, 254–260 (2017).
63. Choudhuri, D. *et al.* Enhancing strength and strain hardenability via deformation twinning in fcc-based high entropy alloys reinforced with intermetallic compounds. *Acta Materialia* **165**, 420–430 (2019).
64. Gangireddy, S., Gwalani, B., Liu, K., Banerjee, R. & Mishra, R. S. Microstructures with extraordinary dynamic work hardening and strain rate sensitivity in Al_{0.3}CoCrFeNi high entropy alloy. *Materials Science and Engineering: A* **734**, 42–50 (2018).
65. Gwalani, B. *et al.* Modifying transformation pathways in high entropy alloys or complex concentrated alloys via thermo-mechanical processing. *Acta Materialia* **153**, 169–185 (2018).
66. Gwalani, B. *et al.* Tensile yield strength of a single bulk Al_{0.3}CoCrFeNi high entropy alloy can be tuned from 160 MPa to 1800 MPa. *Scripta Materialia* **162**, 18–23 (2019).
67. Shukla, S. *et al.* Hierarchical features infused heterogeneous grain structure for extraordinary strength-ductility synergy. *Materials Research Letters* **6**, (2018).
68. Wani, I. S. *et al.* Tailoring nanostructures and mechanical properties of AlCoCrFeNi_{2.1} eutectic high entropy alloy using thermo-mechanical processing. *Materials Science and Engineering: A* **675**, 99–109 (2016).
69. Bhattacharjee, T. *et al.* Effect of low temperature on tensile properties of AlCoCrFeNi_{2.1} eutectic high entropy alloy. *Materials Chemistry and Physics* **210**, 207–212 (2018).

70. Li, Z., Pradeep, K. G., Deng, Y., Raabe, D. & Tasan, C. C. Metastable high-entropy dual-phase alloys overcome the strength–ductility trade-off. *Nature* **534**, 227–230 (2016).
71. Tasan, C. C. *et al.* Composition Dependence of Phase Stability, Deformation Mechanisms, and Mechanical Properties of the CoCrFeMnNi High-Entropy Alloy System. *JOM* **66**, 1993–2001 (2014).
72. Yao, M. J., Pradeep, K. G., Tasan, C. C. & Raabe, D. A novel, single phase, non-equiatomic FeMnNiCoCr high-entropy alloy with exceptional phase stability and tensile ductility. *Scripta Materialia* **72–73**, 5–8 (2014).
73. Deng, Y. *et al.* Design of a twinning-induced plasticity high entropy alloy. *Acta Materialia* **94**, 124–133 (2015).
74. Wu, Z., Bei, H., Pharr, G. M. & George, E. P. Temperature dependence of the mechanical properties of equiatomic solid solution alloys with face-centered cubic crystal structures. *Acta Materialia* **81**, 428–441 (2014).
75. Yang, T. *et al.* Nanoparticles-strengthened high-entropy alloys for cryogenic applications showing an exceptional strength-ductility synergy. *Scripta Materialia* **164**, 30–35 (2019).
76. Zhao, Y. Y., Chen, H. W., Lu, Z. P. & Nieh, T. G. Thermal stability and coarsening of coherent particles in a precipitation-hardened (NiCoFeCr)₉₄Ti₂Al₄ high-entropy alloy. *Acta Materialia* **147**, 184–194 (2018).
77. He, J. Y. *et al.* A precipitation-hardened high-entropy alloy with outstanding tensile properties. *Acta Materialia* **102**, 187–196 (2016).
78. Tong, Y. *et al.* Outstanding tensile properties of a precipitation-strengthened FeCoNiCrTi_{0.2} high-entropy alloy at room and cryogenic temperatures. *Acta Materialia* **165**, 228–240 (2019).
79. Nene, S. S. *et al.* Reversed strength-ductility relationship in microstructurally flexible high entropy alloy. *Scripta Materialia* **154**, 163–167 (2018).
80. Jo, Y. H. *et al.* Cryogenic strength improvement by utilizing room-temperature deformation twinning in a partially recrystallized VCrMnFeCoNi high-entropy alloy. *Nature Communications* **8**, ncomms15719 (2017).
81. Ming, K., Bi, X. & Wang, J. Precipitation strengthening of ductile Cr₁₅Fe₂₀Co₃₅Ni₂₀Mo₁₀ alloys. *Scripta Materialia* **137**, 88–93 (2017).
82. Chen, L. B. *et al.* Heavy carbon alloyed FCC-structured high entropy alloy with excellent combination of strength and ductility. *Materials Science and Engineering: A* (2018) doi:10.1016/j.msea.2018.01.045.
83. Li, Z. Interstitial equiatomic CoCrFeMnNi high-entropy alloys: carbon content, microstructure, and compositional homogeneity effects on deformation behavior. *Acta Materialia* **164**, 400–412 (2019).
84. Lu, W. *et al.* Interfacial nanophases stabilize nanotwins in high-entropy alloys. *Acta Materialia* **185**, 218–232 (2020).
85. Stepanov, N. D. *et al.* Effect of thermomechanical processing on microstructure and mechanical properties of the carbon-containing CoCrFeNiMn high entropy alloy. *Journal of Alloys and Compounds* **693**, 394–405 (2017).

86. Li, Z. & Raabe, D. Influence of compositional inhomogeneity on mechanical behavior of an interstitial dual-phase high-entropy alloy. *Materials Chemistry and Physics* **210**, 29–36 (2018).
87. Zhang, C., Zhu, C., Harrington, T. & Vecchio, K. Design of non-equiatom high entropy alloys with heterogeneous lamella structure towards strength-ductility synergy. *Scripta Materialia* **154**, 78–82 (2018).
88. Miao, J. *et al.* The evolution of the deformation substructure in a Ni-Co-Cr equiatom solid solution alloy. *Acta Materialia* **132**, 35–48 (2017).
89. Slone, C. E., Miao, J., George, E. P. & Mills, M. J. Achieving ultra-high strength and ductility in equiatom CrCoNi with partially recrystallized microstructures. *Acta Materialia* **165**, 496–507 (2019).
90. Zhao, Y. L. *et al.* Heterogeneous precipitation behavior and stacking-fault-mediated deformation in a CoCrNi-based medium-entropy alloy. *Acta Materialia* **138**, 72–82 (2017).
91. Gangireddy, S., Gwalani, B. & Mishra, R. S. Grain size dependence of strain rate sensitivity in a single phase FCC high entropy alloy Al_{0.3}CoCrFeNi. *Materials Science and Engineering: A* **736**, 344–348 (2018).
92. Dasari, S. *et al.* Recovery of cold-worked Al_{0.3}CoCrFeNi complex concentrated alloy through twinning assisted B₂ precipitation. *Acta Materialia* **202**, 448–462 (2021).
93. Pohan, R. M. *et al.* Microstructures and mechanical properties of mechanically alloyed and spark plasma sintered Al_{0.3}CoCrFeMnNi high entropy alloy. *Materials Chemistry and Physics* 62–70 (2017) doi:10.1016/j.matchemphys.2017.09.013.
94. Zaddach, A. J., Niu, C., Koch, C. C. & Irving, D. L. Mechanical Properties and Stacking Fault Energies of NiFeCrCoMn High-Entropy Alloy. *JOM* **65**, 1780–1789 (2013).
95. Tsai, K.-Y., Tsai, M.-H. & Yeh, J.-W. Sluggish diffusion in Co–Cr–Fe–Mn–Ni high-entropy alloys. *Acta Materialia* **61**, 4887–4897 (2013).
96. Otto, F., Hanold, N. L. & George, E. P. Microstructural evolution after thermomechanical processing in an equiatom, single-phase CoCrFeMnNi high-entropy alloy with special focus on twin boundaries. *Intermetallics* **54**, 39–48 (2014).
97. Eleti, R. R., Bhattacharjee, T., Zhao, L., Bhattacharjee, P. P. & Tsuji, N. Hot deformation behavior of CoCrFeMnNi FCC high entropy alloy. *Materials Chemistry and Physics* **210**, 176–186 (2018).
98. Gali, A. & George, E. P. Tensile properties of high- and medium-entropy alloys. *Intermetallics* **39**, 74–78 (2013).
99. Bhattacharjee, P. P. *et al.* Microstructure and texture evolution during annealing of equiatom CoCrFeMnNi high-entropy alloy. *Journal of Alloys and Compounds* **587**, 544–552 (2014).
100. Sathiaraj, G. D., Tsai, C. W., Yeh, J. W., Jahazi, M. & Bhattacharjee, P. P. The effect of heating rate on microstructure and texture formation during annealing of heavily cold-rolled equiatom CoCrFeMnNi high entropy alloy. *Journal of Alloys and Compounds* **688**, 752–761 (2016).
101. Alkan, S., Ojha, A. & Sehitoglu, H. Determination of latent hardening response for FeNiCoCrMn for twin-twin interactions. *Acta Materialia* **147**, 149–164 (2018).
102. Samarasekera, I. V. Hot rolling. in *Encyclopedia of Materials: Science and Technology (Second Edition)* 3836–3843 (2001).

103. Kalidindi, S. R. Modeling the strain hardening response of low SFE FCC alloys. *International Journal of Plasticity* **14**, 1265–1277 (1998).
104. Guy, A. G. *Introduction to materials science*. (1971).
105. Aernoudt, E., Van Houtte, P. & Leffers, T. Deformation and Textures of Metals at Large Strain. in *Materials Science and Technology* (2006).
106. Humphreys, F. J., Rohrer, G. S. & Rollett, A. D. The Deformed State. in *Recrystallization and Related Annealing Phenomena* 13–79 (Elsevier, 2017).
107. Hutchinson, B. Deformation microstructures and textures in steels. *Philosophical Transactions of the Royal Society of London. Series A: Mathematical, Physical and Engineering Sciences* **357**, 1471–1485 (1999).
108. Kocks, U. F., Tomé, C. N. & Wenk, H. R. *Texture and Anisotropy. Preferred Orientations in Polycrystals and Their Effect on Material Properties*. (2000).
109. Liu, S. F. *et al.* Stacking fault energy of face-centered-cubic high entropy alloys. *Intermetallics* **93**, 269–273 (2018).
110. Xu, X. D. *et al.* Transmission electron microscopy characterization of dislocation structure in a face-centered cubic high-entropy alloy Al_{0.1}CoCrFeNi. *Acta Materialia* **144**, 107–115 (2018).
111. Huang, S. *et al.* Temperature dependent stacking fault energy of FeCrCoNiMn high entropy alloy. *Scripta Materialia* **108**, 44–47 (2015).
112. Ikeda, Y., Tanaka, I., Neugebauer, J. & Körmann, F. Impact of interstitial C on phase stability and stacking-fault energy of the CrMnFeCoNi high-entropy alloy. *Phys. Rev. Materials* **3**, 113603 (2019).
113. Klimova, M. *et al.* Microstructure and Mechanical Properties Evolution of the Al, C-Containing CoCrFeNiMn-Type High-Entropy Alloy during Cold Rolling. *Materials* **11**, 53 (2018).
114. Olson, G. B. & Cohen, M. A general mechanism of martensitic nucleation: Part I. General concepts and the FCC → HCP transformation. *MTA* **7**, 1897–1904 (1976).
115. Humphreys, J., Rohrer, G. S. & Rollett, A. Mobility and Migration of Boundaries. in *Recrystallization and Related Annealing Phenomena (Third Edition)* (eds. Humphreys, J., Rohrer, G. S. & Rollett, A.) 145–197 (Elsevier, 2017). doi:10.1016/B978-0-08-098235-9.00005-7.
116. Asgari, S., El-Danaf, E., Kalidindi, S. R. & Doherty, R. D. Strain hardening regimes and microstructural evolution during large strain compression of low stacking fault energy fcc alloys that form deformation twins. *Metall Mater Trans A* **28**, 1781–1795 (1997).
117. Kocks, U. F. & Mecking, H. Physics and phenomenology of strain hardening: the FCC case. *Progress in Materials Science* **48**, 171–273 (2003).
118. Mecking, H. & Kocks, U. F. Kinetics of flow and strain-hardening. *Acta Metallurgica* **29**, 1865–1875 (1981).
119. Karaman, I., Sehitoglu, H., Chumlyakov, Y. I., Maier, H. J. & Kireeva, I. V. Extrinsic stacking faults and twinning in hadfield manganese steel single crystals. *Scripta Materialia* **44**, 337–343 (2001).
120. Mori, T. & Fujita, H. Dislocation reactions during deformation twinning in Cu-11at.% Al single crystals. *Acta Metallurgica* **28**, 771–776 (1980).

121. Huang, H. *et al.* Critical stress for twinning nucleation in CrCoNi-based medium and high entropy alloys. *Acta Materialia* **149**, 388–396 (2018).
122. Das, A. Revisiting Stacking Fault Energy of Steels. *Metall Mater Trans A* **47**, 748–768 (2016).
123. Allain, S., Bouaziz, O. & Chateau, J.-P. *Proc int conf SHSS* (2010).
124. Bouaziz, O. *et al.* Effect of chemical composition on work hardening of Fe—Mn—C TWIP steels. *Materials Science and Technology* **27**, 707–709 (2011).
125. Bouaziz, O., Allain, S., Scott, C. P., Cugy, P. & Barbier, D. High manganese austenitic twinning induced plasticity steels: A review of the microstructure properties relationships. *Current Opinion in Solid State and Materials Science* **15**, 141–168 (2011).
126. Traversier, M. *et al.* Nitrogen-induced hardening in an austenitic CrFeMnNi high-entropy alloy (HEA). *Materials Science and Engineering: A* **804**, 140725 (2021).
127. Hamdi, F. & Asgari, S. Evaluation of the Role of Deformation Twinning in Work Hardening Behavior of Face-Centered-Cubic Polycrystals. *Metall Mater Trans A* **39**, 294–303 (2008).
128. Sleswyk, A. W. & Verbraak, C. A. Incorporation of slip dislocations in mechanical twins—I. *Acta Metallurgica* **9**, 917–927 (1961).
129. Mahato, B. *et al.* An effective stacking fault energy viewpoint on the formation of extended defects and their contribution to strain hardening in a Fe—Mn—Si—Al twinning-induced plasticity steel. *Acta Materialia* **86**, 69–79 (2015).
130. Remy, L. Kinetics of f.c.c. deformation twinning and its relationship to stress-strain behaviour. *Acta Metallurgica* **26**, 443–451 (1978).
131. Christian, J. W. & Mahajan, S. Deformation twinning. *Progress in Materials Science* **39**, 1–157 (1995).
132. Bronkhorst, C. A., Kalidindi, S. R. & Anand, L. Polycrystalline plasticity and the evolution of crystallographic texture in FCC metals. *Philosophical Transactions of the Royal Society of London. Series A: Physical and Engineering Sciences* **341**, 443–477 (1992).
133. Di Gioacchino, F. & Quinta da Fonseca, J. An experimental study of the polycrystalline plasticity of austenitic stainless steel. *International Journal of Plasticity* **74**, 92–109 (2015).
134. Duggan, B. J., Hutchinson, W. B. & Hatherly, M. Recrystallization studies in 70:30 brass using a high voltage electron microscope. *Scripta Materialia* **12**, 293–295 (1978).
135. Ma, E. Unusual dislocation behavior in high-entropy alloys. *Scripta Materialia* **181**, 127–133 (2020).
136. Ding, Q. *et al.* Tuning element distribution, structure and properties by composition in high-entropy alloys. *Nature* **574**, 223–227 (2019).
137. Smith, T. M. *et al.* Atomic-scale characterization and modeling of 60° dislocations in a high-entropy alloy. *Acta Materialia* **110**, 352–363 (2016).
138. Wolf, K., Gudladt, H.-J., Calderon, H. A. & Kostorz, G. Transition between planar and wavy slip in cyclically deformed short-range ordered alloys. *Acta Metallurgica et Materialia* **42**, 3759–3765 (1994).

139. Praveen, S., Basu, J., Kashyap, S. & Kottada, R. S. Exceptional resistance to grain growth in nanocrystalline CoCrFeNi high entropy alloy at high homologous temperatures. *Journal of Alloys and Compounds* **662**, 361–367 (2016).
140. Liu, G. *et al.* Solute segregation effect on grain boundary migration and Hall–Petch relationship in CrMnFeCoNi high-entropy alloy. *Materials Science and Technology* **35**, 500–508 (2019).
141. Humphreys, F. J., Rohrer, G. S. & Rollett, A. D. Recovery After Deformation. in *Recrystallization and Related Annealing Phenomena* 169–213 (Elsevier, 2017).
142. Humphreys, J., Rohrer, G. S. & Rollett, A. The Structure and Energy of Grain Boundaries. in *Recrystallization and Related Annealing Phenomena (Third Edition)* (eds. Humphreys, J., Rohrer, G. S. & Rollett, A.) 109–143 (Elsevier, 2017). doi:10.1016/B978-0-08-098235-9.00004-5.
143. Read, W. T. & Shockley, W. Dislocation Models of Crystal Grain Boundaries. *Phys. Rev.* **78**, 275–289 (1950).
144. Ratanaphan, S. *et al.* Grain boundary energies in body-centered cubic metals. *Acta Materialia* **88**, 346–354 (2015).
145. Humphreys, J., Rohrer, G. S. & Rollett, A. Recrystallization of Single-Phase Alloys. in *Recrystallization and Related Annealing Phenomena (Third Edition)* (eds. Humphreys, J., Rohrer, G. S. & Rollett, A.) 245–304 (Elsevier, 2017). doi:10.1016/B978-0-08-098235-9.00007-0.
146. Burke, J. E. & Turnbull, D. Recrystallization and grain growth. *Progress in Metal Physics* **3**, 220–292 (1952).
147. Cahn, R. W. A New Theory of Recrystallization Nuclei. *Proc. Phys. Soc. A* **63**, 323–336 (1950).
148. Mishra, S. K., Pant, P., Narasimhan, K., Rollett, A. D. & Samajdar, I. On the widths of orientation gradient zones adjacent to grain boundaries. *Scripta Materialia* **61**, 273–276 (2009).
149. Hutchinson, W. B. Recrystallisation textures in iron resulting from nucleation at grain boundaries. *Acta Metallurgica* **37**, 1047–1056 (1989).
150. Churyumov, A. Y., Pozdniakov, A. V., Mondoloni, B. & Prosviryakov, A. S. Effect of boron concentration on hot deformation behavior of stainless steel. *Results in Physics* **13**, 102340 (2019).
151. Haghdadi, N. *et al.* Dynamic recrystallization in AlXCoCrFeNi duplex high entropy alloys. *Journal of Alloys and Compounds* **830**, 154720 (2020).
152. Zhang, S., Zeng, W., Zhou, D., Lai, Y. & Zhao, Q. The particle stimulated nucleation in Ti–35V–15Cr–0.3Si–0.1C alloy. *Materials Letters* **166**, 317–320 (2016).
153. Zang, Q. *et al.* Improvement of anisotropic tensile properties of Al-7.9Zn-2.7Mg-2.0Cu alloy sheets by particle stimulated nucleation. *Journal of Alloys and Compounds* **828**, 154330 (2020).
154. Inokuti, Y. & Doherty, R. D. Transmission kossel study of the structure of compressed iron and its recrystallization behaviour. *Acta Metallurgica* **26**, 61–80 (1978).
155. Faivre, P. & Doherty, R. D. Nucleation of recrystallization in compressed aluminium: studies by electron microscopy and Kikuchi diffraction. *J Mater Sci* **14**, 897–919 (1979).
156. Hughes, D. A. Scaling of deformation-induced microstructures in fcc metals. *Scripta Materialia* **47**, 697–703 (2002).

157. Wang, S. *et al.* Modeling the recrystallized grain size in single phase materials. *Acta Materialia* **59**, 3872–3882 (2011).
158. Somerday, M. & Humphreys, F. J. Recrystallisation behaviour of supersaturated Al–Mn alloys Part 2 – Al–0.3 wt-%Mn. *Materials Science and Technology* **19**, 30–35 (2003).
159. Hjelen, J., Ørsund, R. & Nes, E. On the origin of recrystallization textures in aluminium. *Acta Metallurgica et Materialia* **39**, 1377–1404 (1991).
160. Humphreys, J., Rohrer, G. S. & Rollett, A. Hot Deformation and Dynamic Restoration. in *Recrystallization and Related Annealing Phenomena* 469–508 (Elsevier, 2017).
161. Drury, M. R. & Humphreys, F. J. The development of microstructure in Al-5% Mg during high temperature deformation. *Acta Metallurgica* **34**, 2259–2271 (1986).
162. Ardakani, M. G. & Humphreys, F. J. High Temperature Deformation and Dynamic Recrystallization of some Two-Phase Copper Alloys. in *M. Fuentes and J. Gil Sevillano (Eds.), Recrystallization '92* 213 (1992).
163. Sakai, T. & Jonas, J. J. Overview no. 35 Dynamic recrystallization: Mechanical and microstructural considerations. *Acta Metallurgica* **32**, 189–209 (1984).
164. Gourdet, S. & Montheillet, F. Effects of dynamic grain boundary migration during the hot compression of high stacking fault energy metals. *Acta Materialia* **50**, 2801–2812 (2002).
165. McQueen, H. J. & Ryan, N. D. Constitutive analysis in hot working. *Materials Science and Engineering: A* **322**, 43–63 (2002).
166. Porter, D. A., Easterling, K. E. & Sherif, M. Y. *Phase Transformations in Metals and Alloys*. (CRC Press, 2009). doi:10.1201/9781439883570.
167. Lillywhite, S. j., Prangnell, P. b. & Humphreys, F. j. Interactions between precipitation and recrystallisation in an Al–Mg–Si alloy. *Materials Science and Technology* **16**, 1112–1120 (2000).
168. Leslie, W. C., Michalak, J. T. & Aul, F. W. The annealing of cold-worked iron. *Iron and its dilute solid solutions* 119–216 (1963).
169. Joseph, J. *et al.* Comparative study of the microstructures and mechanical properties of direct laser fabricated and arc-melted Al_xCoCrFeNi high entropy alloys. *Materials Science and Engineering: A* **633**, 184–193 (2015).
170. Bain, E. C. & Griffiths, W. E. An introduction to the iron-chromium-nickel alloys. *Trans. Aime* **75**, 166–211 (1927).
171. Treitschke, W. & Tammann, G. Enthalpy of formation for σ -phase solid solutions at 1060 K. *Anorganische Chemie* **55**, 707 (1907).
172. Sato, Y. S. & Kokawa, H. Preferential precipitation site of sigma phase in duplex stainless steel weld metal. *Scripta Materialia* **40**, 659–663 (1999).
173. Shinohara, K., Seo, T. & Kumada, K. Recrystallization and Sigma Phase Formation as Concurrent and Interacting Phenomena in 25%Cr-20%Ni Steel. *Transactions of the Japan Institute of Metals* **20**, 713–723 (1979).
174. Jo, Y. H. *et al.* Role of brittle sigma phase in cryogenic-temperature-strength improvement of non-equi-atomic Fe-rich VCrMnFeCoNi high entropy alloys. *Materials Science and Engineering: A* **724**, 403–410 (2018).

175. Peng, H., Hu, L., Li, L. & Zhang, W. Ripening of L12 nanoparticles and their effects on mechanical properties of Ni₂₈Co₂₈Fe₂₁Cr₁₅Al₄Ti₄ high-entropy alloys. *Materials Science and Engineering: A* **772**, 138803 (2020).
176. Hatherly, M., Malin, A. S., Carmichael, C. M., Humphreys, F. J. & Hirsch, J. Deformation processes in hot worked copper and α brass. *Acta Metallurgica* **34**, 2247–2257 (1986).
177. Drury, M. R., Humphreys, F. J. & White, S. H. Effect of dynamic recrystallization on the importance of grain-boundary sliding during creep. *J Mater Sci* **24**, 154–162 (1989).
178. Patnamsetty, M., Saastamoinen, A., Somani, M. C. & Peura, P. Constitutive modelling of hot deformation behaviour of a CoCrFeMnNi high-entropy alloy. *Science and Technology of Advanced Materials* **21**, 43–55 (2020).
179. McQueen, H. J. & Jonas, J. J. Recent advances in hot working: Fundamental dynamic softening mechanisms. *J. Applied Metalworking* **3**, 233–241 (1984).
180. Haghdabi, N., Martin, D. & Hodgson, P. Physically-based constitutive modelling of hot deformation behavior in a LDX 2101 duplex stainless steel. *Materials and Design* **106**, 420–427 (2016).
181. Jafari, M., Najafizadeh, A. & Rasti, J. Dynamic Recrystallization by Necklace Mechanism During Hot Deformation of 316 Stainless Steel. *Iron & Steel Society of Iran* **4**, 16–23 (2007).
182. Mirzadeh, H., Parsa, M. H. & Ohadi, D. Hot deformation behavior of austenitic stainless steel for a wide range of initial grain size. *Materials Science and Engineering: A* **569**, 54–60 (2013).
183. Rout, M., Biswas, S., Ranjan, R., Pal, S. K. & Singh, S. B. Deformation Behavior and Evolution of Microstructure and Texture During Hot Compression of AISI 304LN Stainless Steel. *Metall Mater Trans A* **49**, 864–880 (2018).
184. Dong, F. *et al.* Hot deformation behavior and processing maps of an equiatomic MoNbHfZrTi refractory high entropy alloy. *Intermetallics* **126**, 106921 (2020).
185. Samal, S., Rahul, M. R., Kottada, R. S. & Phanikumar, G. Hot deformation behaviour and processing map of Co-Cu-Fe-Ni-Ti eutectic high entropy alloy. *Materials Science and Engineering: A* **664**, 227–235 (2016).
186. Stepanov, N. D. *et al.* High temperature deformation behavior and dynamic recrystallization in CoCrFeNiMn high entropy alloy. *Materials Science and Engineering: A* **636**, 188–195 (2015).
187. Wang, Y. *et al.* Effect of Zener–Hollomon parameter on hot deformation behavior of CoCrFeMnNiCo_{0.5} high entropy alloy. *Materials Science and Engineering: A* **768**, 138483 (2019).
188. Wang, J. *et al.* Hot Deformation and Subsequent Annealing on the Microstructure and Hardness of an Al_{0.3}CoCrFeNi High-entropy Alloy. *Acta Metall. Sin. (Engl. Lett.)* (2021) doi:10.1007/s40195-021-01251-z.
189. Jeong, H. T., Park, H. K. & Kim, W. J. Hot deformation behavior and processing map of a Sn_{0.5}CoCrFeMnNi high entropy alloy with dual phases. *Materials Science and Engineering: A* **801**, 140394 (2021).
190. Jeong, H. T., Park, H. K., Park, K., Na, T. W. & Kim, W. J. High-temperature deformation mechanisms and processing maps of equiatomic CoCrFeMnNi high-entropy alloy. *Materials Science and Engineering: A* **756**, 528–537 (2019).

191. Prasad, N., Bibhanshu, N., Nayan, N., Avadhani, G. S. & Suwas, S. Hot deformation behavior of the high-entropy alloy CoCuFeMnNi. *Journal of Materials Research* **34**, 744–755 (2019).
192. Nayan, N. *et al.* Hot deformation behaviour and microstructure control in AlCrCuNiFeCo high entropy alloy. *Intermetallics* **55**, 145–153 (2014).
193. Nicolaÿ, A. Microstructure et propriétés de l’Inconel 718 forgé en presse à vis. (Mines ParisTech, 2019).
194. Kim, K., Lee, J. & Cho, H. Analysis of pulsed Nd:YAG laser welding of AISI 304 steel. *J Mech Sci Technol* **24**, 2253–2259 (2010).
195. Buyco, E. H. & Davis, F. E. Specific heat of aluminum from zero to its melting temperature and beyond. Equation for representation of the specific heat of solids. *ACS Publications* (1970) doi:10.1021/je60047a035.
196. Armstrong, L. D. & Grayson-Smith, H. High temperature calorimetry: ii. atomic heats of chromium, manganese, and cobalt between 0° and 800 °c. *Can. J. Res.* **28a**, 51–59 (1950).
197. Blumm, J. & Kaisersberger, E. Accurate Measurement of Transformation Energetics and Specific Heat by DSC in the High-temperature Region. *Journal of Thermal Analysis and Calorimetry* **64**, 385–391 (2004).
198. Wu, Z., Bei, H., Otto, F., Pharr, G. M. & George, E. P. Recovery, recrystallization, grain growth and phase stability of a family of FCC-structured multi-component equiatomic solid solution alloys. *Intermetallics* **46**, 131–140 (2014).
199. Haghdadi, N. *et al.* On the hot-worked microstructure of a face-centered cubic Al_{0.3}CoCrFeNi high entropy alloy. *Scripta Materialia* **178**, 144–149 (2020).
200. Thirathipviwat, P. *et al.* A comparison study of dislocation density, recrystallization and grain growth among nickel, FeNiCo ternary alloy and FeNiCoCrMn high entropy alloy. *Journal of Alloys and Compounds* **790**, 266–273 (2019).
201. Zuo, J. *et al.* Investigation of deformation induced precipitation and the related microstructure evolution of Al–Zn–Mg–Cu alloy. *Mater. Res. Express* **7**, 106529 (2020).
202. Zhang, S. L., Sun, X. J. & Dong, H. Effect of deformation on the evolution of spheroidization for the ultra high carbon steel. *Materials Science and Engineering: A* **432**, 324–332 (2006).
203. Sellars, C. M. & Tegart, W. J. M. Hot Workability. *International Metallurgical Reviews* **17**, 1–24 (1972).
204. Akben, M. G., Weiss, I. & Jonas, J. J. Dynamic precipitation and solute hardening in A V microalloyed steel and two Nb steels containing high levels of Mn. *Acta Metallurgica* **29**, 111–121 (1981).
205. McQueen, H. J., Gurewitz, G. & Fulop, S. Influence of dynamic restoration mechanisms on the hot workability of Waspaloy and concentrated FCC alloys. *High Temperature Technology* **1**, 131–138 (1983).
206. Samarasekera, I. V. Hot Rolling. in *Encyclopedia of Materials: Science and Technology* (eds. Buschow, K. H. J. et al.) 3836–3843 (Elsevier, 2001). doi:10.1016/B0-08-043152-6/00683-5.
207. Calvo, J., Collins, L. & Yue, S. Design of Microalloyed Steel Hot Rolling Schedules by Torsion Testing: Average Schedule vs. Real Schedule. *ISIJ International* **50**, 1193–1199 (2010).

208. Maccagno, T. M. *et al.* Determination of Recrystallization Stop Temperature from Rolling Mill Logs and Comparison with Laboratory Simulation Results. *ISIJ International* **34**, 917–922 (1994).
209. Llanos, L., Pereda, B., Lopez, B. & Rodriguez-Ibabe, J. M. Hot deformation and static softening behavior of vanadium microalloyed high manganese austenitic steels. *Materials Science and Engineering: A* **651**, 358–369 (2016).
210. Hachet, D., Gorsse, S. & Godet, S. Microstructure study of cold rolled Al_{0.32}CoCrFeMnNi high-entropy alloy: Interactions between recrystallization and precipitation. *Materials Science and Engineering: A* 140452 (2020) doi:10.1016/j.msea.2020.140452.
211. Kumar, N. *et al.* High strain-rate compressive deformation behavior of the Al_{0.1}CrFeCoNi high entropy alloy. *Materials & Design* **86**, 598–602 (2015).
212. Moon, J. *et al.* Effects of homogenization temperature on cracking during cold-rolling of Al_{0.5}CoCrFeMnNi high-entropy alloy. *Materials Chemistry and Physics* **210**, 187–191 (2018).
213. Patel, A. *et al.* Strain-path controlled microstructure, texture and hardness evolution in cryo-deformed AlCoCrFeNi_{2.1} eutectic high entropy alloy. *Intermetallics* **97**, 12–21 (2018).
214. Tang, Q. *et al.* The effect of grain size on the annealing-induced phase transformation in an Al_{0.3}CoCrFeNi high entropy alloy. *Materials & Design* **105**, 381–385 (2016).
215. Anand, K. K., Mahato, B., Haase, C., Kumar, A. & Ghosh Chowdhury, S. Correlation of defect density with texture evolution during cold rolling of a Twinning-Induced Plasticity (TWIP) steel. *Materials Science and Engineering: A* **711**, 69–77 (2018).
216. Kheiri, S., Mirzadeh, H. & Naghizadeh, M. Tailoring the microstructure and mechanical properties of AISI 316L austenitic stainless steel via cold rolling and reversion annealing. *Materials Science and Engineering: A* **759**, 90–96 (2019).
217. Kumar, B. R., Singh, A. K., Das, S. & Bhattacharya, D. K. Cold rolling texture in AISI 304 stainless steel. *Materials Science and Engineering: A* **364**, 132–139 (2004).
218. Sathiaraj, G. D., Pukenas, A. & Skrotzki, W. Texture formation in face-centered cubic high-entropy alloys. *Journal of Alloys and Compounds* **826**, 154183 (2020).
219. Sidor, J., Petrov, R. H. & Kestens, L. Texture Control in Aluminum Sheets by Conventional and Asymmetric Rolling. in *Comprehensive Materials Processing* (eds. Hashmi, S., Batalha, G. F., Van Tyne, C. J. & Yilbas, B.) 447–498 (Elsevier, 2014). doi:10.1016/B978-0-08-096532-1.00324-1.
220. Sakai, T., Belyakov, A., Kaibyshev, R., Miura, H. & Jonas, J. J. Dynamic and post-dynamic recrystallization under hot, cold and severe plastic deformation conditions. *Progress in Materials Science* **60**, 130–207 (2014).
221. Leffers, T. & Ray, R. K. The brass-type texture and its deviation from the copper-type texture. *Progress in Materials Science* **54**, 351–396 (2009).
222. Mecking, H. *Preferred orientation in deformed metals and rocks: An introduction to modern texture analysis.* (1985).
223. Engler, O. Deformation and texture of copper–manganese alloys. *Acta Materialia* **48**, 4827–4840 (2000).
224. Tewary, N. K., Ghosh, S. K., Bera, S., Chakrabarti, D. & Chatterjee, S. Influence of cold rolling on microstructure, texture and mechanical properties of low carbon high Mn TWIP steel. *Materials Science and Engineering: A* **615**, 405–415 (2014).

225. De Cooman, B. C., Estrin, Y. & Kim, S. K. Twinning-induced plasticity (TWIP) steels. *Acta Materialia* **142**, 283–362 (2018).
226. Lee, Y.-K., Lee, S.-J. & Han, J. Critical assessment 19: stacking fault energies of austenitic steels. *Materials Science and Technology* **32**, 1–8 (2016).
227. Curtze, S. & Kuokkala, V.-T. Dependence of tensile deformation behavior of TWIP steels on stacking fault energy, temperature and strain rate. *Acta Materialia* **58**, 5129–5141 (2010).
228. Allain, S., Chateau, J.-P., Bouaziz, O., Migot, S. & Guelton, N. Correlations between the calculated stacking fault energy and the plasticity mechanisms in Fe–Mn–C alloys. *Materials Science and Engineering: A* **387–389**, 158–162 (2004).
229. Liu, J. *et al.* Deformation twinning behaviors of the low stacking fault energy high-entropy alloy: An in-situ TEM study. *Scripta Materialia* **137**, 9–12 (2017).
230. Ashby, M. F. The deformation of plastically non-homogeneous materials. *The Philosophical Magazine: A Journal of Theoretical Experimental and Applied Physics* **21**, 399–424 (1970).
231. Hosford, W. F. Plane-strain compression of aluminum crystals. *Acta Metallurgica* **14**, 1085–1094 (1966).
232. Shih-Chin, C., Duen-Huei, H. & Yun-Kie, C. The effect of textures and grain shape on the shear band formation in rolled F.C.C. metals. *Acta Metallurgica* **37**, 2031–2033 (1989).
233. Bracke, L., Verbeken, K., Kestens, L. & Penning, J. Microstructure and texture evolution during cold rolling and annealing of a high Mn TWIP steel. *Acta Materialia* **57**, 1512–1524 (2009).
234. Barcik, J. The kinetics of σ -phase precipitation in AISI310 and AISI316 steels. *MTA* **14**, 635–641 (1983).
235. Padilha, A. F. & Rios, P. R. Decomposition of Austenite in Austenitic Stainless Steels. *ISIJ International* **42**, 325–327 (2002).
236. Weiss, B. & Stickler, R. Phase instabilities during high temperature exposure of 316 austenitic stainless steel. *MT* **3**, 851–866 (1972).
237. Hsieh, C.-C. & Wu, W. Overview of Intermetallic Sigma (σ) Phase Precipitation in Stainless Steels. *International Scholarly Research Notices* **2012**, (2012).
238. Haghdadi, N. *et al.* Austenite-ferrite interface crystallography dependence of sigma phase precipitation using the five-parameter characterization approach. *Materials Letters* **196**, 264–268 (2017).
239. De la Cuevas, F. A further study of the kinetics of recrystallization and grain growth of cold rolled TWIP steel. *Revista de Metalurgica* **54**, (2018).
240. Kocks, U. F., Argon, A. S. & Ashby, M. F. *Thermodynamics and kinetics of slip*. (1975).
241. Wu, J., Yuan, Y., Gong, H. & Tseng, T.-L. (Bill). Inferring 3D ellipsoids based on cross-sectional images with applications to porosity control of additive manufacturing. *IISE Transactions* **50**, 570–583 (2018).
242. Gwalani, B. *et al.* Interplay between single phase solid solution strengthening and multi-phase strengthening in the same high entropy alloy. *Materials Science and Engineering: A* **771**, 138620 (2020).

243. Laplanche, G. *et al.* Temperature dependencies of the elastic moduli and thermal expansion coefficient of an equiatomic, single-phase CoCrFeMnNi high-entropy alloy. *Journal of Alloys and Compounds* **623**, 348–353 (2015).
244. Ma, S. G. *et al.* Superior high tensile elongation of a single-crystal CoCrFeNiAl_{0.3} high-entropy alloy by Bridgman solidification. *Intermetallics* **54**, 104–109 (2014).
245. Kelly, P. M. The effect of particle shape on dispersion hardening. *Scripta Metallurgica* **6**, 647–656 (1972).
246. Tian, Y. Z. *et al.* A novel ultrafine-grained Fe₂₂Mn_{0.6}C TWIP steel with superior strength and ductility. *Materials Characterization* **126**, 74–80 (2017).
247. Annasamy, M., Haghdadi, N., Taylor, A., Hodgson, P. & Fabijanic, D. Static recrystallization and grain growth behaviour of Al_{0.3}CoCrFeNi high entropy alloy. *Materials Science and Engineering: A* **754**, 282–294 (2019).
248. Mishra, R. S., Kumar, N. & Komarasamy, M. Lattice strain framework for plastic deformation in complex concentrated alloys including high entropy alloys. *Materials Science and Technology* **31**, 1259–1263 (2015).
249. Fribourg, G., Bréchet, Y., Deschamps, A. & Simar, A. Microstructure-based modelling of isotropic and kinematic strain hardening in a precipitation-hardened aluminium alloy. *Acta Materialia* **59**, 3621–3635 (2011).
250. Tian, Q. *et al.* The strengthening effects of relatively lightweight AlCoCrFeNi high entropy alloy. *Materials Characterization* **151**, 302–309 (2019).
251. Xiong, T., Zheng, S., Pang, J. & Ma, X. High-strength and high-ductility AlCoCrFeNi_{2.1} eutectic high-entropy alloy achieved via precipitation strengthening in a heterogeneous structure. *Scripta Materialia* **186**, 336–340 (2020).
252. Soleimani, M., Kalhor, A. & Mirzadeh, H. Transformation-induced plasticity (TRIP) in advanced steels: A review. *Materials Science and Engineering: A* **795**, 140023 (2020).
253. de Formanoir, C. *et al.* Micromechanical behavior and thermal stability of a dual-phase $\alpha+\alpha'$ titanium alloy produced by additive manufacturing. *Acta Materialia* **162**, 149–162 (2019).
254. Anber, E. A. *et al.* Insight into the kinetic stabilization of Al_{0.3}CoCrFeNi high-entropy alloys. *Materialia* **14**, 100872 (2020).
255. Cheng, L. M., Poole, W. J., Embury, J. D. & Lloyd, D. J. The influence of precipitation on the work-hardening behavior of the aluminum alloys AA6111 and AA7030. *Metall Mater Trans A* **34**, 2473–2481 (2003).
256. Proudhon, H., Poole, W. J., Wang, X. & Bréchet, Y. The role of internal stresses on the plastic deformation of the Al–Mg–Si–Cu alloy AA6111. *Philosophical Magazine* **88**, 621–640 (2008).
257. Li, Z. *et al.* Improving mechanical properties of an FCC high-entropy alloy by γ' and B₂ precipitates strengthening. *Materials Characterization* **159**, 109989 (2020).
258. Dillamore, I. L., Roberts, J. G. & Bush, A. C. Occurrence of shear bands in heavily rolled cubic metals. *Metal Science* **13**, 73–77 (1979).
259. Meric de Bellefon, G., van Duysen, J. C. & Sridharan, K. Composition-dependence of stacking fault energy in austenitic stainless steels through linear regression with random intercepts. *Journal of Nuclear Materials* **492**, 227–230 (2017).

260. Okamoto, N. L. *et al.* Size effect, critical resolved shear stress, stacking fault energy, and solid solution strengthening in the CrMnFeCoNi high-entropy alloy. *Scientific Reports* **6**, 35863 (2016).
261. Butt, M. Z. & Feltham, P. Solid-solution hardening. *JOURNAL OF MATERIALS SCIENCE* **28**, 2557–2576 (1993).
262. Yang, X. & Zhang, Y. Prediction of high-entropy stabilized solid-solution in multi-component alloys. *Materials Chemistry and Physics* **132**, 233–238 (2012).
263. Tripathy, S., Gupta, G. & Chowdhury, S. G. High Entropy Alloys: Criteria for Stable Structure. *Metall and Mat Trans A* **49**, 7–17 (2018).
264. Shen, Y. F., Li, X. X., Sun, X., Wang, Y. D. & Zuo, L. Twinning and martensite in a 304 austenitic stainless steel. *Materials Science and Engineering: A* **552**, 514–522 (2012).
265. Fu, X., Schuh, C. A. & Olivetti, E. A. Materials selection considerations for high entropy alloys. *Scripta Materialia* **138**, 145–150 (2017).
266. Bragg, W. H. The intensity of reflexion of X rays by crystals. *The London, Edinburgh, and Dublin Philosophical Magazine and Journal of Science* **27**, 881–899 (1914).
267. Dini, G., Uejji, R., Najafizadeh, A. & Monir-Vaghefi, S. M. Flow stress analysis of TWIP steel via the XRD measurement of dislocation density. *Materials Science and Engineering: A* **527**, 2759–2763 (2010).
268. ASTM E562-11. Standard Test Method for Determining Volume Fraction by Systematic Manual Point Count, ASTM International. *ASTM International, West Conshohocken, PA* (2011).
269. Baudin, T. Analyse EBSD - Principe et cartographies d'orientations. *Tech. l'ingénieur* (2010).
270. Hadadzadeh, A., Mokdad, F., Wells, M. A. & Chen, D. L. A new grain orientation spread approach to analyze the dynamic recrystallization behavior of a cast-homogenized Mg-Zn-Zr alloy using electron backscattered diffraction. *Materials Science and Engineering: A* **709**, 285–289 (2018).
271. Yang, J. Ultrafast Electron Microscopy with Relativistic Femtosecond Electron Pulses. *Electron Microscopy - Novel Microscopy Trends* (2018) doi:10.5772/intechopen.81405.